Advances in Diffusion MRI

By

José M. Guerrero-González

A dissertation submitted in partial fulfillment of

the requirements for the degree of

Doctor of Philosophy

(Medical Physics)

at the

UNIVERSITY OF WISCONSIN-MADISON

2020

Date of final oral examination: 07/29/2020

The dissertation is approved by the following members of the Final Oral Committee:

Andrew L. Alexander, Professor, Medical Physics
Walter F. Block, Professor, Medical Physics
Guang-Hong Chen, Professor, Medical Physics
Nagesh Adluru, Associate Scientist, Waisman Laboratory for Brain Imaging and Behavior
Peter A. Ferrazzano, Professor, Pediatrics

For

Jose Luis y Agustina …

… Alvaro, Isabel, Luis, y Marilu …

… Adan y Elena …

… El resto de la Familia Guerrero, Guzman, Gonzalez …

… Teofilita y Sandra, and the rest of the Ocon and Nava Families…

… Ron and Mindy …

… Carlos, Emmanuel, Mendieta, and Connor …

… Vero, Cesar, Nancy, Victor …

You are the village it takes.

Abstract

Diffusion-weighted MRI (dMRI) represents a well-established field for the study of micro-structure in tissue and other porous media. Yet, the pipeline from image acquisition to analysis and application of imaging markers is dynamic and components within it are ever evolving. The field continues to enthuse researchers to extend, refine, and create imaging instruments as well as data processing and analysis methods. It is in this spirit that this work set out to improve – or augment to – the dMRI pipeline in areas associated with modeling, analysis, and validation.

Biophysical models represent an important instrument for establishing links between the dMRI signal and biological properties of tissue microstructure. However, due to the number of parameters needed to faithfully describe the signal in terms of the complex tissue micro-architecture, biophysical modeling methods need to rely on assumptions that are often oversimplifying. One component of this work conducted an empirical study of the model in Neurite Orientation Dispersion and Density Imaging (NODDI) regarding assumptions for the intra-cellular parallel intrinsic diffusivity.

Understanding individual variability of dMRI-based markers is an important task when studying conditions with high inter-subject heterogeneity such as traumatic brain injury and autism. A second component of this work focused on developing a framework based on the Mahalanobis Distance, as a multivariate approach for individualized evaluation of imaging-based measures.

Validation of apparent diffusion coefficients (ADCs) estimated from dMRI measurements requires the use of test media with known diffusion coefficients as well as their temperature dependence. A third component of this work sought to develop a test object (phantom)

constructed from liquids whose diffusion constants at multiple temperatures were previously characterized. Models of the diffusion-temperature relationships where investigated for their potential use in estimating the temperature of the phantom from dMRI measurements.

Acknowledgements

It has been a privilege to have had Dr. Andrew Alexander as my advisor. In key moments of my PhD journey he was the source of encouragement, guidance, and persistence. Yet, his mentorship conveyed in me a sense of autonomy for venturing and exploring my own interests. Most importantly, he has been a kind and generous mentor.

I am also thankful to have had the counsel of Dr. Nagesh Adluru. Our endless office conversations about physics, math, and life, and his unwavering enthusiasm for learning of any kind kept me engaged and brought great joy to my days at the lab. All of this work would have not been what it is without his support.

The support from Dr. Douglas Dean III has been especially valuable in my career as well. His insights and expertise helped me to advance and make progress at various stages of my work. His early work on multivariate analysis helped to inspire and launch a good portion of this dissertation.

I would also like to thank Dr. Steve Kecskemeti for his willingness to share with me his MRI physics knowledge. I am especially thankful to him for his assistance on work that included phantom studies.

It has been a treat to have shared an office with Gregory Kirk. His superluminal mind let us into spending more time than we would like to confess conversing about number theory, wars, computer science, politics, quantum physics, food, neuroscience, and life.

I am grateful to have had the chance to overlap with other graduate students in our lab: Dr. Samuel Hurley and Dr. Andrew Hoy who welcomed me into the lab and provided me with great

initial advice and support; Austin Bazydlo and Jason Moody who I shared great moments with in the lab and at conferences.

It is an honor to have been part of Dr. Alexander's Lab, the Waisman Center, and the Medical Physics Program. All provided an environment which surrounded me with the technical resources and expertise that made this work possible. I'm particularly thankful to Michael Anderle, David Thompson, and Ty Christian.

I am also honored to have had the members of my preliminary exam and thesis mentoring committee, which include Dr. Edward Jackson, Dr. Guang-Hong Chen, Dr. Walter Block, Dr. Peter Ferrazzano, Dr. Nagesh Adluru, and Dr. Andrew Alexander.

I feel lucky to have taken part in Dr. Guang-Hong Chen's computer tomography class, which was a transformative experience in my quest for achieving a deeper understanding of the fundamentals of imaging. I looked forward to his lectures and indulged in his beautiful derivations of imaging principles.

I am thankful for my high school and undergraduate professors and advisors: Tim Kulak, Jorge España, Dr. Leonard Weisenthal, Dr. Joseph Kozminski, Dr. Chuck Crowder, and Dr. Dallin Durfee. They helped to shape the base of my career and have unconditionally supported me throughout the years.

I would like to recognize the Science and Medicine Graduate Research Scholars Fellowship Program, the National Science Foundation Graduate Research Fellowship Program, and the Morse Society Fellowship Program for their financial support.

Finally, I am forever indebted to my Family and Sandra Ocon for their unbendable support throughout the years, both moral and financial, in seeing this through the end. Esto es de ustedes.

TABLE OF CONTENTS

List of Figures

List of Tables

Chapter 1 - Introduction

1.1 Dissertation Overview

This dissertation is composed with work from three main projects regarding the imaging modality known as diffusion-weighted MRI as well as a basic discussion of its history and theory. Though, apparently different from each other, the three projects are interconnected and have the common goal of improving or adding to specific aspects of the diffusion imaging framework.

The main objective of the first project, presented in Chapter 3, is to inspect the assumptions of an existing biophysical model, which aims to describe the diffusion MRI signal by assuming certain geometries about tissue microstructure. The second project, presented in Chapter 4, has as its main goal to develop a method for the simultaneous use of multiple diffusion imaging-based measures in carrying out single-subject analyses. And the third project, presented in Chapter 5, aimed to develop a test object for validation of diffusion coefficient measurements in isotropic materials that could also be used to estimate the temperature of the materials.

1.2 Dissertation Outline

Chapter 2 dives into historical and theoretical aspects of MRI and diffusion-weighted MRI. Many of the principles introduced there will be revisited throughout Chapters 3-5. The chapter begins with a discussion of Brownian motion and Einstein's derivation of the diffusion equation that is fundamentally connected to diffusion imaging. What follows is a historical recount

accompanied by relevant theoretical inserts, which aims to connect relevant events starting from the development of nuclear magnetic resonance (NMR), passing through the discovery of molecular diffusion as a source of signal attenuation artifacts and then developed as a useful tool to estimate diffusion coefficients, and ending with the transition from NMR to MRI methods of imaging from projections, Fourier space imaging, and rapid imaging with echo-planar imaging.

Next, the development of the diffusion tensor imaging (DTI) technique is discussed as a widely used approach for studying anisotropic diffusion behavior in biological tissue. DTI plays a central role in Chapter 5 as the source of scalar metric maps used in the study traumatic brain injury. Additionally, the framework presented in Chapter 5 makes use of a method known as tractography, which is also introduced in Chapter 2 as a way for utilizing directional information derived from DTI in tracing pathways that are used to represent white matter tracks in the human brain. Inherent limitations of the diffusion tensor model are highlighted, including the nonspecific nature of anisotropy measurements, awareness of non-prolate tensors in the brain, and the inability of the tensor model to resolve crossing fibers within a voxel. Chapter 2 concludes with a brief look at several promising techniques that move beyond the Gaussian model of diffusion, such as diffusion kurtosis imaging and other multicompartment biophysical models, as well as technological advances that serve to enhance the current state of the field and continue to move it into new horizons.

Chapter 3 dives into a biophysical multicompartment model technique known as neurite orientation dispersion and density imaging (NODDI), which is introduced in Chapter 2.

Advantages offered by NODDI over DTI are discussed along with how the technique experienced a rapid uptake by researchers in the field, using it in a wide array of applications that include investigations of normal brain development as well as pathological conditions. A discussion of the assumptions of the model is presented along with the limitations incurred by the technique as a result. One of the limitations of the model having to do with the intra-cellular parallel diffusivity being fixed is reviewed and emphasized, and a framework for testing the strength of the assumption is described. This framework is centered on an empirical approach and includes fitting the model to data sets varying in imaging protocol as well as in sex and age of the participants. The analysis aims to expose the performance of the model fit under the original assumption for the varying characteristics of the data and to seek the optimal performance of the model fit when the assumption is relaxed. Results show that age group, imaging protocol, and tissue type, influence the model fit. Specifically, the model fitting performance can be optimized for the infant brain and gray matter if the assumption of fixed parallel diffusivity is relaxed to take values that are lower than the original fixed value.

Chapter 4 describes a novel framework for studying single subject variability of white matter microstructure. The chapter reviews the reasons for desiring to develop a technique that is able to compare an individual to reference group for studying conditions with high inter-subject variability such as autism and traumatic brain injury. The project outlined in this chapter seeks to have a method that is spatially specific enough compared to traditional region of interest methods, but more forgiving in the number of multiple comparisons and image alignment requirements compared to voxel-based approaches. In the proposed approach, microstructure

between one individual and a reference group is compared using a composite measure from multiple DTI scalar metrics known as the Mahalnobis distance. The comparisons are conducted at discrete pieces along a white matter pathway represented by a tractogram. The way in which tractograms are generated is described. This includes the processing of diffusion weighted images with a method known as constrained spherical deconvolution, which is briefly discussed in chapter 2, and feeding the result into a deep learning-based tool for extracting specific white matter pathways. The discretization of a pathway into several pieces is also described as part of a method known as tractometry, which is used for generating profiles of different scalar metrics along the pathway. The chapter proceeds with the demonstration of the framework in the single subject comparison of 22 severe traumatic brain injury cases to a reference group of 49 healthy age matched controls. The results show the methods ability to find abnormalities in several locations along several white matter pathways in the TBI cases.

The chapter describes how the data from the TBI patients was collected at different sites and with different scanner brands and models. It also contains a detailed analysis of a test object (or phantom) that was used in gathering scans from a subset of sites and comparing them to data for the same phantom collected at the control group site. The phantom contains vials whose diffusion coefficient values at zero degrees Celsius are known. The measured diffusion coefficients from the imaging data were matched across sites and correction relationships were derived for use in applying a correction to the human scans for those sites. The multivariate analysis for those specific subjects was replicated with the corrected diffusion values. The results show great correspondence between corrected and uncorrected values, indicating site effects were not problematic for this analysis.

The phantom work in Chapter 4 leads nicely into **Chapter 5**, which also focuses on a diffusion-based phantom. The fundamental link between diffusion and temperature is introduced in Chapter 2, but an explicit relationship between temperature and diffusion is detailed in Chapter 5. The need for a test object in checking for consistency of measurements in multi-center studies is emphasized by the work presented in Chapter 4. However, the requirement of scanning the phantom at zero degrees (or other known temperature) introduces unwanted effects related to the often tedious and involved preparation procedures. The work in Chapter 5 is an exploration into an alternative approach. This consists of using the known diffusion-temperature relationship between two materials to derive an equation that allows for estimating the temperature of the materials using the diffusion weighted images themselves. Further, the approach is independent of the diffusion weighting quantity known as *b-value*, which is a prescribed parameter for each scan and is susceptible to both system and human error. Five different materials, including water, are selected for developing the method and a temperature control and monitoring system is built for validation purposes.

The chapter outlines how this project faced challenges related to low viscosity of the materials being used and convection currents introduced by vibration of the scanner table. These vibrations are related to the strong diffusion gradients from the scan acquisitions. When the motion coincides with the direction of diffusion sensitization, the signal experiences attenuation that is not due to molecular diffusion. These artifacts proved difficult to correct and the fundamental issues that caused them could not be overcome. The chapter concludes with a description of measures implemented for addressing the vibration issues, which included

placing weights on the scanner table. Potential future actions to address the vibration issues are discussed.

Finally, contributions and key findings from the work presented in chapters 3-5 are summarized in **Chapter 6**. In concluding the chapter, possible future developments and potential applications are discussed.

Chapter 2 - Background

Portions of this chapter have been submitted for publication in the 2nd Edition of the book "*Functional Neuroradiology: Principles and Clinical Applications*", by Scott H. Faro (Editor), Feroze B. Mohamed (Editor), Meng Law (Editor), John T. Ulmer (Editor),
as the chapter entitled *Diffusion Tensor Magnetic Resonance Imaging – Physical Principles*. Jose M. Guerrero, Thomas A. Gallagher, Andrew L. Alexander, and Aaron S. Field.

2.1 Abstract

One of the intentions for this chapter is to familiarize the reader with the background information that is relevant to the work presented in chapters 3, 4, and 5, and to provide some historical context to the field of diffusion MRI. First, the molecular hydrodynamics that give rise to the macroscopic diffusion phenomenon that is observable with the naked eye are introduced. The mathematical principles of the diffusion coefficient and statistics of molecular displacement are presented as the foundation for studying Gaussian diffusion. Then, the historical milestones that permit determination of apparent diffusion coefficients with nuclear magnetic resonance and magnetic resonance imaging are reviewed. The extension of the Gaussian model of diffusion to the multidirectional case in diffusion tensor imaging is discussed for imaging anisotropic features in microscopically porous materials. The procedure for filling a diffusion tensor matrix and extracting its eigenvalues and eigenvectors is explained and the role of these parameters in shaping a Gaussian "ellipsoid" into a visual representation of anisotropic diffusion is presented. Scalar metrics derived from the diffusion tensor eigenvalues, including fractional anisotropy (FA), are discussed, followed by an introduction to white matter fiber tracking ("tractography"). Inherent limitations of the tensor model are highlighted throughout the discussion, including the nonspecific nature of anisotropy measurements and the inability

of the tensor model to resolve crossing fibers within a voxel. Restricted diffusion imaging is discussed with multicompartment biophysical models as way to address the lack of specificity in DTI. Fiber orientation distribution mapping is presented as an alternative to resolve crossing fibers within a voxel. The chapter concludes with a brief look into other techniques that go beyond the Gaussian model for diffusion as well as promising emerging technological advances that continue to move the field forward.

2.2 What is there to measure? – Random Walks

While diffusion may seem an intuitive process on a macroscopic scale, the happenings at the microscopic scale are of great importance to the magnetic resonance specialist who wishes to image diffusion phenomena. Consider the familiar example of releasing a drop of water-soluble dye into the center of a glass of water. We expect the dye to "diffuse" outward from its origin in all directions, migrating from areas of higher concentration toward areas of lower concentration. Intuitively we know that the longer we observe the process, the more the dye will be distributed throughout the glass. This process appears to be quite predictable—almost orderly, from our macroscopic vantage point—but if we could zoom in and observe the behavior of a *single* molecule strolling about its molecular neighborhood, a fundamentally *disorganized* world would emerge, which begs the question: what exactly "powers" the process of diffusion? In 1827, botanist Robert Brown first described the curious jiggling motion of tiny pollen grains under a microscope (Figure 2.1). Puzzled as to whether it represented some sort of fundamental "life energy," he sought and found similar *Brownian motion* in inorganic materials, suggesting that some physical phenomenon was at work [1].

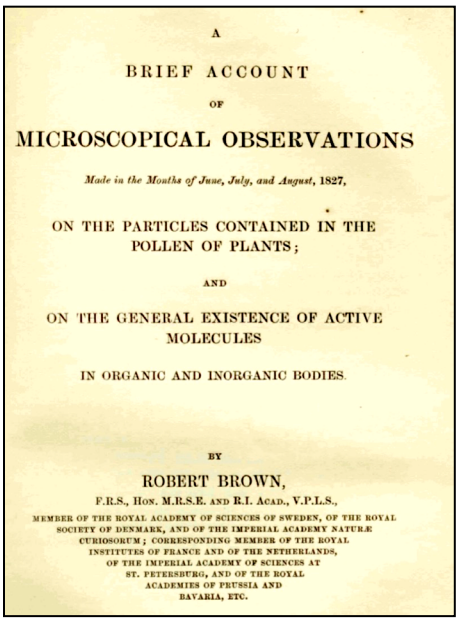

A

BRIEF ACCOUNT

OF

MICROSCOPICAL OBSERVATIONS

Made in the Months of June, July, and August, 1827,

ON THE PARTICLES CONTAINED IN THE POLLEN OF PLANTS;

AND

ON THE GENERAL EXISTENCE OF ACTIVE MOLECULES

IN ORGANIC AND INORGANIC BODIES.

BY

ROBERT BROWN,

F.R.S., Hon. M.R.S.E. and R.I. Acad., V.P.L.S.,

MEMBER OF THE ROYAL ACADEMY OF SCIENCES OF SWEDEN, OF THE ROYAL SOCIETY OF DENMARK, AND OF THE IMPERIAL ACADEMY NATURÆ CURIOSORUM; CORRESPONDING MEMBER OF THE ROYAL INSTITUTES OF FRANCE AND OF THE NETHERLANDS, OF THE IMPERIAL ACADEMY OF SCIENCES AT ST. PETERSBURG, AND OF THE ROYAL ACADEMIES OF PRUSSIA AND BAVARIA, ETC.

Figure 2.1 The 1828 published work cover in which Robert Brown described the curious motion in particles of pollen under a microscope. Adapted from [2].

It was later proposed by Albert Einstein (and others) that individual molecules were normally in a constant state of random motion and could achieve random displacements as a result of local thermodynamic conditions, namely heat. It is thermodynamically necessary for all systems to become more disorganized as time marches forward, which we know as the law of entropy. Accordingly, an organized group of molecules will tend to become more dispersed and disorganized the longer we observe them. Molecules at higher temperature tend to do this faster, undergoing more frequent random collisions and greater displacements. Einstein's great contribution was to formally quantify this phenomenon, and in doing so, lent support to the existence of atoms (which was further validated by Perrin, earning him a Nobel prize in 1926).

Taking into consideration (temperature and viscosity-dependent) molecular displacement Δr and the observation time interval Δt, a diffusion coefficient for a group of molecules can be determined from the Einstein's diffusion equation:

$$D = \frac{< \Delta r^2 >}{2n\,\Delta t}$$ Equation 2.1

where $< \Delta r^2 >$ is the mean-squared displacement, n is the number of spatial dimensions, and D is the diffusion coefficient.

We can now imagine diffusion without boundaries, termed *isotropic* diffusion, in 3 dimensions as an expanding sphere whose radius represents mean displacement, which is proportional to the square root of the diffusion coefficient D and the observation time according to Einstein's equation [3]:

$$< \Delta r > = \sqrt{6D\Delta t}$$ Equation 2.2

How then does Brownian motion, sometimes referred to as the "random walk" of a molecule, often denoted *B(t)* with *t* = time, help explain the macroscopically very predictable phenomenon of diffusion? Attempts to distill a function describing a random walk prove to be challenging. If a molecule starts out at point *B*(0) at time = 0 and ends at point *B*(*t*) at time *t*, we would at least expect a continuous path through space, and if plotted as a function of time, we do indeed observe a continuous function for *B*(*t*). Upon close inspection, however, the haphazard, random displacements that comprise a molecule's swagger render its position as a function of time completely non-differentiable (Figure 2.2), meaning essentially that the molecule's path defies a mathematical description without resorting to probability theory.

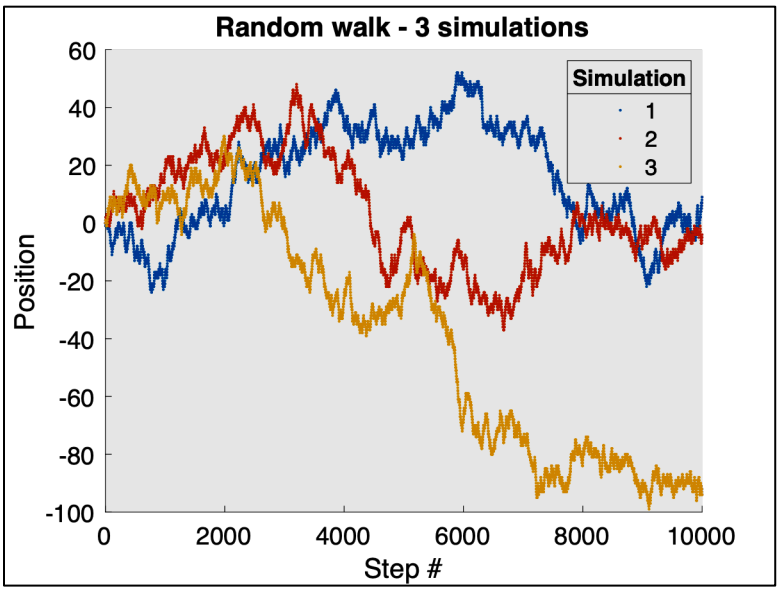

Figure 2.2 Illustration for three different simulations of displacement as a function of steps. 10000 steps were allowed for a molecule subject to Brownian motion, each case being equally probable yet highly variable. These are stochastic functions continuous over time but not differentiable. Adapted from [2].

While nothing definite can be said about the future path of a single molecule, we can talk about expected displacement for a large group of molecules undergoing random motion by employing a so-called *probability density function* (PDF), the most well-known being a "normal" or *Gaussian* distribution. Probability theory and the PDF are the mathematical substrates for modeling molecular diffusion and play a central role in diffusion tensor MRI (DTI).

To better understand the role of probability in diffusion, we can construct a simple, albeit idealized experiment. Consider a group of water molecules centered at an origin, with each molecule given the independent possibility of stepping either forward or backward along the *x*-axis for each of n steps. If we allow 4 steps, we then have $(2)^4$ possible combinations of steps and thus 16 different possible paths. Since many of these paths will yield the same net displacement, and since some paths are more likely than others, a distribution of net displacements is expected. For instance, for a molecule undergoing some random combination of 3 steps forward (F) and 1 step back (B), there prove to be 4 different ways to achieve this

$(FFFB, FFBF, FBFF, BFFF)$, all resulting in the same net displacement of 2 steps to the right of the origin. If we examine the distribution for all possible combinations of displacements after $n = 4$ steps, we perform the following calculations utilizing the formula:

$$\frac{(n)\cdots n!}{(k)\cdots k!\,(n-k)!\quad p^k(1-p)^{n-k}} \qquad \text{Equation 2.3}$$

where $n = total\ \#\ steps$ (or Bernoulli trials), $k = steps\ taken$, $p = q = 0.5$, (i.e. the probability of p (step forward) 0.5 and q (step backwards) 0.5).

$\frac{4!}{0!(4-0)!} = 1\ possibility,$
$\frac{4!}{1!(4-1)!} = 4\ possibilities,$
$\frac{4!}{2!(4-2)!} = 6\ possibilities,$
$\frac{4!}{1!(4-1)!} = 4\ possibilities,$
$\frac{4!}{0!(4-0)!} = 1\ possibility$

If we choose to look at this graphically, we can plot the findings as featured in Figure 2.3(A). Water molecules that have achieved the greatest net displacement (4 steps to the right or 4 steps to the left) are in the great minority, simply because the probability for such an occurrence is much lower, 1 out of 16. Alternatively, there are 4/16 ways to end up 2 steps to the right, 4/16 ways to end up 2 steps to the left, and 6/16 (37% of water molecules) ways to end up where they started (this is known as *zero-displacement probability* in the parlance of *q*-space and diffusion spectrum imaging, to be discussed in a later section). In general, we can summarize our experiment by arbitrarily assigning the probability of p (step forward) 0.5 and q (step backwards) 0.5. It necessarily follows that $p + q = 1$ since there is certainty that either of these events will take place. Further, we can attempt to model the distribution of results for n steps by $(p + q)^n$, which may look familiar as the basis for the binomial distribution. With n

sufficiently large, the binomial distribution approximates a normal distribution (Figure 2.3(B)). Instead of only 4 steps as in our example, imagine that $n = 50$ steps are allowed for a random walk. We would expand the binomial distribution $(p + q)^{50}$ and calculate the coefficients and resultant terms. To avoid a quite laborious process, we can use Equation 2.3. To keep things simple, let us investigate the probability that a molecule could get 50 steps away from the origin. In this case, $n = k = 50$ and $p = q = 0.5$. We have:

$$\frac{50!}{50!(0)!} = (0.5)^{50} \times (1 - 0.5)^{0} \text{ or } (0.5)^{50} \text{ with coefficient 1.}$$

Since we have 2^{50} total possibilities, the overall probability is 1 divided by 2^{50}, which is an exceedingly small value. If n is taken sufficiently large, our discrete binomial distribution will approach a continuous, normal distribution (Figure 2.3) featuring a mean displacement that is also reflected in Einstein's equation.

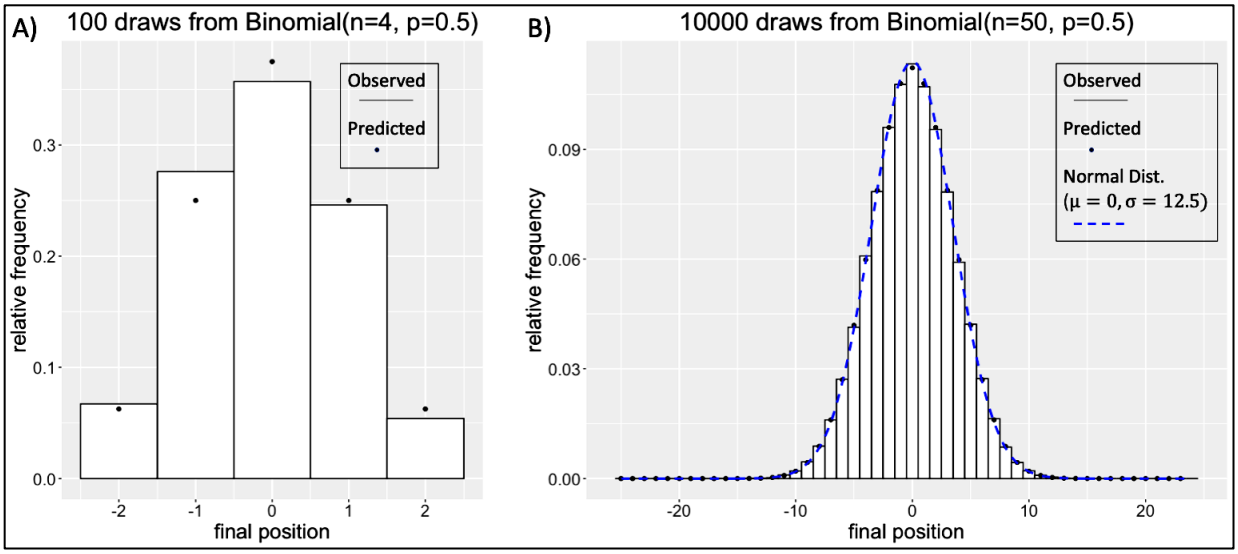

Figure 2.3 Illustrations of expected and observed displacement distribution arising from a water molecule undergoing two different number of independently random steps (forward or backward). A) 4 steps played out 100 times. B) 50 steps played out 10000 times. As more steps are allowed more molecules (larger proportion) finish farther from the origin. The sum of all proportions is of course necessarily equal to 1. Adapted from [2].

With all other factors remaining equal, we envision diffusion as a sphere with radius equal to the mean displacement, enlarging with the square root of time (Figure 2.4).

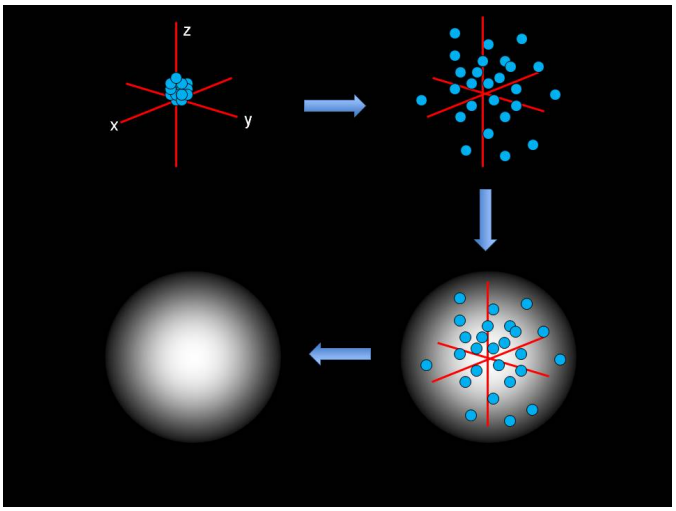

Figure 2.4 3-D Probability density function (PDF). In 3-dimensional space, displacements due to diffusion can take place in any random direction. For a collection of points, the PDF has the appearance of a spherical cloud with higher concentration near the center. Using the root mean squared displacement as the spherical cloud radius, an *isoprobability* surface on the sphere is created. The PDF is isotropic when no barriers are present. The spherical cloud will grow with increased diffusion coefficient or increased time. This model is only appropriate when no physical hindrances are present (isotropic diffusion). For physiologic diffusion, displacement occurs along and between white matter tracts and comes across all kinds of barriers (anisotropic diffusion), leading to modeling difficulties as will be seen. Adapted from [2] and courtesy of Thomas Gallagher, Aaron Field, and Andrew Alexander.

2.3 What to measure with? – NMR then MRI

2.3.1 The Phenomenon of Nuclear Magnetic Resonance

In a series of momentous events that would open the door to mapping of diffusion coefficient estimates by way of MRI, the first great scientific leap was the pioneering experiments on nuclear magnetic resonance (NMR) by Felix Bloch and Edward Purcell in the mid 1940s [4]–[6]. The crucial moment came with the realization that the proton's nuclear spin could be coupled to and manipulated with external magnetic fields. In their experiments, a macroscopic magnetization could be achieved from the collective contributions of individual nuclei magnetic

moments in a water sample polarized by a constant magnetic field. That is, when placed in the strong magnetic field, initially randomly oriented moments would align with the field's direction, some parallel some anti-parallel to the field. The excess number of parallel moments would give rise to a macroscopic magnetization (Figure 2.5). One remarkable observation was the precessing of the magnetization around the magnetic field with a frequency, ω_0, that was specific to the constant field, B_0, and to the proton species (e.g. Hydrogen) by way of its gyromagnetic ratio, γ. The specific frequency, ω_0, is known as the Larmor frequency and $\omega_0 = \gamma B_0$ as the Larmor equation.

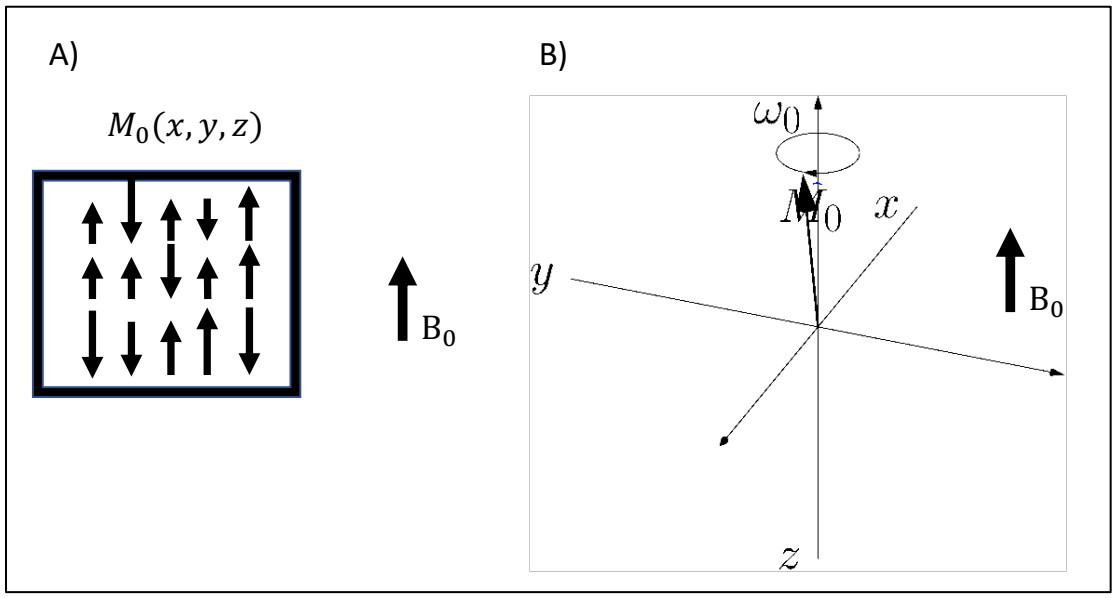

Figure 2.5. A) Illustration of Individual magnetic moments in a nuclear sample, polarized by constant magnetic field B_0. B) Total magnetic moment (magnetization) resulting from excess parallel spins, denoted by vector $\mathbf{M_0}$ precessing about an axis parallel to the direction of B_0, with frequency ω_0.

Bloch reported that, once polarized, the macroscopic magnetization could subsequently be subjected to a pulsating field, B_1, applied at right angles to the strong polarizing field. As the Larmor frequency approached that of the pulsating field (resonance), the magnetization would process around the constant magnetic field at decreasing latitudes (Figure 2.6(A,B)). This could

be interpreted as two events simultaneously occurring to the magnetization due to the applied external fields: precession about the strong static field, B_0, and nutation about the pulsating orthogonal field, B_1. Bloch's report also showed that while the magnitude of the magnetization was very small (~$3\ x\ 10^{-6}\ gauss$) and difficult to detect on its own, its transverse component precessing about the constant field produced a detectable voltage signal in a receiving detector coil near the sample. It became customary to describe the precession phenomenon in a rotating coordinate system with angular frequency -ω_0, such that moving into this frame of reference makes the total magnetization $\boldsymbol{M_0}$ appear stationary (Figure 2.6(C)).

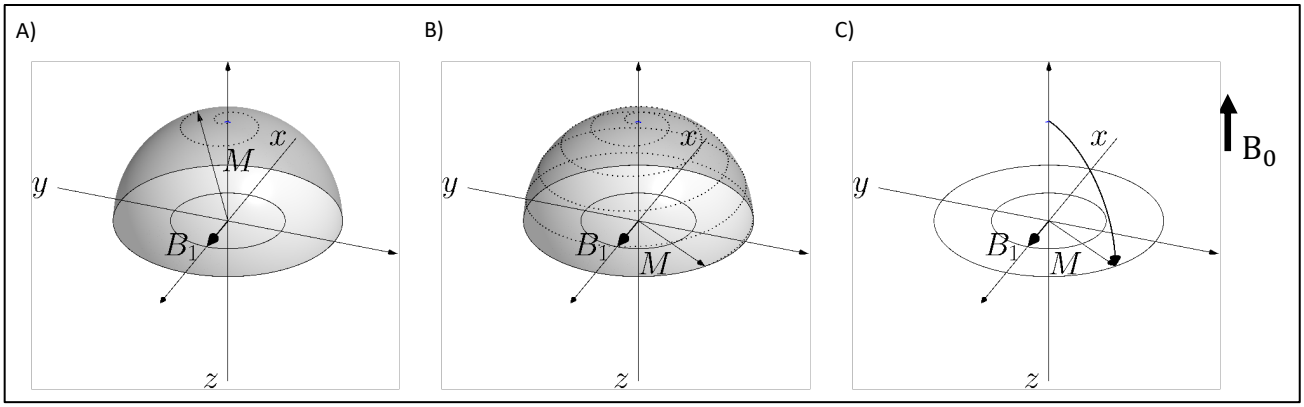

Figure 2.6. A, B) Illustration of net magnetization experiencing the combined processes of precession around the direction of B_0 at decreasing latitudes from the xy-plane, and nutation by pulsating radio frequency field B_1, as observed from the laboratory frame of reference. C) Observed from a frame of reference rotating at -ω_0, the net magnetization appears to only experience nutation by B_1. After removal of the pulsating field, a component of the net magnetization precesses with ω_0 about the z-axis on the equatorial plane defined by the x and y axes.

The behavior of the magnetization in the presence of the external magnetic fields and with respect to time is elegantly described by the Bloch equations, named after the Swiss-born American physicist and his pursuit for characterizing spin-magnetic field interactions.

2.3.2 Transverse signal time evolution

Regarding the Bloch equations, of particular interest to our discussion is the solution to the time differential equation that describes the time evolution of the component of the magnetization precessing at right angles to the constant magnetic field, $M_{\perp}$. This is the component of magnetization that gives rise to a voltage signal in a detector coil placed next to the sample,

$$M_{\perp} = M_0 e^{-i\omega_0 t}\, e^{-\frac{t}{T2}} \qquad \text{Equation 2.4}$$

Equation 2.4 predicts that, following the removal of the pulsating field, the magnetization will continue to precess with ω_0 but its amplitude will decrease (relax) with a rate determined by a time constant $T2$, defined as the time when transverse magnetization has lost 63% of its original amplitude M_0. T2 is an intrinsic property of materials (as is T1, the time constant describing the recovery rate of the main polarized magnetization known as longitudinal magnetization).

Transverse relaxation is related to local proton-proton (spin-spin) interactions as a result of progressively increasing local magnetic field inhomogeneity. That is, the physical principles underlying decay caused by T2 have to do with how easily energy is transferred between spins and how that transfer impacts their local magnetic environment. For example, in tissue the many protons sequestered in molecules of fat have a more efficacious transfer of energy and thus signal loss is quicker than for protons in water, resulting in a longer T2 for water than for

fat. T2 also depends on temperature, since temperature directly influences the frequency of molecular interaction.

2.3.2 Signal attenuation by Diffusion in NMR

The next great scientific leap in this account occurred when it was realized that diffusing spins added another source of decay in the magnitude of the transverse signal. Shortly after the publication of the Bloch and Purcell seminal papers, Erwin Hann made the observation in his famous spin-echo experiments in 1950 (described in the next section) that the amplitude of the transverse magnetization signal (echo) would decrease due to the random thermal motion of spins in the presence of magnetic field inhomogeneities [7].

Individual magnetic moments experience flips (phase changes) as time passes and the number of neighboring molecule interactions increase. These phase differences accumulate over time (phase accumulation or dephasing) leading to T2 relaxation and are exacerbated by Brownian motion of the spins. Random-position-fluctuating spins will undergo rapid changes in the field they experience, hence, changes in phase.

Much in the same way as the random walk description in the first section of this chapter (Figure 2.2), paths (or phase changes) traced by discrete, random spin-jumps of individual molecules would be impossible to predict, but the accumulated phase distribution of a spin ensemble can be described using a probabilistic approach. This key observation, initially made by Hann, was subsequently exploited by Carr and Purcell in relating transverse signal attenuation to a distribution of phase accumulation due to random, discrete spin

displacements, and led them to one of the first published measurements of the self-diffusion coefficient of water by way of NMR [8].

According to Carr and Purcell, for a large number m of spins diffusing in one dimension, in the presence of a background gradient field G, and in a homogenous sample, their phase distribution after N steps approaches a Gaussian probability distribution centered around its mean value – safely assumed according to the central limit theorem. With the mean phase change being zero, the probability of finding the i^{th} spin with accumulated phase, ϕ, is

$$P(\phi) = \frac{e^{-\frac{\phi^2}{2<(\phi_i)^2>}}}{\sqrt{2\pi < (\phi_i)^2 >}} \qquad \text{Equation 2.5}$$

For a time τ_s between each step, and step size d, the average squared accumulated phase for the i^{th} spin at time t was approximated as

$$< (\phi_i)^2 > = \frac{1}{3} G^2 \gamma^2 d^2 \frac{t^3}{\tau_s} \qquad \text{Equation 2.6}$$

Averaging over the ensemble according to $P(\phi)$, the decay of the magnetization due to the collective random spin walk is given by

$$M_0 e^{-\frac{<(\phi_i)^2>}{2}} = M_0 e^{-\frac{1}{2}\left(\frac{1}{3}G^2\gamma^2 d^2 \frac{t^3}{\tau_s}\right)}$$

Noting from Einstein's diffusion equation that

$$\frac{d^2}{2\tau_s} = D$$

the attenuation of the transverse signal as a function of diffusion and T2 is given by

$$M_{\perp} = M_0 e^{-i\omega_0 t}\, e^{-\frac{t}{T2}}\, e^{-\left(\frac{1}{3}G^2\gamma^2\, t^3 D\right)} \qquad \text{Equation 2.7}$$

It is common to write this as

$$M_{\perp} = M_0 e^{-i\omega_0 t}\, e^{-\frac{t}{T2}}\, e^{-bD} \qquad \text{Equation 2.8}$$

where

$$b = \frac{1}{3} G^2\gamma^2\, t^3 \qquad \text{Equation 2.9}$$

is the quantity describing the *amount* of diffusion weighting commonly referred to as the *b-value.*

A formal addendum to the Bloch equations was made by Torrey in order to account for diffusion (and coherent flow) at the foundation level of the theory [9]. The formalism became

known as the Bloch-Torrey equations. At the time, interestingly, diffusion effects were seen as artifactual and detrimental to NMR signals (echoes). Carr and Purcell in their seminal publication come to device a mechanism for mitigating the effects of diffusion. Nonetheless, the ensuing decade saw a number of reports beginning to use NMR deliberately as a tool for estimating self-diffusion coefficients.

2.3.3 The Pulsed Gradient Spin-Echo Experiment

It is here, in the timeline towards MRI-based diffusion mapping, that next came the work of Stejskal and Tanner. Their contribution in the form of magnetic field pulse and gradient sequences for intentionally making diffusion be the dominant source of decay in the NMR signal and relating it to molecular displacement has transcended across the decades. Their diffusion preparation design is still the most widely used basic unit in diffusion-based imaging sequences today (Figure 2.8, Figure 2.12).

In 1965, Stejskal and Tanner unveiled their famous pulsed-gradient spin echo experiment for the direct measurement of diffusion with NMR [10]. Years earlier, Carr and Purcell had shown (based on initial observations by Hann) that dephasing effects due to inhomogeneities of the constant field could be reversed by application of a second oscillating field, following the pulse used to tip the longitudinal magnetization onto the transverse plane by 90 degrees. This field would be applied in a direction parallel to the transverse plane a short time after the first $\pi/2$ pulse, flipping the direction of the angular dephasing magnetic moments by 180 degrees.

Some time TE after the reversal, the spins would come in phase briefly to form an echo (peak in the signal) and start dephasing again, see Figure 2.7.

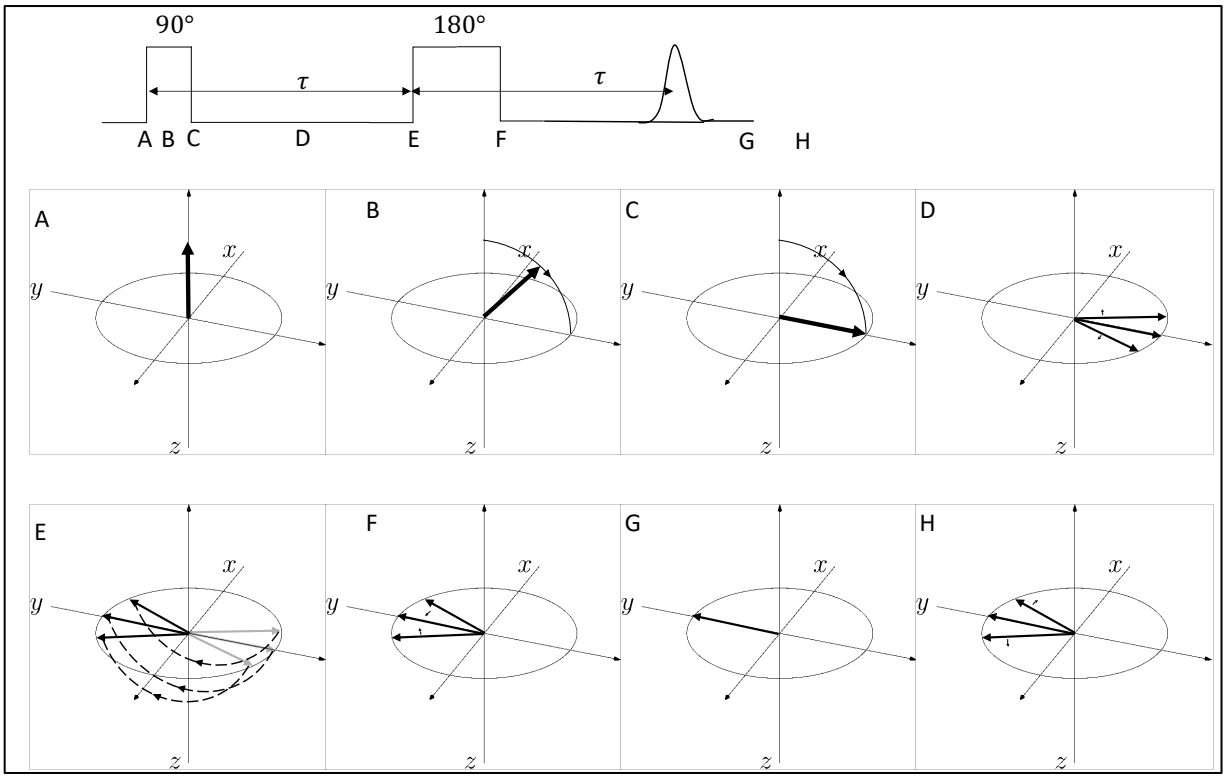

Figure 2.7. Illustration of spin-echo formation as observed from the rotating coordinate system. A) Net magnetization at equilibrium position at time $t = 0$. B) Application of an RF field B_1 orthogonal to B_0 leads to the magnetization vector rotation about B_1. C) Application and removal of the $90°$ pulse leaves the net magnetization on the equatorial plane defined by the x and y axes precessing with ω_0. D) Non-uniformities in the main magnetic field, B_0, lead to small differences in the individual moment Larmor frequencies, and fanning of the individual magnetic moments begins to occur as some moments get ahead and others fall behind in their precession. E) The RF field B_1 is applied a second time at time $t = \tau$ for a duration that is enough to rotate the magnetic moments by $180°$ such that at the end of the pulse they are still left to rotate about the z-axis on the equatorial plane. F) Following the $180°$ pulse, the individual moments continue to rotate with the same frequency they possessed before the pulse and retain their relative positions with one another. As a result, they begin to gather as time advances. G) At time $t = 2\tau$ a perfect regathering of the individual moments occurs and a maximum voltage is induced in the receive coil. This occurrence of maximum signal is referred to as 'echo'. H) Fanning begins to occur again and the signal experiences decay.

Stejskal and Tanner's insight was to introduce a pair of large magnetic field gradients strategically placed in time such that they flanked the refocusing 180-degree pulse (Figure 2.8).

The idea being that while the first pulse would purposely dephase all spins in the imaging volume, the second pulse would reverse this effect. For stationary spins, the effects of the second pulse cancel those of the first, i.e., phase coherence is reestablished during the second pulse and no diffusion-related signal loss results. However, moving spins that underwent a net displacement in the direction of the applied gradients would experience a slightly different magnetic environment during the second pulse because of their new position, and would accumulate phase shifts proportional to their displacement. This dephasing would result in exponential decay of MR signal proportional to both, the spin displacement as reflected by their diffusion coefficient, D, and the *diffusion weighting, b-value*. Equation 2.9 for the *b-value* can be modified to account for duration, δ, and spacing of the diffusion gradients, Δ, to give

$$b = (\gamma G \delta)^2 [\Delta - (\delta/3)] \qquad \text{Equation 2.10}$$

.

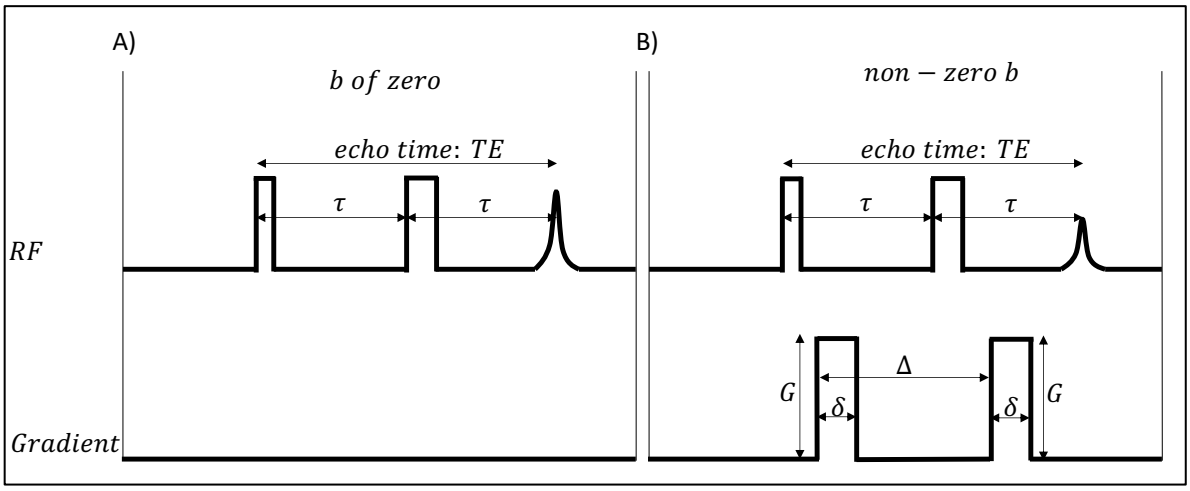

Figure 2.8 Illustration of pulsed-gradient spin echo experiment for sensitization of NMR signal to molecular displacement due to thermal motion. A) sequence for measurement without diffusion weighting b=0. B) sequence for measurement with diffusion weighting specified by non-zero b-value.

Two measurements, then, conducted at two different *b-values*, permit the calculation of the diffusion coefficient of a material by way of NMR. Typically, one of the *b-values* is set to 0. Thus, from Equation 2.8 and in a frame of reference rotating with frequency -ω_0 so that the precession term $e^{-i\omega_0 t}$ cancels out, the signal $S_{b=0}$ at time $t = TE$ is

$$S_{b=0} = S_o\,(e^0)\,(e^{-\frac{TE}{T2}})$$

$$S_{b=0} = S_o\,(e^{-\frac{TE}{T2}}) \qquad \text{Equation 2.11}$$

You will recognize that this is the equation for simple spin-spin T2 decay (Equation 2.4). For the second measurement with some non-zero diffusion weighting b_1, we have:

$$S_{b1} = S_o\,(e^{-b_1 D})\,(e^{-\frac{TE}{T2}}) \qquad \text{Equation 2.12}$$

Simply dividing the diffusion weighted measurement by the *b*-zero measurement gives:

$$\frac{S_{b1}}{S_{b=0}} = e^{-b_1 D} \qquad \text{Equation 2.13}$$

Here we see that all terms cancel except $e^{-b_1 D}$, which is a diffusion-weighted measurement (diffusion weighting given by b_1) that is devoid of T2 effects. This is commonly known as the

"exponential" measurement (exponential image in MRI). Finding the diffusion coefficient is now a simple matter:

$$D = -\frac{1}{b_1}\ln\left(\frac{S_{b1}}{S_{b=0}}\right) \qquad \text{Equation 2.14}$$

2.3.4 From NMR to MRI

The next important scientific feat in the path towards diffusion-weighted MRI came about in the 1970s when NMR crossed into the imaging realm. Chemist Paul Lauterbur published his groundbreaking manuscript titled "Image Formation by Induced Local Interactions: Examples Employing Nuclear Magnetic Resonance" in 1973 [11]. Lauterbur demonstrated that the spatial origin of NMR signals could be located by imposing a spatially varying magnetic field on a sample of precessing magnetic moments.

When the only external field interacting with the spins in a sample is B_0 in the z direction, all the spins precess with the same frequency ω_0. When excited with an additional external field B_1, tuned to the Larmor frequency, then left to precess, the spins do so with the same frequency ω_0. As they precess, the spins act as individual oscillators and become the sources of a radio frequency signal (at ω_0) that can be recorded on a proximal detector coil. More importantly, the region of precessing spins represents a spatial distribution of magnetization with amplitude that can be described by a function $m(x, y, z)$. Lauterbur recognized that if it

were possible to measure the amplitude of magnetization at different spatial locations, a reconstruction of $m(x, y, z)$ could be produced.

It is not possible to excite and record the magnetization of each spatial location of the object. Instead, each point of the recorded signal comes from the entire sample at a specific point in time. As all spins precess with the same frequency, the individual signals all remain in phase, and the total time signal is a sum of constructive interreference at all time points. If the spins were to precess at different frequencies their individual signals would go in and out of phase creating a time interference pattern. That is, the total time signal would vary as individual signals add constructively and destructively at different points in time depending on their frequency.

From the Larmor equation, it is easy to see that imposing a field gradient that varies the field strength linearly with space would alter the frequency profile of the oscillating spins. For example, a gradient parallel to the $x\ axis$, G, would give way to a spatially dependent frequency profile $\omega(x) = \omega_0 + \gamma G x$. Therefore, a controlled linearly varying field introduces a controlled linear variation in frequency. Most importantly, if our object is a distribution defined in a 2-D space, $m(x, y)$, a linear gradient magnetic field along one dimension, say x, will define frequency bins parallel to the other direction (y). The frequency of each bin being a function of their spatial location in x. The signal generated when the gradient G is present after excitation, is composed from contributions of emitting oscillators over the range of frequencies defined by G. All of the spins within a frequency bin oscillate with the same frequency. Therefore, adding the individual magnetization amplitudes along a frequency bin, yields the amount of that frequency present in the recorded signal. Sums along bins (line integrals) spanning the width of

the distribution in the x direction constitute a projection of the object in a direction parallel to the y axis.

Lauterbur demonstrated that a linear magnetic field gradient overlaid on a sample of excited spins produced a time signal whose Fourier transform yielded the frequency content in the signal. Each frequency component corresponding to the contributions of a spin-band at some x location. The frequency spectrum corresponded to the frequency per bin or the projection of the magnetization distribution in the direction of the applied gradient. A one-dimensional view, thus, could be formed since each x coordinate was encoded as a temporal frequency in the signal. This gave rise to the method of imaging by projections (Figure 2.9), one of the two basic MR imaging methods; the other being Fourier encoding (described in the next section).

For projection angle 0, projection of $m(x, y)$ along y is given by the Fourier transform of the time signal $s_r(t)$ when the gradient is applied in the x direction. Projections at other angles can be obtained by applying gradients along different directions. It is important to note, that when rotating the direction of the gradient, the direction of the field remains in the z direction. The filtered back projection method was well stablished by then in the reconstruction of x-ray computerized tomography (CT) images. Therefore, by acquiring a sufficient number of projections (views) via the excitation and reception of signals from different gradient directions, a reconstruction of $m(x, y)$ could be achieved through filtered back projection.

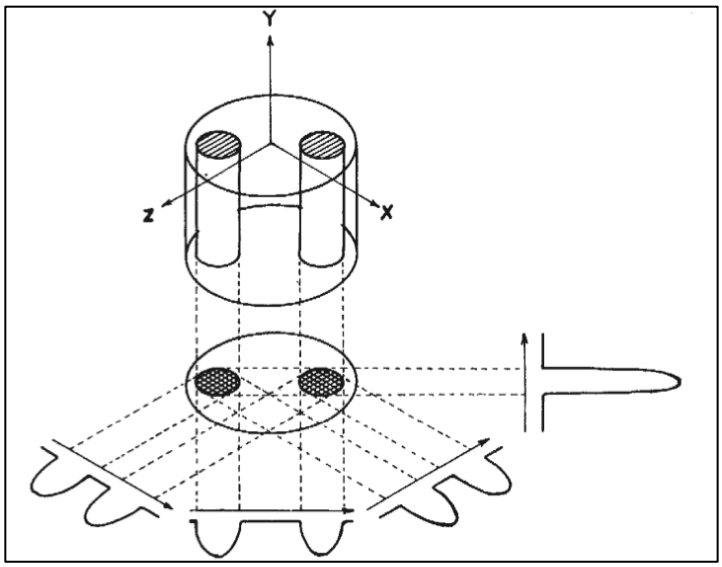

Figure 2.9. Historical figure of the method of imaging by projections. P. Lauterbur - "Image Formation by Induced Local Interactions: Examples Employing Nuclear Magnetic Resonance", 1973.

Mathematically, ignoring the relaxation and diffusion terms in Equation 2.8, the signal from an oscillating spin at position (x, y) can be written as

$$m(x,y)e^{-i\omega t}$$

which is a rotating vector of amplitude $m(x, y)$ and frequency ω. If a gradient G in the x direction is present, the frequency ω is a function of the spatial coordinate x as $\omega(x) = \omega_0 + \gamma G x$. Integrating over the whole xy-plane of excited spins the total recorded signal, $s_r(t)$, can be expressed as

$$s_r(t) = \int_x \int_y m(x,y)\, e^{-i(\omega_0 + \gamma G x)t}\, dxdy \qquad \text{Equation 2.15}$$

Again, if we assume a frame of reference that rotates with frequency -ω_0 so that the *baseline* precession frequency term $e^{-i\omega_0 t}$ cancels out, we can write the adjusted signal $s(t)$ as

$$s(t) = e^{+i\omega_0 t} S_r(t)$$

$$= \int_x \int_y m(x,y)\, e^{-i(\gamma G x)t}\, dxdy$$

We can then integrate the variable y out by letting

$$h(x) = \int_y m(x,y)\, dy$$

which is the projection of $m(x,y)$ along y, so that

$$s(t) = \int_x h(x) e^{-i(\gamma G x)t}\, dx$$

Dividing and multiplying by a factor of 2π in the exponent, gives us

$$s(t) = \int_x h(x) e^{-i2\pi\left(\frac{\gamma G}{2\pi} t\right) x}\, dx \qquad \text{Equation 2.16}$$

The integral on the right can be recognized as the Fourier transform of the projection $h(x)$. Therefore, the inverse Fourier transform of the time signal $s(t)$ can be performed to recover the projection of $m(x, y)$ along y as

$$h(x) = \int_t s(t) e^{i2\pi\left(\frac{\gamma G}{2\pi}x\right)t}\, dt \qquad \text{Equation 2.17}$$

Although this result is specific for projection angle $\theta = 0$, it can be generalized by defining gradients x and y in terms of the projection angle as $G_x = G cos\theta$ and $G_x = G cos\theta$.

2.3.5 Fourier Space Imaging

In the years after Lauterbur's groundbreaking publication, works by Sir Peter Mansfield, Richard Ernst, and William Edelstein among others, laid the framework for a method that became known as Fourier imaging [12]–[14]. The premise of the method lies in the existence of a space in which the two-dimensional Fourier transform of the magnetization distribution resides. Obtaining sufficient measurements of the distribution in this space would allow to recover the spatial distribution by a simple inverse 2-D Fourier transform. The description below shows how the Fourier space is defined.

It is clear from Equation 2.16, that the frequency *amount* that can be encoded in the time signal depends on the strength of G and the time t that G is on. More explicitly, the extent which frequencies from thinner and thinner bins are *visible* in the Fourier-transformed projection $s(t)$

is determined by how far the quantity $\left(\frac{\gamma G}{2\pi}t\right)$ moves from its baseline value of zero. It is possible for this quantity to take on negative values because the gradient G is with respect to the constant main field B_0. In terms of frequencies, the spatially dependent frequencies are defined with respect to the central frequency ω_0, such that if at a certain x coordinate the field is $(B_0 + G)$ then $\omega(x) = \omega_0 + \gamma G x$. On the other hand, when at another x coordinate the field is $(B_0 - G)$ then $\omega(x) = \omega_0 - \gamma G x$. This peculiar characteristic permits for having a Fourier-transformed-projection axis with negative values, an origin, and positive values.

Additionally, as gradients can be applied in arbitrary directions, it is possible to apply a gradient in the y direction *truly* orthogonal to the gradient in the x direction that we have been considering until now. Thus, two orthogonal gradients imposed on a plane of excited spins can be used to define a coordinate system on the sample in which spatial positions and frequencies are uniquely linked.

In fact, the projection reconstruction method implies the existence of such coordinate system. By applying a gradient oriented in a direction different from that of the x-axis, the resulting 1-D Fourier transform of the projection provides information along a radial slice of the 2-D Fourier transform of the distribution $m(x, y)$ at the angle θ. This is known as the central slice theorem. The radial slice is defined in a 2-D coordinate system where the horizontal axis is given by $\left(\frac{\gamma G(x)}{2\pi}t_x\right)$ and the vertical axis is given by $\left(\frac{\gamma G(y)}{2\pi}t_y\right)$.

The interference pattern (the recorded signal) resulting from the interaction of RF signals emitted from individual spins is the same whether it is observed as function of time or as function of phase. That is, moving through different phases of the signal is the same as moving

through different time points in the signal. One could turn on a gradient with constant strength G in the y direction for a time t and record the interference pattern over that time. Alternatively, one could vary the strength of the gradient G, play the gradient field for a predetermined time interval t_y in order to achieve a certain phase, and generate points of the interference pattern as desired by simply varying the strength G. The former approach moves us in time, the latter one moves us in phase.

This effectively allows for constructing a coordinate system where the vertical axis is built one step at time as we vary the strength of $G(y)$ in $\left(\frac{\gamma G(y)}{2\pi} t_y\right)$ at each of N steps, and the horizontal axis being set as *typical* by $\left(\frac{\gamma G(x)}{2\pi} t\right)$, which is achieved by a constant gradient over time t.

For each step n in the vertical direction, the amplitude distribution $m(x, y)$ is moved in phase as

$$m(x, y)e^{-i\gamma G_{(y,n)} y t_y} = m(x, y; n)$$

At a given phase, once the required time interval t_y has expired and G_y is turned off, the amplitude distribution in this *state* is projected onto the horizontal axis by playing gradient G_x over time t, thus, a time signal can be generated and recorded.

The total signal in the rotating frame can be written as

$$s(t;t_y) = \int_x \int_y m(x,y)\, e^{-i\gamma G_{(y,n)} y t_y} e^{-i\gamma G_x x t}\, dxdy \qquad \text{Equation 2.18}$$

For any give value of G_y, the interval t_y is set and t is variable. As before, we can integrate the variable y out by letting

$$h_{t_y}(x) = \int_y m(x,y)\, e^{-i2\pi\left(\frac{\gamma G_{(y,n)}}{2\pi} t_y\right) y} dy$$

which is nothing more than the projection of $m(x,y;n)$ along y. Then

$$s(t;t_y) = \int_x h_{t_y}(x) e^{-i2\pi\left(\frac{\gamma G_x}{2\pi} t\right) x}\, dx \qquad \text{Equation 2.19}$$

which tells us that at each step n in the vertical axis, the recorded signal is the Fourier transform of the projection of the phase-moved amplitude distribution, $m(x,y;n)$.

When a sufficient number of projections is collected, a two-step inverse Fourier transform can be performed to recover $m(x,y)$. When the Fourier transform is performed in the horizontal direction, the time signals are transformed into projections, with each projection corresponding to a step in the vertical axis. A second Fourier transform on this vertical stack of projections, but performed along the vertical direction, yields back the distribution $m(x,y)$. See Figure 2.10.

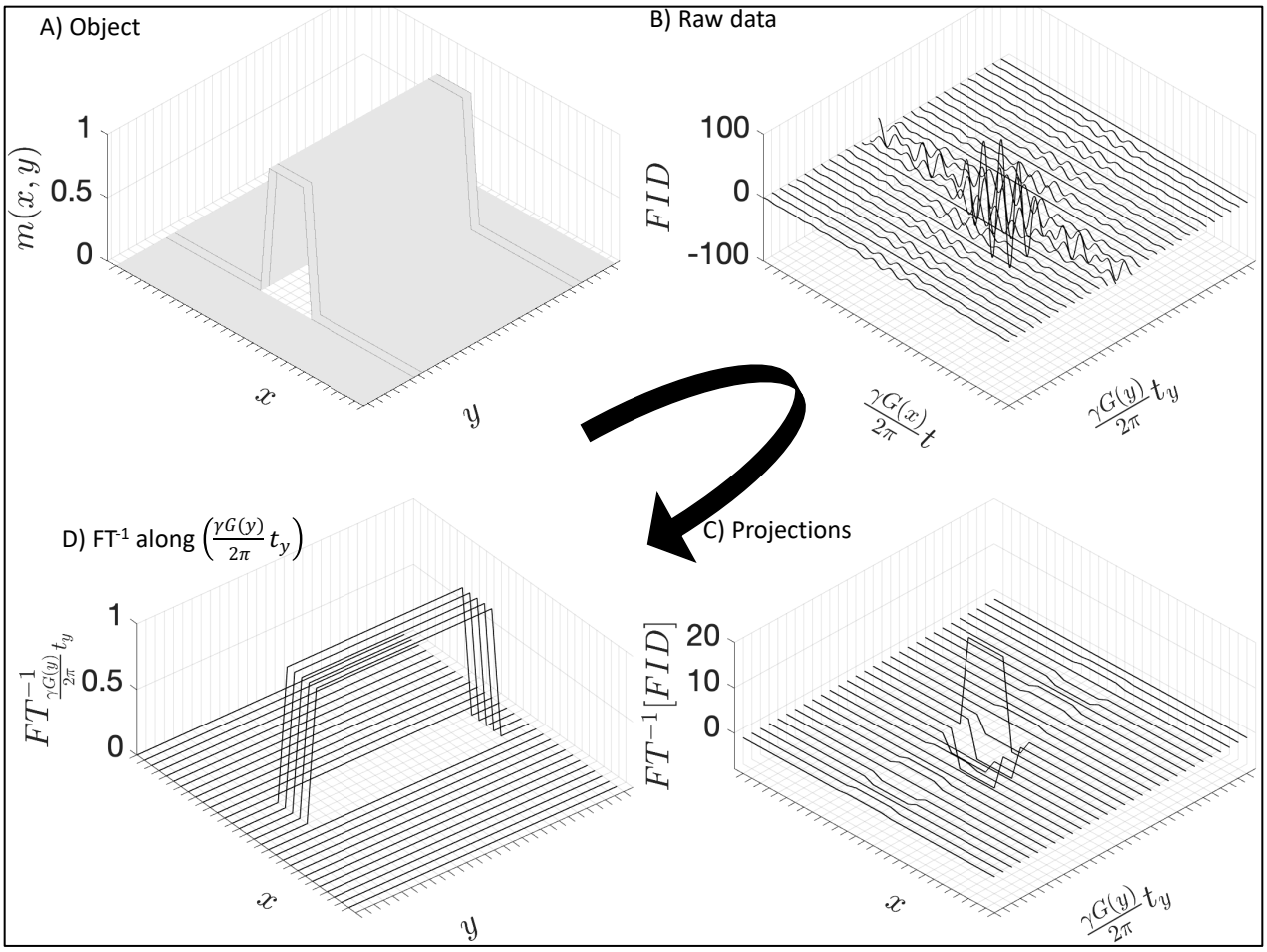

Figure 2.10. Fourier imaging example. A) Object represented by distribution $m(x, y)$. B) For each n=30 $G_{(y,n)}t_y$ configurations, a signal (or FID) of the resulting $m(x, y; n)$ is recorded. C) Fourier spectra of each of n=30 FIDs obtained by a Fourier transform of each FID along the $\left(\frac{\gamma G_x}{2\pi} t\right)$ axis. This gives a projection of each of the 30 phase-moved $m(x, y; n)$. D) A second Fourier transform performed along the $\left(\frac{\gamma G_{(y,n)}}{2\pi} t_y\right)$ axis recovers the object $m(x, y)$.

2.3.6 Rapid Imaging with EPI

In the basic 2-D FT imaging sequence, a single line of Fourier space is read out after each excitation. The interval between readouts also known as repetition time, TR, is long. In the early days of MRI, the time in acquiring a single slice made of N_y lines (TR · N_y) was on the order of several minutes. This imposed a great limitation in the ability to image dynamic processes (e.g. diffusion) in biological organisms, as well as in dealing with motion effects.

In the decade spanning years 1977 through 1987, Sir Peter Mansfield helped to establish a technique that became known as echo-planar imaging (EPI) [15]–[17]. This scheme did not require multiple excitations before a number of readouts could be recorded, reducing the time to acquire an entire slice from minutes to tens of milliseconds.

With echo-planar imaging, after a single RF excitation, the data necessary to reconstruct an image of reasonable quality can be collected using a train of echoes with a short step in the vertical Fourier space direction between each echo. Coverage of Fourier space is performed in a raster trajectory collecting multiple readout lines per excitation (Figure 2.11).

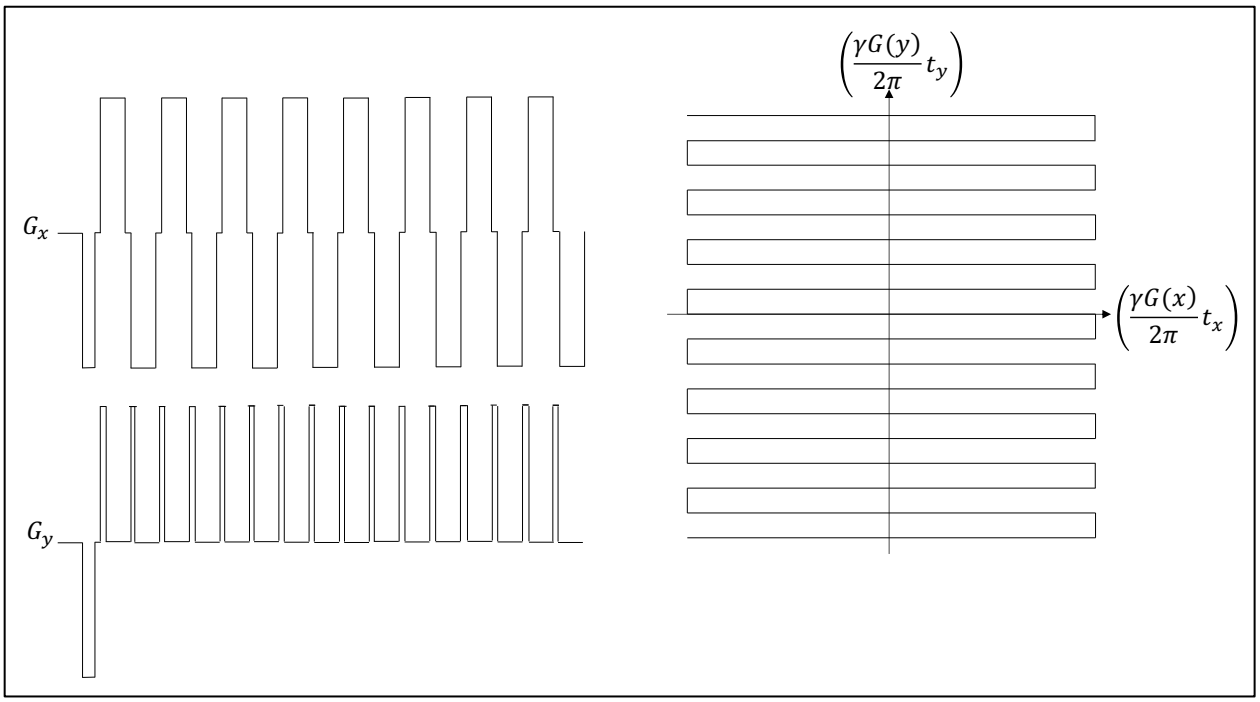

Figure 2.11. *Echoplanar gradient waveforms and Fourier-space trajectory. Time-varying gradient waveforms (left panel) that enable coverage of an entire Fourier space plane (right panel) after a single RF excitation.*

2.3.7 The last stretch: diffusion NRM to diffusion MRI

The beginning of diffusion coefficient mapping with MRI was occurring in parallel with the rapid evolution experienced in the field in the decades of 1970 and 1980. Taylor and Bushell reported

in 1985 the first MRI image weighted by molecular diffusion in a hen's egg [18]. In 1986, Denis LeBihan reported the first brain MRI images weighted by diffusion of healthy human brains as well as brains with cancer tumors using a whole-body scanner. His report included some of the first brain maps of diffusion coefficients [19].

But it was the advent of echo-planar imaging that fully opened the door to the beginning of diffusion mapping with MRI as we know it, because it provided a mechanism to cope with motion in living organisms. A typical diffusion-weighted MRI sequence today (Figure 2.12) consists of a pulsed gradient T2 spin echo acquisition with a single shot echo planar readout (SS-EPI).

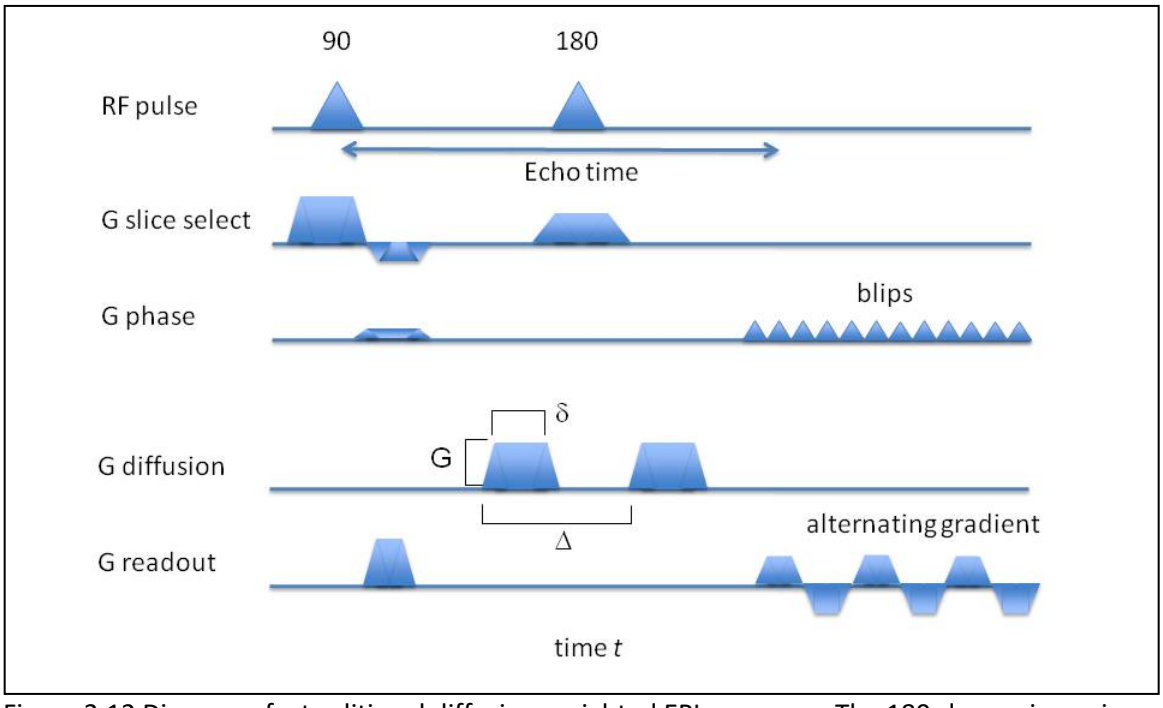

Figure 2.12 Diagram of a traditional diffusion-weighted EPI sequence. The 180-degree inversion pulse is sandwiched by two large diffusion encoding gradients. The quantity known as the *b-value* is composed by the strength, duration, and spacing of the diffusion encoding gradients. Alternating read-out gradients between phase-encoding blips rapidly fill Fourier space. Adapted from [2] and courtesy of Thomas Gallagher, Aaron Field, and Andrew Alexander.

The transition of the theory from diffusion NRM into diffusion MRI with the PGSE-SS-EPI sequence is a seamless affair. The measurements S_{b1} and $S_{b=0}$ in Equation 2.14 can be acquired as images. A map of diffusion coefficients (or apparent diffusion coefficients as described next) of the human brain can be achieved using Equation 2.14 as described in Figure 2.13.

In the laboratory, the diffusion coefficient for pure water without any hindrances (isotropic diffusion) at 20°C is 2 x 10^{-3} mm^2/s while at body temperature of 37°C it is 3 x 10^{-3} mm^2/s. (Chapter 6 provides a more detailed description of the temperature dependence of D). In the brain, diffusion coefficients are variable and generally less than 3 x 10^{-3} mm^2/s [20]. This is a direct consequence of natural barriers, such as myelinated axons, which are most relevant to DTI (9-13). Other barriers become evident when water is partially "trapped" within or between cells, which may be swollen or more densely packed than normal, such as occurs in the setting of cytotoxic edema and hypercellular tumors, respectively. Moreover, any incoherent molecular motions (i.e., motion that appears to be random on a spatial scale corresponding to an imaging voxel), such as motion related to active transport or flow phenomena, may result in molecular displacements that manifest as "pseudodiffusion" on DWI. For these reasons, the term *apparent diffusion coefficient* (ADC) was introduced to distinguish the coefficient that we measure in tissue from Einstein's "self" diffusion coefficient for free media. In parts of this work D will continue to be used for simplicity with the understanding that it is indeed only apparent.

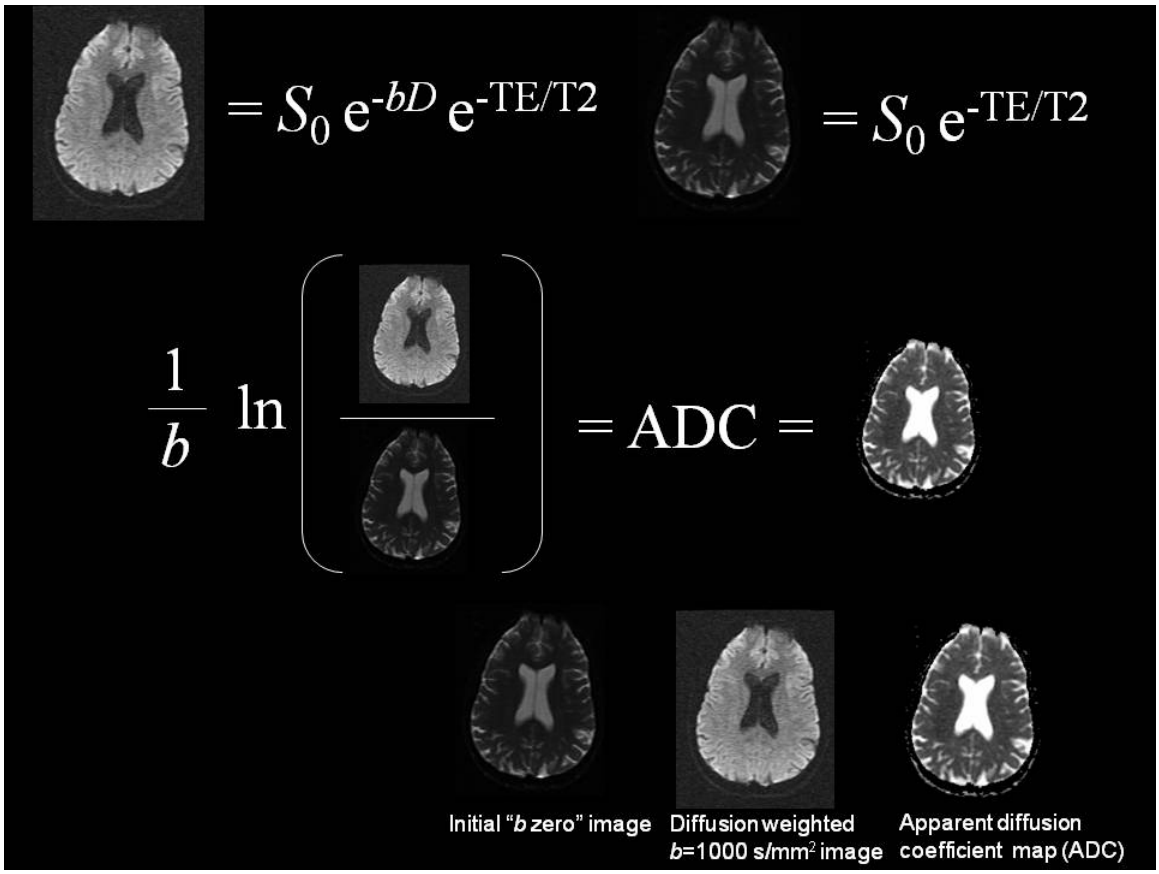

Figure 2.13 Apparent diffusion coefficient map calculation. The initial b_0 image cancels T2 effects by using it to divide the diffusion weighted image. The natural logarithm of the exponential image divided by the b_0 image, multiplied by the inverse of the diffusion weighting b, gives the apparent diffusion coefficient, ADC. Adapted from [2] and courtesy of Thomas Gallagher, Aaron Field, and Andrew Alexander.

This concludes what has been, by a long shot, a vastly under-sampled account of the rise of diffusion imaging with NMR and MRI in this section. The full account is not only rich in detail but comes with drama and failures and it is a fascinating one. In this brief account, important characters have been left out which include Callaghan who developed an elegant theory of MRI microscopy and Rabi who had first observed the MR phenomenon in a beam of particles in the 1930s. Details that have been left out include those about the great innovations in engineering, physics, and computer science as well as other imaging feats such as slice selective excitation that were necessary for the field to evolve into the complexity that it possesses today. All which

allows the type of quality that is required for imaging properties of the insides of living organisms. Entire books have been dedicated to telling the story of MRI and diffusion MRI from the beginning to the present. This chapter section only aimed to present some of the relevant background for better understanding the work that was conducted and presented in the remaining chapters.

2.4 ANISOTROPIC DIFFUSION

In the early 1990s, it was reported that the value of the apparent diffusion coefficient depends on the direction of the applied diffusion encoding gradient [21], [22]. This suggested that the organization of the underlying tissues, namely white matter, influenced the observed diffusion profile in a manner that depends on the "perspective of the observer." Among the many candidate sources of this diffusion anisotropy, including intracellular cytoskeletal elements, axonal membranes, myelin sheaths, and active transport mechanisms, it was determined that intact axonal cell membranes serve as the major basis for anisotropy in the central nervous system[23]–[26], which can be further influenced by the presence or absence of myelin. Myelin, however, does not appear to be the principal determinant of anisotropy [25].

In a DWI acquisition, the diffusion-encoding gradients can be applied in just one direction at a time (though a recent category of acquisition schemes allows for diffusion-encoding along multiple directions simultaneously, this is discussed at the end of this chapter), resulting in a single diffusion-weighted image of the brain along with an ADC map reflecting the magnitude of diffusion *in the direction of the applied gradients.* Suppose we obtain a diffusion-weighted image and associated ADC map of the brain with the diffusion-encoding gradients applied

roughly parallel to the x- (left-right) axis. These images will demonstrate relatively less diffusion in the posterior limbs of the internal capsules, where the corticospinal tracts course roughly perpendicular to the direction of the applied gradients. If we instead apply the diffusion-encoding gradients along the z- (craniocaudal) axis, the optic radiations, corpus callosum, and other white matter tracts coursing in the axial plane, rather than the corticospinal tracts, will now appear to have relatively less diffusion. Considering that white matter tracts run in essentially all directions and that these directions are arbitrary with respect to the scanner geometry, acquiring a simple, unidirectional diffusion-weighted image would be a highly unpredictable affair and may yield an image that is difficult to interpret. This phenomenon, whereby normal physio-anatomical diffusion anisotropy interacts unpredictably with the image acquisition parameters, is the diffusion-imaging equivalent of the radiologist's adage, "one view is no view." In order to ameliorate these anisotropic effects, clinical DWI typically consists of three acquisitions, each with the diffusion gradients applied in a direction orthogonal to the other two. The mean of these images becomes the final diffusion-weighted image we view clinically. The respective apparent diffusion coefficients are also averaged to yield the final ADC map. (This averaged ADC is sometimes called the *trace* for reasons that will be explained in the following section.)

2.5 DIFFUSION TENSOR IMAGING (DTI)

2.5.1 Tensors

Diffusion tensor MR imaging extrapolates on the same basic principles of conventional DWI, however the ultimate goal is rather different. As explained in the previous section, conventional DWI involves the averaging of three image sets obtained with mutually orthogonal diffusion-

encoding directions, in order to rid the final image of physio-anatomical anisotropic effects. In contrast, diffusion tensor imaging (DTI) was designed to depict and quantify those effects, the ultimate goal being a more complete characterization of the 3-dimensional diffusion profile, voxel by voxel. This procedure was first described by Basser et al. [27].

If challenged to arrange weights around a tire so that it would rotate smoothly around a central axis, you would not clump all of them closely together before giving it a spin. The tire would wobble incessantly, much like the way an uneven load in a washing machine may cause it to shimmy across the floor. Intuition tells us to arrange the points of mass symmetrically around a central axis to preserve smooth rotation. Each point of mass in a rotating system, depending on its radius from the center of rotation, has angular momentum and a moment of *inertia*, which contributes to the overall motion of the object in question. In three dimensions, we can summarize all of these contributions with a *tensor*.

Essentially, a tensor is an array or matrix of numbers used to describe a quantity that is too complex to be represented by a single number (a *scalar)* or even a list of numbers (a *vector*). Quantities whose values change according to direction in three-dimensional (3-D) space, such as mechanical stress or moment of inertia—or diffusion—are some common examples of tensor quantities.

For the *inertia tensor*, which is a square, 3x3 matrix, each entry corresponds to the moment of inertia in a different direction within the *x, y,* and *z* coordinate axes (entries I_{xx}, I_{xy}, I_{xz}, etc). If we gave the whole coordinate axis a random spin, depending on the distribution of mass, the *preferred* axis of rotation of the system may not agree with the one you have

provided, and the system may become unstable. In order to predict a smooth axis of rotation, we can perform a series of mathematical operations on a tensor that will provide us with its *eigenvalues* and *eigenvectors*. The prefix *eigen* is a German term indicating "self" or "characteristic" and in the mathematical context of "*eigen*value," it refers to the "self-defining" or "characteristic" values of a tensor.

Even a seemingly chaotic system, once captured by a tensor, may have a hidden, underlying structure or central organization that may allow us to predict where it is headed or how it will behave. To identify this underlying structure, we find its *eigenvalues* (λ_1, λ_2, λ_3) and *eigenvectors* ($\mathbf{e}_1$, $\mathbf{e}_2$, $\mathbf{e}_3$). Eigenvectors have direction, with magnitude conferred by their corresponding eigenvalues. Matrix *diagonalization* is a mathematical process that removes the off-diagonal entries in a matrix, leaving the eigenvalues along the main diagonal. An eigenvector column matrix, **E**, and its matrix transpose, $\mathbf{E}^T$, flank the newly diagonalized matrix (Figure 2.14).

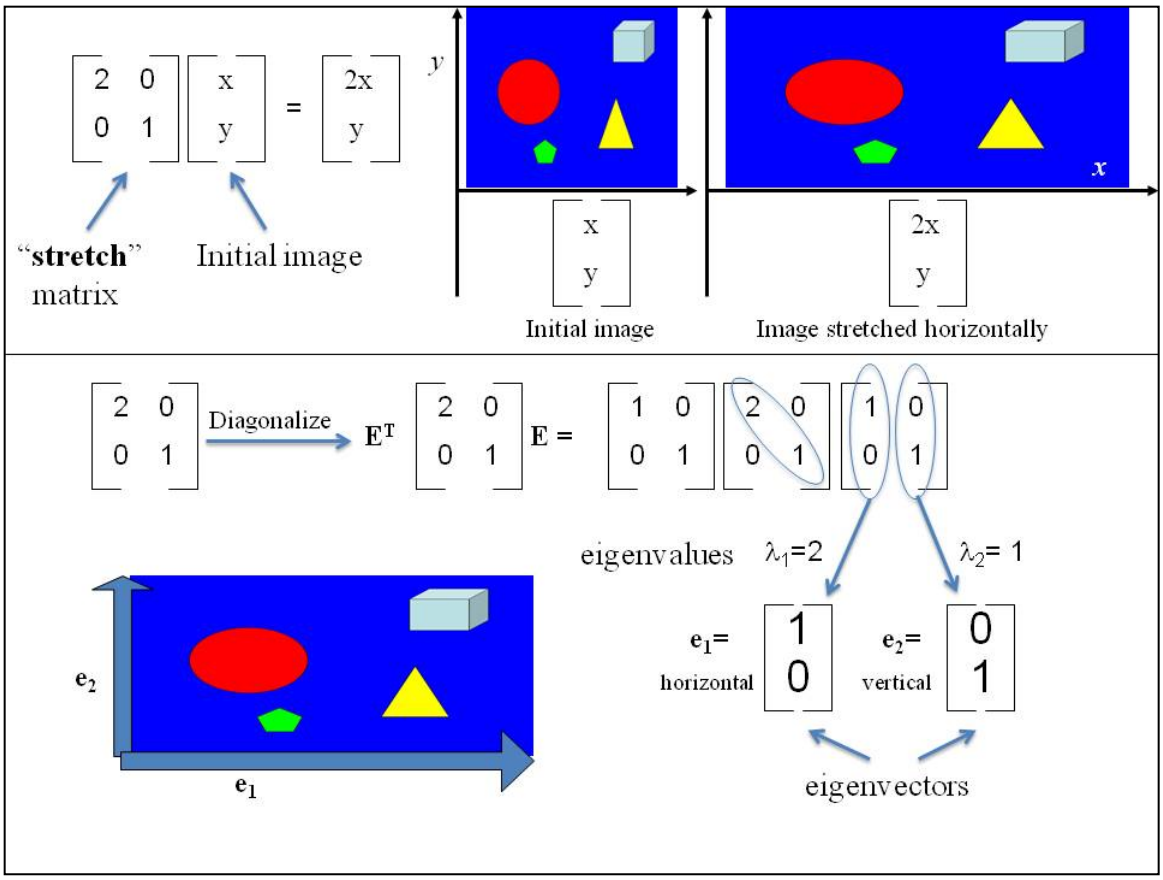

Figure 2.14 Example illustrating a simple linear transformation in 2-D space. The "stretch" 2 x 2 matrix is diagonalized to start with, leaving the eigenvalues (2 and 1) in plain sight along the main diagonal. **E** (the eigen vector matrix) and its transpose ($\mathbf{E}^T$) flak the "stretch" matrix. The dominant (principal) direction of the "streching" is indicated by the fact that e_1 is twice the magnitude (larger eigenvalue λ_1) of e_2. Adapted from [2] and courtesy of Thomas Gallagher, Aaron Field, and Andrew Alexander.

Eigenvalues and eigenvectors represent the *principal magnitudes* and *axes of a system*, respectively. Essentially, by incrementally adjusting weights around a tire so that it rotates smoothly around its central axis, we are "removing" off-diagonal elements from the matrix governing the angular momentum of the tire (Figure 2.15).

By themselves, a set of diffusion coefficients may not immediately suggest what is happening at the microstructural scale. It is here where balancing a tire and imaging white matter tracts in the brain overlap, since the same basic principles of tensor theory apply. Each voxel in the brain

can be envisioned as a small system of water molecules diffusing in directions that are referenced to the *x, y,* and *z* axes of the scanner bore. Examining this phenomenon with directionally specific diffusion gradients, we obtain a set of directionally specific diffusion coefficients that reflect the microstructural orientation of the underlying tissue. These diffusion coefficients can then be entered into a tensor, the 3 x 3 diffusion tensor matrix*,* **D**. Similar to a rotating body with an arbitrary distribution of mass for which we might wish to determine the "preferred" axis of rotation, a system of diffusing water molecules constrained by axonal membranes has a "preferred" direction that reflects the underlying organization of the tissues. Just as the "preferred" axis of a wobbling tire differs from that of the axle, the principal axis of diffusion in a voxel is generally arbitrary, and thus unpredictable with respect to the *x, y, z* coordinate system of the MRI scanner [28].

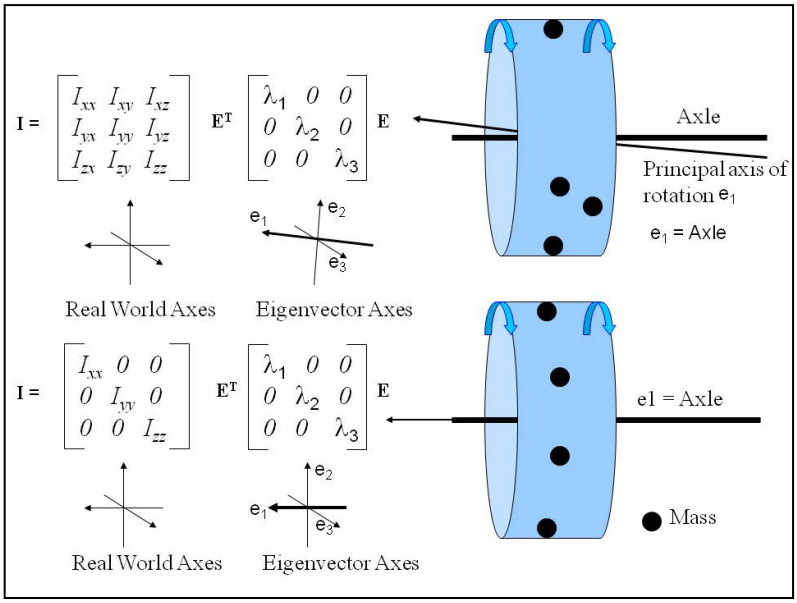

Figure 2.15 Similarities between DTI and the balancing of a tire. The distribution of mass in a rotating body such as a tire is summarized by the inertia tensor I. Generating the eigenvalues and eigenvectors of a matrix by *diagonalization* removes *off-diagonal* terms. A tire will wobble as it rotates about a fixed axle (principal Eigenvector e1) if the mass is unequally distributed. Weights can be added or rearranged in order to adjust the inertia tensor, essentially aligning the principal axis of rotation the fixed axle. Adapted from [2] and courtesy of Thomas Gallagher, Aaron Field, and Andrew Alexander.

Diagonalizing the diffusion tensor matrix reveals the eigenvalues and eigenvectors that relate the voxel-specific magnitudes and directions of the three-dimensional diffusion "profile" (i.e., the probability density function previously defined) to the scanner coordinate system (Figure 2.16). The largest eigenvalue (denoted λ_1) and corresponding eigenvector $\mathbf{e}_1$ represent the principal magnitude and axis of diffusion for that voxel, respectively. The diffusion tensor matrix is symmetric about the main diagonal because diffusion in the "positive" and "negative" directions along a given axis is indistinguishable. Therefore, while 9 possible entries are available for the 3 x 3 matrix, some are redundant and only 6 values are ultimately necessary to model diffusion in 3 dimensions. For example, measuring *D* in the x→y direction will result in the same *D* as that in the y→x direction, thus $D_{xy} = D_{yx}$, and similarly $D_{yz} = D_{zy}$ *and* $D_{xz} = D_{zx}$.

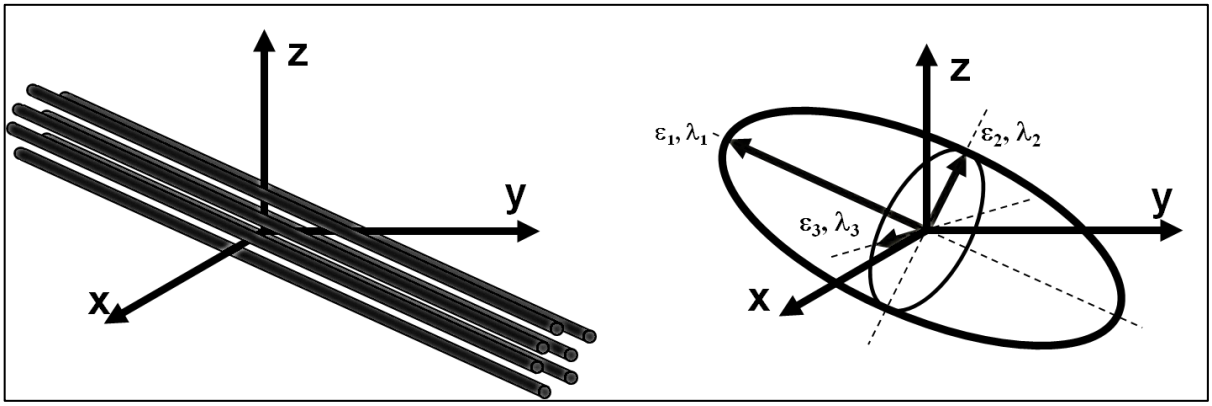

Figure 2.16 Estimating the principle axes of diffusion in a voxel. Estimations of the Eigenvalues and Eigenvectors of the diffusion tensor can be used to show the principle axes of diffusion in a voxel, which is influenced by underlying structural components (e.g. myelinated axons). Adapted from [2] and courtesy of Andrew Alexander.

Assuming Gaussian diffusion, the eigenvalues and eigenvectors of the diffusion tensor define the shape and orientation of an ellipsoid (or sphere in the case of isotropic diffusion), our 3-D probability density function (Figure 2.17). We start with

$$\frac{x^2}{a} + \frac{y^2}{b} + \frac{z^2}{c} = 1 \qquad \text{Equation 2.20}$$

which is familiar as the equation for an ordinary ellipsoid with parameters a, b, and c representing the respective radii in three orthogonal directions. If we modify this relationship with diffusion coefficients from the Einstein diffusion equation (Equation 2.1), we have:

$$\frac{x^2}{\sqrt{D_x\, 6\, \Delta t}} + \frac{y^2}{\sqrt{D_y\, 6\Delta t}} + \frac{z^2}{\sqrt{D_z 6\Delta t}} = 1 \qquad \text{Equation 2.21}$$

To define this relationship for each voxel in the brain, we substitute the corresponding eigenvalues of the diffusion tensor matrix *(*λ_1, λ_2, λ_3) for D_x , D_y , *and* D_z :

$$\frac{x^2}{\sqrt{\lambda_1\, 6\, \Delta t}} + \frac{y^2}{\sqrt{\lambda_2\, 6\Delta t}} + \frac{z^2}{\sqrt{\lambda_3 6\Delta t}} = 1 \qquad \text{Equation 2.22}$$

This can be simplified as:

$$\frac{x^2}{\sqrt{\lambda_1}} + \frac{y^2}{\sqrt{\lambda_2}} + \frac{z^2}{\sqrt{\lambda_3}} = \sqrt{6\Delta t} = \text{constant for a given } \Delta t$$

As a check on the math, consider the case of isotropic (Gaussian) diffusion in three dimensions, which, as we have seen earlier, should produce a sphere of radius $\sqrt{D6\Delta t}$. Then we have $D = \lambda_1$

= $\lambda_2 = \lambda_3$ which, when inserted into the ellipsoid relationship, reduces to $x^2 + y^2 + z^2 = \sqrt{D6\Delta t}$, as expected.

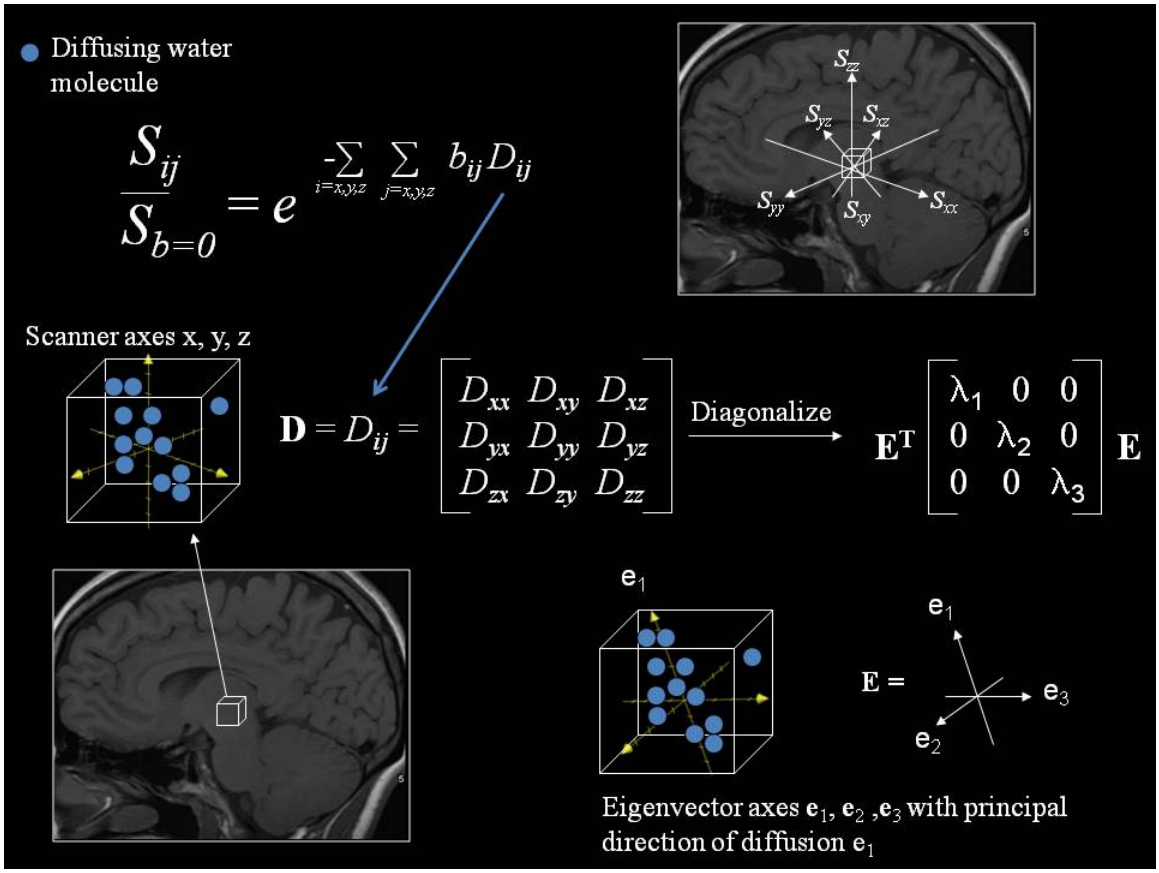

Figure 2.17 Filling a diffusion tensor. *S*= signal, *D* = diffusion coefficient, **E** = eigenvector matrix, $\mathbf{E}^T$ = transpose of the eigenvector matrix, **e** = eigenvector, λ = eigenvalue. Adapted from [2] and courtesy of Thomas Gallagher, Aaron Field, and Andrew Alexander.

The orientation of the ellipsoid in three dimensions is dictated by the principal eigenvector $\mathbf{e}_1$. It has been shown that for a voxel containing a single, dominant population of linearly oriented axonal fiber bundles, $\mathbf{e}_1$ corresponds to the orientation of those bundles [27] (Figure 2.18).

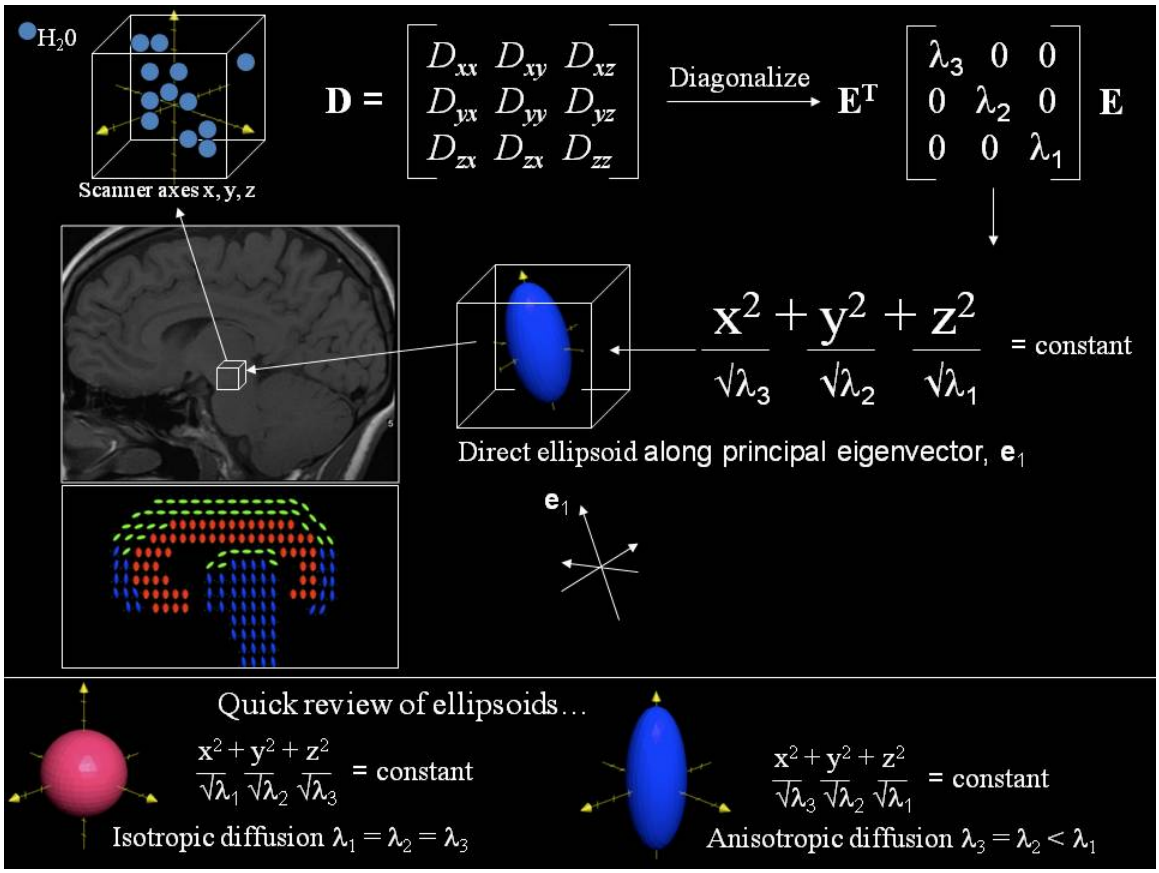

Figure 2.18 Generating diffusion tensor ellipsoids. The diffusion tensor matrix is filled with diffusion coefficients and diagonalized to get Eigenvalues and Eigenvectors. If the probability density function (PDF) is assumed to be a Gaussian, the equation for an ellipsoid can be applied using the respective Eigenvalues as diameters along the principal axes. The ellipsoid is then oriented in the direction dictated by the principal eigenvector, $\mathbf{e}_1$, for each voxel in the brain. A simplified rendering of the brain illustrating the cingulum (blue and green ellipsoids), corpus callosum (red), fornix (green), and brainstem (blue) serves as a basic example of a directionally encoded ellipsoid map. Adapted from [2] and courtesy of Thomas Gallagher, Aaron Field, and Andrew Alexander.

Recall that in three dimensions, whether for angular momentum or diffusion, a 3 x 3 tensor requires a minimum of 6 measurements to be fully specified (since the matrix is symmetric about the main diagonal, some entries are redundant by definition, as discussed previously). The diffusion tensor matrix **D** can thus be determined by a set of 6 diffusion coefficients, acquired through the application of diffusion-encoding gradients in 6 different directions. Our

equation for exponential signal decay can now be reintroduced after a vector treatment of its terms reflecting directional specificity [29]–[31]:

$$\frac{S_{ij}}{S_{b=o}} = e^{-\sum_{i=x,y,z}\ \sum_{j=x,y,z} b_{ij} D_{ij}} \qquad \text{Equation 2.23}$$

$$b_{ij} = (\gamma G_{ij} \delta)^2 [\Delta - (\delta/3)] \qquad \text{Equation 2.24}$$

Diffusion coefficients can then be obtained for D_{xx}, D_{yy}, D_{zz}, D_{xy}, D_{xz}, D_{yz} relative to the MR scanner *x*, *y*, *z* orthogonal frame of reference. The diffusion tensor can be filled accordingly and diagonalized to find its eigenvalues and eigenvectors.

2.5.2 Common Artifacts

As fast SS-EPI scans are typically utilized in DTI, the same artifacts and technical limitations that frequently plague these acquisitions should be sought out and recognized in the final DTI images. Susceptibility artifacts near the skull base and in areas of hemosiderin deposition, such as in the setting of a cavernoma, can distort the local magnetic field and fail to return reliable results in these areas. Rapidly changing gradients may introduce eddy currents and image distortions that can be reduced with the application of bipolar gradients [32], [33]. As will be discussed in a later section, in-plane parallel imaging techniques can help accelerate the echo train acquisition time and reduce several EPI distortions.

Correction of patient motion is also critical for high quality DTI. An important strategy for reducing the impact of motion is to shorten the total scan time. While the use of in-plane parallel imaging reduces the total number of phase encoding steps, the diffusion encoding time blocks remain unaffected. Thus, total scan time remains lengthy. A real impact in the reduction of total scan time is possible by the implementation of a method known as simultaneous multi-slice acquisition [34], through the simultaneous excitation, diffusion contrast encoding, and readout of multiple slices with a single diffusion-encoding block. This will also be described in more detail in a later section.

Cardiac pulsation can also lead to motion artifacts in DW images. Cardiac gating can significantly reduce these artifacts although it is not commonly performed. An optimum DTI acquisition would benefit from cardiac gating, as the gain in signal to noise appears to outweigh the extra scanning time and preparation [32], leading to overall increased confidence in the calculation of tensor components, principal eigenvector, and DTI metrics such as FA.

2.5.3 Number of Diffusion-Encoding Directions

In an idealized environment featuring perfectly Gaussian diffusion and no noise effects, 6 non-colinear diffusion-encoding directions would be sufficient to accurately characterize the diffusion profile in three dimensions. In reality, image noise is a significant hurdle in DTI [35], and the actual diffusion profile is not truly Gaussian, such that the tensor model is merely an estimate that can be improved by increasing the number of directions sampled. When more than 6 directions are sampled, these measurements are essentially “averaged” (through

multiple linear least squares methods or nonlinear modeling) in order to reduce them to the 6 required entries in the diffusion tensor matrix.

The optimal number of unique encoding directions for fitting the tensor model is generally regarded to be in the range of 20-30 and uniformly oriented around a sphere [32], [36], [37]. There does not appear to be a significant advantage to sampling greater than 30 directions for the tensor model (although more directions are required for more sophisticated modeling, discussed in a later section).

2.5.4 Ratio of *b*=0 Images to Diffusion-Weighted Images

Recall that a reference *b*=0 image without diffusion weighting is always required to solve the exponential equation for the diffusion coefficient. For conventional DWI, where just 3 diffusion-weighted images are acquired and averaged, one reference image is sufficient. However, multiple *b*=0 images are often recommended for DTI acquisitions featuring higher numbers of encoding directions, because noise or other errors in the reference image will impact many more calculations in this setting. A "rule of thumb" states that 1 b_0 image should be obtained for every 5 encoding directions [32].

2.5.5 Signal to Noise Ratio

Besides spatial accuracy, an important measure of image quality is the signal to noise ratio (SNR). Reliable estimation of the diffusion tensors depends on sufficient SNR, therefore, the factors that affect this metric should be considered before a diffusion imaging experiment is

performed. Main factors include the imaging hardware (main static magnetic field and receive coils), the voxel size, the sampling time, the number of averages, parallel imaging, and fluctuations in the signal due to relaxation effects and amount of diffusion weighting.

The starting magnitude of the longitudinal magnetization in the imaged sample is proportional to the strength of the main magnetic field. This means that the overall signal grows with larger magnetic fields. However, challenges related to using larger main magnetic fields such inhomogeneities in the radiofrequency field (used for the exciting the magnetization in the sample) will have an impact on SNR and must be considered as well. Other complications arising from use of higher main fields such as worsening of geometric distortion and increased power deposition from the radio frequency fields can potentially outweigh the SNR benefits. The signal also increases with the number of receive coils. However, the gains are differential in distance with more significant increments occurring near the coil.

The volume of a voxel is proportional to the number of water molecules that contribute to the magnitude of magnetization for that voxel. Larger voxels then translate to larger SNR. For perspective, decreasing the voxel size by one half results in an eight-fold SNR reduction. The sampling time, also known as the ‘dwell time’, is the time spent collecting a single point in Fourier space. Longer sampling time means an increment in SNR because the noise in the signal for a particular Fourier space point decreases with the square root of the dwell time. This is because the recorded signal point is really an average of the signal over a number of time units. However, larger sampling time also increases the readout time which worsens the distortions from main magnetic field inhomogeneities. The inverse of the sampling time is referred to as the bandwidth.

Averaging across repeats of the same acquisition also decreases the noise as the square root of the number of averages, leading to improved SNR. For example, to recover the SNR penalty from halving the voxel size (eight-fold decrease) would require 64 repeats, provided other factors remain unchanged. In-plane or 2-D parallel imaging generally implies a decrease in SNR from collecting fewer lines of Fourier space. In SS-EPI-based diffusion imaging, however, acceleration also shortens the echo time, which reduces signal decay due to T2 relaxation. Spatial accuracy (i.e. less geometric distortion) is improved using 2-D accelerated acquisitions by shortening the time that it takes to cover a plane of Fourier space.

Other sources of signal decay will also affect the SNR. In general, all diffusion- weighted images will have some level of T2 signal decay. This can be reduced by using shorter echo times, but shorter echo times in turn need support from stronger diffusion gradients for achieving sufficient diffusion contrast. Recovery of the longitudinal signal before it is tipped back down also affects the overall magnitude of magnetization. This is affected by the T1 recovery rate, which in turn depends on the repetition time or TR. Of course, the signal magnitude is decreased with diffusion weighting. However, varying amounts of diffusion weighting will lead to different SNR levels. Higher b-values will induce larger decay in the signal and the overall SNR will be lower.

2.6 RENDERING DTI DATA

The eigenvalues of the diffusion tensor provide us not only with a mechanism to sculpt diffusion ellipsoids, but also serve as the raw materials for several useful scalar measures

including trace, fractional anisotropy, and longitudinal and transverse diffusivity, as detailed in the sections that follow.

2.7.1 Spherical, Oblate, Prolate Tensors and DTI "Data Mining"

Depending on the relative magnitudes of the 3 eigenvalues, 3 dominant ellipsoid shapes can be produced. By convention, eigenvalues are numbered 1 (largest) through 3 (smallest). Isotropic diffusion implies that all 3 eigenvalues are equal $\lambda_1 = \lambda_2 = \lambda_3$ and the result is a spherical tensor. Diffusion primarily constrained to a plane may have two large diffusion coefficients and a smaller third (i.e. $\lambda_1 = \lambda_2 >> \lambda_3$). The result is a "disc-shaped" or *oblate* tensor. Similarly, if diffusion is primarily constrained along a single axis ($\lambda_1 >> \lambda_2 = \lambda_3$), this results in a "cigar-shaped" or *prolate* tensor (Figure 2.19).

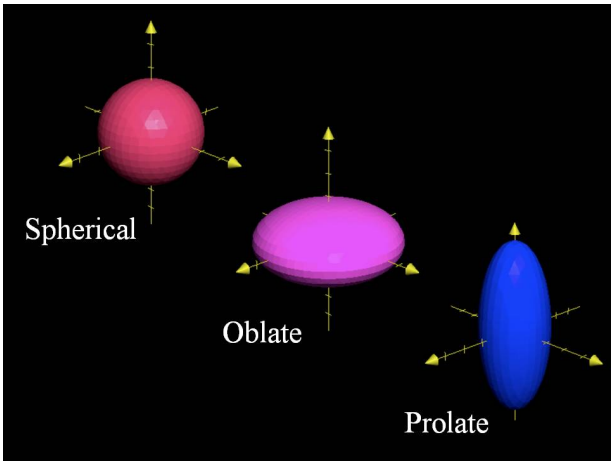

Figure 2.19 The three dominant shapes of diffusion tensor ellipsoids. Adapted from [2] and courtesy of Thomas Gallagher, Aaron Field, and Andrew Alexander.

Westin et al. developed scalar indices to quantify the shape of the ellipsoid with regard to its sphericity C_s, linearity C_l (prolateness), and planarity C_p (oblateness) [38]:

$$C_s = \frac{3\lambda_3}{\lambda_1 + \lambda_2 + \lambda_3} \qquad \text{Equation 2.25}$$

$$C_l = \frac{\lambda_1 - \lambda_2}{\lambda_1 + \lambda_2 + \lambda_3}$$ Equation 2.26

$$C_p = \frac{2(\lambda_2 - \lambda_3)}{\lambda_1 + \lambda_2 + \lambda_3}$$ Equation 2.27

with $C_s + C_l + C_p = 1$. An anisotropy index, C_a, can be obtained by taking $1 - C_s$, which gives a numerical value indicating *how different* a tensor is from the spherical state.

To aid in visualizing DTI data clinically, ellipsoids are often color-coded green, red, and blue for anterior-posterior, right-left, and superior-inferior, respectively, with intermediate color hues used for fiber tracts oriented in various directions between these axes (Figure 2.23) [39].

2.6.2 Trace

Trace (Tr) is the sum of the diagonal elements in a square matrix, which also happens to equal the sum of its eigenvalues, an invariant property of a square matrix. Trace is an estimation of directionally averaged diffusivity in a voxel. *Mean diffusivity* is taken as the trace of the diffusion tensor divided by 3, or the average of its three eigenvalues (Tr/3). This value is equivalent to the averaged ADC for three orthogonal directions as acquired for conventional (non-tensor) diffusion weighted imaging.

2.6.3 Fractional Anisotropy

Relative anisotropy (RA) and *fractional anisotropy* (FA) are common scalar quantities derived from the three diffusion tensor eigenvalues [40]. These are essentially measures of the degree

to which the tensor ellipsoid shape deviates from spherical. They provide a quantitative answer to the question, “How different are the eigenvalues of the diffusion tensor from each other?” FA is the most widely used value and is defined such that it ranges from zero (isotropic) to one (maximum anisotropy). Regions of decreased FA in white matter imply decreased directional coherence, and have been studied as a proxy for microstructural changes otherwise occult on conventional MR imaging. Note that FA is mathematically non-specific because it does not equate to tensor shape (i.e., multiple tensor shapes, both prolate and oblate, can have the same FA). It should be emphasized that areas of reduced FA do not necessarily imply pathology, as crossing fibers within a voxel may result in low FA despite a highly intricate intersection of intact fibers. Further, in the setting of true pathology, reductions in FA should be considered pathologically nonspecific as part of the final common pathway of many different disorders (Figure 2.20). The derivation of FA and other scalar metrics are shown in Figure 2.22.

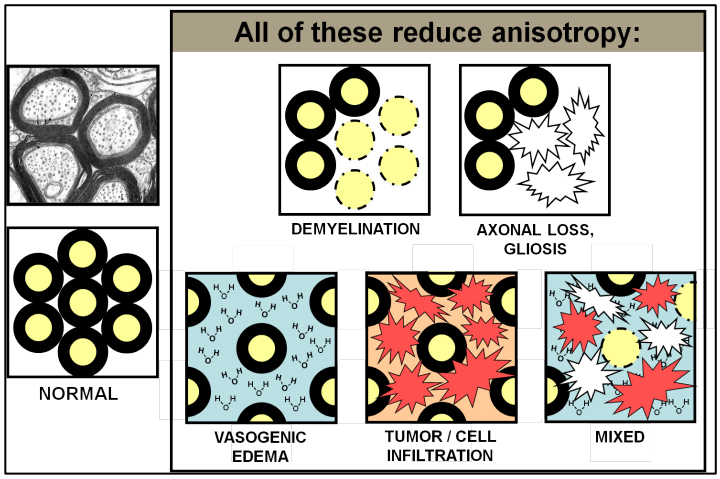

Figure 2.20 Areas of reduced FA are pathologically nonspecific. Reduction in fractional anisotropy is common to several different pathologic states. Adapted from [2] and courtesy of Aaron Field.

2.6.4 Longitudinal and Transverse Diffusivity

Longitudinal or *axial* diffusivity is typically assumed to be represented by the major (largest) eigenvalue, λ_1, while *transverse* or *radial* diffusivity is often estimated by taking the mean of the medium and minor eigenvalues, λ_2 and λ_3. It is important to remember, however, that these assumptions presume a prolate tensor; i.e., a single, dominant, unidirectional population of fiber bundles in a voxel. The meaning of "longitudinal" and "transverse" is an entirely different matter for non-prolate tensors. As shown in Figure 2.21, there are many voxels in the brain where the tensors are non-prolate.

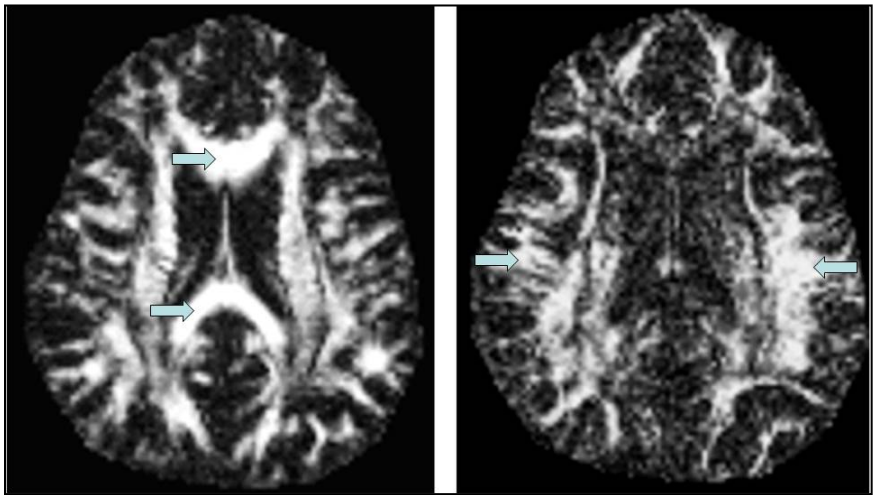

Figure 2.21 Prolate (left) and oblate (right) distributions in the brain. Quantitative DTI metrics such as longitudinal and transverse diffusivity are only appropriate in areas of the brain populated by prolate tensors implying strong direction coherence. This is clear in the axial image on the left, where the corpus callosum is very bright. Inherently non-prolate distributions in the brain do not afford a clearly dominant eigenvector/eigenvalue for which longitudinal and transverse diffusivity can have meaning. The image on the right emphasizes nonprolate distributions in the brain, demonstrating brighter areas now in the subcortical regions with darker appearance of the corpus callosum. Adapted from [2] and courtesy of Andrew Alexander.

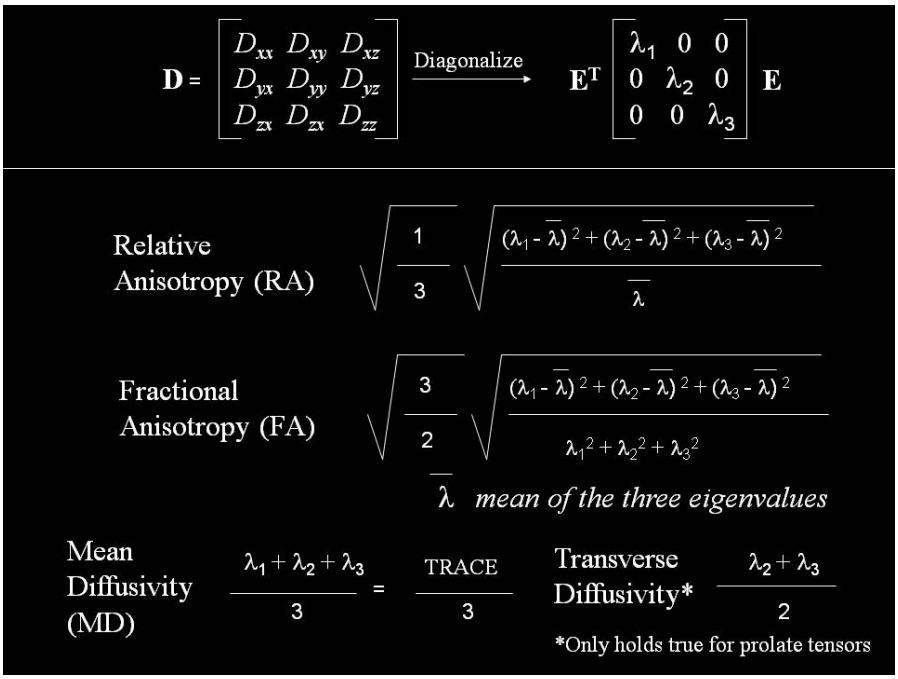

Figure 2.22. Scalar indices derived from diffusion tensor eigenvalues. The transverse diffusivity only is valid in voxes of the brain with prolate tensors. Adapted from [2] and courtesy of Thomas Gallagher, Aaron Field, and Andrew Alexander.

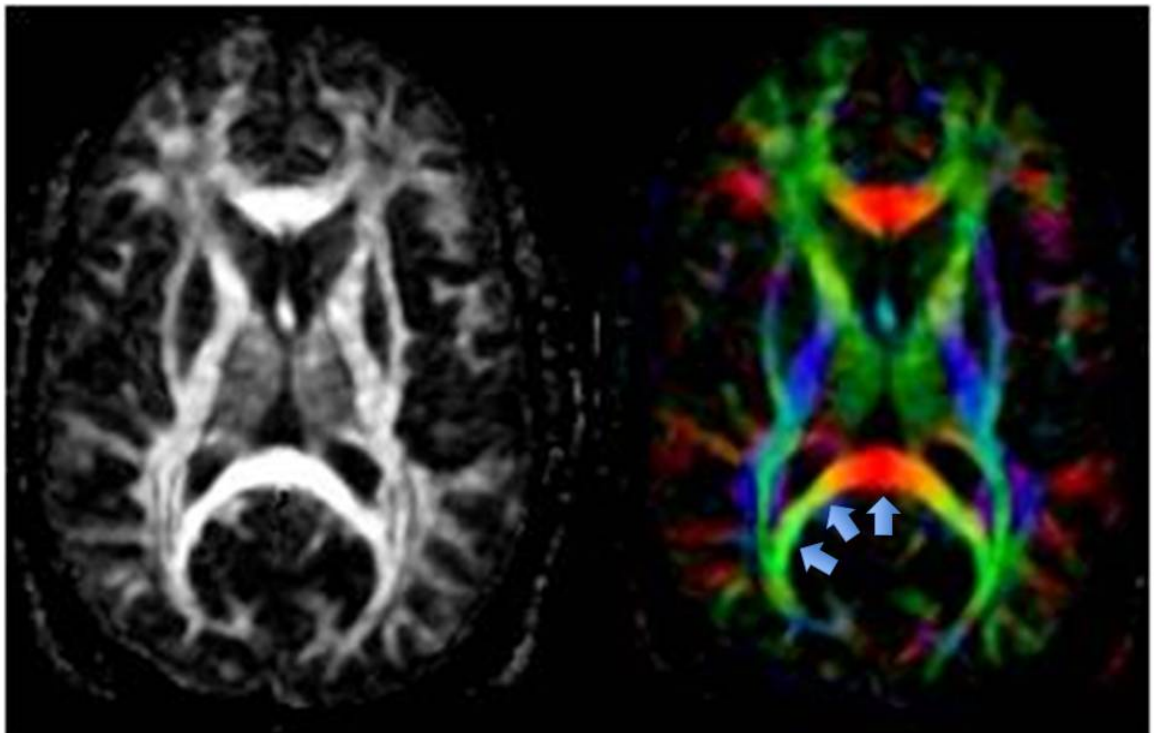

Figure 2.23 FA maps axial views, gray scale (left) and directionally encoded (right). In the gray-scale FA map voxel brightness correlates directly with fractional anisotropy (FA). In the directionally encoded color FA map the major eigenvector information is also contained in each voxel. The major white matter tracts can usually be resolved by their distinctive orientations which, by convention, are color coded green (anterior-posterior) red (right-left) and blue (superior-inferior). Changes in direction are assigned intermediate hues, evident in the splenium of the corpus callosum (arrows) as it extends from midline (red) arching posterolaterally (orange → yellow → green). Adapted from [2] and courtesy of Thomas Gallagher, Aaron Field, and Andrew Alexander.

2.7 BASICS OF TRACTOGRAPHY

Diffusion tensor tractography or "fiber tracking" attempts to map white matter tracts by constructing 3-D computer-graphical representations of them, based on the directional diffusion information available on a voxel-wise basis. There are two general methods available for tractography, *deterministic* and *probabilistic*.

Deterministic methods are most commonly employed in clinical settings. In deterministic tractography, a region of interest (ROI) is selected, usually in an anatomic area traversed by a known white matter bundle to be targeted for tracking. A voxel or group of voxels in this ROI

serves as a *seed point(s)* to initiate the algorithm. Fiber representations are then "grown" from the seed points by iteratively taking a series of small, consecutive steps, the direction of each step determined by the local orientation of principal diffusion tensor eigenvectors, which are assumed to be tangent to the major white matter tract in question [41], [42].

The raw materials for tractography remain the eigenvalues and eigenvectors of the diffusion tensor. We divide the brain into voxels and insert the principal eigenvector pertaining to each voxel at its center. In so doing, we have created a *discrete vector field* of the dominant white matter tracts in the brain. We say *discrete* because the principal eigenvectors are mapped to voxel centers. As pointed out by Mori et al. [41], if we imagine ourselves at the center of a seed voxel, we are surrounded by 26 voxels (8 comprising the walls in our two-dimensional [2-D] axial plane, 9 for our roof, and 9 for our floor). Of these 26 possibilities, we would choose the voxel featuring a principal eigenvector that is most like our own and step in that direction. When drawn out in space, the tract would extend from the center of our voxel to the center of the next voxel, where we would inherit the same predicament of 26 choices. Of course, we know that the trajectories of white matter tracts need not conform to discrete voxels, and their true paths are not adequately represented by purely discrete methods. For example, it is quite reasonable to assume that a tract may only skim the corner of a neighboring voxel as it changes its trajectory. Further, the step-length (i.e., the distance the tract grows before the next step or change in trajectory) is not likely to remain constant for all steps.

To more accurately model the trajectory of white matter tracts, we envision the brain as a *continuous vector field,* able to intercept the margins and corners of a voxel as the tract propagates through space. We still make the assumption that the principal eigenvector within a

voxel is tangent to the curve drawn out by the major underlying white matter tract, however, rather than beginning at the center of the seed voxel, we start from multiple points within the seed voxel. One of the most widely used fiber tracking algorithm of this type is *fiber assignment by continuous tracking* (FACT) introduced by Mori et al. [41]. In this model, principal eigenvectors serve as intermittent "road signs" along a continuous trajectory that passes through contiguous voxels. Starting from different points within a seed-voxel, different tracts extend outward, always keeping parallel to the principal eigenvector, until they reach the edge of that voxel. Once at the edge, the growing tract assumes the trajectory of the neighboring voxel's principal eigenvector. The key feature of the FACT algorithm is that the *step-length is not equal for all steps.* If we begin from a very eccentric position in the seed voxel and head along a particular trajectory, we may very well reach the edge of the voxel (a new step) after a much shorter length than if we had started elsewhere in the same voxel. We may then encounter a completely different neighboring voxel at the next step. A collection of fibers is grown from the different origins in the same seed-voxel or voxels (Figure 2.24).

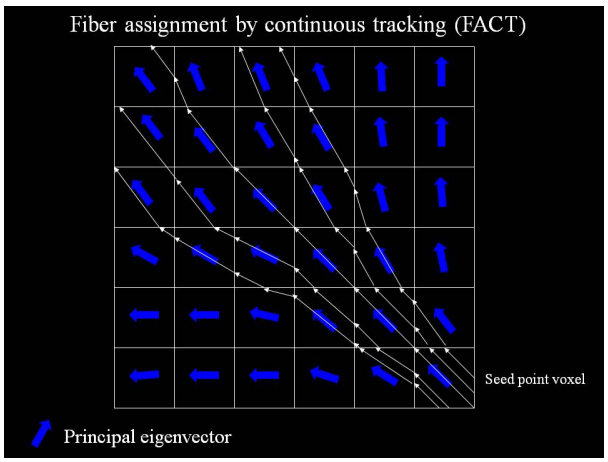

Figure 2.24 Illustration of the FACT algorithm**.** In FACT a continuous vector field in the brain is assumed as well as the principal eigenvectors assigned to each voxel being tangent to the graphical trajectory representing the underlying white matter tract. Notice that the step lengths (white arrows) are not equal at each step (a "step" is defined as the growing tract encounters the edge of a voxel). Adapted from [2] and courtesy of Thomas Gallagher, Aaron Field, and Andrew Alexander.

To avoid non-anatomical trajectories, *stopping criteria* are used to constrain the algorithm. For example, only gradual changes in trajectory angle are allowed, while nonanatomical “hairpin” turns are prevented by disallowing trajectory angles exceeding some predetermined threshold, such as 45 degrees. Stopping criteria also typically include a threshold on anisotropy, because estimates of fiber orientation become less reliable as diffusion becomes more isotropic; for example, the algorithm might be terminated when FA falls below 0.2 [26], [29].

Stopping criteria can be made less stringent as needed to explore a larger array of potential tracts. Since a given ROI may be traversed by more than one discrete white matter fiber bundle, multiple ROIs may be chosen to parse a specific tract; this is accomplished by constructing many trajectories but retaining only those that traverse all selected ROI’s (typically two) [26] (Figure 2.25). Examples of various white matter pathways derived from fiber tracking are shown in Figure 2.26.

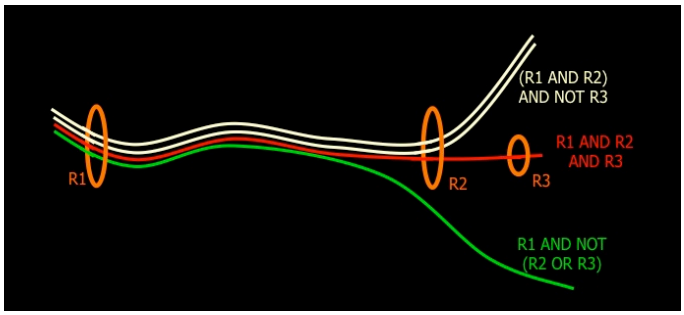

Figure 2.25 Growing tracts can be modified by Boolean operators, the choice of which will restrict advancing fiber bundles along a particular trajectory. n Adapted from [2] and courtesy and Andrew Alexander.

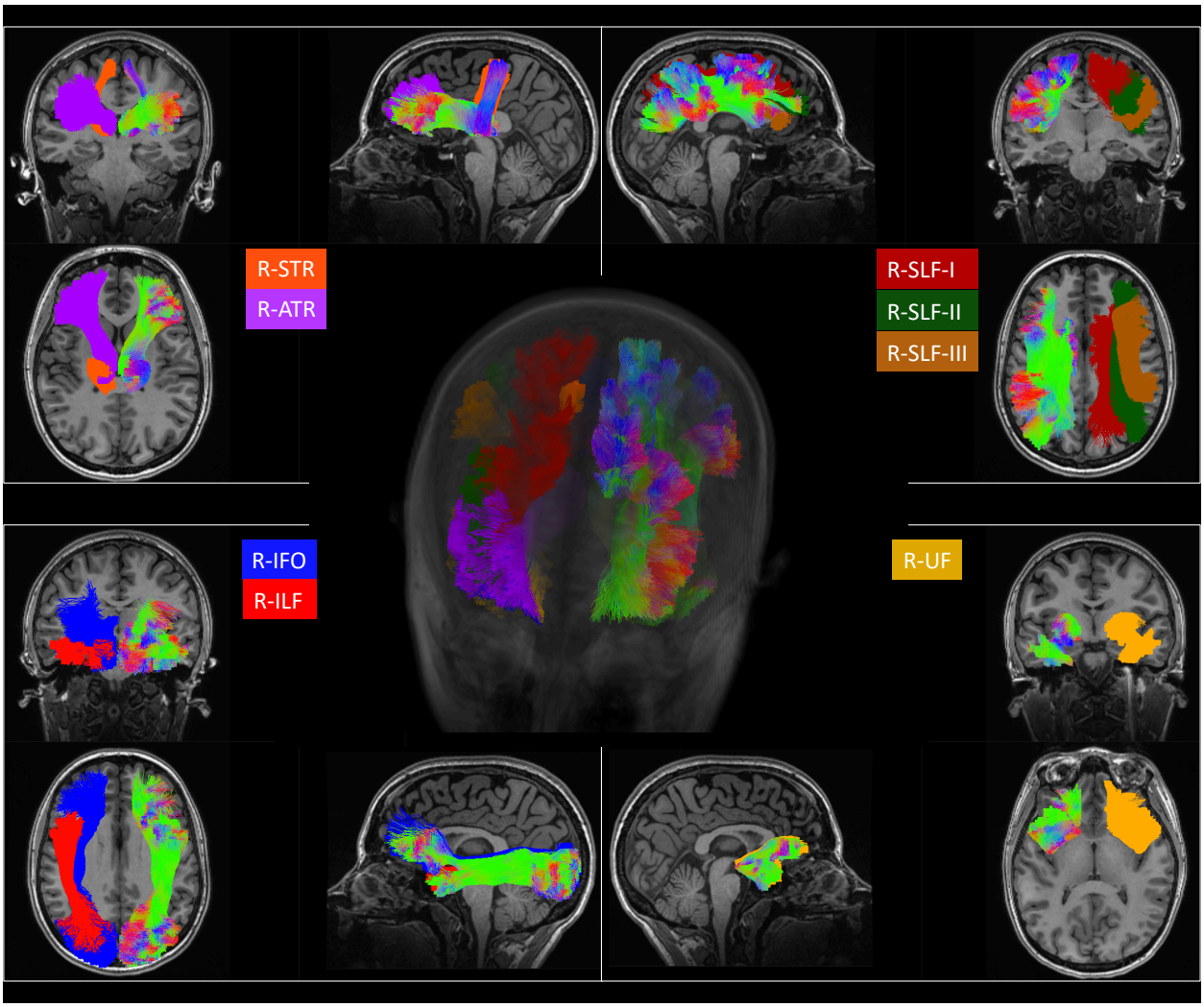

Figure 2.26 Example white matter pathways derived from fiber tracking. Left-side bundles are color coded green (anterior-posterior) red (right-left) and blue (superior-inferior). Right-side bundles are colored in solid colors: R-STR: Superior thalamic radiation, right side. R-ATR: Anterior thalamic radiation, right side. R-SLF: Superior Longitudinal Fasciculus, right side. Components I, II, III R-IFO: Inferior Occipito-frontal Fasciculus, right side. R-ILF: Inferior Longitudinal Fasciculus, right side. R-UF: Uncinate Fasciculus, right side.

The reliability and reproducibility of fiber tracking depend largely on the degree of uncertainty regarding the major eigenvector orientations. Critical factors contributing to greater uncertainty include underlying image noise as well as the presence of non-prolate tensors in the trajectory path, such as those resulting from intravoxel crossing fibers (which cannot be resolved by the tensor method) (Figure 2.27). It follows that higher reproducibility and more accurate results will come from higher-SNR image acquisitions and from mapping anatomically

"easier" white matter tracts, featuring intrinsically high FA, a preponderance of prolate tensors, and lacking major fiber crossings.

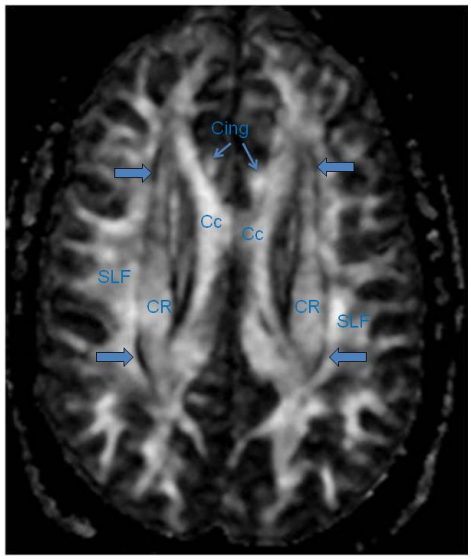

Figure 2.27 Illustration of near-zero FA in areas of crossing fibers. Crossing fibers within a voxel cannot be resolved by DTI. This is an inherent limitation of the tensor method which affords only 3 dominant ellipsoid shapes and will "directionally average" crossing fibers into one of those shapes. locally diminished FA is evident at the margin of crossing fibers. This can be observed as black lines (blue arrows) at the interface of the corona radiata (CR) and superior longitudinal fasciculus (SLF). Other such black lines delineate the paired cingula (Cing) from the corpus callosum (CC). Adapted from [2] and courtesy of Aaron Field.

In contrast to deterministic methods, probabilistic methods offer an explicit accounting of uncertainty in constructing fiber trajectories, something akin to a distribution of possible tracts to pursue when venturing forward from the edge of a voxel. In the end, the voxels in the brain are assigned a numeric percentage based on the number of pathways derived from the seed point that passes through the voxel in question. For example, a voxel assigned 1% indicates that only 1 out of 100 tracts initiated by the seed point includes the voxel in question. As distributions of potential tracts are created, probabilistic methods may be less dependent initially on the choice of seed point eigenvector, offering the possibility to initiate tracts from areas of lower FA. Probabilistic methods, however, are just as sensitive to propagation of error as deterministic methods despite relatively high reproducibility [26]. They remain maps of probability and should be interpreted as such.

2.8 Beyond DTI

Diffusion tensor imaging is a fast and efficient means of generating clinically relevant images that can be obtained in just a few minutes. It does, however, suffer from certain inherent limitations. Most importantly, DTI assumes that the 3-D displacement profile due to diffusion in each voxel is “sculpted” by the local axonal architecture into a Gaussian ellipsoid fully described by three eigenvectors and their associated eigenvalues. It is unlikely that truly Gaussian diffusion occurs in tissues, however, prompting investigators to develop methods of accounting for deviations from Gaussian behavior and for exploiting the limits of Gaussian displacement by identifying more sophisticated, non-Gaussian PDFs.

2.8.1 Diffusion Kurtosis

The signature of non-Gaussianity can be appreciated from the natural logarithm of the signal with respect to b-value (Figure 2.28). At *b-values* less than 1000 s/mm^2, the function exhibits a linear behavior characteristic of the mono-exponential model (*Eq. 9*). At higher b-values, the log-linear behavior transitions to one with more quadratic-like characteristics. At stronger b-values the content of the signal is more representative of molecules displacing through more tortuous, shorter distances (i.e. the signal contribution from faster-diffusing molecules nearly completely dissipates for very strong diffusion weighting). Diffusion kurtosis imaging (DKI) [44] accounts for this departure from linearity at higher b-values by incorporating an additional quadratic term to the exponent of the mono-exponential model.

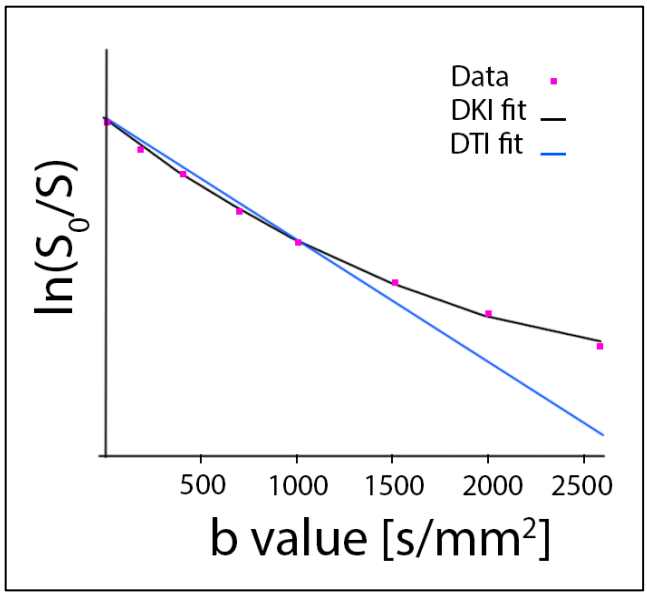

Figure 2.28 Illustration plots of DKI and DTI. Model fits to measured diffusion weighted data at multiple b values.

The DKI method estimates an apparent diffusion coefficient plus an additional parameter termed the apparent kurtosis. The latter directly quantifies how different from a Gaussian shape a given molecular displacement distribution is. Kurtosis is a well-characterized mathematical entity in the field of probability theory. It quantifies the *peakedness* of a distribution in comparison to a Gaussian form: positive kurtosis represents a distribution with a higher peak and heavier tails, negative kurtosis represents lower peak and faster decaying tails, and zero value kurtosis indicates Gaussian shape. Molecules diffuse faster at the beginning of an imaging experiment, but the process slows down as the molecules have more time to interact with surrounding structures. Larger values of kurtosis then are thought to reflect a more irregular landscape of the studied sample, one that is 'quick' at impeding the molecules to diffuse freely.

As with DTI, kurtosis can be characterized directionally with a 3 x 3 tensor. From this tensor, useful parameters can be computed, the most common of which are: the mean of the

kurtosis in all directions (mean kurtosis), the average kurtosis in directions perpendicular to the long axis of the diffusion ellipsoid (radial kurtosis), and kurtosis parallel to the long axis of the diffusion ellipsoid (axial kurtosis). In comparison to DTI, at least 15 different diffusion encoding directions need to be sampled to reconstruct the kurtosis tensor. Additionally, at least two non-zero b-values are required with recommended settings of b~1000 s/mm^2 for the first b-value and b~2000 s/mm^2 for the second value [45]. DKI has been applied to study a wide range of conditions including gliomas [46]–[48], stroke [49]–[51], Alzheimer's disease [52], [53], multiple sclerosis [54], [55], and traumatic brain injury [56]–[59].

2.8.2 Time Dependent Diffusion with Oscillating Gradients

While DKI accounts for deviations in Gaussianity of the molecular displacement resulting from the interactions between molecules and surrounding hindrances, a technique known as temporal diffusion spectroscopy exploits such interactions for extracting more direct information about tissue microarchitecture.

As outlined in Section 1 of this chapter, the mean-squared displacement Δr in Einstein's diffusion equation (Equation 2.1) depends on the observation time interval or diffusion time Δt. In a uniform medium with no boundaries, diffusion is isotropic or unrestricted. In inhomogeneous media, barriers will hinder the diffusing molecules and the encountering of molecules with obstacles is proportional to the observation time. ADC estimates, thus, change with diffusion time as the imaging measurements go from free to restricted diffusion regimes.

For example, for molecules constrained entirely to move inside a spherical pore of radius *a,* diffusion estimates will appear almost unrestricted for $\Delta t << r^2/2D$ and closer to the true value

D. For $\Delta t >> r^2/2D$, however, all molecules will have had enough time to interact with the walls of the pore and are equally likely to be found anywhere inside it independent of their starting positions, yielding estimates of the diffusion coefficient that are less than the true *D*.

Obtaining measurements across a range of diffusion times opens the possibility to extract information pertaining to the geometry of the surrounding medium in which the molecules diffuse. Unfortunately, typical dMRI acquisitions that make use of PGSE sequences are limited to long diffusion times due mainly to hardware limitations of clinical scanners. In most cases, the limited strength of gradient coils implies the use of long diffusion times in order to achieve high enough *b-values* for a sufficiently diffusion weighted MRI signal.

Investigators have circumvented the need for strong gradients by modifying the shape of the rectangular pulses in a PGSE sequence like the one shown in Figure 2.12 to take on oscillatory forms (e.g. sinusoid) with a specific frequency [60], [61]. Different frequencies will result in different diffusion times, thus allowing to conduct imaging experiments at varying time scales. Estimates of unrestricted diffusion coefficients can then be obtained from very short diffusion times (high frequency of the oscillating gradients) using oscillating gradient sequences. Additionally, diffusion time dependency has been reported to provide micro-structural information about cell size [62], [63] and axonal diameter [64]. Diffusion time dependency measurements have also been conducted in healthy and pathological brain tissue of animal [65] and human brains [66], [67].

2.8.3 Geometric Multi-Compartment Models

Diffusion-weighted imaging models like DTI and DKI are based on diffusion distribution properties. As a consequence, parameters from these models may not have a specific biophysical basis. To address the poor biological specificity of DTI and DKI metrics, several multi-compartment biophysical modeling techniques have been proposed in the last decade.

The *Composite Hindered and Restricted Model of Diffusion (CHARMED)* [68] attempts to resolve both hindered (extra-axonal) and restricted (intra-axonal) diffusion with higher *b*-values. The underlying assumption in *CHARMED* is that extra-axonal and intra-axonal diffusion behave differently. In areas of crossing fibers, two "restricted" intra-axonal compartments are presumed and sought out with higher b-value diffusion-sensitizing gradients. Isoprobability surfaces similar to Gaussian ellipsoids can then be created for each voxel, which visually render this more complex model of diffusion.

The *Neurite Orientation Dispersion and Density Imaging* (*NODDI*) [69] technique assumes a multi-compartment model for describing the diffusion MRI signal as originating from three microstructural environments. The model and other assumptions of the NODDI technique will be discussed in more detail in the next chapter. As with *CHARMED*, the *NODDI* model proposes an intra-axonal compartment, but with the difference that molecular displacement is completely restricted to occur in directions parallel to the long axis of cylindrical axons. A second compartment is extra-axonal, where diffusion is assumed anisotropic and modeled with a diffusion tensor. A third compartment is free water, assumed to have unrestricted, isotropic

diffusion, primarily from cerebrospinal fluid (CSF). The *NODDI* model describes the axons' diffusion signal as a function of their density and orientation dispersion. This is done by estimating an intra-axonal volume fraction and a concentration parameter of the axons orientation distribution. The *NODDI* method is practical in terms of acquisition time and diffusion weighting. The optimal imaging protocol in [69] consists of two non-zero *b-values* with the lower b-value (~700-1000 s/mm^2) applied along 15-30 directions and the second, higher b-value (~2000-3000 s/mm^2) applied along 30-60 directions. With a typical clinical scanner, this protocol can be achieved in under 10 minutes of total scan time. The clinical feasibility of the protocol has been reported in multiple studies [70]–[73]. The model parameter estimates have been widely used to investigate brain tissue microstructure as a function of early development, aging, cognitive function, and a variety of neurological disorders [74]–[79].

2.8.4 "Model-Free" Techniques

As discussed in other sections, DTI fails to resolve crossing fibers as consequence of the limited tensor model itself. To better understand this, imagine a voxel featuring the intersection of three equally robust axonal fiber populations running parallel to the *x*, *y*, and *z* axes. A (perfect) conventional DTI acquisition (free of any noise effects) would correctly deliver the result of three equal eigenvalues, however, we are left with a perfect sphere with FA= 0. Despite the highly intricate arrangement of three orthogonally crossing fiber tracts in this voxel, DTI reports isotropic diffusion, a gross misrepresentation of the underlying structure. The same fundamental limitations will manifest in any voxel where white matter tracts cross and thus cannot be resolved as separate with the tensor method. This is evident, for example, when

attempting to follow pyramidal tracts cephalad from the brainstem toward the motor cortex; in the centrum semiovale, the pyramidal tracts intersect with the superior longitudinal fasciculus and tractography often terminates at this intersection. To overcome these limitations, several methods of high angular resolution diffusion encoding have been devised to better characterize the 3-dimensional diffusion profile within a voxel.

High Angular Resolution Diffusion Imaging (HARDI) [80] is one such technique that utilizes the spherical variance of ADC values obtained at higher b-values (3,000 s/mm^2) utilizing over 40 encoding directions. When plotted as a function of the encoding direction angles, a complex 3-D surface can be generated that more accurately represents the diffusion profile within a voxel. This procedure is capable of resolving crossing fibers using spherical harmonic decomposition (SHD) methods [81], [82].

Diffusion spectrum imaging (DSI) and q-Ball imaging (QBI) completely break from the constraints of model-based techniques. These methods attempt to more directly measure spin displacements in 3 dimensions. We will briefly review these techniques here. However, before we begin, we must introduce the concept of *q*-space and how it relates to essentially all diffusion-weighted imaging.

Q-space is a three-dimensional space that maps diffusion signal information as a function of encoding gradient strength and direction. Each “point” in *q*-space represents a unique diffusion-weighted image encoded in a specific direction with a specific degree of diffusion

weighting. A *q-vector* extending from the origin locates points in *q*-space. The length (magnitude) of the *q*-vector is proportional to the applied diffusion weighting (i.e., the b-value). The direction of the *q*-vector indicates the direction of the applied diffusion encoding gradient [83]. Sampling of diffusion signal *S* in *q*-space should demonstrate mirror symmetry about the origin, reflecting that it is inherently an *even* function, that is $S(qx, qy, qz) = S(-qx, -qy, -qz)$. A conventional diffusion-weighted trace image acquisition would be represented by three distinct points in *q*-space, equally distant from the origin, with *q*-vectors perpendicular to each other (three orthogonal directions, one *b*-value). A diffusion tensor acquisition would necessitate a minimum 6 points (six non-collinear directions, one *b*-value) in *q*-space.

Diffusion spectrum imaging (DSI) is a model-free q-space imaging technique that brilliantly resolves areas of intricately crossing white matter architecture [84]–[86]. Rather than utilizing the tensor model to define only three principal axes for the diffusion profile, DSI seeks to more directly and more completely assess diffusion by measuring diffusion-related signal attenuation in as many as 500 or more directions with varying *b*-values, resulting in a very densely sampled *q*-space. The distribution of displacements, or probability density function, are estimated by 3-D Fourier transformation of the 3-D *q*-space signals. This does not assume that the diffusion has any specific functional form including Gaussian diffusion, which is the basis for DTI. The directional components of the probability density function are often represented and visualized by computing an orientation density function (ODF), which is estimated by summing the displacement distribution for each direction. Glyph representations of the ODFs are often volume rendered to visualize the peak directions (Figure 2.29). This more complete and

accurate directional information is used to resolve crossing fibers for white matter tractography. When connected and grown as fibers, even complex intravoxel crossing white matter tracts can be resolved, such as within the optic chiasm (Figure 2.30). It should be noted that noise effects may significantly impact image quality in model-free techniques like DSI. As diffusion is essentially measured "directly;" a spurious peak in the displacement distribution can seriously alter the appearance of the ODF and translate into a non-anatomic correlate at the molecular level [26] (14).

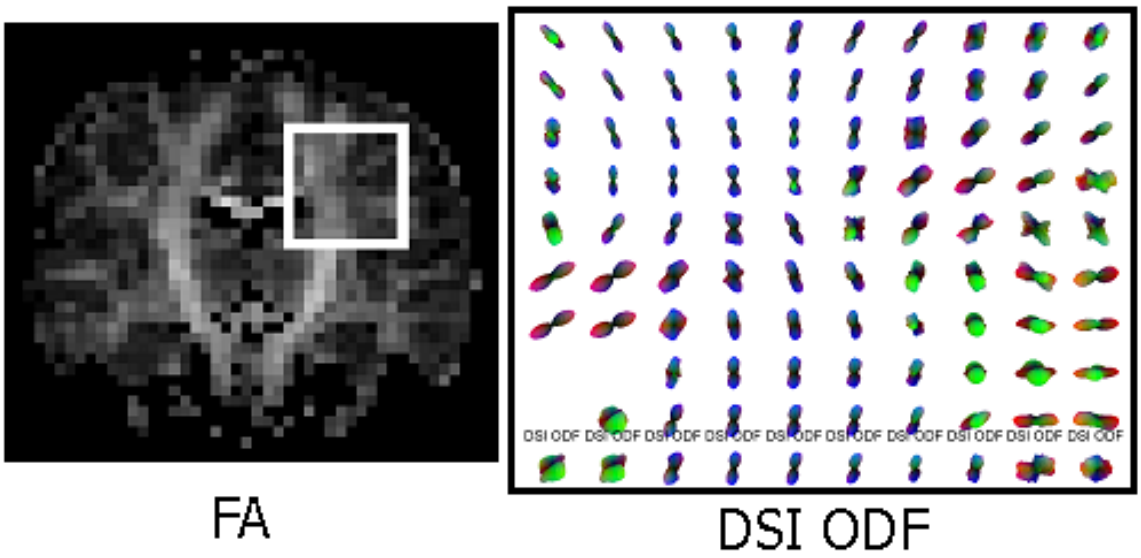

Figure 2.29 Fiber orientation distribution function (fODF) mapping. Glyph representation of the fODF in diffusion spectrum imaging (DSI). Dense sampling of diffusion signal in *q*-space can be translated into directionally specific displacement distributions, from which fODFs are created and rendered as a 3D glyph for each voxel. In contrast to the Gaussian model of diffusion in DTI, DSI makes no underlying assumptions about the functional form of diffusion. In this way, DSI attempts to *directly* characterize spin displacements for many different directions. Adapted from [2] and courtesy of Andrew Alexander.

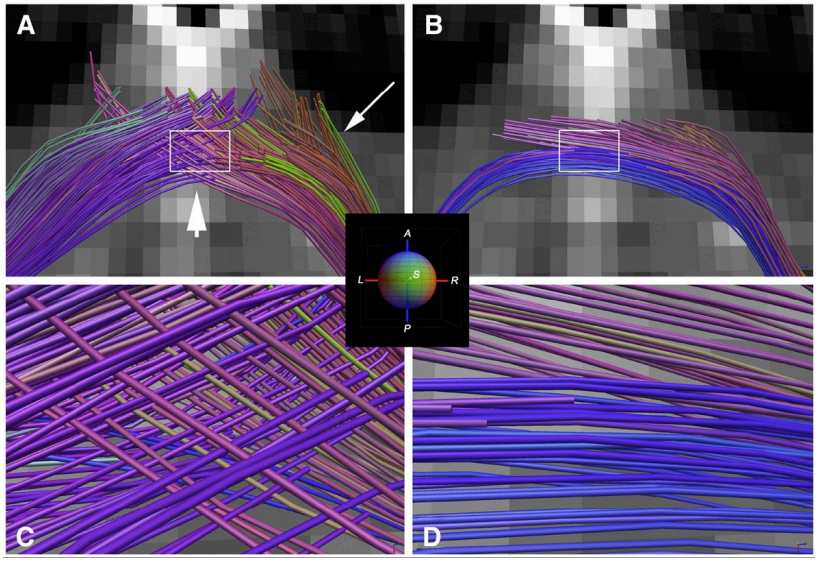

Figure 2.30 DSI (right) and DTI (left) renderings of crossing fibers in the optic chiasm of the monkey brain. Adapted from Weeden et al. 2008.

Different schemes of filling of *q*-space can also approximate the ODF (Figure 2.31). *Q*-ball imaging (QBI) [87], for instance, is another model-free technique. Utilizing a novel acquisition scheme, *q*-space is filled evenly over the surface of a sphere (the *q*-ball). The acquired data is subjected to a complex mathematical process called the Funk-Radon transform, similar to the Fourier transform, from which an ODF can be generated that very closely approximates the ODF of DSI [41], [84]. While fewer encoding directions (> 60 as opposed to >500) are necessary for *q*-ball imaging when compared to DSI, both techniques feature higher *b*-weighting than is typically used in DTI [83]. Both DSI and QBI are particularly relevant to advanced tractography and ongoing explorations of functional connectivity, where the ability to resolve crossing fibers will be essential.

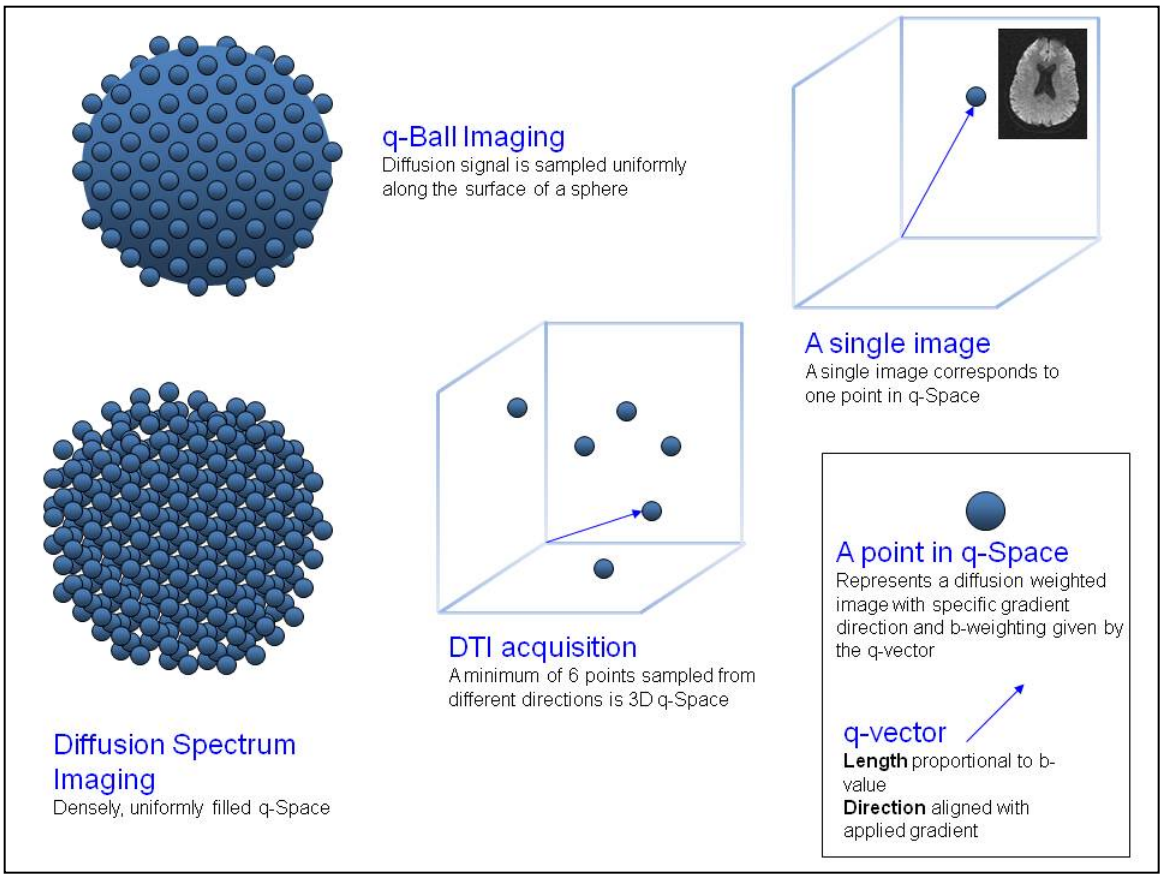

Figure 2.31 Diagram depicting q-space imaging. Each point in *q*-space represents a unique diffusion weighted acquisition at a specific *b*-value and direction, given by a *q*-vector. Adapted from [2] and courtesy of Thomas Gallagher, Aaron Field, and Andrew Alexander.

2.9 A WORD ON PARALLEL IMAGING

Practical and successful implementation of the DWI techniques presented in this chapter is conditional on feasible acquisition times as well as the quality of the data in terms of SNR, spatial accuracy, angular and spatial resolution, and appropriate diffusion contrast. While SS-EPI is very fast at acquiring entire volumes compared to multi-shot (e.g. line by line) methods, readout times (the time lapsed before the next magnetization excitation) are much longer for SS-EPI. Long EPI readout times are behind the common artifacts that affect SS-EPI including distortion, ghosting and blurring. Even with rapid SS-EPI, the acquisition times can be quite long

for DWI studies with many directions and b-values. Below a brief description is given of how advances in parallel imaging have been used to circumvent these limitations.

2.9.1 In-plane Parallel Imaging

Two-dimensional parallel imaging methods shorten acquisition times by collecting fewer data points over a single slice and rely on multi-channel coils and their sensitivity maps to mitigate artifacts associated with the under-sampling. Insufficient sampling of the signal violates a principle known as the Nyquist Criterion and leads to portions of the image being folded-over inside the field of view and overlap on each other when reconstructed. This type of artifact is known as *aliasing* and the amount of overlap is related to the sampling spatial frequency of the MRI signal. In absence of additional information to differentiate the intensities of the overlapping images, correction of aliasing artifacts is unattainable. When multi-channel coils are used to collect the signal, however, the differences in spatial sensitivity of each coil provide a unique piece of information at each voxel that can be used to de-alias (or unfold) and relocate each voxel to its appropriate position [88], [89].

By using in-plane parallel imaging, higher resolution images may be acquired in similar times to lower resolution SS-EPI without any acceleration. The Fourier space under-sampling and corresponding accelerated sampling rate is applied in the 'phase encode' direction, which reduces the distortions caused by inhomogeneities in the main magnetic field and reduces image blurring from T2*. The faster readout may also reduce the echo time, TE, which will increase the SNR. It should be noted that high acceleration rates lead to penalties in the SNR. Another limitation of this method is the difficulty to remove residual aliasing in areas where the

sensitivity profiles of the different coils are very similar. This is more severe in regions closer to the center of the sensitivity maps where sensitivity is lowest for all coils.

2.9.2 Simultaneous Multi-Slice EPI

A significant reduction in total acquisition time may be achieved by a higher-level variant of parallel imaging known as multi-band or simultaneous multi-slice imaging (SMS) [73]. With this method, signals from multiple slices are acquired simultaneously with a single shared contrast-encoding block. The efficiency in data acquisition is proportional to the acceleration factor, which itself is equal to the number of slices simultaneously acquired. SMS requires that coils are distributed along the slice direction in order to allow for the use of coil sensitivities in separating the signals from the individual slices. The process for separating the overlapping slices is essentially similar to that used with in-plane acceleration. The technicalities of multi-band imaging and its adaptation to EPI [34] are beyond the scope of this work, but it is worth emphasizing that multiband acquisition has had major implications in all of 2D MR imaging, particularly in techniques for which time consideration is essential such as in functional and diffusion MRI.

The benefits of SMS imaging in diffusion are evidenced in results from the Human Connectome Project (HCP) [90]. For example, HCP *HARDI* scans were achieved at greater than 60% reduction in acquisition time by simultaneous encoding and collection of three slices at 1.5 mm isotropic resolution. Combined contributions from faster, stronger gradients to reduce diffusion encoding time, reduced number of phase encoding lines collected with parallel imaging, q-

space compressed sensing, and simultaneous multi-slice, the Connectome scanner protocol was able to acquire high quality DSI data in under 5 minutes.

Though substantial improvements to the scanner hardware aided in achieving the enhanced acquisition times in the HCP, other studies have reaffirmed the time efficiency of SMS using clinical scanners with less advanced hardware designs [91], [92]. In general, SMS acquisitions will reduce scan times of DWI studies by factors of 2-2.5 relative to conventional single-slice DWI methods. SMS may be used to complement in-plane parallel acceleration. This will improve spatial accuracy by reducing geometric distortions. However, when used alone, SMS does not suffer from the SNR penalties associated with in-plane parallel imaging since no Fourier space lines are omitted.

2.10. Beyond DTI and Biophysical Models: Multidimensional Diffusion MRI

In the previous sections we have discussed that DTI and DKI offer very sensitive but non-specific parameters to alterations of the underlying structure. For example, changes in either cellular density or direction can lead to the same observed change in FA or MK. This makes the interpretation of the imaging parameters ambiguous in terms of the underlying tissue micro-structure. In order to disentangle the effects of different features of the microstructure on the observed signal, researchers in the field have resorted to biophysical model techniques such as Neurite Orientation Dispersion and Density Imaging (NODDI) [69]. However, due to the number of parameters needed to faithfully describe the signal in terms of the complex tissue micro-architecture, biophysical modeling methods need to rely on model assumptions that are often

oversimplifying. For example, in the next chapter we show that current assumptions of the NODDI model are suboptimal in specific age groups and tissue types [93].

Two of the current challenges in dMRI have to do with quantifying the intra-voxel heterogeneity of diffusion properties and disambiguating the biological interpretation of imaging parameters. The collective consensus in the field is that the ability to make progress on these two fronts depends on successfully devising ways to incorporate more information in the data.

To that end, a *different* category of methods that includes data acquisition with advanced gradient modulation schemes and data processing approaches, referred to as multidimensional diffusion MRI, offers the ability to quantify tissue micro-compartment properties and to also produce more interpretable parameters [94]–[98]. Generally, these methods consider two components of diffusional heterogeneity within a voxel. An anisotropic variance component that stems from differences in cell eccentricity and cell structures: microscopic anisotropy. And an isotropic variance component that is due to different isotropic diffusivities reflecting different cell sizes and densities as well as mixtures of tissues: isotropic heterogeneity.

The fundamental bid behind this type of approaches for disentangling sources of diffusional variance is to pack additional information in the data by augmenting one dimension to the measurement. This is done by encoding for diffusion along multiple directions before sampling the signal, then collecting data with multiple configurations of the diffusion encoding wave forms. By contrast, with the traditional method that underlies the basic data acquisition unit in DTI, DKI, and NODDI, images are read one diffusion-direction at a time. Diffusion encoding, then, goes from vector description in the conventional acquisition to a tensor

description in the multidimensional case. For this reason, multidimensional diffusion encoding is also known as b-tensor or tensor-valued encoding.

Initially, multidimensional diffusion encoding sequences were only feasible under specific hardware constraints and therefore limited to high performance systems. In recent years, however, there has been a great effort in the field for designing multidimensional diffusion encoding sequences that are more amenable to the specifications of clinical scanners.

Diffusion encoding along two orthogonal directions in NMR experiments dates back to as far as the early 1990s [99]. More recently, a technique known as “isotropic diffusion weighting by magic angle spinning of the q-vector” was introduced to successfully map microscopic anisotropy unconfounded by orientation dispersion [95]. In the recent years, b-tensor encoding has emerged as the general category which isotropic diffusion weighting and single diffusion (or conventional encoding) are special cases of.

The gradient waveforms in the earlier implementations of b-tensor encoding were very demanding on the MRI system hardware, requiring high performance gradients and prolonged acquisition times. Fortunately, continued research has sought optimizations of the early waveforms that are more forgiving of lower performing hardware and permit for modest scanning times in clinical scanners. For example, a recent study demonstrated the feasibility of tensor-valued encoding sequences in 1.5 T scanners with gradients performing as low as 33 mT/m in amplitude [100]. Similarly, a study of intracranial tumors with multidimensional diffusion MRI reported scan times (<3 minutes) that are feasible in clinically relevant time domains [101].

A number of methodologies have been reported for the analysis of data acquired with tensor-valued encoding sequences [95], [97], [102], [103]. One of the most common approaches is known as diffusional variance decomposition [95]. This assumes that the measured diffusional processes can be approximated by a distribution of microscopic diffusion tensors. The first step in this process is to parameterize the tensor distribution by a mean diffusivity and two components of microscopic variance (isotropic + anisotropic). The next step is to proceed to estimate the mean diffusivity as well as the effects of each variance component by using a combination of shapes of the b-tensor for diffusion encoding.

The shapes of the b-tensor vary from linear b-tensor on one end of the spectrum to spherical b-tensor on the other. The linear b-tensor is simply the conventional single diffusion encoding and the resulting signal accounts for the total intra-voxel variance (i.e. the sum of the isotropic and anisotropic components). On the other extreme, with spherical tensor encoding, diffusion encoding occurs equally and simultaneously in three orthogonal directions. This makes the signal sensitive only to the isotropic component of the variance, effectively removing the effects of the anisotropic variance component [98].

Thus, the mean diffusivity and total variance can be estimated by modeling the linear tensor encoding signal for a sufficient number of b-values and diffusion directions [104]–[106]. The isotropic variance component can be measured by using spherical tensor encoding repeated for the same number of b-values as in the linear tensor encoding. Finally, the anisotropic variance component can be recovered by subtracting the isotropic from the total variance. This approach also allows for estimating microscopic FA and an orientation order parameter [97]. While macroscopic FA as estimated from DTI is affected by both the diffusion

anisotropy as well as directionality, microscopic FA has been shown to be more specific to the anisotropy in diffusion [96].

2.11 Conclusion

In this chapter we have reviewed historical and theoretical context around MRI and diffusion MRI. The theoretical underpinnings of DTI were emphasized a great deal in this chapter as this is still the most popular form of diffusion imaging despite its well-known limitations. Other techniques including model-based and model-free approaches were described in this chapter and we will be coming across some of them in the next three chapters. Finally, exciting and promising technological and theoretical advances were reviewed, which will continue to move the field forward.

Chapter 3 - Investigating the assumption of fixed parallel intrinsic diffusivity in the neurite orientation dispersion and density imaging technique

Portions of this chapter have been published in the journal of the Public Library of Science (PLoS) ONE in August 2019. (Guerrero, J. M., Adluru, N., Bendlin, B. B., Goldsmith, H. H., Schaefer, S. M., Davidson, R. J., ... & Alexander, A. L. (2019). Optimizing the intrinsic parallel diffusivity in NODDI: An extensive empirical evaluation. *PloS one*, *14*(9).)

3.1 Abstract

NODDI is widely used in parameterizing microstructural brain properties. The model includes three signal compartments: intracellular, extracellular, and free water. The neurite compartment intrinsic parallel diffusivity $d_{\parallel}$ is set to 1.7 μm^2·ms^{-1}, though the effects of this assumption have not been extensively explored. In this chapter, work is presented from investigations on the optimality of $d_{\parallel}$=1.7 μm^2·ms^{-1} under varying imaging protocol, age groups, sex, and tissue type in comparison to other biologically plausible values of $d_{\parallel}$. Model residuals were used as the optimality criterion. The model residuals were evaluated as a function of $d_{\parallel}$ over the range from 0.5 to 3.0 μm^2·ms^{-1}. This was done with respect to tissue type (i.e., white matter versus gray matter), sex, age (infancy to late adulthood), and diffusion-weighting protocol (maximum b-value). Variation in the estimated parameters with respect to $d_{\parallel}$ was also explored. Results show $d_{\parallel}$ =1.7 μm^2·ms^{-1} is appropriate for adult brain white matter but it is suboptimal for gray matter with optimal values being significantly lower. $d_{\parallel}$ =1.7 μm^2·ms^{-1} was also suboptimal in the infant brain for both white and gray matter with optimal values being significantly lower. Minor optimum $d_{\parallel}$ differences were observed versus diffusion

protocol. No significant sex effects were observed. Additionally, changes in $d_{\parallel}$ resulted in significant changes to the estimated NODDI parameters.

3.2 Introduction

As mentioned in the previous chapter, in diffusion weighted magnetic resonance imaging (dMRI), biophysical models are used for relating the dMRI signal to microstructural properties in white and gray matter [45], [68], [69], [107]–[110]. Neurite orientation dispersion and density imaging (NODDI) [69], separates the brain tissue microstructure landscape into three compartments: intracellular space or neurites (axons, dendrites), extracellular tissue matrix, and a free water compartment. In spite of its shortcomings, much like the case of other techniques such as diffusion tensor imaging (DTI), NODDI offers useful information and has been widely used in the investigation of brain tissue microstructure as a function of early development, cognitive function and aging as well as a number of neurological conditions [74]–[79].

Biophysical modeling relies on simplifying assumptions about the tissue properties. Besides the separation of tissue into three compartments, the NODDI model is characterized by the following features or assumptions. Each compartment is represented by its own normalized signal and volume fraction. Water exchange between compartments is assumed negligible. Neurites are modeled as sticks (cylinders of zero radius) for capturing highly anisotropic architecture of neuronal tissue. Diffusion inside the neurites is described by a diffusivity parallel to the sticks, which is referred to as the *intrinsic diffusivity*, $d_{\parallel}$, and zero diffusivity perpendicular to them. The orientation distribution function (ODF) of the sticks at each voxel is

modeled by an axially symmetric Watson distribution, *W* [111], which itself is characterized by a concentration parameter κ and mean orientation $\boldsymbol{\mu}$. Highly aligned sticks like those seen in white matter bundles are reflected by high κ values, while highly dispersed sticks like those seen in gray matter fibers are reflected by low κ. The extra-neurite compartment is directionally correlated with the neurite ODF and modeled as a Gaussian anisotropic compartment.

The local parallel diffusivity of the extracellular space is set equal to the intra-neurite intrinsic diffusivity, $d_{\parallel}$, whereas the perpendicular diffusivity $d_{\perp}$ is related to the neurite water fraction, f_{ic}, and $d_{\parallel}$ by the mean-field tortuosity model [112] as $d_{\perp} = (1 - f_{ic})\, d_{\parallel}$. The free-water compartment is modeled as having isotropic diffusion with free diffusivity $d_{iso} = 3\ \mu m^2\ ms^{-1}$ and volume fraction f_{iso}. The intrinsic diffusivity $d_{\parallel}$ for NODDI is assumed to be 1.7 $\mu m^2 ms^{-1}$. This is selected to be a biologically reasonable value, which approximates the mean parallel diffusivity from DTI in a healthy coherent white matter region [107]. The parameters that are estimated from acquired data using non-linear gradient descent and heuristic initializations are the water fraction of the neurite compartment f_{ic}, the concentration (κ) and mean orientation ($\boldsymbol{\mu}$) of the Watson distribution. The signal $S(b, \mathbf{g})$ from the unit diffusion gradient direction $\mathbf{g}$ for sticks oriented along unit vector $\mathbf{n}$ and b-matrix ($b\mathbf{g}\mathbf{g}^t$) is given by

$$S(b, \boldsymbol{g}) = S_0 \left((1 - f_{iso})(f_{ic} A_{ic} + (1 - f_{ic}) A_{ec}) + f_{iso} A_{iso}\right) \qquad \text{Equation 3.1}$$

where

$$\begin{cases} A_{ic} = E\left[e^{-bd_{\parallel}(\boldsymbol{g}^t\boldsymbol{n})^2}\right] \\ A_{ec} = e^{-bE[\,\boldsymbol{g}^t D_e(\boldsymbol{n})\boldsymbol{g}]} \\ A_{iso} = e^{-bd_{iso}} \end{cases}$$

$$E[x] = \oint_{S^2} x\, W(\boldsymbol{n}, \boldsymbol{\mu}; \kappa)\, d\boldsymbol{n}, \text{ such that } \boldsymbol{g}, \boldsymbol{n}, \boldsymbol{\mu} \in S^2.$$

A_{ic}, A_{ec}, and A_{iso}, are the intra-cellular, extra-cellular, and free-water isotropic compartments signal contributions respectively (see Figure 3.1). $W(\mathbf{n}, \boldsymbol{\mu}; \kappa)$ is the Watson distribution with κ concentration and oriented along $\boldsymbol{\mu}$. S_0 is the un-attenuated signal i.e. $S(0, 1)$, and $D_e(\mathbf{n}) = f_{ic} d_{\parallel} \mathbf{n}\mathbf{n}^t + (1 - f_{ic})\, d_{\parallel} I_3$ is the axially symmetric extra-cellular apparent diffusion tensor.

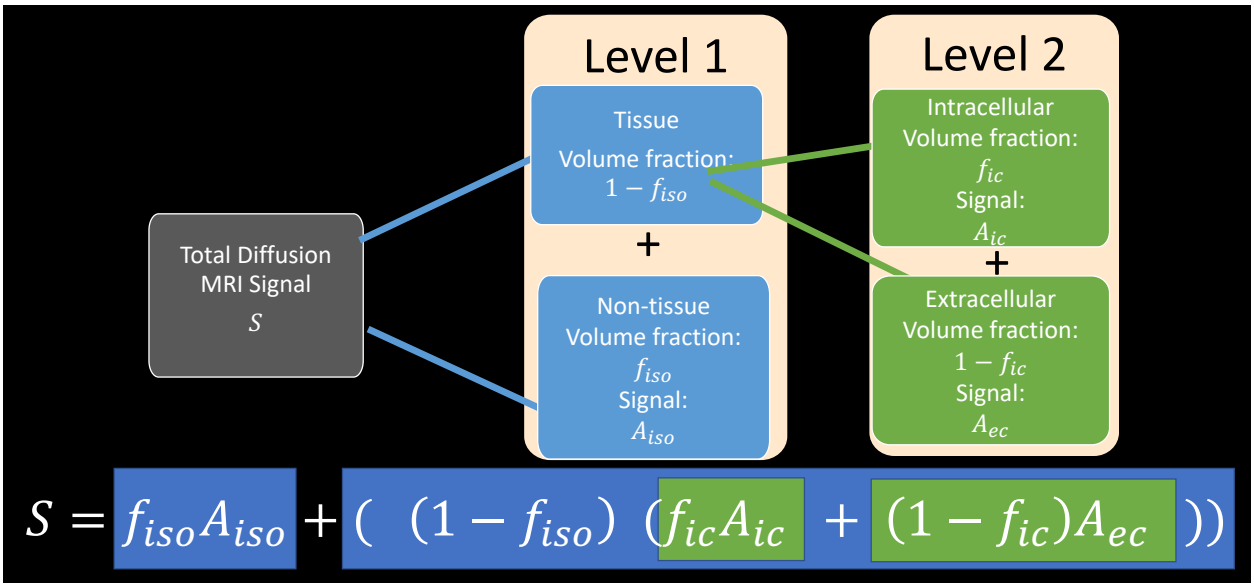

Figure 3.1 Illustration of the different levels of the NODDI model.

Recently, the model assumptions have become a topic of discussion in the field. The more relevant discussions have focused around the fixed parallel intrinsic diffusivity and equality between parallel intrinsic diffusivity of the extra- and intra-cellular compartment [113]. Of the

two, the equality assumption is the more difficult to assess, but has been explored in several reports. While no consensus has been reached, most reports suggest that the intra-cellular parallel intrinsic diffusivity is larger than the extra-cellular one [96], [114]–[116]. Yet, this may depend on tissue type [117] and most studies have focused on white matter. Also, some sustain that the differences may not be substantial and independent validation experiments are needed [113].

With respect to the fixed diffusivity assumption, Kaden et al., [118] proposed a framework for relaxing the fixed constraints. The study reported that microscopic parallel diffusivities varied across the brain, and that white matter values where considerably larger than that assumed by NODDI. It is important to note, however, that the ability to "estimate intrinsic diffusivity" in [118] comes at a cost, which is the reduction to two-compartment model. In this sense, then, the model in that report is not fully comparable to the model in NODDI, since the former gives up on estimating the CSF volume fraction. Others [119], [120] have also relaxed the fixed diffusivity constraint and made it a free parameter. However, this resulted in unwanted effects on the other parameters in the form of unstable and degenerate estimates. Originally, it was considered unlikely that variation in $d_{\parallel}$ across regions and subjects was significant enough to remove trends in the estimated parameters [107]. Additionally, the fixing of $d_{\parallel}$ is necessary for stability in the parameter estimates and for speeding up convergence of the fitting procedure. Plus, the value that was chosen was the value that minimized the fitting errors for voxels in the midsagittal plane of the corpus callosum [107].

Taking into consideration the non-consensus on the equality assumption and the still widespread use of the technique, here we choose to build on earlier work [121] which

investigated the assumption of fixed diffusivity. This consisted of looking at optimal values of the parallel intrinsic diffusivity according to the model residuals. Results suggested that the default value was reasonable in white matter, but it was sub-optimal in gray matter. While recent publications have found our method useful [122], [123], this earlier work only considered a single axial slice from three age matched participants and dMRI data acquired with the same imaging protocol. For this reason, we propose a more extensive investigation that considers a diverse array of data in terms of age populations, imaging protocols, and is conducted across the full brain.

We elected to conduct this analysis only for the case of the original NODDI technique [69] and not for its variants [124], [125], or its tumor-specific version VERDICT [126] as the vast majority of applications have implemented the original version.

3.3 Materials and methods

3.3.1 Data

Datasets acquired with multiple *b*-value sequences (suitable for implementing the NODDI technique [69]) were readily available for use in this work from a number of existing neuroimaging studies. These include imaging data from individuals with a broad range of ages and acquired with imaging protocols that vary in regard to number and magnitude of *b* values as well as number of diffusion encoding directions. dMRI sets include infants, adolescents, young adults, adults, and aging adults. All dMRI sets were collected on a 3T MR750 Discovery scanner (General Electric, Waukesha, WI). A brief description of each study is provided below

and details are summarized in Table 3-1. All procedures for the included studies were approved by the University of Wisconsin—Madison Institutional Review Board.

Table 3-1 Relevant characteristics of studies from which data were used for this work.

Study	Sex	Age	b-values [ms μm^{-2}]	Directions
Neonates	50 males 54 females	1 month	0.35, 0.8, 1.5	63
Teen-I	24 males 168 females	11-15 years	0.32, 0.8, 2.5	62
Teen-II	51 males 79 females	14-20 years	0.5, 0.8, 2.0	57
Midlife-I	57 males 89 females	25-65 years	0.5, 0.8, 2.0	57
AD-risk	18 males 53 females	47-76 years	0.3, 1.2, 2.7, 4.8, 7.5	105

Neonates study (Neonates). Participants are from a study of neonatal white matter microstructure. Diffusion scans contain 6 non-diffusion weighted volumes and diffusion encoded along 63 directions. Other imaging parameters include: *TR*/*TE* = 8400/94ms, 2mm isotropic resolution.

Teen study (Teen-I). Participants in this cohort were drawn from a study of emotion in adolescents. Diffusion scans contain 6 non-diffusion weighted volumes and diffusion encoded along 62 non-collinear directions. Other imaging parameters include: *TR*/*TE* = 8400/94 ms and 2 mm isotropic resolution.

Twin teen study (Teen-II). Participants are from a cohort of 130 adolescent twins. Diffusion scans contain 6 non-diffusion weighted volumes and diffusion encoded along 57 directions. Other parameters include 2.0 mm isotropic resolution and *TR*/*TE* = 8000/66.2 ms.

Midlife meditation study (Midlife-I). Participants in this cohort were drawn from a study of emotion regulation, asthma, and sleep part of the National Center for Complementary and Alternative Medicine (NCCAM). Diffusion scans contain 6 non-diffusion weighted volumes and

diffusion encoded along 57 directions. Other parameters include 2.0 mm isotropic resolution and *TR*/*TE* = 8000/66.2 ms.

Preclinical Alzheimer's disease risk study (AD-Risk). Participants were cognitively unimpaired individuals with and without increased risk for Alzheimer's disease recruited from the Wisconsin Registry for Alzheimer's Prevention and Wisconsin Alzheimer's Disease Research Center. Diffusion scans contain 7 non-diffusion weighted volumes and diffusion encoded along 105 non-collinear directions. Other imaging parameters include: *TR*/*TE* = 6500/102 ms, sagittal slices 3*mm* thick, and in-plane resolution of 2.5 mm × 2.5 mm.

3.3.2 Intrinsic diffusivity optimization

Optimality of $d_{\parallel}$ = 1.7 $\mu m^2 ms^{-1}$ was considered by minimizing the model residuals as in [107]. Other biologically plausible values were considered for comparison in the interval [0.5, 3.0] $\mu m^2 ms^{-1}$ in increments of 0.1 $\mu m^2 ms^{-1}$. For each of the 26 values, the model was fitted to the measured dMRI signal voxel by voxel using the Matlab (The MathWorks, Inc., Natick, MA) NODDI toolbox (http://nitrc.org/projects/noddi_toolbox). Predictions of the signal were then calculated at each voxel from the estimated parameters. With the measured and predicted signals for each $d_{\parallel}$ setting, the root mean squared (RMS) residual was computed at each voxel. A linear search across the 26 different points was then performed for locating the value of $d_{\parallel}$ corresponding to the lowest RMS residual value per voxel. This was done in order to generate a brain map of optimum $d_{\parallel}$ and for looking at the optimality of $d_{\parallel}$ = 1.7 $\mu m^2 ms^{-1}$ across brain regions.

3.3.3 Tissue type segmentations

White matter (WM) and gray matter (GM) masks were obtained for each individual in order to probe the influence of tissue type on the fitting residuals. This was conducted by running FSL's [127] FAST tool [128] with mean diffusivity (MD) and fractional anisotropy (FA) maps as input channels. FA and MD maps were obtained from tensor fits using a weighted least squares method. For the AD-risk study, the shells with b values of 4.8 and 7.5 msμm^{-2} were excluded in the tensor fitting.

3.3.4 Subgroups for Studying Influences of Age, Sex, and Protocol

The availability of data from the various studies allowed for selection of several subgroups that were organized according to age, sex, and protocol. With the data sets organized this way, the residual analysis was performed for the following three cases:

Groups for age analysis. Subgroups of 16 participants (roughly half male and half female) were selected from three studies as follows: One group of 16 subjects age approximately one month from the Neonates study. One group of 16 subjects ages between 10 and 19 from the Teen-II study. Six groups, 16 subjects each, extracted from the Midlife-I study, for the six age categories of: 20-29, 30-39, 40-49, 50-59, and 60-65 years. Note that, except for the neonates, these data sets have matching protocols so that the main difference per category was age. In order to help disambiguate protocol from age influences, two additional scans were obtained for one adult: one with the infant protocol and one with the adult protocol.

Groups for sex analysis. From the Teen-I study, two subgroups one of 30 females and one of 30 males were selected. The two groups were matched by age (13 years old), so that the main difference between the groups was sex.

Groups for protocol analysis. Two groups of 16 subjects (roughly half females and half males) with ages ranging from 50-59 years were selected, one from the Midlife-I study and one from the AD-risk study. In this case, the assumed main difference between the groups was the acquisition protocol.

3.4 Results

The results are organized as follows. **(1)** We first show how variation in $d_{\parallel}$ translates to variability in the estimated parameters. **(2)** Then, the model RMS residuals, with respect to $d_{\parallel}$ are shown to differ between tissue types. **(3)** This is followed by the presentation of voxel-wise optimized $d_{\parallel}$ maps and the ways in which the optimality of $d_{\parallel}$ = 1.7 μm^{2}ms^{-1} is influenced by age, sex, protocol and tissue type.

3.4.1 Estimated model parameters and $d_{\parallel}$

Upon completion of the various model fits, the dependence of the estimated model parameters to variations in $d_{\parallel}$ was explored. For all model parameter maps, mean values were calculated over WM and GM regions. Figure 3.2 shows these values plotted with respect to $d_{\parallel}$. This analysis reveals a dependence on $d_{\parallel}$ for all three parameters irrespective of the study as well as variation in the comparison of parameters among the studies. For example, for gray matter values of $d_{\parallel}$ that are lower than the assumed value would weaken variation of the neurite

density across the teen and adult subjects. On the other hand, lower values of $d_{\parallel}$ in gray matter would enhance differences in the ODF concentration parameter across all studies.

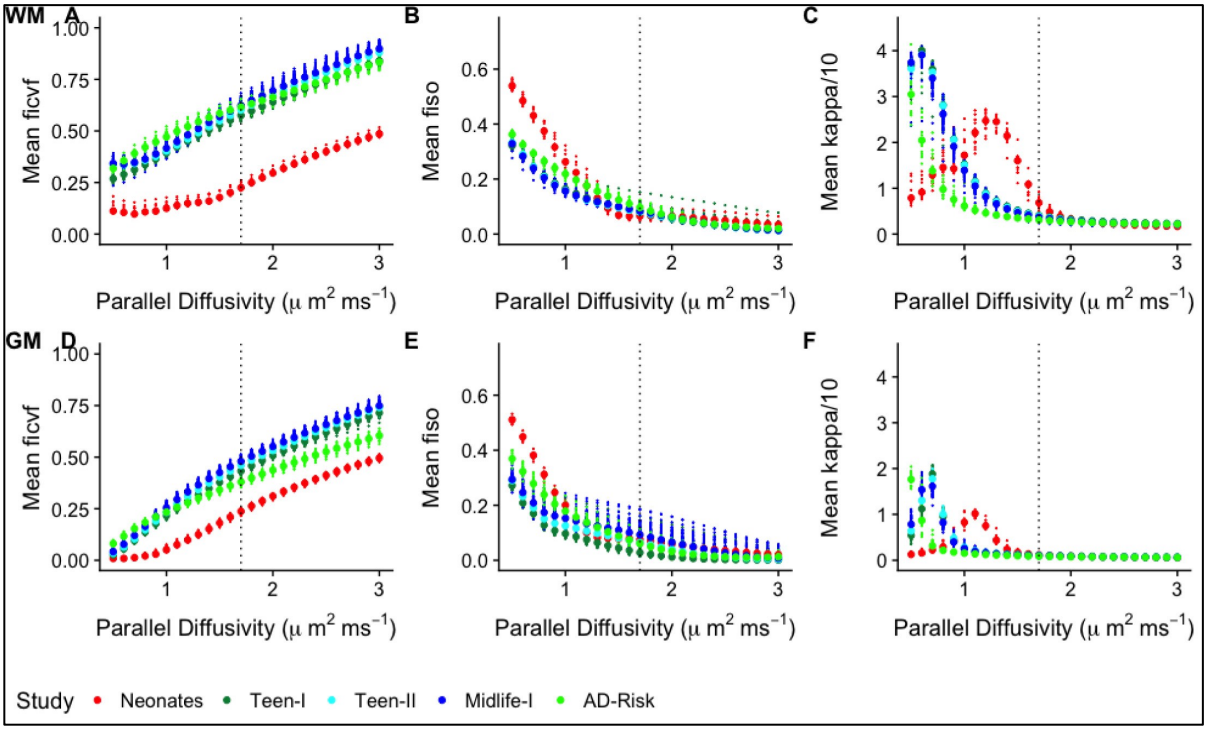

Figure 3.2 NODDI parameter trajectories with respect to $d_{\parallel}$. For each parameter (Intra-cellular compartment volume fraction, f_{ic}, isotropic compartment volume fraction, f_{iso}, orientation concentration parameter, κ), the analysis is broken by white matter (WM) and gray matter (GM) regions. Each point on the curves represents the mean parameter over WM or GM at the specific $d_{\parallel}$ value. The default operating point is marked by the blue dashed vertical line.

3.4.2 Model residuals with respect to $d_{\parallel}$

The values of $d_{\parallel}$ that result in the closest agreement between the measured and predicted signals as dictated by the RMS residuals were explored next. For each of the resulting 26 RMS residual maps, mean values across WM and GM were calculated. These are plotted with respect to $d_{\parallel}$ in Figure 3.3. These plots reveal that $d_{\parallel}$ values in GM that achieve minimum RMS residuals deviate from the default setting (1.7 μm^2 ms^{-1}) for all studies. For WM, the lowest values in the RMS residual curves occur in the neighborhood of the default setting. Notably,

most WM curves, with the exception of the Neonate study, exhibit broad ranges of lowest values as compared to the majority of GM curves. The better-defined minima in WM for the infants could be related to a maximum *b* value that better matches the characteristics of the young brain tissue (i.e. longer T_2, higher water content) such that diffusion weighting in the signal is more adequate. This is in line with the AD-risk study, which used a max *b*-value of 7.5 msμm^{-2} and the WM RMS residual curves are noticeably more convex. The remaining studies have maximum *b* values that are likely on the low end of the optimal range for capturing effects of more restrictive intra-neurite environment, which could help explain the shallower curves in WM.

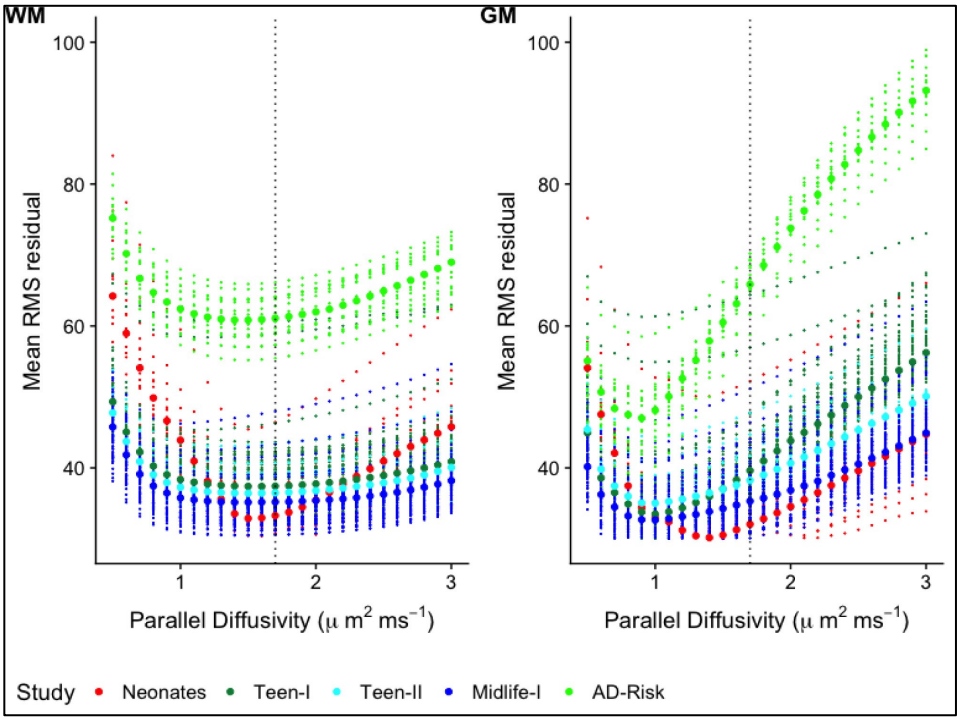

Figure 3.3 **.** Model residuals with respect to $d_{\parallel}$. Average root-mean-square (RMS) residual with respect to $d_{\parallel}$ for all subjects in each study. Each of the small size dots represents the mean RMS residual over white matter **(A)** or gray matter **(B)** at the specific $d_{\parallel}$ value. The large size dots represent the median value over all the subjects in the study at the specific $d_{\parallel}$ value. The default operating point is marked by the blue dashed vertical line.

3.4.3 Optimized $d_{\parallel}$ maps

Optimum intrinsic diffusivity whole brain maps were created by selecting at each voxel the value that corresponded to the smallest RMS residual. Resulting optimal $d_{\parallel}$ maps were median filtered using a box kernel (size 3x3x3 in voxels). The filtering helps to enhance the underlying structure in the distribution of values between white and gray matter. The pattern is spatially consistent before filtering, but it is more difficult to appreciate due to the shallowness of the residual curves for white matter for some of the studies (i.e. Teen-I, Teen-II, Midlife-I). Figure 3.4 shows optimum $d_{\parallel}$ maps for one subject selected randomly from each of the six studies. These maps reveal moderate to substantial contrast between WM and GM regions. The non-uniformly distributed $d_{\parallel}$ in these maps suggests that $d_{\parallel}$ = 1.7 μm^{2}ms^{-1} may not be appropriate for all brain regions and all populations.

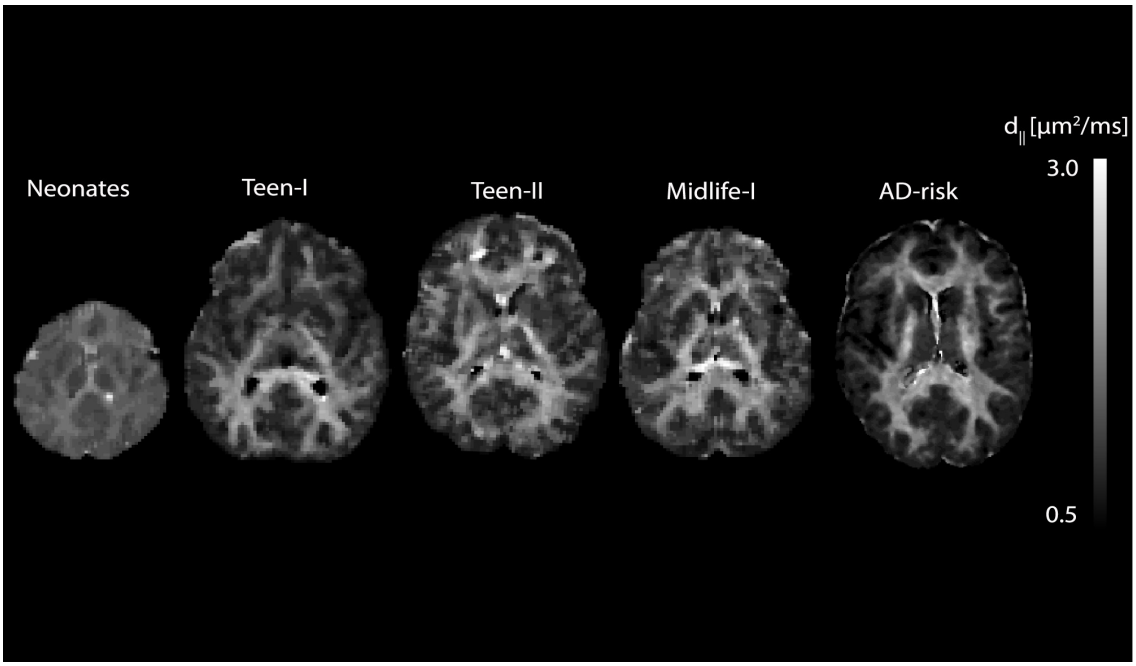

Figure 3.4 Optimum $d_{\parallel}$ maps. **(C)** Axial view of optimum $d_{\parallel}$ map for one subject selected from each of the studies.

3.4.4 Optimized $d_{\parallel}$ and age

Optimal $d_{\parallel}$ maps were computed for the cohort organized by age group. These maps were further masked into WM and GM regions and average optimal $d_{\parallel}$ values were obtained for each region. Figure 3.5(A) shows the distributions of average optimal $d_{\parallel}$ values according to age group. These plots show distinct distributions between WM and GM average optimal $d_{\parallel}$ for all age groups greater than 10 years. The majority of WM optimal $d_{\parallel}$ values are distributed around the default operating point (1.7 $\mu m^2 ms^{-1}$), while all GM optimal $d_{\parallel}$ values are reduced by at least 0.4 $\mu m^2 ms^{-1}$. These trends are fairly consistent for all distributions corresponding to ages 10 years and above. For the group of less than 1 year (i.e. infants) there is a greater degree of closeness between the WM and GM distributions of average optimal $d_{\parallel}$ in comparison to the rest of the age groups. In this case, optimal $d_{\parallel}$ values fall approximately between 1.4 and 1.5 $\mu m^2 ms^{-1}$ for WM and 1.2 and 1.3 $\mu m^2 ms^{-1}$ for GM. For each age group, a pairwise t-test was conducted in order to assess statistical significance of the tissue-wise difference in average optimal $d_{\parallel}$. The testing showed that for all groups the optimum $d_{\parallel}$ for GM and WM were significantly different ($p < 0.01$). A multiple group test revealed that average optimal $d_{\parallel}$ is significantly different between the infant and the rest of the older age groups in both WM and GM, while no significant differences were found between any of the other groups. The mean optimum $d_{\parallel}$ values for the two additional scans on one adult, Figure 3.5(B), are in agreement with those values from same age group for both the infant and adult protocols, pointing to the fact that the observed trends are more a result of differences in age rather than in protocol.

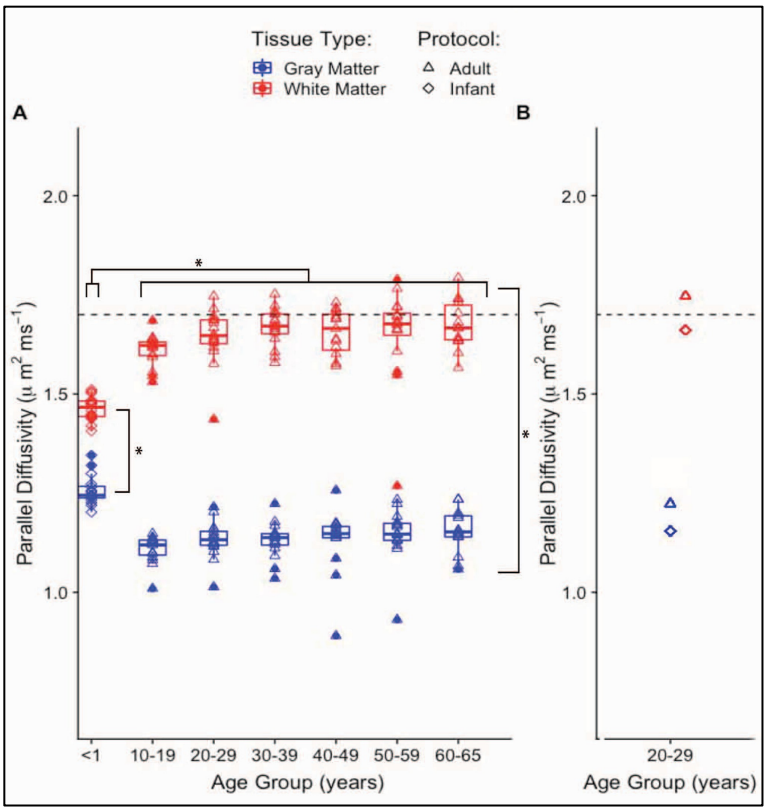

Figure 3.5 Optimized $d_{\parallel}$ as function of age group and tissue type. (**A**) Mean value of optimal $d_{\parallel}$ as function of age group and tissue type. The scanning protocol for the <1 year group is slightly different than that of the rest of the groups (Table 1). The numbers from scanning one adult with the two protocols are shown in **B**. The dashed horizontal line marks the default $d_{\parallel}$ value.

3.4.5 Optimized $d_{\parallel}$ and sex

Optimal $d_{\parallel}$ maps were also computed for the cohort organized according to sex. Average optimal $d_{\parallel}$ values were obtained across WM and GM regions. The distributions of average optimal $d_{\parallel}$ values according to sex category revealed significantly different values between WM and GM with ranges that are consistent with the same age group (10-19 years) from the age-dependence analysis. Yet, no significant effects of sex were observed, a result that is compatible with the age-dependent analysis, which also showed no obvious split in optimal $d_{\parallel}$ between the male and female participants.

3.4.6 Optimized $d_{\parallel}$ and acquisition protocol

Finally, optimal $d_{\parallel}$ maps were also computed for the cohort of subjects with data acquired under differing imaging protocols. Based on the observation that the age dependence analysis revealed no obvious age effects for ages 10 and above, data from the Teen-I study was also included in this cohort despite the unmatched age. This resulted in 3 protocol categories. Figure 3.6 shows the distribution of WM and GM average optimal $d_{\parallel}$ values according to imaging protocol.

The data sets from the groups with the highest b value protocol show optimal $d_{\parallel}$ values that are lower than $d_{\parallel}$ = 1.7 μm^{2}ms^{-1}. In GM, this analysis reveals a seemingly decaying trend in optimal $d_{\parallel}$ distributions with respect to maximum b value. Pair-wise t-tests revealed all distributions in GM are significantly shifted down compared to WM distributions, consistent with the observed trend in the previous age and sex comparisons.

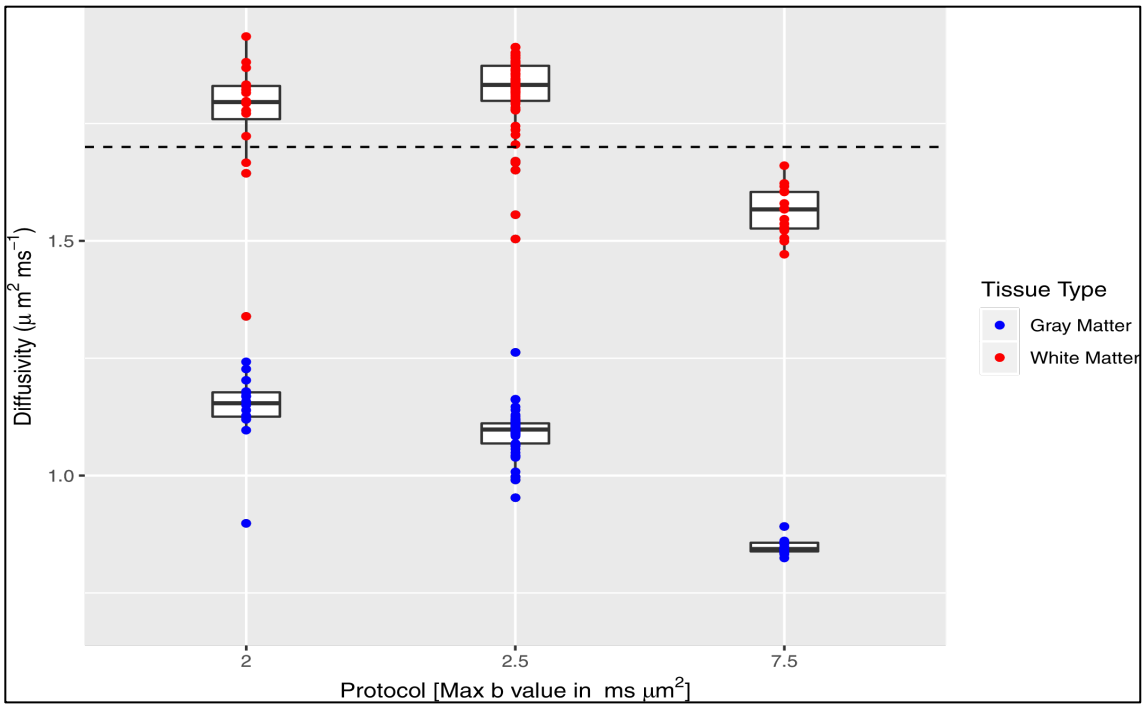

Figure 3.6 Optimized $d_{\parallel}$ as function of imaging protocol. Mean value of optimal $d_{\parallel}$ as function of imaging protocol and tissue type. The dashed horizontal line marks the default $d_{\parallel}$ value.

3.5 Discussion

In this work we studied the implications of diverse multi-shell dMRI data on the optimality of the NODDI parallel intrinsic diffusivity $d_{\parallel}$ = 1.7 μm^{2}ms^{-1}. The results suggest model assumptions for $d_{\parallel}$ may be suboptimal for specific ages (i.e., infants) and also in gray matter. Although not examined, the optimality of $d_{\parallel}$ = 1.7 μm^{2}ms^{-1} may also vary with pathology. We also observed that suboptimal $d_{\parallel}$ leads to biases in the estimated NODDI parameters. Of particular interest would be a drop of neurite density in gray matter, a result that is consistent with findings in a recent study [117].

For gray matter, the optimal $d_{\parallel}$ is significantly lower than 1.7 μm^{2}ms^{-1}. In white matter of the adult brain, values of the optimal $d_{\parallel}$ hover around the default $d_{\parallel}$ = 1.7 μm^{2}ms^{-1} and just below the range [1.9, 2.2] μm^{2}ms^{-1} of intra-axonal diffusivities in white matter reported

elsewhere [129], though, further analysis (see below) suggested high FA regions in the adult brain contained average optimal $d_{\parallel}$ that falls in this range. It is important to note, however, that the ranges of residual minima in white matter were broad and shallow.

Further, a finer grain analysis indicates that protocol and age also have an impact on the optimality of $d_{\parallel}$ = 1.7 μm^{2}ms^{-1}, both in white and gray matter. The age-dependence analysis revealed that the newborn brain optimum $d_{\parallel}$ in white and gray matter are closer in value compared to those in the adult brains. Both WM and GM values of optimum $d_{\parallel}$ are different, however, from that used in recent studies [120], [130] that have implemented NODDI in the infant brain. The value in these studies was set to 2.0 μm^{2}ms^{-1}, likely because average DTI axial diffusivity in high FA regions (see below) of newborns is close to this number. Interestingly, at this setting, and using the 1.7 μm^{2}ms^{-1} for the adult brain, nearly any difference between the infants ODF concentration parameter and that of the older age brains would be removed in gray matter. Using the optimal setting for $d_{\parallel}$, would result in appreciable differences in ODF concentration parameter between the adults and the infants. On the other hand, using the optimal settings for $d_{\parallel}$, would weaken the differences in intra-cellular volume fraction between the infant and the older subjects.

This analysis also showed that in the adult brain optimum intrinsic diffusivity values do not vary appreciably with age. However, optimum $d_{\parallel}$ values in GM are much lower than those in WM and different from the default $d_{\parallel}$ = 1.7 μm^{2}ms^{-1}. With regards to imaging protocol, high b value and more diffusion weighted volumes appeared to yield less noisy and more stable optimal intrinsic diffusivity and NODDI parameter estimates.

In hindsight, the sub-optimality of the assumed $d_{\parallel}$ = 1.7 μm^{2}ms^{-1} in gray matter is not surprising since this value was originally estimated in the adult corpus callosum [107]. Also, suboptimality of the current state of the model in gray matter might be related to the idea that the impermeable 'stick' representation of neurites is only adequate for myelinated axons but not for dendrites or non-myelinated axons, as others have suggested [131]. In general, however, the variation of optimal intrinsic diffusivity across tissue types is in agreement with findings of axial diffusivity variation across the brain reported in [117].

Studies have reported decreasing DTI axial diffusivity with age [132]–[134]. Thus, the trend of increasing optimum $d_{\parallel}$ with age in WM seen in Figure 3.5(A) prompted further investigation. For comparison, averages of DTI axial diffusivity over WM and GM were computed for all subjects in all age groups (Figure 3.7).

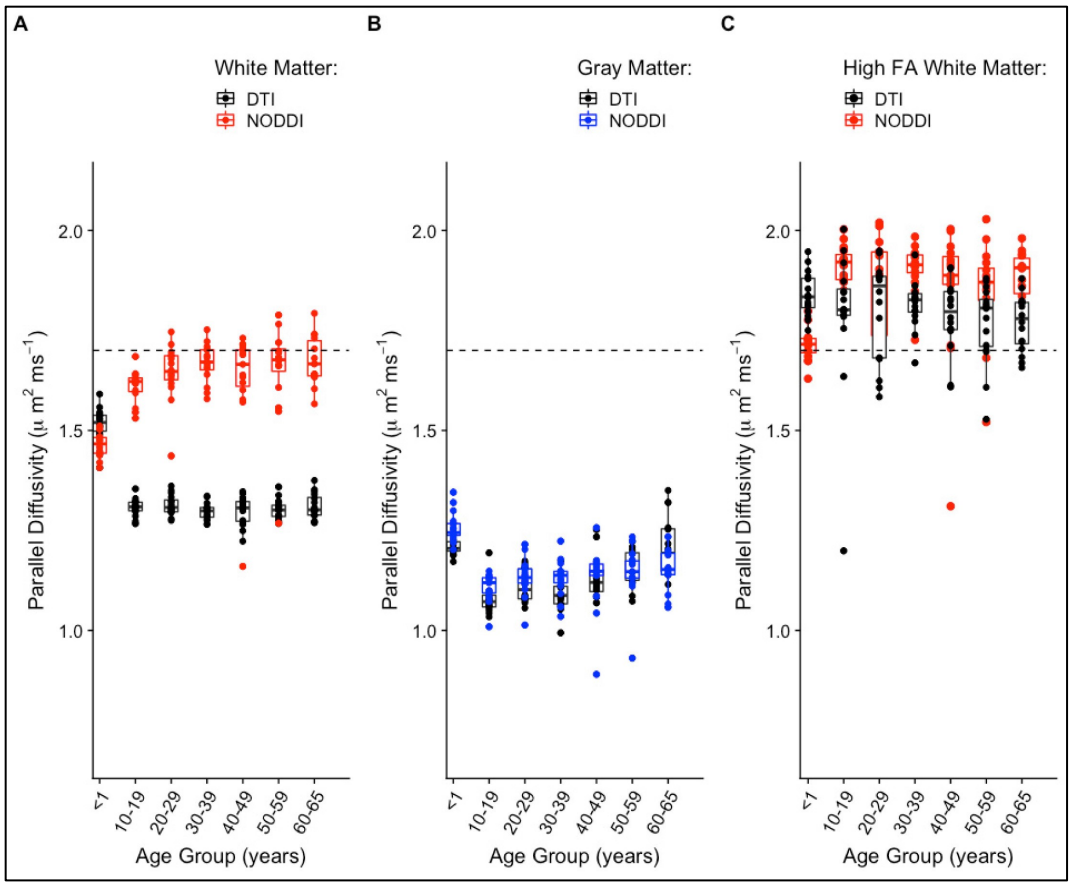

Figure 3.7 NODDI and DTI. Comparison of age trajectories between NODDI optimum parallel intrinsic diffusivity and DTI axial diffusivity in global white matter **(A)**, global gray matter **(B)**, and high FA white matter **(C)**. The dashed horizontal line marks the NODDI default $d_{\parallel}$ = 1.7 μm^{2}ms^{-1} value.

The resulting axial diffusivity age trajectories are in agreement with previous studies [132]–[134]. However, while these numbers pertain to the whole of white matter, regional differences in developmental trajectories of DTI quantities in the neonate brain have been observed [135]. In the infants, a further look into high FA (>0.5) regions, which reduce to portions of the corpus callosum and the internal capsule, revealed that average optimal $d_{\parallel}$ in these regions is comparable to that seen in the adult global WM. These regions in the infant are thought to be myelinated by one month after birth and to have higher fiber coherence than other white matter areas [135]. The lower FA regions (not shown) in the infant brain, which

presumably reflect less or not-yet myelinated axons and or lower fiber coherence, exhibit values of average optimal $d_{\parallel}$ that are similar to those of whole WM. For the older age groups, the axial diffusivity distributions in gray matter mimic those of the optimal $d_{\parallel}$. For the infants, this is true for both the WM and GM distributions. Also, the optimal $d_{\parallel}$ distribution separation between WM and GM is less for the infants than for the rest of the older age groups. Based on all this, it could be speculated that the neonatal gray matter neurites and white matter neurites are more similar than they are in the adults. Therefore, the model fit for less coherent, nonmyelinated fibers in neonatal white matter would be more similar to the fit in the neonatal gray matter than to the fit in the adult whole WM, as it is illustrated in Figure 3.5(A).

3.6 Limitations

3.6.1 Assumed equal intra- and extra-cellular $d_{\parallel}$

As mentioned in the introduction, another important assumption of the model is that of equal $d_{\parallel}$ in the intra- and extra-cellular compartments. Thus, one of the great limitations of this work is that it was carried out while maintaining this and other assumptions of the model.

In order to glimpse at the appropriateness of this assumption as it pertains to this work, a similar model residual optimization was done for the case where the extra- to intra-cellular parallel diffusivity ratio took on values different than 1. In this case, the model was adjusted so that the extra-cellular diffusivity was expressed as a fraction of the intra-cellular diffusivity value. The ratios ranged from 0.1 to 1.3 in 0.1 increments. In this case the number of fits increases dramatically for each subject (26x13 = 338), as do the memory and time

requirements. Therefore, the analysis was restricted to two subjects, one infant and one adult, and for a single axial slice. Additionally, in order to circumvent the long fitting times using the Matlab tool box, for this part of the analysis the AMICO NODDI toolbox [136] was used instead. Model RMS residuals were calculated for each of the 26 intra-cellular $d_{\parallel}$ values in [0.5 μm^{2}ms^{-1}, 3.0 μm^{2}ms^{-1}] and each of the 13 extra- to intra-cellular $d_{\parallel}$ ratio values in [0.1,1.3]. Average RMS residuals over WM and GM were plotted with respect to both, the intra-cellular $d_{\parallel}$ and the ratio of extra- to intra-cellular $d_{\parallel}$. These results are shown by the contour plots in Figure 3.8. Both in white and in gray matter, the regions of minimum residual values extend over several values in the two dimensions of the graphs. These poorly defined minima point to a multiplicity of solutions when constraints on the model diffusivities are not imposed. Similar results have been presented by other reports [117], [119], which show that unconstrained multicompartment biophysical models lead to issues in parameter estimation. Particularly, the shape of the lowest residual regions in these contour plots is evocative the pipe-like structures for the fitting cost function landscapes of non-constrained multi-compartment models reported in [117] and [119].

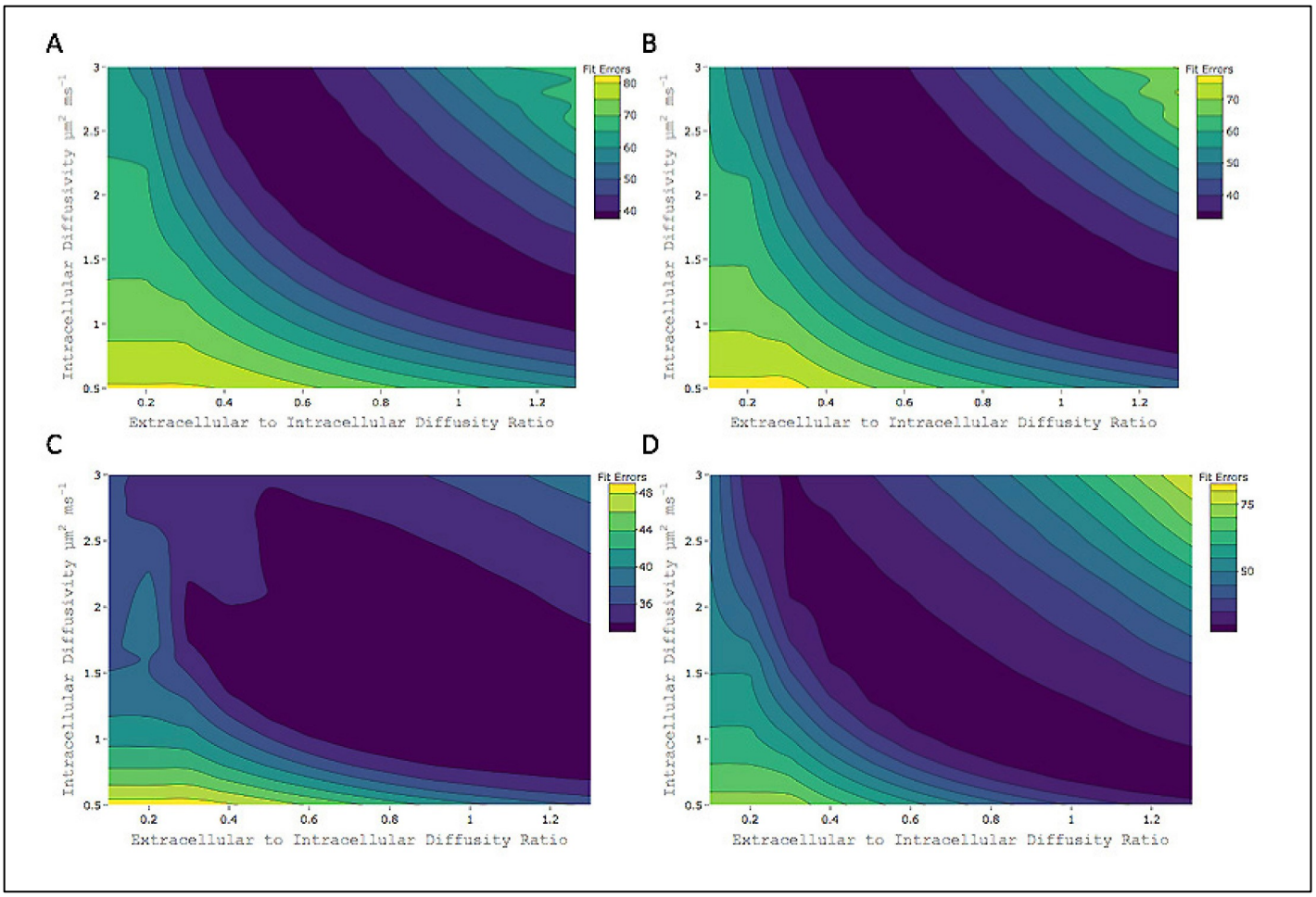

Figure 3.8 **Model residuals and non-equal diffusivities.** Fit errors (RMS residuals) of NODDI model with respect to both variation in intra-cellular $d_{\parallel}$ and variation in the ratio of extra- to intra-cellular $d_{\parallel}$. (**A**) Infant subject average fit errors over white matter. (**B**) Infant subject average fit errors over gray matter. (**C**) Adult subject average fit errors over white matter. (**D**) Adult subject average fit errors over gray matter.

3.6.2 SNR effects on model residuals

We recognize that this evaluation is mainly based on model fitting residuals. However, smaller residuals do not always mean that the model can probe microstructure more accurately, but rather they are just a goodness of fit measurement. When the SNR is low, smaller residuals could mean the model fits the noise better but does not reveal accurate tissue characteristics. To address this issue, we implement image denoising as part of the data pre-processing, which

should help to reduce noise bias issues and we can more safely rely on the residuals. Additionally, the SNR data from the studies shown in Figure 3.9 exceed the *rule of thumb* threshold SNR value for white matter of 20. The SNR is considerably greater in GM, which is where we see small residuals at lower intrinsic diffusivity. Even more, for the infant data the SNR is higher overall and that is also the group that had small residuals at lower intrinsic diffusivity. This gives us more confidence that the small residuals at lower values do not come from fitting noise rather than signal.

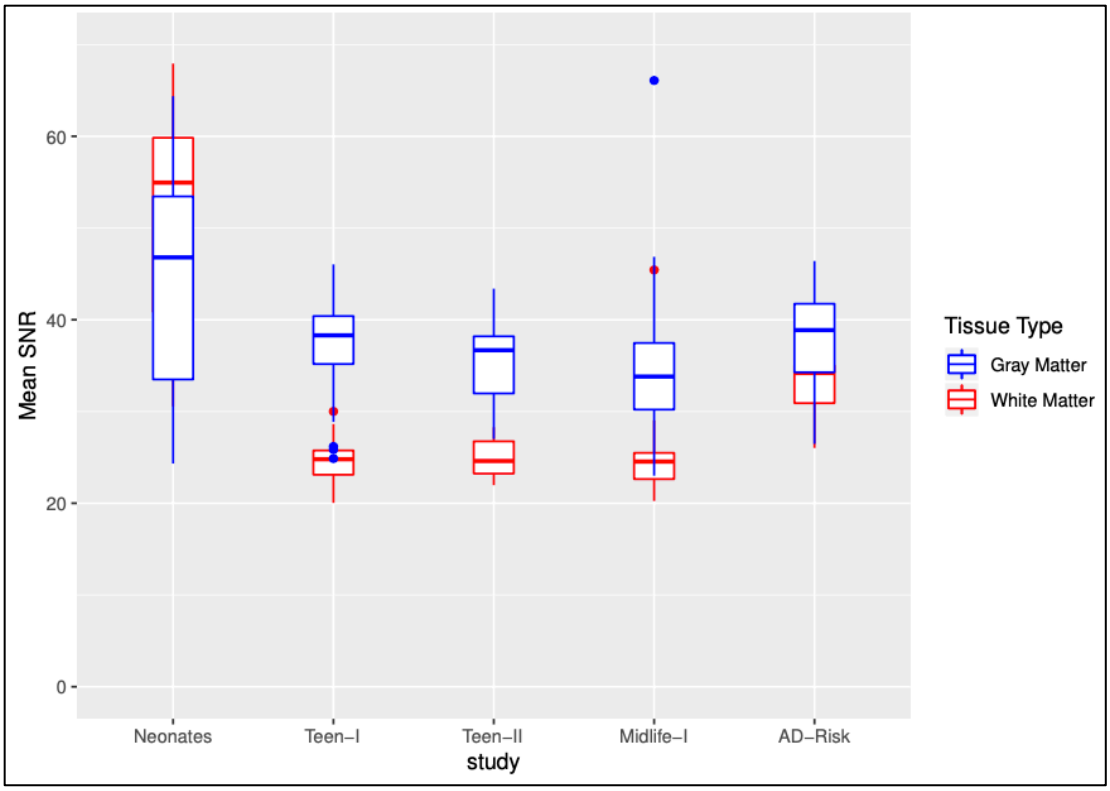

Figure 3.9 Mean SNR by study and tissue type.

3.6.3 Generalizability

Finally, great effort was made in order to make this as an exhaustive analysis as possible in terms of the diversity of the data that was used. Yet, we acknowledge it is not fully

generalizable to the wider scope of neuroimaging biophysical modeling diffusion research, for which it should consider, among others, conditions of pathology and ex-vivo experiments. Nonetheless, we believe that these results are highly informative considering the broad range of ages and imaging protocols investigated. Finally, this analysis was performed for Watson-NODDI only, not for other flavors of the technique which include Bingham-NODDI [124]or NODDIx [125], or its tumor specific version VERDICT [126].

3.7 Conclusion

In this work, dependence of the estimated NODDI parameters on the parallel intrinsic diffusivity $d_{\parallel}$ was observed. Optimum $d_{\parallel}$ in white matter of the adult brain is similar to the currently used value $d_{\parallel}$ = 1.7 μm^{2}ms^{-1} but significantly lower in gray matter. Optimal $d_{\parallel}$ is also lower than the default value for the newborn brain in white and gray matter. Effects of imaging protocol on the optimum $d_{\parallel}$ were also observed. Finally, it is important to consider that, despite its limitations, recent analysis suggests that NODDI metrics provide information that is congruent with histologically equivalent metrics [137].

Chapter 4 - A framework for single-subject multivariate analyses of white matter tissue microstructure along specific white matter pathways

4.1 Abstract

Imaging-based quantitative measures from diffusion-weighted MRI (dMRI) offer the ability to non-invasively study the human brain. Group-level comparisons of such measures represent an important approach to study abnormal conditions. These types of analyses are especially useful when the regions of abnormality coincide across subjects. When this is not true, however, approaches for individualized analyses are necessary. Examples of conditions exhibiting heterogeneity between subjects are traumatic brain injury (TBI) and autism. This work presents a framework for single-subject multidimensional analysis based on the Mahalanobis Distance. This is conducted along specific white matter pathways represented by fiber-tracking-derived streamline bundles. The method is demonstrated with a study of DTI scalar metrics obtained from severe TBI patients and healthy control subjects.

4.2 Introduction

Diffusion tensor imaging represents an important neuroimaging instrument for investigating white matter microstructural alterations in ASD [138] and TBI studies [139]. Changes in white matter are commonly assessed on fractional anisotropy or mean diffusivity perturbations relative to a control group or baseline values, or in relationship to non-imaging-based measures (e.g. behavioral). While investigations of ASD and TBI have revealed group differences across brains of individuals with and without the conditions, discordance in replication of results across studies has also become apparent [140], [141]. Replication disparities in the findings can

be attributed to factors such as variability of the samples in the studies or differences in the techniques for analysis. It is likely that these are also linked to both, the not-well-understood underlying neurobiological complexity and the assumption that pathology is expressed consistently across individuals. The latter is particularly true for TBI, where there clearly exists high inter-subject heterogeneity in region of injury (see Figure 4.1).

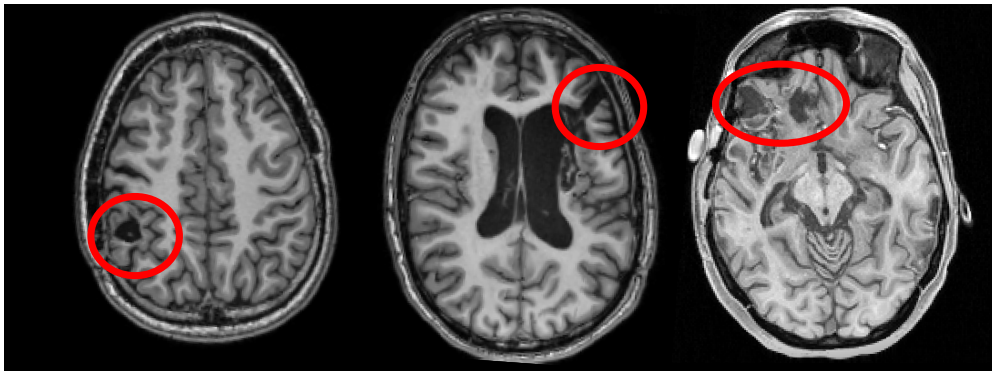

Figure 4.1 Traumatic brain injury cases (T1 weighted axial slices). This example portrays the high spatial heterogeneity of lesions across patients.

Individual DTI differences in a group of TBI patients may be smoothed out by the inherent averaging effect of group analyses and be characterized as normal variation. Initial region of injury and varying degrees of severity in clinical TBI means that no two cases are alike, making it challenging to build a statistically significant group difference in a region of interest (ROI) or in individual voxels. Thus, methods that can capture patterns of individual deviations should prove extremely useful in identifying and understanding the neurobiological implications in these and other multifaceted brain conditions.

To that end, in a recent study Dean et al. (2017) [140] conducted comparisons of single autistic individuals to a typically developing group. Individuals were compared to the group, both, by a univariate approach using the Z-score and by a multivariate approach using the

Mahalanobis distance [142]. The study reported that relative to univariate comparisons, improvements in discrimination between autistic and typically developing individuals were achieved by simultaneous consideration of DTI parameters averages in multiple brain ROIs with the Mahalanobis distance. Similarly, Shaker et al, (2017) [143] applied a multidimensional-based TBI analysis where a distribution of a single DTI parameter in multiple ROIs of a reference healthy group was modeled to account for inter-region interactions. Deviation of patients from the healthy group was also characterized individually by estimating the Mahalanobis distance between the patient's multiple ROI measures to the group model. The analysis reported the multivariate approach to have a superior ability to correctly classify subjects as patients or controls compared univariate alternatives.

These two studies are examples of analyses focused on DTI measures extracted as averages from specific ROIs. An inherent disadvantage of the ROI approach is the loss of spatial specificity within the delineated region. One way to overcome this is to conduct a voxel-by-voxel survey of the brain. Voxel-based approaches (VBA) [144] offer the ability to study the entire brain while making it possible to preserve the scope of subject-to-subject variation in the spatial distribution of pathology, a feature which gets masked out by ROI based approaches. Additionally, with VBA no prior knowledge or assumptions about the location of pathology is necessary.

An implementation of the voxel-wise framework for single subject characterization of TBI patients based on univariate Z-scores was presented by Kim et al., 2013 [145]. The study reported the ability to detect unique spatial patterns attributable to TBI at the subject level. As demonstrated by Dean et al. (2017) in their autism study, the classification power of the VBA

framework in Kim et al., 2013 would likely benefit from incorporation of additional DTI parameters through a multidimensional-based analysis.

This was the motivation for a novel method we have previously introduced for voxel-wise implementation of the Mahalanobis distance using DTI parameters to compare an individual to a reference sample (Guerrero et al., 2018). This simulation study demonstrated the ability to capture individual variability in DTI parameters at the voxel level. We have extended this framework to study ASD (results not shown) but have found that it is extremely susceptible to inter-subject image misalignment and the multiple-comparisons problem is a massive one as with most VBA methods. A recent application of the VBA Mahalanobis distance method in the study of epilepsy reported similar limitations [146].

This report presents continuing work, which set out to develop a novel computational and statistical framework for testing whether an individual is different from a reference group in a multidimensional space defined by the diffusion tensor Eigenvalues. The method uses the Mahalanobis distance as the multivariate metric in testing for abnormality. The testing is performed at individual segments along specific white matter tracts. This reduces the number of tests by orders of magnitude compared to VBA but retains better spatial specificity than the averaging-over-ROI approach. Additionally, this method is more forgiving of spatial image misalignment than the VBA approach.

The approach is based on the concept of tractometry [147]. The procedure involves the mapping of DTI parameters along specific white matter pathways, slicing the pathway into several segments guided by a centroid streamline, and extracting average parameter values from each segment to create a vector of segment-averages, which is typically referred to as a

tract profile. We demonstrate the method with individual comparisons of 22 severe pediatric TBI patients against a group of 49 age-matched healthy control subjects.

4.3 Methods

4.3.1 Tractometry

As mentioned in the previous section, the framework rests on the concept of tractometry. The steps of tractometry include: 1) tract extraction, 2) projection of a quantitative parameter onto tractogram streamlines, 3) slicing of the tractogram into segments, and 4) profiling the segment-average parameter along the pathway defined by the tractogram. The ways in which these steps were achieved for this work are described next. These steps are summarized in Figure 4.2 using the tractogram for the inferior longitudinal fasciculus as an example.

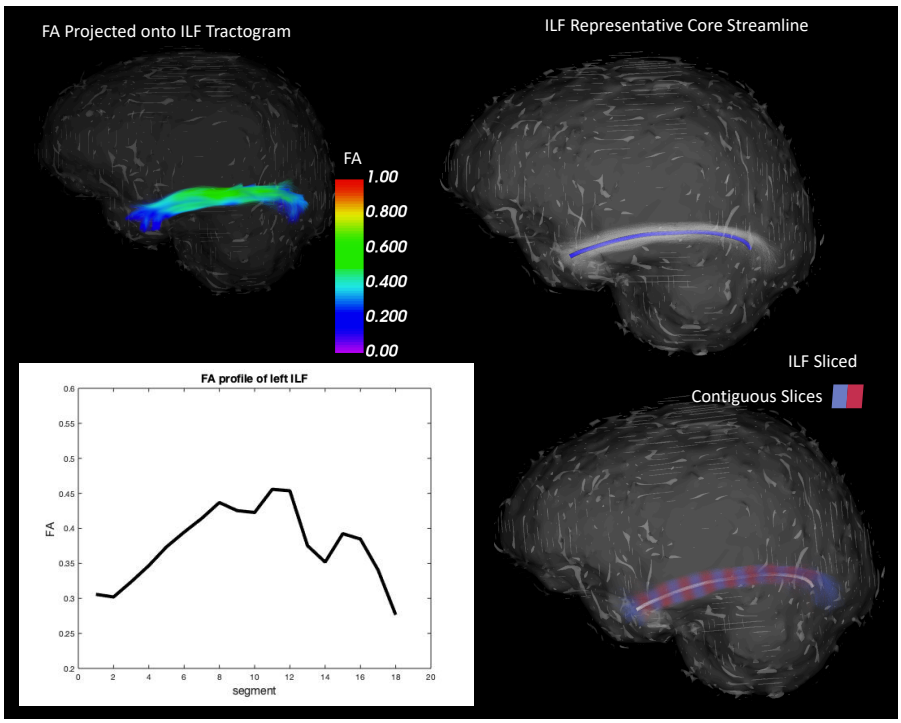

Figure 4.2 Components of the tractometry procedure. The steps of tractometry include: tract extraction, projection of a quantitative parameter onto tractogram streamlines, slicing of the tractogram into segments, and profiling the segment-average parameter along the pathway defined by the tractogram.

4.3.2 Tract Extraction

Tract extraction, the grouping of streamlines into bundles for representing specific white matter tracts, is one of the main requirements in this approach. In this specific implementation, tract extraction is achieved by employing *TractSeg* [148], a recently published convolutional neural network–based method for automated white matter tract extraction. The pipeline, however, is modular in the sense that this way of tract extraction can be substituted without major adverse effects to the framework workflow.

In implementing *TractSeg*, tract extraction can be achieved by simply passing the raw diffusion series with corresponding files for diffusion weighting (b-values) and diffusion gradient directions to the command-line tool. The program will internally estimate fiber orientation distribution function (fODF) maps using constrained spherical deconvolution, distill the peaks of the fODF lobes at each voxel (the orientation of the dominant fiber populations) [81], [149] and use these to perform deterministic or probabilistic fiber tracking (See section 2.7 BASICS OF TRACTOGRAPHY). Alternatively, one can generate the peaks separately and pass those onto the program.

The algorithm was trained using high quality Human Connectome Project (HCP) data from healthy participants as well as with peaks generated from lower quality (e.g. under sampled to lower angular resolution with single *b-values*) HCP data from healthy participants. Additionally, the method generalized well to a variety of data including low resolution (spatial and angular), single-shell low *b-value* (e.g. b=1000), and data from epilepsy patients with enlarged ventricles. Based on these results shown in the published report [148], we deemed the method to be appropriate for this work.

4.3.3 Quantitative imaging-based features

The other important ingredient in this approach is a number (at least two) of parameters or features extracted from the data that will be the basis for comparing an individual to a reference group. In this work, we use parameters derived from diffusion tensor imaging (see section 2.6 RENDERING DTI DATA). However, the method can accommodate other measures that are available at the voxel level.

4.3.4 Parameter tract profiles

Given a streamlines-bundle and an accompanying parameter map we can proceed to generate profiles of the parameter along the bundle (Figure 4.2). First, the voxel parameter values are projected onto the spatial coordinates that define the streamlines making up the bundle (streamlines are essentially sets of points with coordinates in the 3D space defined by the original diffusion images). Next, a core representative streamline, or centroid, is estimated for the bundle. This is done by applying the *QuickBundles* clustering framework [150] using the '*AveragePointwiseEuclideanMetric*' metric as implemented in the *DIPY* opensource library of tools (https://dipy.org) [151] in *Python*. Briefly, all streamlines in the bundle are first resampled to have the same number of segments. For each streamline, the points defining the segments must be equidistant. Then, the algorithm searches for a representative streamline that minimizes the average pointwise Euclidean distance between it and all other streamlines in the bundle. Then, the core streamline itself is sliced into several segments defined by equidistant points (N=20 in this case). What follows is to assign every point of each streamline to its closest

centroid point, effectively extending the segments defined on the centroid across the thickness of the pathway. Each segment definition is then used to compute the average of the parameter values within the segment. Voxel parameter values are weighted by the geodesic distance to the closest centroid point and the number of streamlines that pass through the voxel so that rogue streamlines far from the centroid have less of an impact on the average value. The result is a vector of segment-mean-parameter values, or a parameter tract profile. Because the distal portions of the sliced pathway (i.e. 1^{st} and 20^{th} segments in this case) generally are expected to exhibit more variability across subjects [147], these are clipped off and the analysis is conducted only for the central portion of the bundle (18 segments) defined by these endpoints.

4.3.5 Tract Profile alignment

Typically, tractometry studies running group comparisons of tract profiles have not considered inter-subject tractometry alignment in their analyses. It is assumed that artificially matching of the endpoints of the tracts and dividing them into the same number of segments will result in anatomical correspondence of the segments across subjects. However, recent publications [152], [153] have shown that variability observed across healthy subjects is reduced after alignment of the tract profiles. In the method presented by St-Jean et al., 2019, [151] pairs of one-dimensional parameter profiles are aligned by maximizing their cross-correlation function. On the other hand, the method in Benou et al., 2019, [152] performs curve-matching between the mean trajectories of bundles where the trajectories represent a combined measure of tract geometry and a model parameter (e.g. FA). An optimal set of coordinates for aligning two trajectories is estimated by the Fast Marching Method (FMM) for curve alignment [154].

While these two methods have been shown useful in reducing variability across parameter profiles, they can produce different optimal alignments depending on the type of parameter that is used during the curve-matching optimization. For the current proposed work, it is necessary that the alignment be independent of parameter, since multiple parameters will be evaluated at once on the same slice of the tract. This becomes more important as more features are considered for the computation of the Mahalanobis distance.

For this reason, we propose to use an alignment method that is based on co-registering the fODF maps previous to the tract extraction. In order to achieve this, we 1) create a study specific fODF template; 2) then align each subject fODF to the template via rigid, affine, and non-linear deformations; 3) perform tract extraction of each subject in the template space; 4) apply each subject-to-template transformation to their corresponding scalar maps; 5) finally obtain tract profiles in the template space for each subject.

The pipeline bridging the steps from raw data to parameter profiling along a specific white matter pathway, is illustrated by the flowchart in Figure 4.3

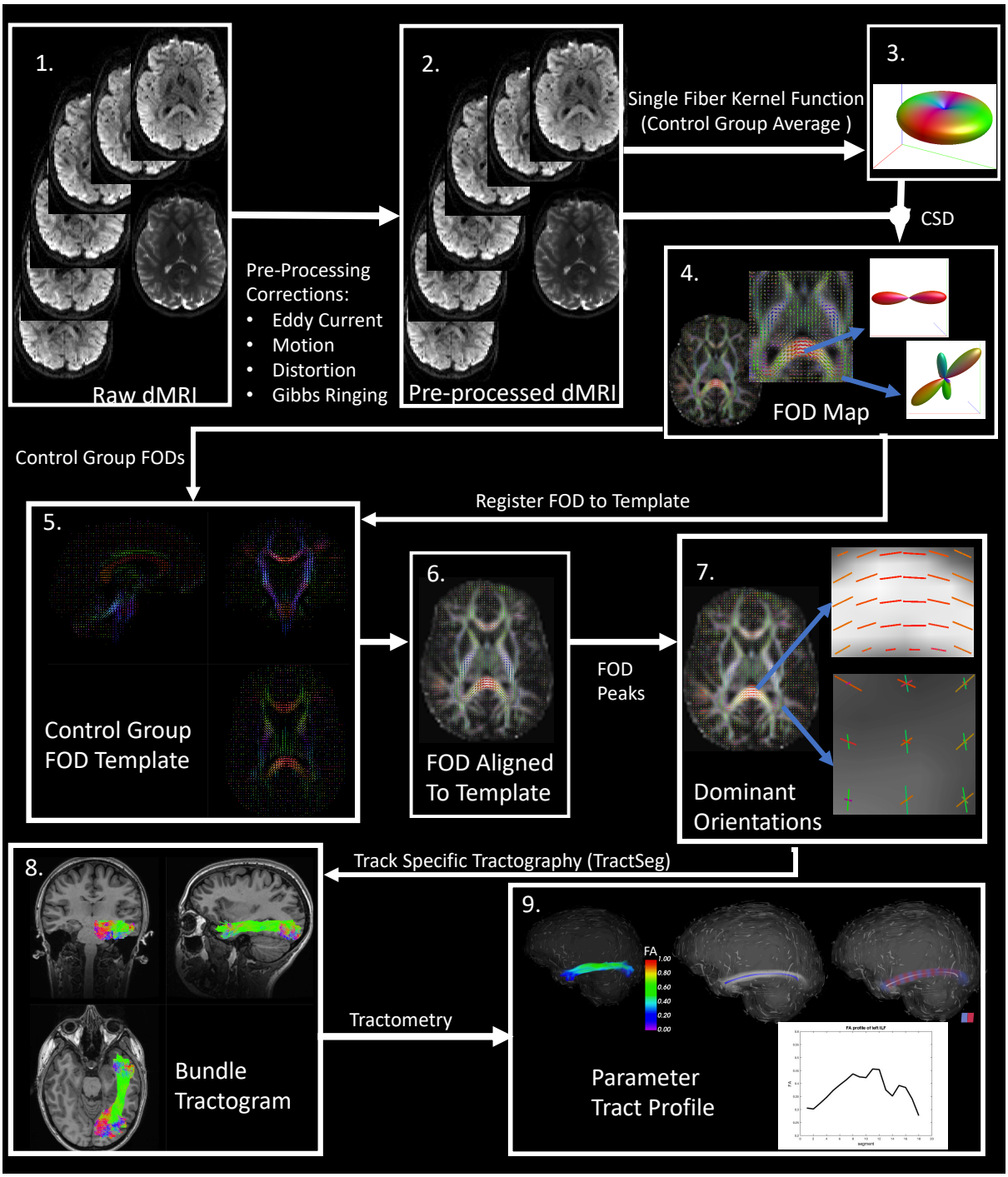

Figure 4.3 Data processing pipeline. Raw data is preprocessed with an assortment of artifact correction procedures. Fiber orientation distribution functions (FODs) are generated from constrained spherical deconvolution between the diffusion signal and the control group average single fiber response function. fODF maps from the control group are used to build an fODF template. All fODF maps including control and other subjects are co-registered to the template. Coregistered fODF maps are used to obtain peaks, or dominant fiber population directions, at each voxel. The peaks maps are fed to *TractSeg* which conducts a track specific probabilistic tractography. Combined with a parameter map, such as FA, an individual tractogram is used to create a profile of the parameter along the tract.

4.3.6 Mahalanobis Distance

For a multivariate normal random vector $\boldsymbol{X} = (x_1, x_2, x_3, \ldots, x_p)$ of dimension p (also referred to as the feature vector) the multivariate normal probability density function is given by

$$p(\boldsymbol{X}) = \frac{1}{(2\pi)^{p/2}\sqrt{|\boldsymbol{\Sigma}|}} e^{-\frac{1}{2}(\boldsymbol{X}-\boldsymbol{\mu})^T \boldsymbol{\Sigma}^{-1}(\boldsymbol{X}-\boldsymbol{\mu})} \qquad \text{Equation 4.1}$$

where $\boldsymbol{\mu}$ is the mean vector of the distribution, $\boldsymbol{\Sigma}$ is the distribution covariance matrix, and T denotes vector transpose. Equation 4.1 assumes the population mean vector and covariance matrix are known, which is typically not the case. Nonetheless, estimates can be calculated from measurements of the random vector from a population sample, $\boldsymbol{X_s}$, where s designates a specific sample. A requirement is that the measurements are made from a single class, c. Assuming this is true, estimates of the mean vector and the covariance matrix can be obtained, respectively, as

$$\widehat{\boldsymbol{\mu}}_{\boldsymbol{c}} = \frac{1}{N_c}\sum_{n=1}^{N_c} \boldsymbol{X}_{s,c}$$

and

$$\widehat{\boldsymbol{\Sigma}}_{\boldsymbol{c}} = \frac{1}{N_c - 1}\sum_{n=1}^{N_c} (\boldsymbol{X}_{s,c} - \boldsymbol{\mu})(\boldsymbol{X}_{s,c} - \boldsymbol{\mu})^T$$

where ^ represents an estimated value and N_c is the number of measurements from class c. As N_c tends to infinity the estimated mean vector and covariance matrix approach the true mean vector and covariance matrix. As a general rule of thumb, reliable estimations of the inverse

covariance matrix require at least 10 samples per dimension of the feature vector. After substituting the estimates, Equation 4.1 becomes

$$p(\boldsymbol{X}) = \frac{1}{(2\pi)^{p/2}\sqrt{|\widehat{\boldsymbol{\Sigma}}|}} e^{-\frac{1}{2}(\boldsymbol{X}-\widehat{\boldsymbol{\mu}})^t \widehat{\boldsymbol{\Sigma}}^{-1}(\boldsymbol{X}-\widehat{\boldsymbol{\mu}})} \qquad \text{Equation 4.2}$$

The squared Mahalanobis distance, $(MaD)^2$ is equal to twice the absolute value of the exponent in Equation 4.1

$$(MaD)^2 = (\boldsymbol{X}-\boldsymbol{\mu})^t \boldsymbol{\Sigma}^{-1}(\boldsymbol{X}-\boldsymbol{\mu}) \qquad \text{Equation 4.3}$$

$(MaD)^2$ encodes information about the separation of a measurement from the population mean relative to the spread of the distribution about the mean. The larger $(MaD)^2$ is, the less likely it is for an observation of the feature vector to occur subject to the population distribution density function. For this reason, the Mahalanobis distance has often been used as a measure of class dissimilarity and a tool for anomaly detection in multivariate data. Similar to Equation 4.3, an estimate for $(MaD)^2$ can be obtained from a population sample by using estimates of the mean vector and covariance matrix

$$(MaD)^2 = (\boldsymbol{X}-\widehat{\boldsymbol{\mu}})^t \widehat{\boldsymbol{\Sigma}}^{-1}(\boldsymbol{X}-\widehat{\boldsymbol{\mu}}) \qquad \text{Equation 4.4}$$

Once a number of parameters have been profiled along a tract for a reference group according to **step 9** in Figure 4.3, the segment-wise Mahalanobis Distance between a single subject and the group at each discrete piece of the tract can be estimated from Equation 4.4 as

$$MaD = \sqrt{(\boldsymbol{X} - \widehat{\boldsymbol{\mu}})^t \widehat{\boldsymbol{\Sigma}}^{-1} (\boldsymbol{X} - \widehat{\boldsymbol{\mu}})} \qquad \text{Equation 4.5}$$

4.3.7 Abnormality Classification

In deciding what value qualifies as abnormal MaD we follow a set of three steps. First, select a level of significance α to control for the false discovery rate (FDR). Then, consider corrections for multiple comparisons and reference sample size. Finally, arrive at a critical value of Mahalanobis distance.

The distribution of $(MaD)^2$ can be approximated by the Chi-squared distribution, and, when dealing with small sample sizes, better approximated by the F distribution [155]. This allows us to achieve the steps outlined for defining abnormal MaD based on Wilk's criterion [155], [156] as

$$MaD_{crit} = \sqrt{\frac{np(n-2)F_{p,n-p-1;\alpha}}{(n-1)(n-p-1)}} \qquad \text{Equation 4.6}$$

This takes in an F statistic at a Bonferroni corrected α and degrees of freedom determined by reference sample size n and size of feature vector p, corrects for n and p and returns the critical value for the Mahalanobis distance, MaD_{crit}.

4.4 Implementation in Severe Traumatic Brain Injury Study

Traumatic brain injury in children is a significant cause of long-term disability and impairment. There is a critical need to better understand the relationships between brain networks as measured by MRI and clinical and behavioral outcomes. This analysis applies the along-the-tract-Mahalanobis-distance framework to evaluate how white matter microstructure is affected in a cohort of children ages 9-18 years who sustained severe traumatic brain injuries. More specifically, based on DTI data collected 1-2 years post injury, this work explores how white matter microstructure as reflected by the multivariate DTI analysis is affected in the following domains:

Default Mode Network (DMN): DMN connects nodes within prefrontal cortex, lateral inferior parietal lobes, medial temporal lobes, and posterior cingulate cortex (PCC). The main tract connecting prefrontal structures and PCC is the cingulum. Dense interconnectivity between frontal and posterior DMN nodes is important for efficiently directing attention and switching between internally directed and task oriented cognitive processes [157]. TBI-induced alterations in the DMN may cause impairments in executive function like decreased ability to self-monitor engagement in goal directed tasks, and may correlate with measures of task initiation, behavioral monitoring, and planning.

Hippocampal Memory Network (HMN): HMN has connections between the hippocampus, parahippocampus, and cortical hub nodes within other brain networks like pCC (DMN), and amygdala (Fronto-Limbic). Injury to hippocampus or its major input/output pathways causes impairments in memory encoding and retrieval. Memory and learning are frequently affected functions in children with TBI [158].

Fronto Limbic Network (FLN): FLN encompasses connections between amygdala and prefrontal cortex, playing a critical role in emotion regulation. The uncinate fasciculus pathway represents the major structural connections between the amygdala and prefrontal cortex. Disruptions in connectivity of this pathway have been observed to relate to anxiety [159] and depression [154]. Studies of microstructure with DTI have observed changes in amygdala MD and uncinate FA in children with TBI, compared to healthy controls, which were associated to anxiety and emotion regulation [160], [161].

Global-Network-Dysfunction: Impairments in multiple functional domains have been observed in children with TBI [162]. Severe or widespread brain injuries are expected to impact multiple networks resulting in impairments to global function. The corpus callosum tracts play an important role in global connectivity, thus injury to areas in this white matter structure has been viewed as a marker for global network disruption [163].

4.4.1 Participants

Subjects older than 9 years old and enrolled in the Approaches and Decisions in Pediatric TBI (ADAPT) trial were recruited for inclusion in this study. The ADAPT trial enrolled 1000 children with severe TBI defined as a post-resuscitation Glasgow Coma Scale (GCS) of 8 or less [164]. A typically developing control cohort without history of TBI or neuropsychiatric diagnoses was recruited for imaging and neurocognitive testing at the University of Wisconsin. The TBI group consisted of 22 subjects (10 males, 12 females) between the ages of 11.6 and 18.9 years (Mean 15.7 ± 2.1 years) at the time of MRI scanning, recruited from 13 sites (Table 3-1). The control group consisted of 49 subjects (24 males, 25 females) between the ages of 9.0 and 18.0 years (mean 13.45 ± 2.8) at the time of MRI scanning. The study was approved by the institutional review board at the University of Wisconsin (UW) and all participating sites. Informed consent was obtained from the subject or legal guardian when appropriate.

4.4.2 Imaging

Brain imaging was performed for each participant using 3T MRI standardized neuroimaging protocols across 13 sites (Table 2). T1-weighted (T1w), T2-weighted (T2w), T2-weighted FLAIR, T2*-weighted, diffusion tensor, and resting state functional images were obtained for each subject. Manufacturer-specific protocols were emulated after protocols[1] used in the multi-site Transforming Research and Clinical Knowledge in TBI (TRACK-TBI) study. Prior to subject enrollment, each site was provided with the scanner-specific protocol to be implemented on their system. A scanning procedure manual was developed for the study and disseminated to

[1] https://tracktbi.ucsf.edu/sites/tracktbi.ucsf.edu/files/TRACK-TBI_MRI_Manual_16December2014%5B2%5D.pdf

all participating sites. Prior to human data collection, sites were required to collect phantom data using the protocol, which was sent to UW to verify protocol compliance. Once the site imaging protocol was approved, sites then enrolled adolescent TBI participants for scanning. Imaging was performed 12-25.5 months post injury with a mean interval between injury and MRI scanning of 20 ± 4.44 months.

Table 4-1 TBI patients sorted by Site, scanner Vendor, and scanner Model.

Site	Patient	Vendor	Model
I	A	GE	MR750
I	B	GE	MR750
II	C	GE	MR750
III	D	Philips	Ingenia
IV	E	Philips	Ingenia
IV	F	Philips	Ingenia
V	G	Philips	Achieva
V	H	Philips	Achieva
V	I	Philips	Achieva
VI	J	Siemens	Skyra
VII	K	Siemens	Skyra
VIII	L	Siemens	Trio
IX	M	Siemens	Trio
X	N	Siemens	Trio
X	O	Siemens	Trio
X	P	Siemens	Trio
X	Q	Siemens	Trio
XI	R	Siemens	Prisma
XI	S	Siemens	Prisma
XII	T	Siemens	Prisma
XII	U	Siemens	Prisma
XIII	V	Siemens	Prisma

The images used for this analysis were the DTI and structural T1w and T2w scans.

T1w structural imaging was performed using a 3D inversion-recovery prepared sequence with a rapid gradient echo readout (i.e., MP-RAGE on Siemens and Philips; BRAVO on GE). The protocol prescription was 3D sagittal images with a 256x256 matrix over a 256 mm field of view

and 192 slices that were 1 mm thick (1 mm isotropic resolution), frequency encoding in Superior/Inferior direction, in-plane parallel imaging with an acceleration factor of 2. On GE scanners, the inversion time, TI, was set to 450 ms, and Siemens & Philips scanners the TI was 900 ms.

T2w structural imaging was performed using a 3D fast spin-echo sequence (i.e., SPACE on Siemens; VISTA on Philips; CUBE on GE). The protocol prescription was 3D sagittal images with 2 averages, a 256x256 matrix over a 256 mm field of view and 192 slices that were 1 mm thick (1 mm isotropic resolution), frequency encoding in Superior/Inferior direction, in-plane parallel imaging with an acceleration factor of 2, and variable flip angle.

Diffusion tensor imaging was performed with a single-shot spin-echo echo-planar imaging pulse sequence. The protocol prescription was 2D sagittal images, a 96x96 matrix, 240 mm FOV, 64 slices, 2.5 mm isotropic resolution, phase encoding in Anterior/Posterior direction, parallel acquisition with a geometric reduction factor of 2. Diffusion settings included diffusion encoding along 64 non-collinear directions with b-value of 1300 s/mm^2, 8 volumes with no diffusion weighting (b=0). TR/TE was 8500/minimum ms for GE and Phillips, 9000/82 ms for Siemens.

4.4.3 Multi-site phantom scans

In order to explore systematic effects related to site on the estimated tensor Eigenvalues, we collected phantom scans from 6 of the 13 sites (sites I, II, III, IX, XI, XIII). These included at least one scan from each scanner vendor (GE, Phillips, Siemens). The phantom was scanned twice at

sites II and IX. Additionally, the phantom was scanned weekly over the course of five weeks at the site where the control group scans were collected (UW-Madison, Site I).

The imaging protocols included DTI, T1w, and T2w with the same prescriptions as those used for the human scans. The scanned phantom was the quantitative isotropic phantom (High Precision Devices, Inc, Boulder, CO) developed by the National Institute of Standards and Technology (NIST) and the Radiological Society of North America (RSNA)'s Quantitative Imaging Biomarker Alliance (QIBA). The phantom contains 13 vials, two for each of 5 concentrations (10%, 20%, 30%, 40%, 50%) of polyvinylpyrrolidone (PVP) in an aqueous solution for modulating the isotropic diffusivity of water protons, plus three vials with no PVP (i.e. 0% concentration) [165]. One of the 0% PVP vials is at the center of the housing and one at each of two concentric rings as shown in Figure 4.4(A). The phantom is scanned at close to 0°C. This is achieved by placing it in an ice-water bath for a minimum of 2.5 hours. Temperature recordings from each site of the phantom before and after scanning were recorded. Preparation instructions were developed at UW-Madison and distributed to the other sites. A copy of the phantom preparation procedure sent to the sites is presented in 4.8 - Appendix A: Ice Water Diffusion Phantom Instructions of this chapter.

A) B)

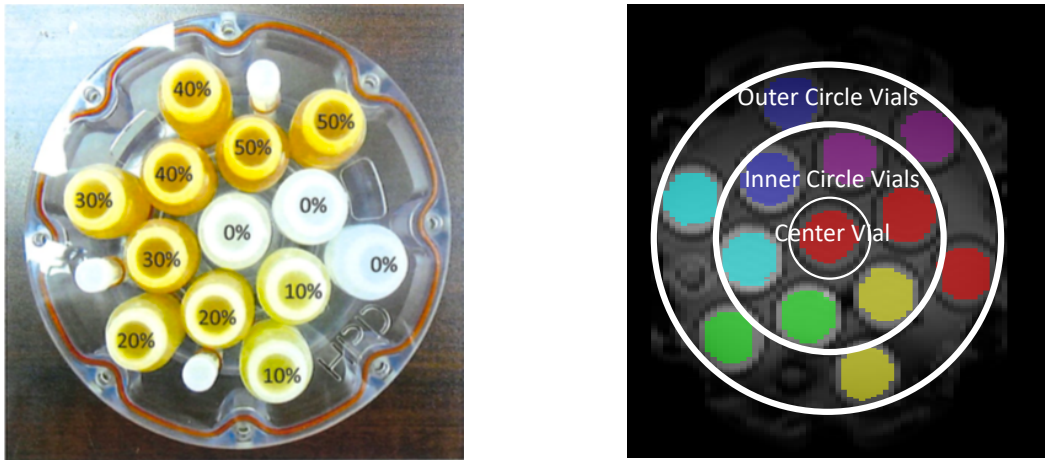

Figure 4.4 NIST PVP diffusion phantom. A) Varying PVP concentration vials. B) b0 image with regions of interest (ROI) represented as binary masks placed within the different concentration regions for analysis. Note there are two vials per concentration, each placed in one of two concentric circles. Except for the 0%, which has 3 vials, one in the center and one in each of the circles.

4.4.4 Data Processing

Structural T1w images were processed using *FreeSurfer* (The General Hospital Corporation, Boston, MA, USA) [145], [166]. In this process, surfaces separating tissue types (boundaries) are estimated for each subject. These separation surfaces are used to perform within subject multi-modal image spatial alignment. In this case, T2w and b=0 diffusion volume (b0) are rigidly aligned to the T1w by maximizing the intensity gradient across tissue boundaries. This known as boundary-based registration (BBR).

Diffusion weighted images were manually assessed for motion artifacts, and individual volumes were dropped if severe signal dropout artifacts were seen. Distortion, translation and rotation from bulk head motion and eddy currents were accounted for by co-registering DWIs using an affine registration tool [167] from the *FMRIB* software library (*FSL*; http://fsl.fmrib.ox.ac.uk/fsl/fslwiki/). Less severe motion related dropout artifacts were

also corrected by this tool, by a method in which intensities of slices contiguous to the affected voxels are used to model the intensity variations. Gradient directions were additionally corrected for rotations [168].

Next, EPI-related geometric distortions were corrected using an image registration-based approach. First, the inverse of the BBR transformations from the b0-to-T1w alignment are applied to the T1 and T2w-to-T1w volumes, so that these are rigidly brought into the b0 space. Then, the mean over the diffusion weighted volumes (meanDWI) is non-linearly co-registered to the rigidly transformed T1w. At the same time, the mean b0 (mean across 8 b0 volumes) and meanDWI are non-linearly co-registered to the rigidly transformed T2w. The alignment optimization is conducted simultaneously for all three contrasts. The non-linear deformations are constrained to occur only in the anterior-posterior direction. During the image acquisition this is prescribed as the phase encoding direction and the direction in which the most severe distortions occur. Finally, the resulting transformations are applied to all the volumes in the diffusion scan series. These operations were implemented in *FreeSurfer* [145], [166] and *ANTs* (http://stnava.github.io/ANTs/) [169] . See Figure 4.5.

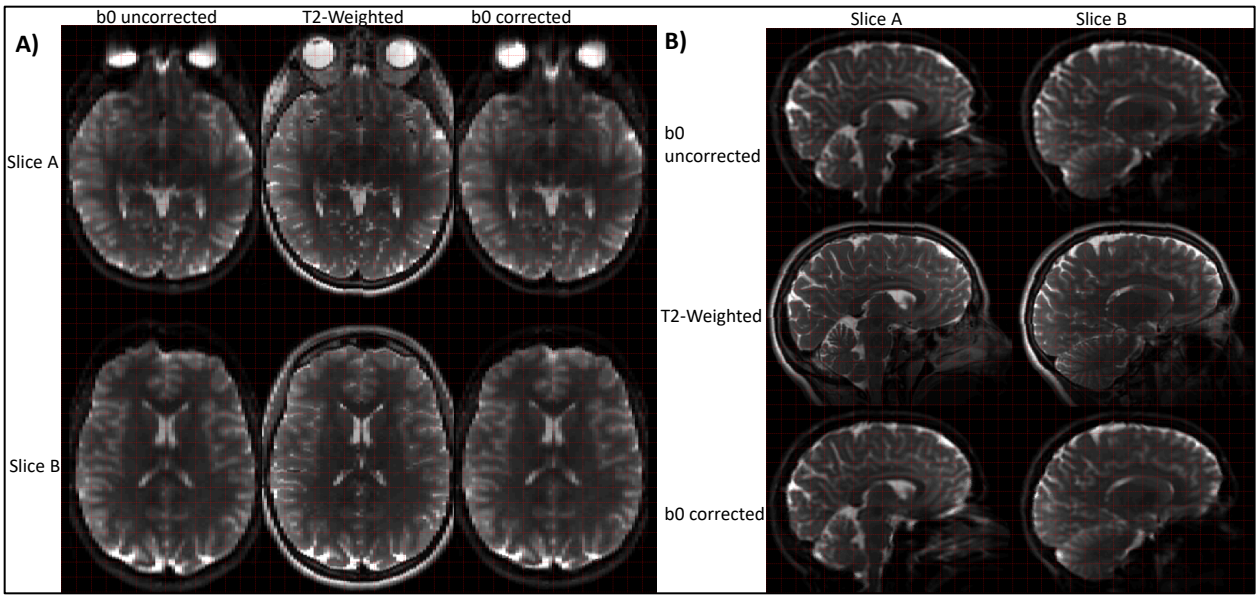

Figure 4.5 EPI distortion correction example. A) Two axial slices (rows) illustrate b0 images before and after correction compared to distortion-free structural T2-weighted image (middle column). B) Same as (A) but with sagittal slices and with rows/columns transposed.

Diffusion tensors were estimated for each voxel using the robust estimation of tensors by outlier rejection (RESTORE) algorithm as part of the diffusion imaging in python (*DIPY*) open source software package [151]. Eigenvalue maps (λ_1, λ_2, λ_3) were generated from the voxel-wise estimates of the diffusion tensor Figure 4.6(A).

Three groups of white matter tracts were selected for this analysis, Figure 4.6 (B,C,D). These are the uncinate bundles (left and right), the cingulum bundles (left and right), and the corpus callosum parcellated into seven subsections (rostrum, genu, rostral body, anterior midbody, posterior midbody, isthmus, splenium), see Figure 4.7. These pathways form part of networks that are known to be implicated in the clinical and behavioral outcome following TBI. Specifically, the cingulum forms important connections of the DMN and HMN, the uncinate is

an important pathway in the FLN, and the corpus callosum represent connections across multiple networks.

The tracts were extracted for all subjects using *TractSeg*. *TractSeg* was used for the tract extraction only after separately estimating fODF maps and peak maps using the *MRtrix* libraries (https://www.mrtrix.org) [170]. White matter and response functions for all control subjects were estimated using the multi-shell multi-tissue '*dhollander*' algorithm. These were averaged across subjects to estimate a mean white matter response function. This averaged white matter response function was then utilized for estimating the fiber orientation distributions by constrained spherical deconvolution for both control and TBI scans.

A population specific fODF template was created using the control group fODF maps. Each individual fODF map (control and TBI) was then aligned to the template via rigid, affine, and non-linear diffeomorphic transformations using *MRtrix* [170]. Once in template space, fODF peak maps were generated for each individual and passed onto *TractSeg* for tract extraction. For comparison, tract extraction was also performed in native space.

All reconstructed tracts were inspected visually for defects. From this visual analysis, it was found that TBI subjects S and D with lesions affecting large portions of the left hemisphere did not have any streamlines for the left uncinate bundles. Patient S also had failed reconstructions for CC_1, CC_3, CC_4. Additionally, Patient D had failed reconstruction of CC_4.

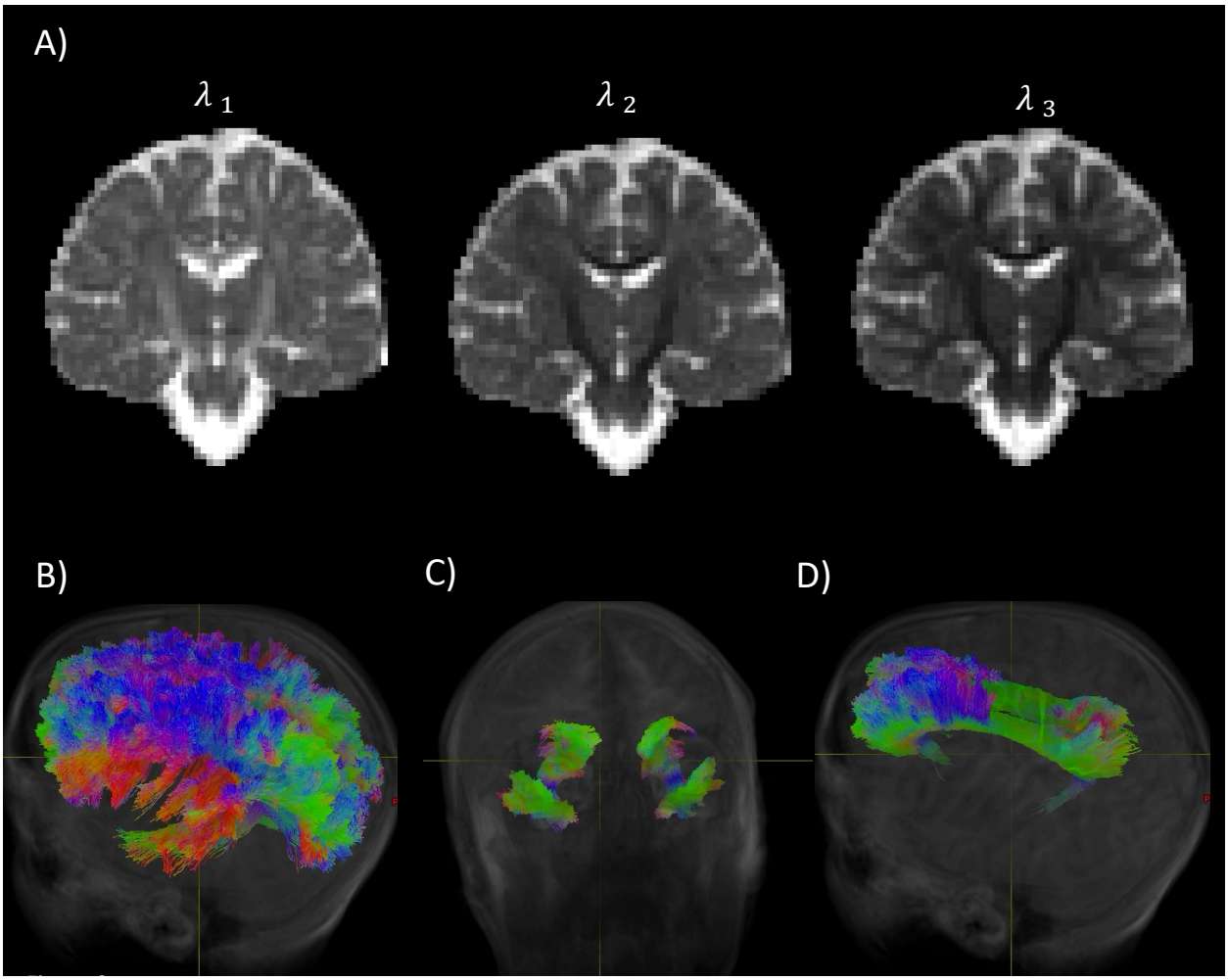

Figure 4.6 Parameters for the Mahalanobis distance calculation and tracts in which the analysis was conducted. A) Example Eigenvalue maps of the diffusion tensor. Example tract segmentations color coded by direction B) Corpus callosum, C) uncinate, D) cingulum.

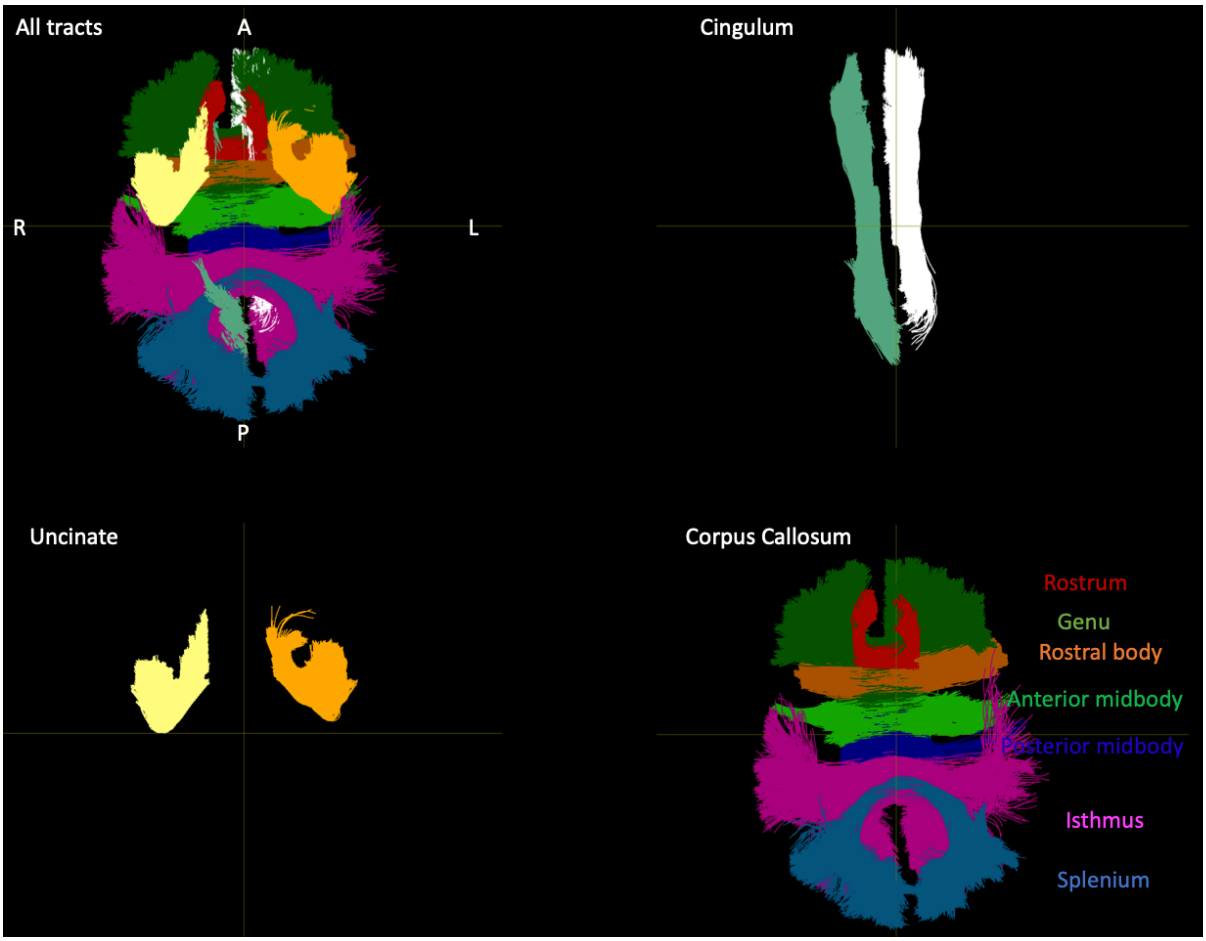

Figure 4.7 Example view (viewed from the inferior side of the brain) of solid color tract segmentations used in the analysis.

Each tract was sliced into 20 discrete segments. We note that while each tract is sliced into 20 segments, the end segments are excluded from the analysis as more variability is observed in the end sections. Thus, the Mahalanobis distance was estimated at 18 segments for the majority of the examined bundles, except the cingulum bundles. As shown in Figure 4.8, there are very large differences between the lengths and paths of some streamlines that define this bundle. While most streamlines start at the prefrontal cortex and run dorsally along the corpus callosum, some will curve slightly laterally, then inferiorly and anterior towards the hippocampus. However, some will curve up towards the superior occipital cortex. This causes

the centroid streamline to terminate prematurely. As a result, slices towards the most anterior part of the tract include both, portions of the hippocampal limb and the main dorsal body of the cingulum. In the interest of simplicity, we decided to exclude these pieces of the tract from the analysis and limit the analysis to the first 13 segments starting from the prefrontal cortex end of bundle.

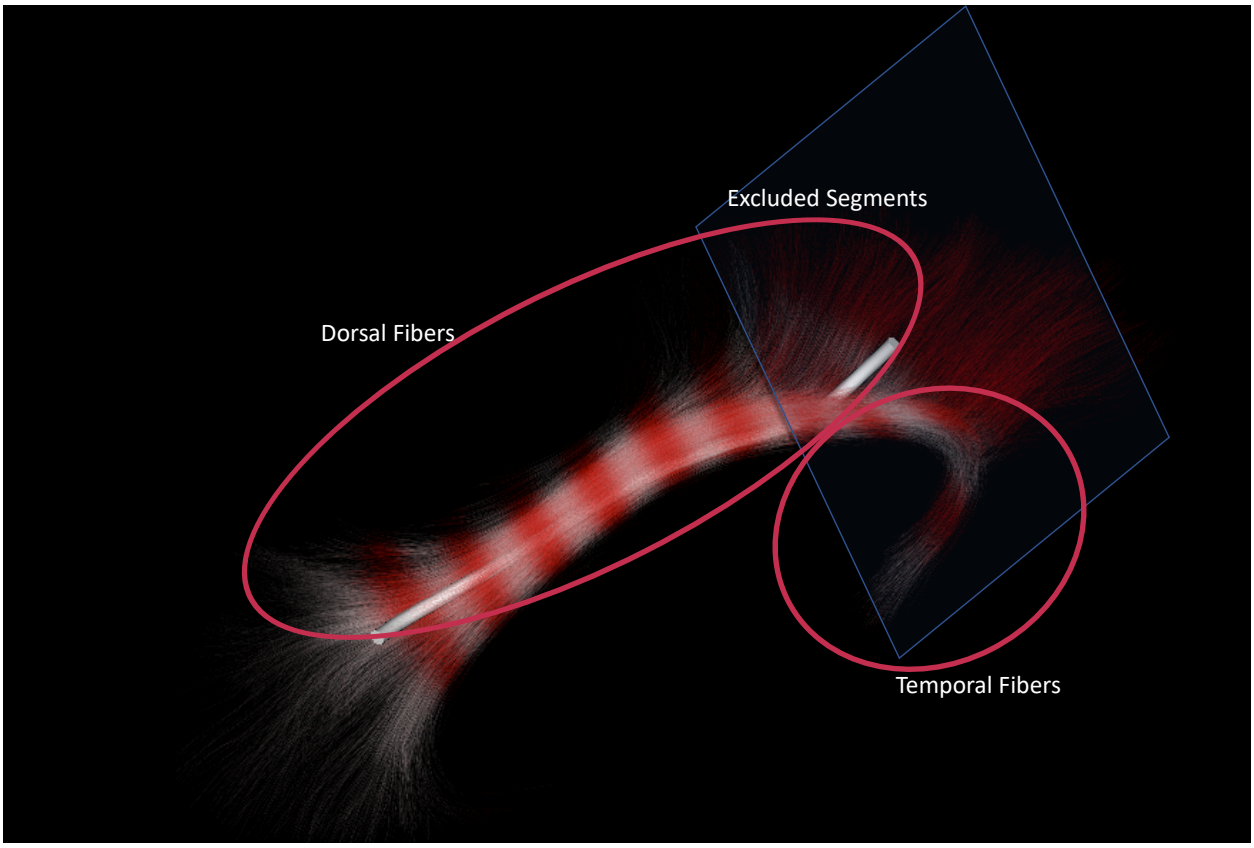

Figure 4.8 Example of the slicing of the cingulum for tractometry. This depicts the two dominant groups of streamlines that result in the guiding core streamline terminating early. The segments within the blue frame are excluded from the analysis.

Profiles of the principal diffusivities (Eigenvalues: (λ_1, λ_2, λ_3)) of the diffusion tensors were generated for all subjects. We decided to use the Eigenvalues as features for the Mahalanobis distance estimation, since, by definition, these parameters are orthogonal to each other. The

parameter profiling was carried out in template space after applying the set of transforms from the fODF map alignment to the parameter maps, which themselves were estimated in native space, as were the fODF maps. Instead of using the tract extractions from the template itself, we decided to use the tracts extracted from the fODF maps of each individual to sample their own diffusivity maps. This means that even in the presence of some level of misalignment between the template and the individual maps, we will be more faithfully sampling the right regions at the subject level.

Given the parameter tract profiles, the Mahalanobis distance between each of 22 TBI patients and the reference control group of 49 subjects was estimated at each segment. Additionally, in a *leave-one-out* fashion, each of the controls was compared to the rest of the group by removing it before estimating the mean vector and covariance matrix. Data structuring and estimation of the Mahalanobis distance (including means and inverse covariance matrices) was conducted with in-house developed scripts in MATLAB computer language (https://www.mathworks.com/products/matlab.html). For a desired significance level of 0.05, p=3, 22 TBI patients, 49 controls, 9 tracts with 18 segments per tract, 2 tracts with 13 segments per tract, Bonferroni corrected α equals $3.7x10^{-6}$ and Equation 4.6 gives a critical value of 6.38.

4.5 Results

4.5.1 Phantom scanning results

Images from the phantom scans were processed the same as the human scans up to the tensor fitting. Mean Eigenvalues (λ_1, λ_2, λ_3) were extracted from the ROIs defined in Figure 4.4(A). The

results from the weekly phantom scans at Site I are plotted in Figure 4.9 and for multi-site phantom scans in Figure 4.10. These are compared with ADC accepted values from NIST (accepted at 98.5 % confidence). Visually, the variability in Eigenvalues across sites does not appear to be much higher than the variability across time in Site I. Additionally, the Eigenvalues are similar to each other for all PVP concentration values as is expected in isotropic media. The values are close to the accepted values for the most part, except for the lowest of diffusion coefficients (or 50% PVP concentration). At this low of diffusion coefficient noise in the measurement will have a larger impact on the estimated value. Also, this is a much lower diffusion coefficient value than what is typically seen in brain.

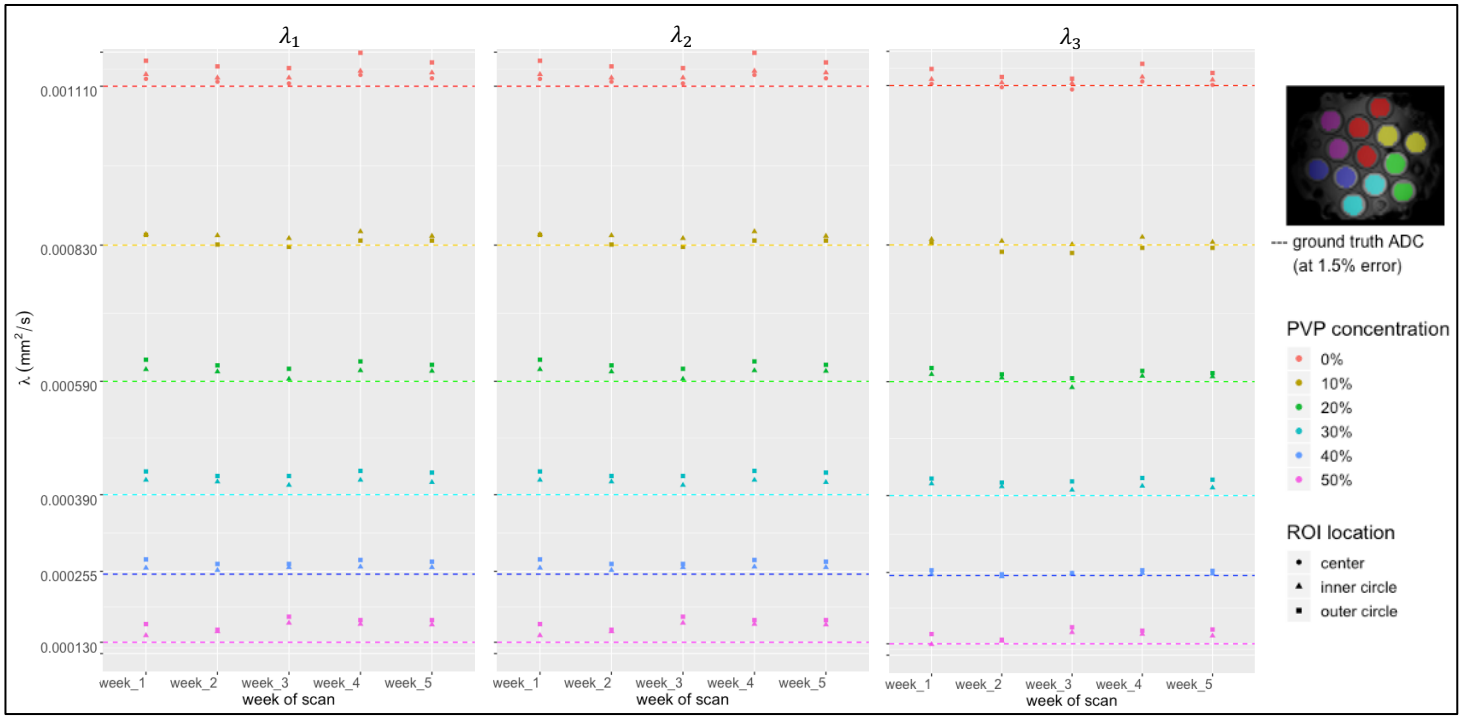

Figure 4.9 Weekly phantom scan results from Site I. The tensor Eigenvalues ($\lambda_1, \lambda_2, \lambda_3$) in isotropic media are expected to be equal (i.e. equal diffusivities in all directions). The dashed lines represent the accepted diffusivity value.

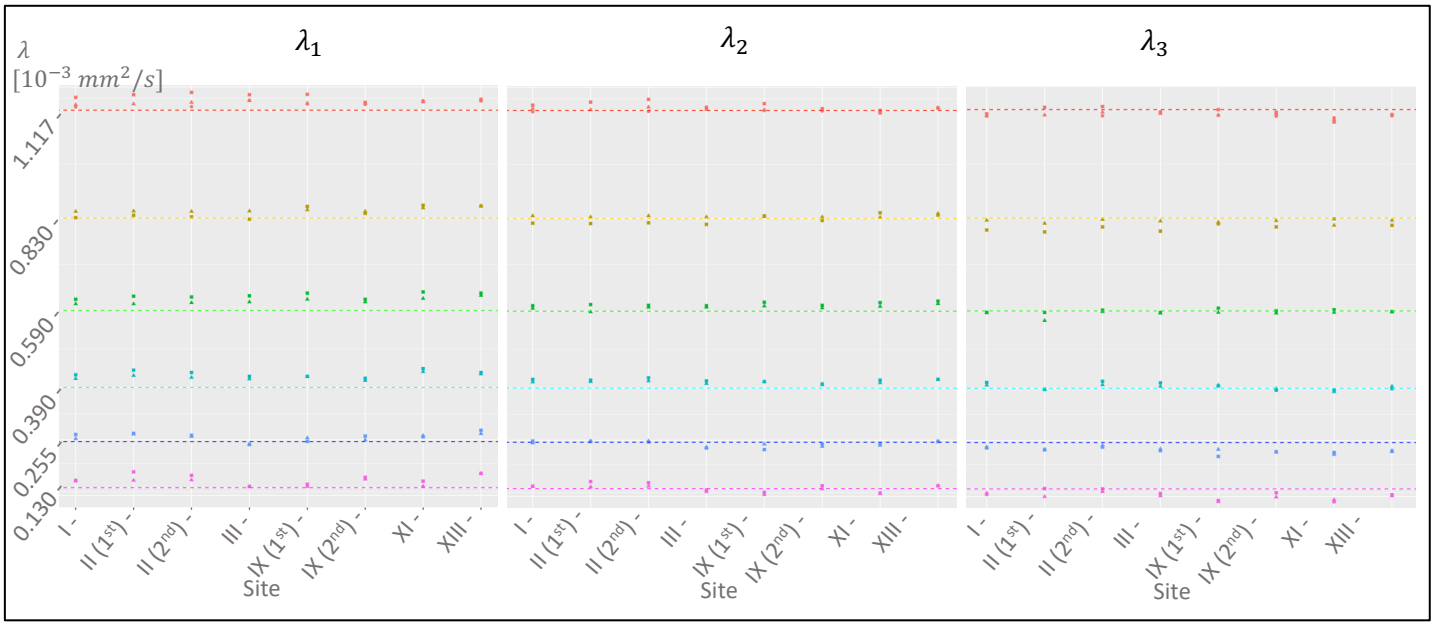

Figure 4.10 Multi-site phantom scan results. The tensor Eigenvalues ($\lambda_1, \lambda_2, \lambda_3$) in isotropic media are expected to be equal (i.e. equal diffusivities in all directions). The dashed lines represent the accepted diffusivity value.

Additionally, the coefficient of variation was calculated for the tensor Eigenvalues across weekly scans for Site I, and across site scans. These are shown in Table 4-2. These results again show that variability across sites is not much higher than across time in Site I, for the most part. For the 50% PVP concentration, CoVs are highest, both for the Site I scans and across sites.

Table 4-2 Coefficient of variation analysis results for both, multi-site and Site-I weekly phantom scans.

		Site I Weekly Scans CoV [%]			Multi-Site Scans CoV [%]		
Eigenvalue (λ)	PVP Conc.	Center Vial	Inner Circle Vials	Outer Circle Vials	Center Vial	Inner Circle Vials	Outer Circle Vials
λ_1							
	0%	0.52	0.47	0.92	0.64	0.38	0.84
	10%		0.52	0.96		0.61	1.76
	20%		1.12	1.01		1.26	1.16
	30%		0.90	1.01		1.79	2.02
	40%		0.90	1.39		3.41	4.47
	50%		6.17	5.32		8.16	8.82
λ_2							
	0%	0.49	0.40	0.93	0.44	0.29	0.98
	10%		0.59	0.82		0.39	1.42
	20%		1.53	1.11		1.00	0.77
	30%		1.00	0.81		1.06	1.16
	40%		0.93	1.25		2.59	3.42
	50%		6.20	5.70		7.14	8.27
λ_3							
	0%	0.46	0.36	0.66	0.49	0.48	1.15
	10%		0.95	0.88		0.61	1.39
	20%		1.89	1.09		1.28	0.68
	30%		1.12	0.80		1.64	2.44
	40%		0.95	1.20		3.10	3.28
	50%		7.28	6.33		7.57	10.61

Additionally, the mean ROI Eigenvalues from Sites II, III, IX, XI, and XIII were explicitly compared to those from the control group, Site I. These results are shown in Figure 4.11. A linear regression was performed between the corresponding concentration values at Site I and each of the other 5 sites. For all comparisons, the slope and intercept are close to 1 and 0 respectively, pointing to good agreement in the measurements. Nonetheless, the resulting relationships were used to harmonize the Eigenvalues from the human scans at each of the 5 sites and Site I. The MaD analysis was replicated with the harmonized values for those patients. This is shown in Figure 4.19. The results show good agreement between MaD with and without correction.

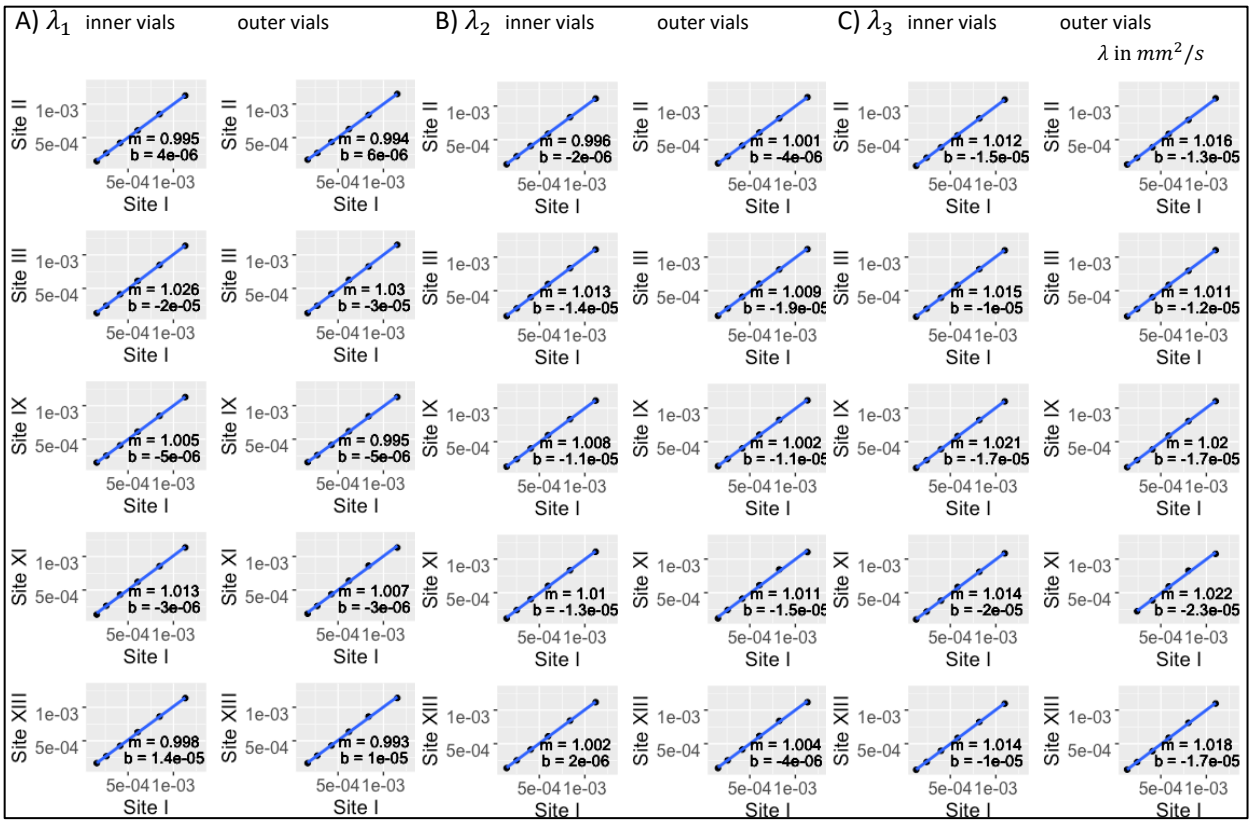

Figure 4.11 Linear regressions between measurements of diffusion coefficient for the 5 PVP concentrations between Site I and each of the other 5 sites in which the phantom was scanned. In all instances the slope an intercept are very close to 1 and 0, respectively. Nonetheless, the regression relationships are used to harmonize the human scans between each of the 5 sites and Site I.

4.5.2 Tract alignment results

To illustrate the broad stroke effects of fODF alignment, core streamlines before and after alignment are shown in Figure 4.12 for the isthmus of the corpus callosum and the left uncinate bundle. It is evident from visual inspection that the centroids of the bundle are brought to good spatial agreement after the fODF alignment

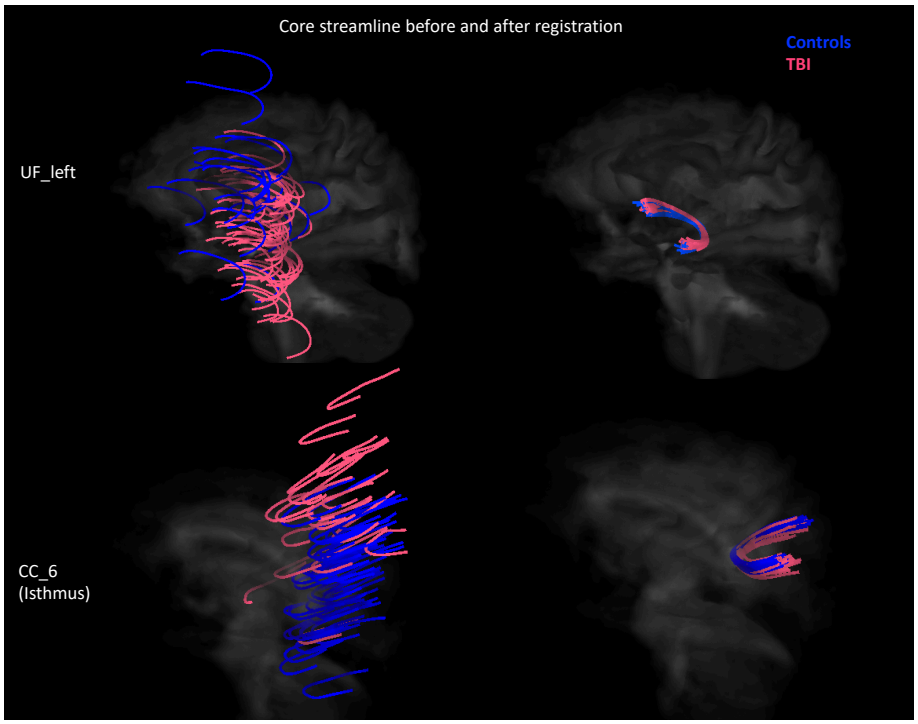

Figure 4.12 Core streamlines before (left) and after (right) fODF map alignment. Visualization of the core streamlines for all the subjects in both the TBI and control groups shows the improvement in spatial correspondence after aligning the individual fODF maps to the fODF template before tracking in the left uncinate and isthmus of the corpus callosum.

Since the length of the core streamline is the main driver for spatial correspondence of tract discrete pieces across subjects, it is relevant to compare the lengths before and after alignment. Figure 4.13 shows the distribution of core streamline lengths before and after alignment for all of the pathways analyzed in this work. This figure shows a reduction in variability of tract lengths for all tracts. Having more similar lengths implies that slicing the tracts into the same number of slices will result in better positional matching of the individual slices across subjects.

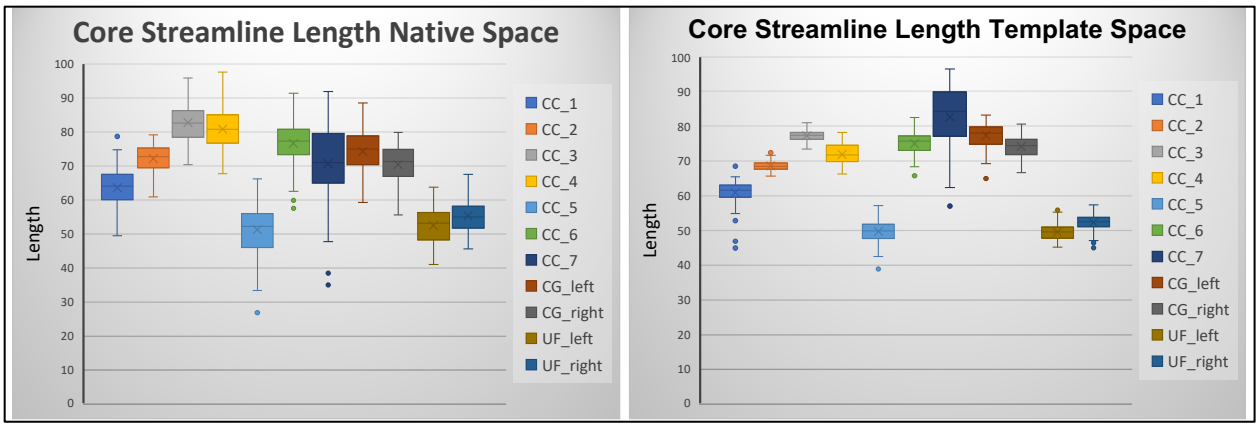

Figure 4.13 Core streamline length distributions. Boxplots of core streamline length by tract across all subjects, before and after co-registration of the individual fODF maps to the fODF template. Overall, all tracts show a reduction in variability after alignment to the template.

Coefficient of variation (CoV) for each Eigenvalue at each segment across all 49 control subjects was estimated in order to explore the effects of fODF alignment on variability in the control group. These results, which are shown in Figure 4.14, suggest that variability in Eigenvalues across healthy subjects is reduced in all tracts after alignment.

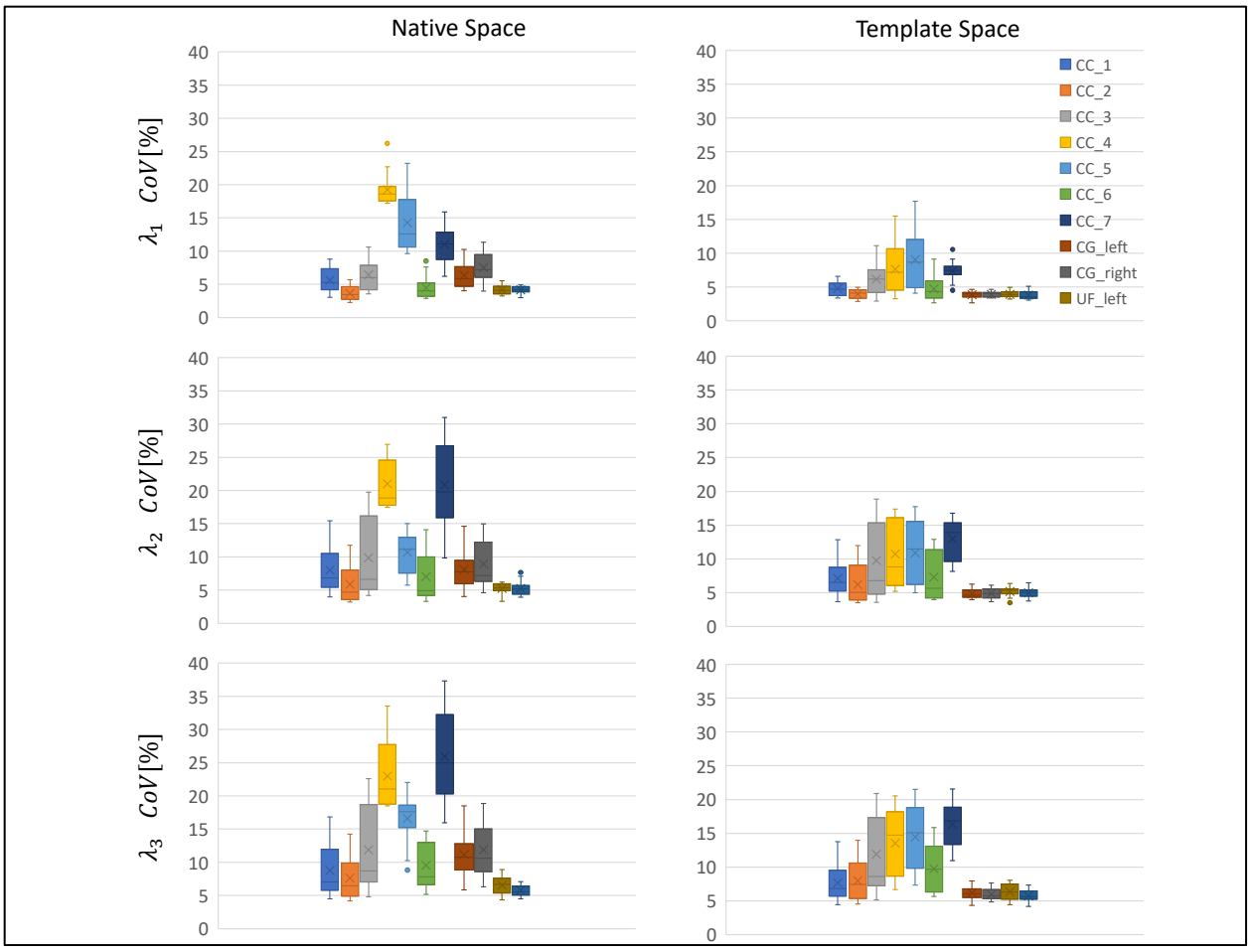

Figure 4.14 Eigenvalue (λ) coefficient of variation (CoV) across control subjects before and after alignment to fODF template. For each tract, the Eigenvalue CoV over the control group is computed at each discrete segment of the tract. The box plots represent the CoV distribution across the 18 discrete segments of the tract (13 for the cingulum). For all three Eigenvalues, a tendency in the median CoV toward lower values can be appreciated after alignment.

4.5.3 Mahalanobis distance along the tract

Visualization of the results can be done in three different ways. First, overall results for the TBI patients are shown in Table 4-3. Patients are given a check mark for a tract if that tract is found to have at least one segment that exceeds the critical Mahalanobis distance value for abnormality. Because there is not enough number of subjects per site, statistical analyses of

site effects are not possible. Yet, displaying the results like they are in Table 4-3 is helpful in revealing any obvious site (or scanner brand) effects.

Table 4-3 TBI patients multivariate analysis findings. If at least one discrete segment along the tract exceeded the critical MaD value of 6.38, the patient was given a check mark (✓) for that tract, otherwise the cell is left blank. A dagger mark (†) represents a tract that could not be reconstructed for that patient, typically due to a large lesion in that region. The patients with the asterisk mark (*) were scanned at UW-Madison (Site I).

Site	Vendor	Patient	CORPUS CALLOSUM							CINGULUM		UNCINATE		# of Tracts with Abnormalities per Subject
			CC_1	CC_2	CC_3	CC_4	CC_5	CC_6	CC_7	CG_left	CG_right	UF_left	UF_right	
I	GE	A*				✓	✓							2
I	GE	B*	✓		✓		✓	✓	✓				✓	6
II	GE	C	✓	✓	✓	†	✓	✓	✓	✓	✓	✓	✓	10
III	Philips	D	✓	✓	✓		✓	✓	✓	✓		†		7
IV	Philips	E		✓	✓	✓	✓	✓	✓	✓				7
IV	Philips	F	✓											1
V	Philips	G												0
V	Philips	H												0
V	Philips	I	✓	✓	✓			✓				✓	✓	6
VI	Siemens	J											✓	1
VII	Siemens	K	✓		✓				✓				✓	4
VIII	Siemens	L	✓	✓	✓	✓	✓	✓	✓	✓			✓	9
IX	Siemens	M				✓	✓	✓						3
X	Siemens	N	✓										✓	2
X	Siemens	O												0
X	Siemens	P								✓	✓			2
X	Siemens	Q						✓	✓					2
XI	Siemens	R	✓											1
XI	Siemens	S	†	✓	†	†	✓	✓	✓	✓	✓	†	✓	7
XII	Siemens	T	✓		✓		✓	✓			✓			5
XII	Siemens	U		✓										1
XIII	Siemens	V	✓	✓		✓	✓		✓	✓	✓	✓	✓	9
# of Patients with Abnormalities per Tract			11	8	8	5	10	10	9	7	5	3	9	

For both TBI patients scanned in the same site as the controls (Site I), abnormal Mahalanobis distance values were found in two of the studied tracts (CC_4, CC_5) for Patient A and in 6 tracts for Patient B (CC_1, CC_3, CC_5, CC_6, CC_7, and UF_right). Out of the 22 patients, 17 were found to have abnormal Mahalanobis distance in at least one of the studied tracts.

Patient C was found to have abnormal Mahalanobis distance values in all of the studied tracts. The data for this patient was collected with a GE MR-750 scanner, the same model as the scanner used to collect the control group scans, but at Site II. Two phantom scans collected at this site did not reveal any obvious systematic differences in Eigenvalues from the other sites.

Additionally, this subject presents extremely large lesions, so that the likelihood that the observed anomalies are the result of site or scanner effects is low.

Patient L had abnormal values in all of the sections of the corpus callosum. This patient also had abnormal Mahalanobis distance values in the left cingulum and in the right-side uncinate for a total of 9 tracts with observed abnormalities. The data for this subject was collected with a Siemens Trio at Site VIII. No phantom scans were collected for this site.

Patient V had a total of 9 tracts with observed abnormalities, same as Patient L. In this case, they were found in both sides of the cingulum and uncinate and in 5 sections of the corpus callosum. The data for this subject was collected at Site XIII with a Siemens Prisma scanner. A phantom scan was also collected at this site and the analysis showed no obvious signs of systematic differences from the other sites in mean diffusivity values.

The next subject with the most tracts with observed anomalies was Subject E. These were found in 6 of the seven sections of the corpus callosum and in the left cingulum. The scan for this patient was collected at Site A with a Phillips Ingenia scanner. A phantom scan at this site did not reveal any obvious differences that could be attributed to site specific effects.

The tract for which the largest number of subjects were found to have anomalies was the rostrum of the corpus callosum.

Some subjects have more than one significantly large Mahalanobis-distance-valued segment, this can be better observed in the plots of Mahalanobis distance profiles for each tract as that

shown in Figure 4.15-Figure 4.18. The profiles of tracts with abnormalities are highlighted in subject-specific colors, those who do not have abnormalities are represented by dots (red: control; black: TBI) in the shaded region. The shaded region represents the region of normalcy, where the upper bound is set by the critical MaD value of 6.38. Subject-specific coloring of profiles with abnormality facilitates the traceability of the profiles.

Profiles of the Mahalanobis distance along the uncinate bundles are shown in Figure 4.15. For comparison the profiles for controls and TBI patients are plotted separately. The distribution of the Mahalanobis distance values at each segment of the control group are all below the critical value of 6.38 for both the left and right uncinate bundles. On the other hand, 9 TBI subjects exhibit abnormal values at one or various pieces along the right uncinate. Three of these patients (C, I, V) show abnormal MaD values in both left and right uncinate bundles.

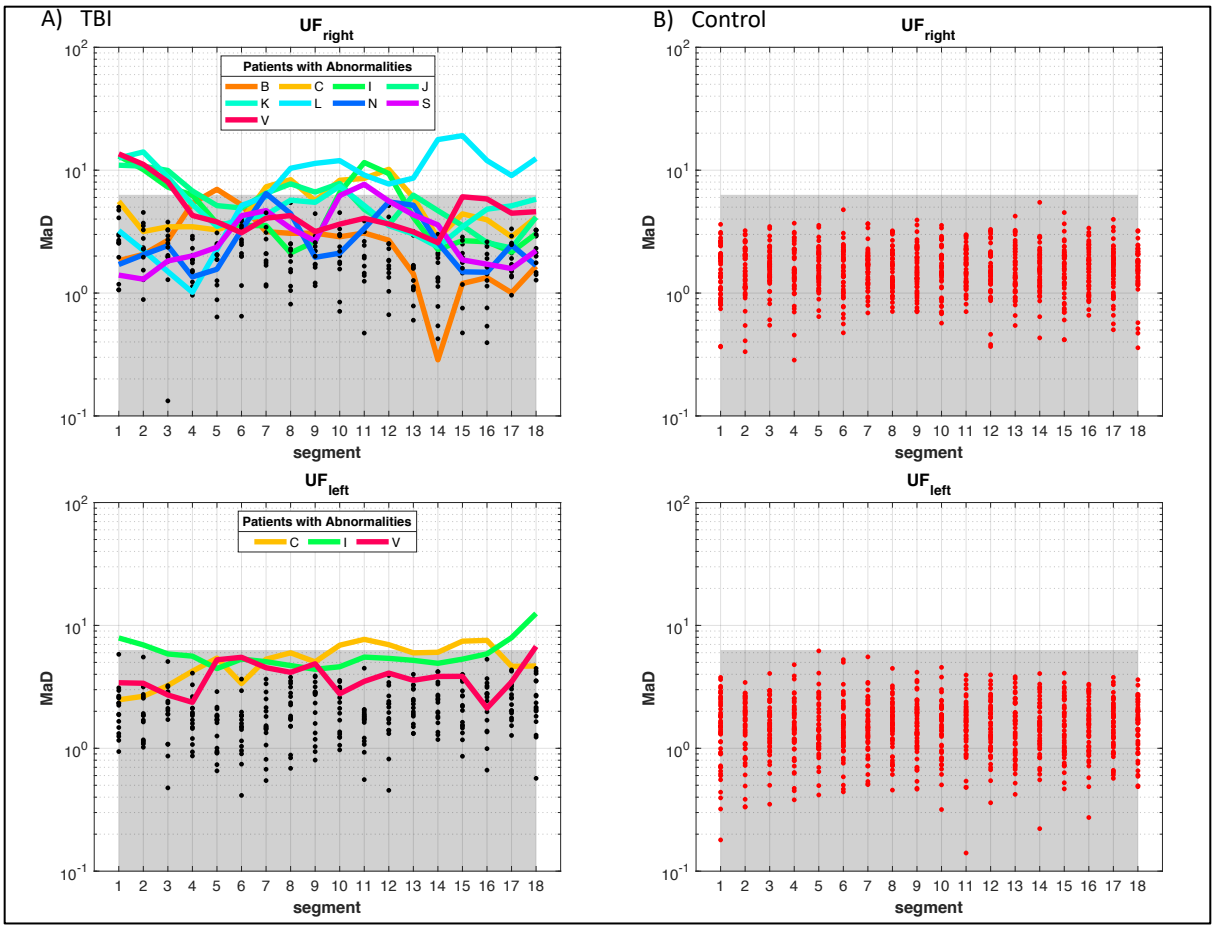

Figure 4.15 Plots of MaD profiles for the uncinate bundles. The profiles of tracts with abnormalities are highlighted in subject-specific colors, those who do not present abnormalities are represented by dots (red: control; black: TBI) in the shaded region. The shaded region represents the region of normalcy, where the upper bound is set by the critical MaD value of 6.38. Subject-specific coloring of profiles with abnormality facilitates the traceability of the profiles.

The resulting Mahalanobis distance profiles for the cingulum bundles are shown in Figure 4.16. Similar to the uncinate tracts, all of the values for the control subjects for all of the tract pieces fell below the critical value for abnormality. As mentioned previously, the cingulum tracts are truncated after the 13th segment in order to exclude pieces that include both, hippocampal and dorsal streamlines. For the right-side cingulum, results show 4 TBI subjects with abnormal Mahalanobis distance. For the left-side cingulum, 6 TBI subjects had segments where the

Mahalanobis distance exceeded the critical value of 6.38. For the right-side cingulum 5 TBI patients had abnormal MaD. Four of these patients (C, P, S, V) had abnormalities in both sides.

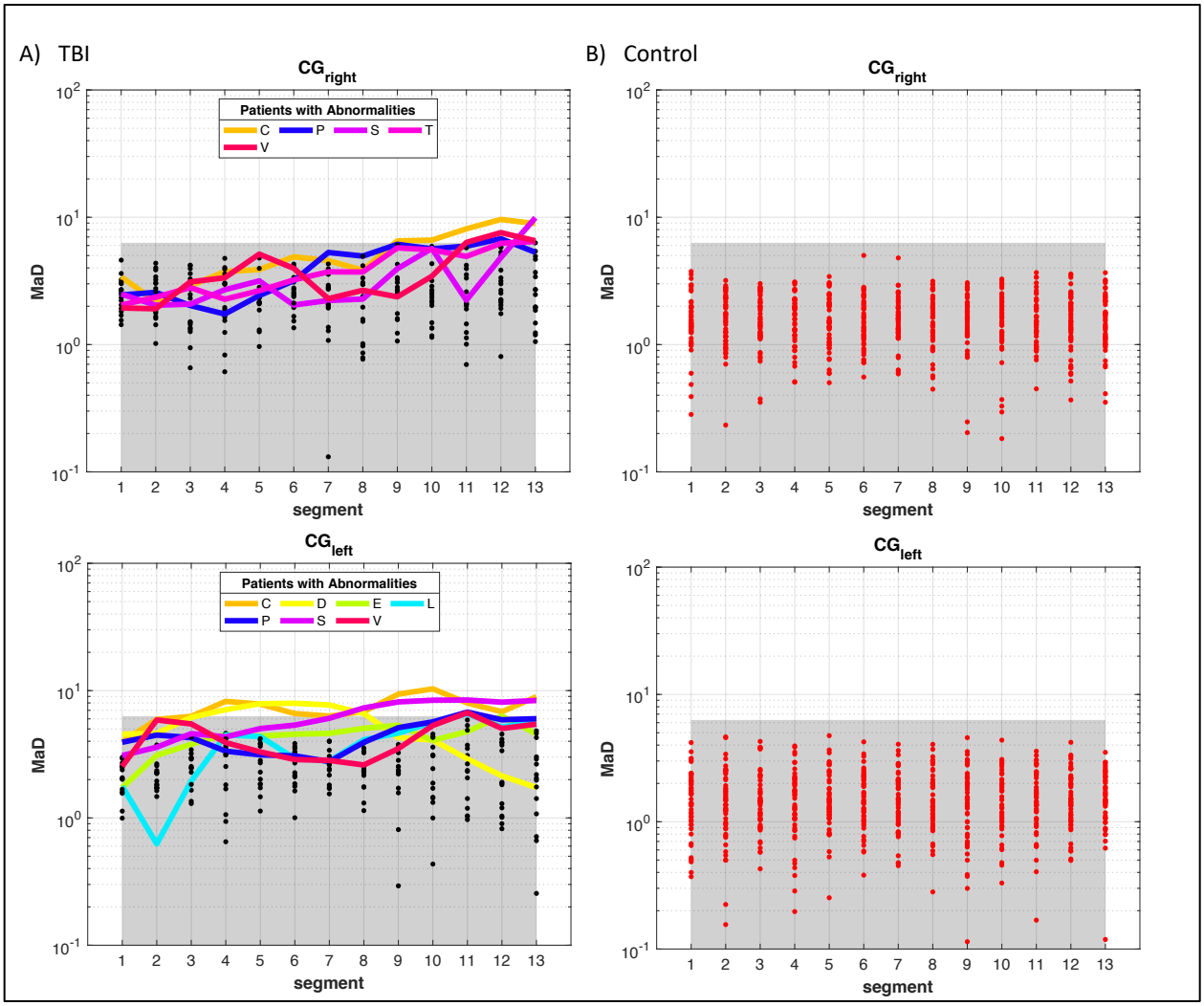

Figure 4.16 Plots of MaD profiles for the cingulum bundles. The profiles of tracts with abnormalities are highlighted in subject-specific colors, those who do not present abnormalities are represented by dots (red: control; black: TBI) in the shaded region. The shaded region represents the region of normalcy, where the upper bound is set by the critical MaD value of 6.38. Subject-specific coloring of profiles with abnormality facilitates the traceability of the profiles.

The results for the 7 sections of the corpus callosum are summarized in Figures Figure 4.17 and Figure 4.18. In contrast to the findings in the cingulum and uncinate bundles, out of the whole control group, there were two cases of higher than the critical value Mahalanobis distance. These were single segment occurrences in two different participants, one in segment #15 of the

genu and one in segment #14 of the posterior midbody. The plots for these are shown in Figure 4.17(B) and Figure 4.18(B). In contrast, the number of TBI subjects that had abnormal values at one or more segments along these tracts was 8 for the genu and 10 for the posterior midbody.

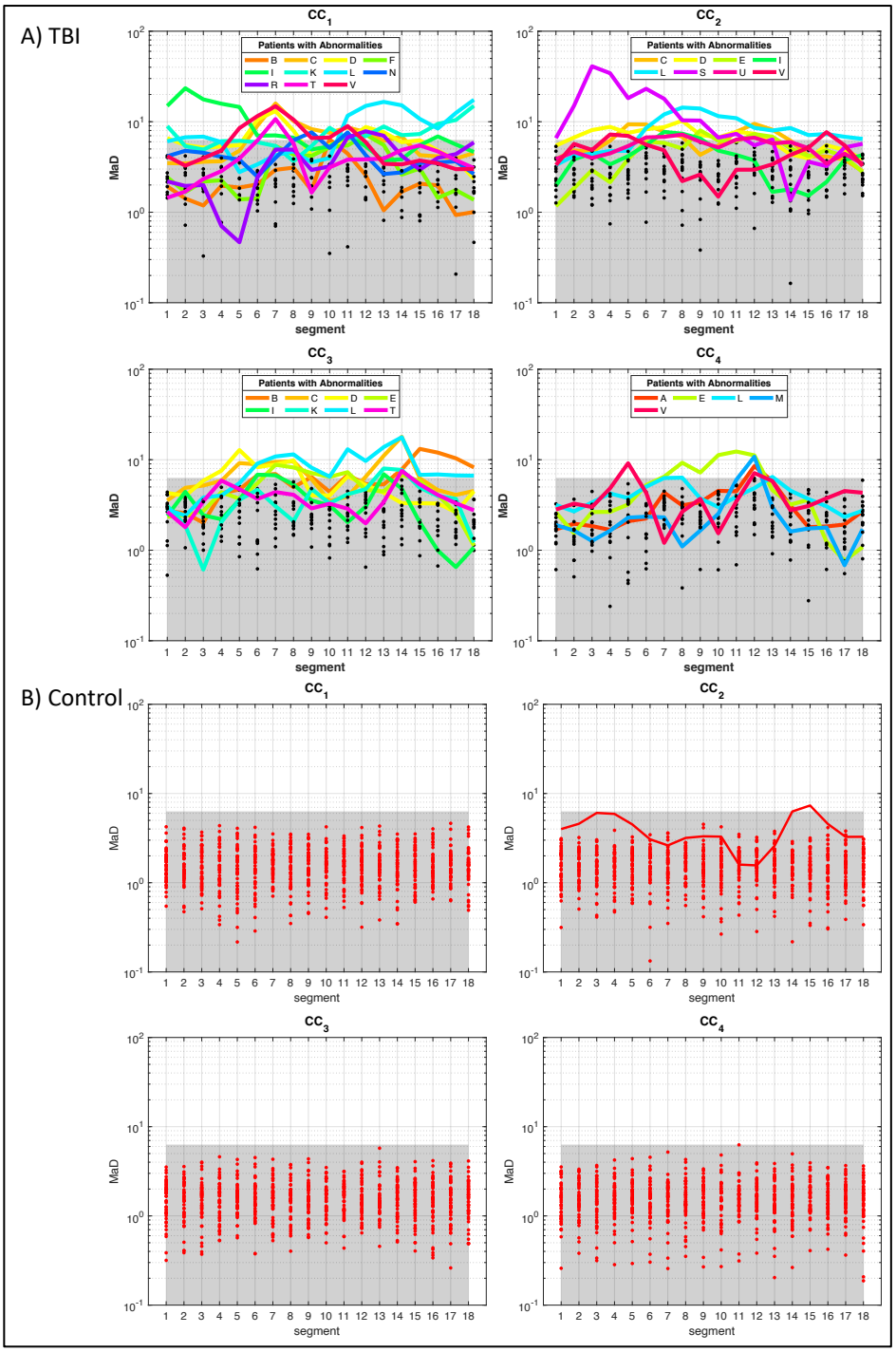

Figure 4.17 Plots of MaD profiles for the rostrum (CC_1), genu (CC_2), rostral body (CC_3), and anterior midbody (CC_4).

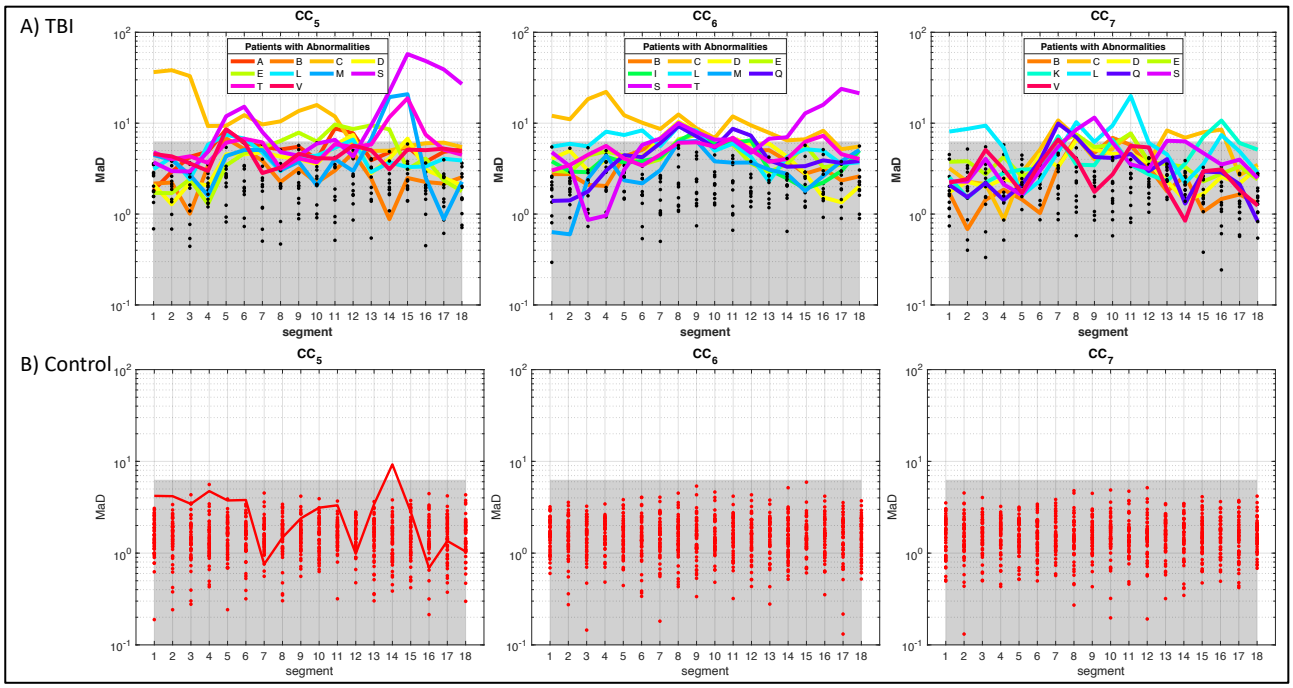

Figure 4.18 Plots of MaD profiles for the posterior midbody (CC_5), isthmus (CC_6), and splenium (CC_7).

The profiles in Figures Figure 4.15-Figure 4.18 were replicated for the TBI patients whose scans where obtained at sites that also had the PVP phantom scans. The replication profiles were generated using the Eigenvalues after harmonization to Site I with the relationships derived from the linear regression analysis in Figure 4.11. These results are shown in Figure 4.19. These results show that the Mahalanobis distance with and without correction are in good agreement.

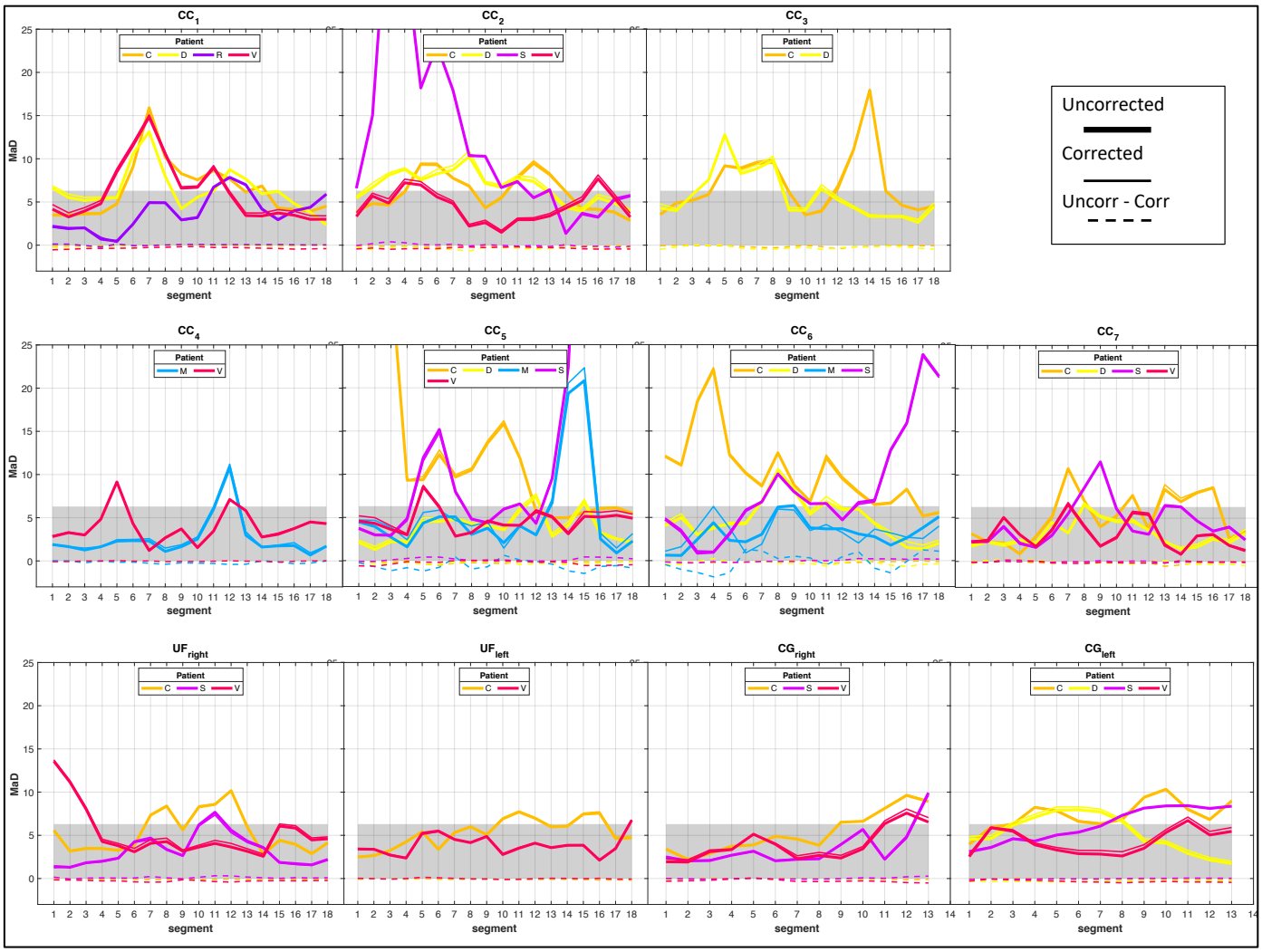

Figure 4.19 Mahalanobis distance analysis results with and without phantom-based corrections. Profiles of Mahalanobis distance along the tract (for all nine pathways) for patients scanned at sites that also participated in the diffusion PVP phantom scanning. The profiles obtained with the uncorrected Eigenvalues are represented by the bold solid lines. The profiles obtained with the corrected Eigenvalues using the regression line relationships in Figure 4.11 are represented by the thin solid lines. The profiles for the differences (Uncorrected minus Corrected) are displayed by the dashed lines. Note the difference profiles are all around zero.

The profiles shown in Figures Figure 4.15-Figure 4.18 are helpful in comparing multiple subjects at once. However, they do not provide a clear sense of anatomical location of abnormality as represented by MaD. This achieved by color-coding the actual tract with the Mahalanobis distance on a specific subject. This is illustrated in Figure 4.20 for TBI Patient L, whose MaD profile is also shown on the right panel in the same figure.

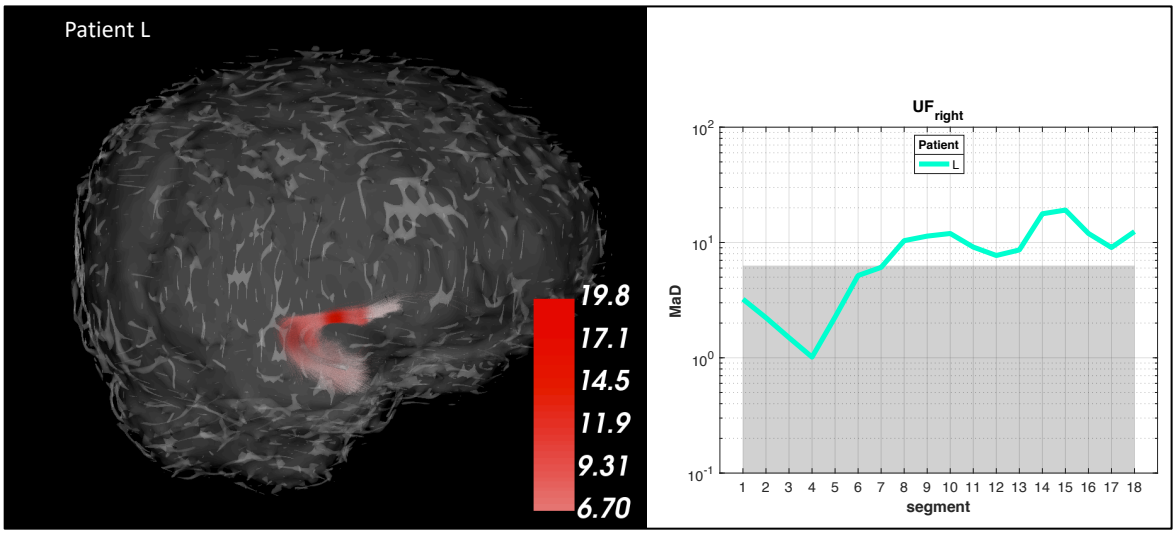

Figure 4.20 Left uncinate bundle for TBI patient L color coded by Mahalanobis distance profile shown on the right.

4.6 Discussion

This work describes a new computational and statistical framework for multidimensional analysis of neuroimaging quantitative measures at discrete segments of specific white matter pathways, which are derived from fiber tracking. Its application to individualized analysis of severe traumatic brain injury in children was demonstrated using the Mahalanobis distance computed from the three Eigenvalues of the diffusion tensor along the cingulum, uncinate, and parcellated corpus callosum tractograms. One at a time, 22 TBI subjects where compared to a

normative sample of 49 controls. A definition for abnormality was constructed off of Wilk's criterion, which accounts for normative sample size, number of features used in the Mahalanobis distance, and number of multiple comparisons.

The analyses showed a clear departure from the normative data in several TBI subjects at one or multiple locations along the analyzed bundles. Each of the controls subjects was also compared to the remaining 48 subjects in the normative group in a *leave-one-out* fashion. With only two segments identified as abnormal out of the entire analysis in the control group, the method demonstrated good specificity.

The presented framework is more spatially specific than averaging-over-ROI methods [140] and substantially reduces the number of multiple comparisons compared to voxel-wise approaches [146], [171]. While it is possible to complete the multidimensional analysis without inter-subject co-registration of the data, this work showed that variability in the normative group can be improved by alignment of the fODF maps before tract extraction (e.g. by better matching the lengths of the centroid lines used to guide the slicing of the bundles into smaller segments). This allowed to still conduct the analysis using each subject's tract extraction as opposed to using the template tract definitions, which can help to alleviate some effects of misalignment.

The data from the TBI patients was collected at different sites and with different scanner brands and models. The work presented in this chapter also shows a detailed analysis of a diffusion-based phantom that was used in gathering scans from a subset of sites and comparing them to data for the same phantom collected at the control group site. The phantom contains

vials with known diffusion coefficient values at zero degrees Celsius. Diffusion coefficients from each of the sites were matched to those in the control group site, and relationships were derived for use in correcting the human scans for those sites. The multivariate analysis for those specific subjects was replicated with the corrected diffusion values. The results show great correspondence between corrected and uncorrected values, indicating site effects were not problematic for this analysis.

Key contributions of this framework are the profiling of a multivariate metric of microstructure along a specific tract, the implementation of Wilk's test as definition for abnormality that accounts for normative sample size and dimensions considered, and the reduction of variability due to gross length mismatch between pathways across subjects by aligning their fODF maps.

4.7 Limitations and future work

The number of slices into which a pathway is discretized was selected off the literature [150]. However, the effects of this number were not analyzed. Because the number of chunks was kept constant regardless of the pathway under analysis, shorter bundles (e.g. uncinate) have smaller chunks than longer bundles (e.g. cingulum) do. This leads to better spatial specificity of detected differences in the shorter bundles. However, the requirements for better inter-subject alignment become stricter, since smaller chunks are less forgiving of some level of error in the image registration. Future work will consider tailoring the number of discrete slices to the length of the analyzed pathway and will evaluate effects of slice size.

The selection of a critical MaD value for abnormality accounts for reference sample size. Nonetheless, the method's performance could be improved by better estimates of the covariance matrix, which in turn could be achieved by increasing the size of the normative group. In the particular application of the method presented in this work, age effects in the DTI Eigenvalues are expected but were not accounted for. This will have a direct impact in the characteristics of the normative group distribution. Future work will investigate ways to account for age and provide adjusted Eigenvalues for computing MaD.

Also particular to the TBI study, while the results from the phantom analysis were encouraging in that the multivariate analysis with and without correction was in agreement for the pertinent patients, the survey of sites with phantom scans needs to be more exhaustive for fully ruling out systematic effects related to site.

Although the emphasis of this work was in developing a single-subject analysis framework, other avenues for exploration have been identified along the way. For example, it would be informative to consider flagged abnormalities with MaD against lesion load. Also, MaD could be utilized as multivariate imaging-based measure in group-level analyses. For instance, ongoing work has identified associations between MaD and behavioral measures that were significant by group in the TBI study for chunks in two sub-tracts of the corpus callosum (Figure 4.21).

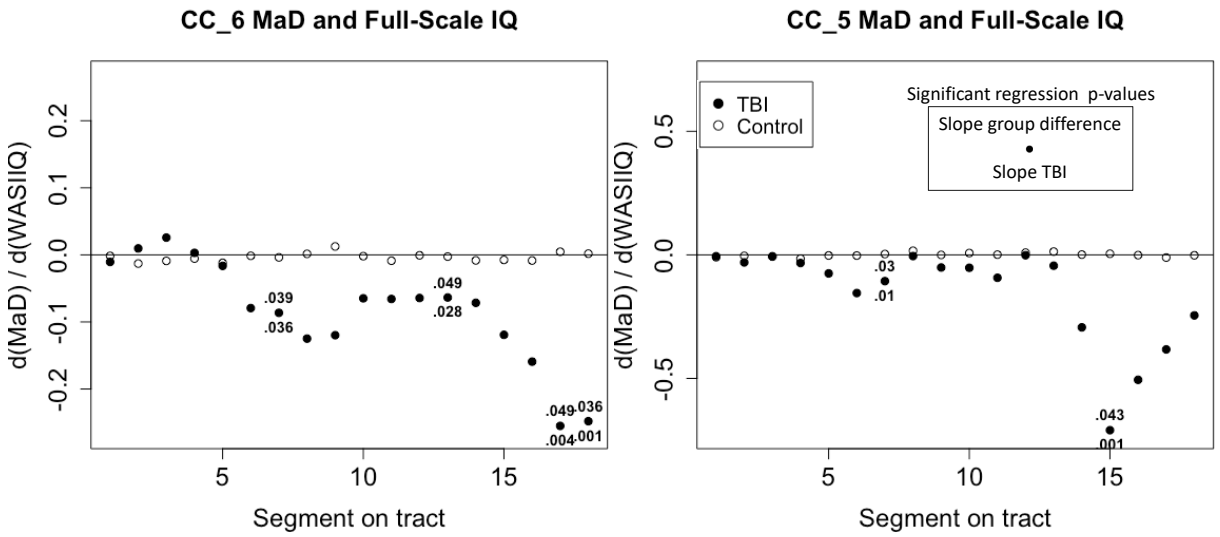

Figure 4.21 Linear regression analysis shows significant associations between MaD and a measure for IQ in segments of CC_5 (posterior mid-body) and CC_6 (isthmus) in the TBI group. These associations were significantly different from those in the control group. The slope values in the plots are adjusted for age.

Finally, the nature of the injuries in the severe TBI study almost guarantees that differences will be found when compared with the healthy group. However, it is envisioned and expected that this multivariate framework will prove useful in detecting abnormalities that are more subtle in conditions such as in autism or Alzheimer's disease. Additionally, incorporating other microstructure metrics derived from non-diffusion data such as relaxometry parameters (e.g. R1) or even other modalities such as PET, could prove useful in contributing potentially new information to the composite measure and improve its discriminating power.

4.8 - Appendix A: Ice Water Diffusion Phantom Instructions

I. INTRODUCTION

This phantom was developed to characterize MRI scanner performance when measuring the apparent diffusion coefficient *(*ADC). Its main components are 30 mL vials of the polymer polyvinylpyrrolidone (PVP) in aqueous solution. These vials have different concentrations of PVP; increasing concentrations of the polymer result in decreased ADC values. *PVP is nontoxic and the phantom contains no toxic materials.*

In order to achieve reproducible ADC measurements, it is necessary to control the temperature of the phantom. An ice water bath serves to maintain temperature at 0 °C. In the following sections, we will outline the phantom's various parts, as well as describe the proper procedures for phantom preparation and imaging.

II. PHANTOM COMPONENTS

The phantom consists of five main parts, exclusive of the PVP vials. These pieces are labeled A-C in the Figure 1. When assembled the phantom is 194 mm in diameter. The phantom has been shipped fully assembled, but dry. In order to fill it with ice water, one has to remove the fill port caps *(*A), easily done by removing the six M6 socket-head screws holding the caps in place. Located in the center of each fill port cap is a secondary fill port sealed with one PEEK M8 pan head screw. This secondary fill port is used to add cold water to remove any remaining air bubbles after reassembly. **Do not disassemble the phantom by separating the two hemispheres** (B).

The vial plate (C) holds 30 mL HDPE vials filled with aqueous solutions of PVP at 0, 10, 20, 30, 40 and 50*% w/w,* as seen in Figure 2. These vials have been arranged such that when vie*w*ed from the top, PVP concentration decreases when moving counterclockwise in both the inner and outer ring of vials. The center vial holds deionized water, and will sit at iso-center when the phantom is properly positioned. The vials' caps have been sealed with a small amount of clear silicone. There are also three 5 mL polypropylene vials that extend above and below the 30 mL vials to serve as MR fiducial markers when examining images. The two arcs located at the top of the vial plate are a means of thermal contact between the top and bottom halves of the phantom.

O-rings are used in order to seal the various mating surfaces of the phantoms. Included in a kit are an extra PEEK scre*w* and O-ring should they be needed. Also, included with the phantom are a NIST-traceable temperature probe (not MRI safe), a non-magnetic token to tighten the pan head screw in the fill port, an adjustable torque wrench (not MRI safe), a level, and a plastic syringe for adding cold water through the secondary fill port when removing any remaining air bubbles after reassembly.

III. PHANTOM PREPARATION

Diffusion is a thermally-driven process: as temperature increases, the apparent diffusion coefficients of the phantom solutions will also increase. While this increase is small for the most

viscous solution of PVP (50 %), the increase is on the order of 2-3 % per degree Celsius for DI water. It is therefore critical that temperature be consistent when scanning the phantom, a goal best achieved by the use of ice water. Please use the following procedure to equilibrate the phantom at 0°C, and maintain temperature during the scan.

The phantom requires at least 2 hours to equilibrate to 0 °C. Make sure to allow enough time to prepare the phantom in anticipation of the scan. Ideally the initial preparations (steps 1-3) should be started at least 2.5 hours before the scan.

1. Prepare an ice water bath in the provided cooler. Begin by obtaining enough two 7 pound bags of cubed iced and two gallons of cool water. Empty the ice into cooler. Add 1.5 gallons of cool water enough to just make the ice float. See Figure 3.
2. Remove the bottom and top fill port caps. Fill both hemispheres with ice. It may help to slightly crush the ice, but not too finely crushed.
3. Without replacing the fill port caps, submerge the phantom in the cooler ice water bath. Then place the fill port caps in the cooler as well. Close the cooler cap tight and leave it in place for at least 2 hours. See Figure 4.

4. 30 minutes before imaging, remove the phantom from the ice water bath and drain out all the water from both hemispheres into the cooler. Pack the bottom hemisphere with as much ice as possible. It may help to slightly crush the ice, but not too finely crushed it may cause unavoidable air pockets in the imaging plane that will generate susceptibility induced artifacts.

Close the bottom fill port using the Adjustable Torque Wrench. Make sure the large O-ring is fully inside the groove before you place the cap. ***Take care to not overtighten the PEEK screws, as you may shear off the head of the scr*****ew.** ***The maximum recommended torque is 9 in lbs****.* The wrench has been previously adjusted to the appropriate torque setting. However, if for any reason the wrench has to be readjusted, the 9 lbs value can be set following the instructions described in Figure 5.

5. Fill the top hemisphere with ice but do not replace the cap yet. When the top half of the phantom is as full of ice as is possible, add ice water from the cooler to the phantom via the top of the upper hemisphere. ***There should be more ice than water to ensure a proper ice water bath at 0 °C. The ice should not float; instead, water should fill the interstitial spaces formed by the ice. See Figure 6.***

6. Replace the top fill port cap. In order to eliminate residual air bubbles in the phantom, one may add water to the phantom via the secondary fill ports. These ports are the M8 pan head screws located in the handle of the top and bottom fill port caps (Figure 7). Use ice water from the cooler to to**p** off the phantom via the secondary fill ports. A plastic syringe is provided for topping off the last few milliliters.

7.Before closing off the phantom's secondary fill ports, check the temperature of the phantom using the provided thermocouple probe. The temperature displayed by the probe should read 0 +-0.5 °C. Check on of the two halves of the phantom and record this value.

8. If more than 10 minutes remain before the scan is started, place the phantom back into the ice water bath in the cooler and leave it there until 5 minutes before imaging. Right before the scan, remove phantom from water bath and dry it off with paper or cloth towel.

IV. Coil selection and positioning

When loading the phantom into the magnet, it is important that the center vial be aligned with magnet iso-center. Use padding to achieve the proper height and secure phantom in place. Ensure that it is as leveled as possible.

Ideally use same coil as was used to acquire the participant scans, but if not, a larger coil is fine, ideally a multichannel coil. If using a quadrature coil, parallel imaging will need to be turned off.

1. Position phantom as shown in Figure 8. Particularly, make sure the serial# sticker is facing toward the table (i.e. if you are looking at the bore of the scanner, the serial# sticker is directly facing you).

2. Once the field of view has be set to properly cover the phantom as is shown in Figure 9, collect the T1 weighted, T2 weighted, and DTI scans from the previously approved list of protocols (i.e. the same protocols used in scanning the TBI participants).

Contact us if you have questions or need any assistance with the protocol.

V. FIGURES

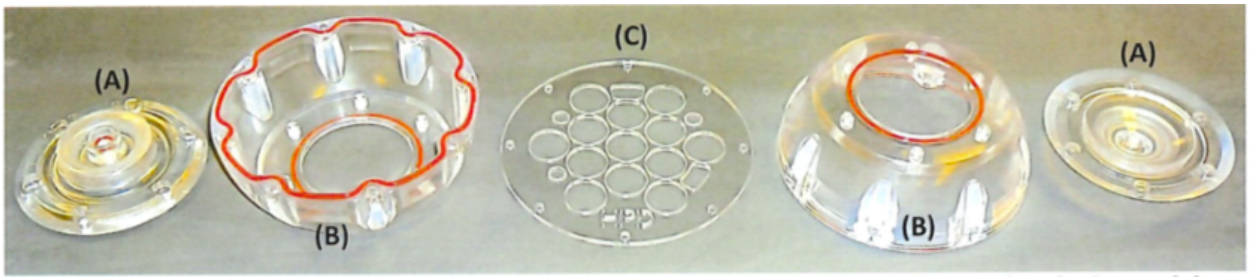

Figure 1. Main phantom shell components. From left to right: bottom fill port, bottom hemisphere, vial plate, top hemisphere, and top fill port. All pieces are polycarbonate material.

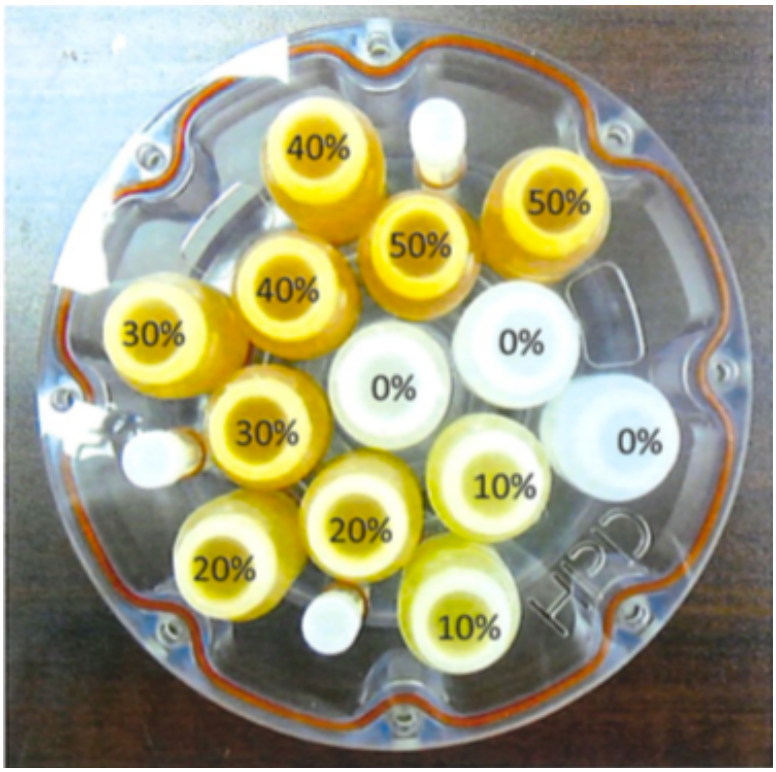

Figure 2. Vial plate. 30 mL vials of aqueous solutions of PVP are arranged in inner and outer circles to allow for testing the spatial dependence of ADC measurements due to gradient non-linearities. The three smaller 5 mL are the fiducial markers.

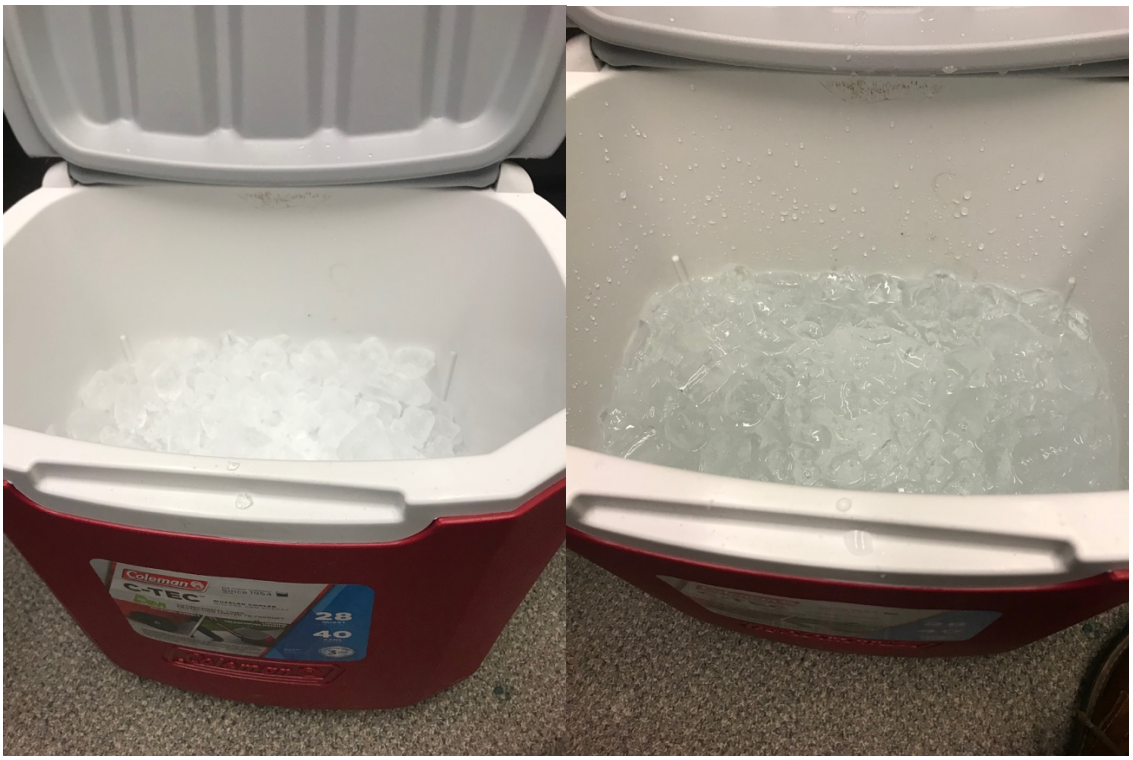

Figure 3. Cooler with ice only (left). Ice water bath (right).

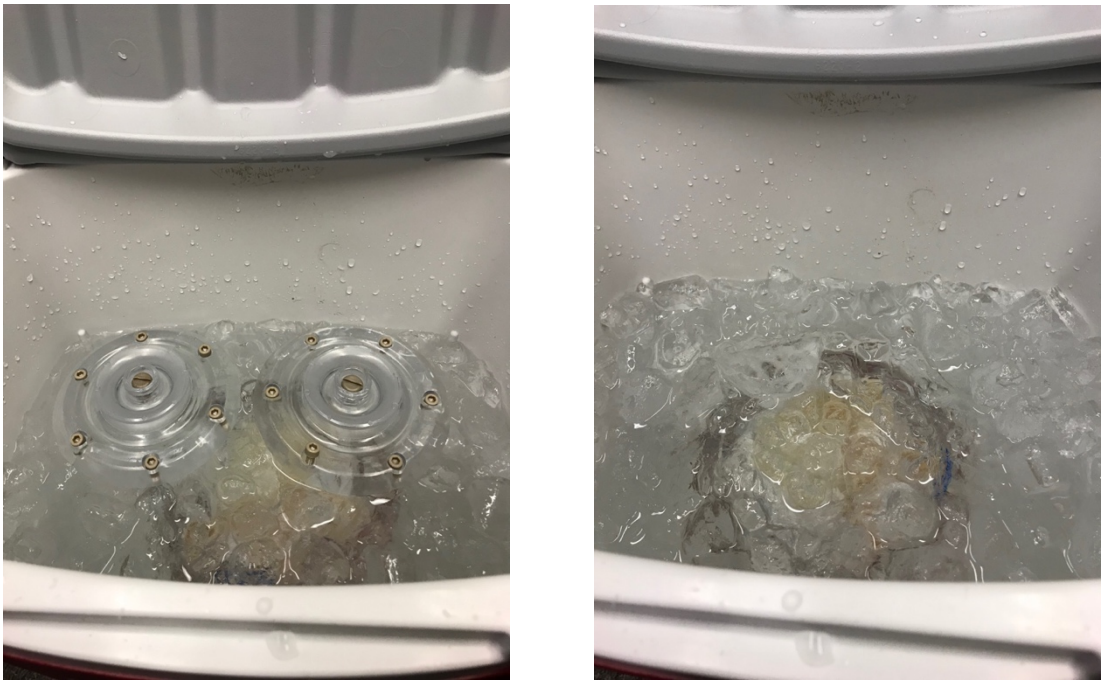

Figure 4. Phantom submerged in the ice water bath (left), Make sure the phantom is fully submerged. (Right) Hemisphere port caps placed in the cooler with the submerged phantom.

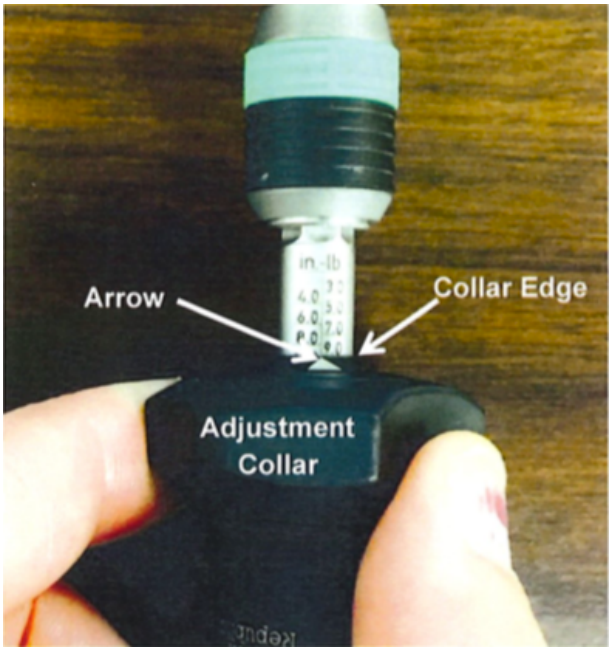

Figure 5. **OPERATING THE ADJUSTABLE TORQUE WRENCH**
To adjust the torque wrench, pull down on the adjustment collar and twist the collar to the desired torque setting by aligning the white arrow to the center line, and the collar edge to the line just below the torque setting (in this case 9.0). When desired setting is obtained, release the adjustment collar. To change out the bit, pull up on the green/black locking sleeve to release the bit. Then pull down on the green/black locking sleeve to lock the bit in place.

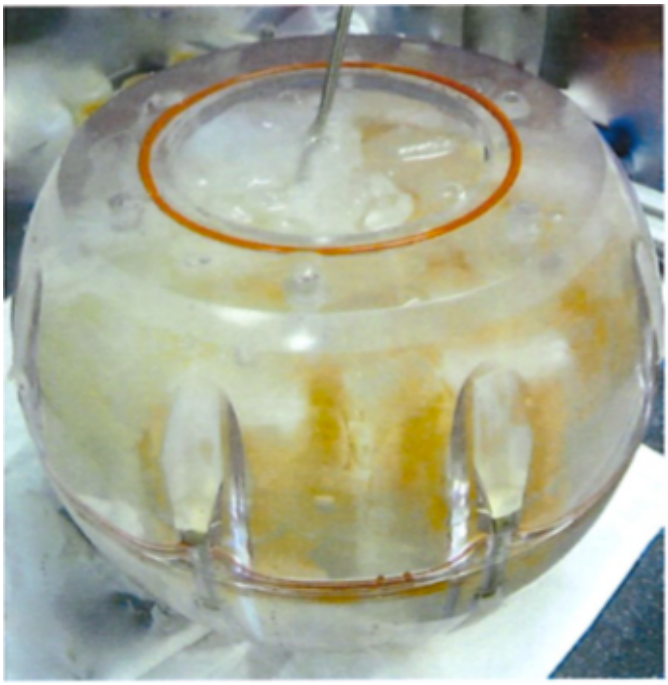

Figure 6. Phantom after filling both hemisphere with ice and water. Bottom hemisphere port cap has been replaced but not top. Note the temperature probe. Make sure that the O-rings are well positioned in the groove before the port cap is placed.

Figure 7. Assembled phantom. The top secondary fill port is closed by the pan head screw in the middle of the handle of the top fill port cap.

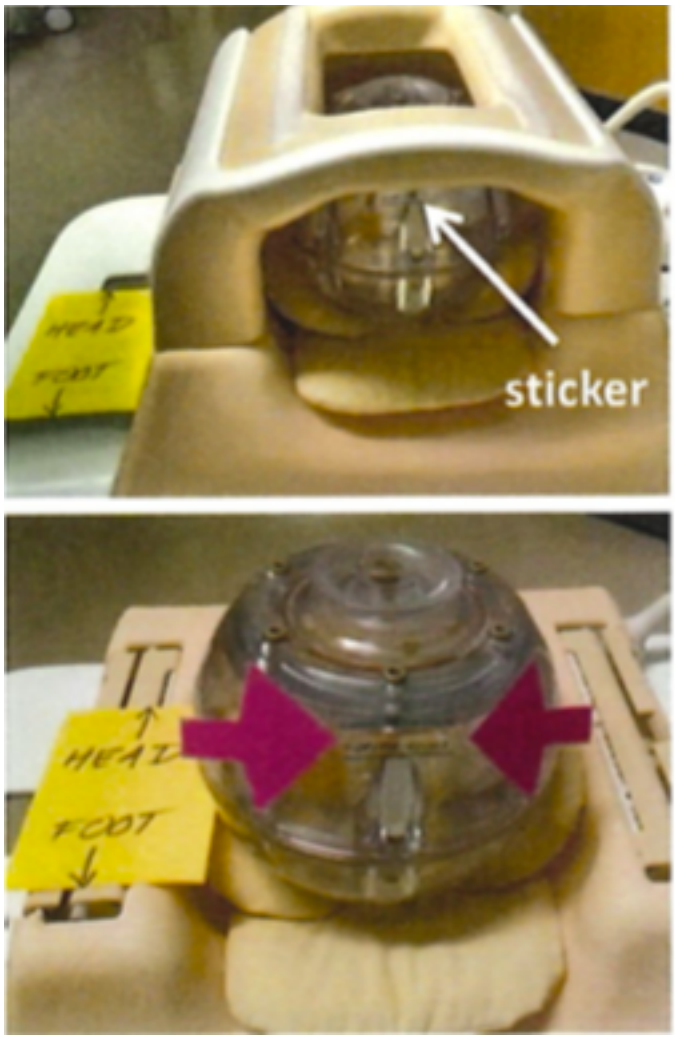

Figure 8. Positioning of the phantom in the head coil. The serial# sticker is emphasized by the arrows.

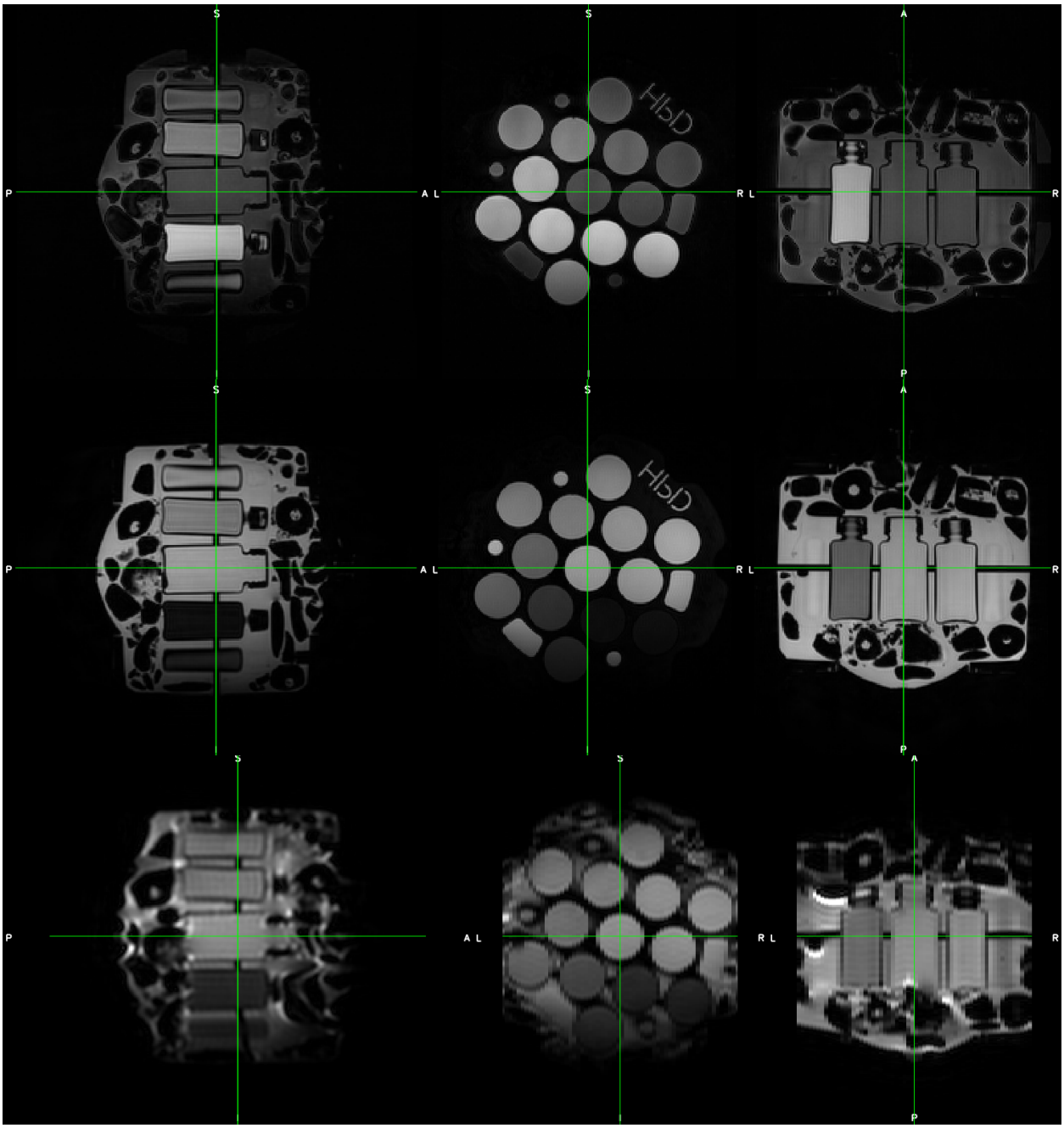

Figure 9. Images of the ice water phantom. 1st row: T1 weighted; 2nd row: T2 weighted; 3rd row: b=0 image of the DTI scan.

Chapter 5 - A diffusion-based phantom for b-value independent temperature estimation

5.1 Abstract

This chapter outlines plans for a diffusion-based phantom. First, the fundamental link between diffusion and temperature introduced in Chapter 2 is expanded. An explicit relationship between temperature and diffusion is detailed. The need for a test object in checking for consistency of measurements in multi-center studies is emphasized by the work presented in Chapter 4. However, the requirement of scanning the phantom at zero degrees (or other known temperature) introduces unwanted effects related to the often tedious and involved preparation procedures. The work in this chapter is an exploration into an alternative approach. This consists of using the known diffusion-temperature relationship between two materials to derive an equation that allows for estimating the temperature of the materials using the diffusion weighted images themselves. Further, the approach is independent of the diffusion weighting quantity known as *b-value*, which is a prescribed parameter for each scan and is susceptible to both systematic and human errors. Five different materials, including water, are selected for developing the method and a temperature control and monitoring system is built for validation purposes. The chapter outlines how this project faced challenges related to low viscosity of the materials being used and convection currents introduced by vibration of the scanner table. These vibrations are related to the strong diffusion gradients from the scan acquisitions. When the motion coincides with the direction of diffusion sensitization, the signal experiences attenuation that is not due to molecular diffusion. These artifacts proved difficult to correct and the fundamental issues that caused them could not be overcome. The chapter

concludes with a description of measures implemented for addressing the vibration issues, which included placing weights on the scanner table in order to help dampen vibrations. Potential future actions to address the vibration issues are discussed.

5.2 Introduction

In the previous chapter, phantom measurements from five other sites were compared to those obtained from the same phantom at the control group site. The diffusivity measurements from the phantom's 5 different concentrations were plotted and compared between Site I and each of the other sites. A linear relationship from these measurements was estimated between each of the 5 sites and the control group site. This relationship was used to harmonize the diffusivity values of the different vials between the control site and each of the other 5 sites.

Another possible way for harmonizing phantom diffusivity measurements, and perhaps a more fundamental one, would be to adjust the prescribed *b-values* from a given site in order for the diffusivity measures from other sites to match those at the control group site. Recall that the factors contributing to the *b-value* are gradient strength, and timing settings for the width and separation of the diffusion gradients. Errors in these settings can lead to deviations in the actual *b-value* from the prescribed one. Such errors can be due to user or hardware-related factors.

Also, as we learned in Chapter 2, diffusion is a thermally driven process. Thus, as temperature increases, the apparent diffusion coefficients of the phantom solutions will also increase. While this increase is expected to be small for the most viscous solution of PVP (50%) in the scanned

phantom, the phantom manufacturer states the increase is on the order of 2-3 % per degree Celsius for the 0% PVP vial. In order to achieve reproducible ADC measurements, temperature must be accounted for. One alternative is to control the temperature of the phantom. For this phantom, an ice water bath serves to maintain temperature at 0 °C.

While this way of controlling for the temperature is effective, the procedures for preparing and scanning the phantom are quite involved and cumbersome as can be seen in "Section 4.8 - Appendix A: Ice Water Diffusion Phantom Instructions" of the previous chapter, which details the instructions sent to the sites for preparing the diffusion PVP phantom. Even when these were simplified from the instructions provided by the manufacturer in order to reduce the risk for errors, at least one of the five sites had to re-scan the phantom due failure in proper following all the preparation steps.

Repeated scans incur costs and time, but if not caught, errors in phantom scans could result in mischaracterization of measurement deviations as systematic.

An alternative approach to controlling the temperature, is to know the temperature of the phantom and know how the diffusion coefficient varies as a function of temperature. In this chapter, work is presented that set out to develop a diffusion phantom using a number of materials with known temperature-diffusion relationships. The project plan included investigating the possibility of using diffusion weighted images between two materials in thermal equilibrium for estimating the temperature of the materials. Additionally, the same images could be used to estimate the diffusion coefficients of the materials and confirm that

those corresponded to the estimated temperature from the known temperature-diffusion relationships.

5.3 Methods

5.3.1 Diffusion vs Temperature

Recall from Chapter 2, the apparent diffusion coefficient (D) can be mapped from the diffusion attenuated MRI signal obtained with a standard Stejskal-Tanner pulsed gradient spin echo (PGSE) sequence by the following expression

$$S = S_0 e^{-\gamma^2 G^2 D \delta^2 \left(\Delta - \frac{\delta}{3}\right)} \quad \text{Equation 5.1}$$

where S_0 corresponds to the signal with no diffusion, γ is the gyromagnetic ratio, G is the diffusion gradient amplitude, δ is the duration of the diffusion gradient pulses, and Δ is the separation between the starting point of the diffusion pulses.

The amount of *diffusion weighting* or *b-value* is given by

$$b = (\gamma G \delta)^2 \left[\Delta - (\delta/3)\right] \quad \text{Equation 5.2}$$

Thus, the diffusion coefficient D can be obtained from Equation 5.1 as

$$D = -\frac{1}{b} \ln\left(\frac{S}{S_0}\right) \quad \text{Equation 5.3}$$

Mobility of molecules is dependent on temperature, and therefore the magnitude of diffusion is sensitive to the temperature of a material. A couple of decades ago, a model for self-diffusion versus temperature based on the Arrhenius activation law [172] was reported by Tofts et al., (2000) [173] as

$$\ln D = \ln D_0 - B\left(\frac{1}{T} - \frac{1}{T_0}\right) + C\left(\frac{1}{T} - \frac{1}{T_0}\right)^2 \qquad \text{Equation 5.4}$$

where B equals E_A/k, the activation energy for translational diffusion of the molecules (E_A) divided by Boltzmann's constant ($1.38\ 10^{-23}\ J\ K^{-1}$), and C is a quadratic term that accounts for small deviations from Arrhenius behavior. D_0 is the diffusion coefficient at a reference temperature T_0 (set to 22 ºC).

Tofts et al., (2000), determine the B and C parameters by fitting this model to diffusion coefficients derived from NMR measurements at 4.7 T (see Table 5-1), for 15 different liquids in a range of temperatures from 15 to 35 ºC. Diffusion coefficients for all materials were also obtained from measurements with a clinical Stejskal-Tanner PGSE sequence at 1.5 T and shown to correspond with those predicted by the model in Equation 5.4 to within 2.1 %. The model estimates for B and C along with other information for all the materials in the study are provided in Table 5-1.

Table 5-1 Measurements of diffusion coefficient at 15-30 using a 4.7 T spectrometer. Each value is the average of 3 or 4 measurements at the same temperature. Proton density, T1 and T2 at 1.5 T (modified from Tofts et al., 2000).

	Diffusion Coefficient $[\mu m^2/ms]$				V	TC	T1	T2	B	C	
	15 °C	20 °C	25 °C	30 °C	(cp)	%/ °C	ms at 1.5 T		K	10^6 K^2	PD
cyclohexane	1.214	1.338	1.482	1.652	0.89	2	2328	1329	1764	1.35	1
cycloheptane	0.803	0.891	1.003	1.139	1.37	2.4	2156	1598	2048	2.38	1.05
cyclooctane	0.432	0.495	0.568	0.653	1.96	2.7	1608	1234	2382	0.88	1.08
n-octane	1.988	2.141	2.354	2.633	0.51	1.9	1932	193	1615	3.35	1
n-nonane	1.525	1.627	1.77	1.961	0.67	1.7	1748	140	1442	3.27	1.01
n-decane	1.165	1.263	1.391	1.559	0.84	1.9	1526	145	1658	2.98	1.02
n-undecane	0.931	1.009	1.113	1.248	1.1	1.9	1331	204	1681	3.13	1.03
n-dodecane	0.708	0.783	0.876	0.996	1.38	2.2	1160	163	1937	2.55	1.03
n-tridecane	0.565	0.634	0.712	0.805	1.72	2.3	999	173	2019	1.05	1.04
n-tetradecane	0.443	0.491	0.554	0.637	2.13	2.4	869	198	2056	3.44	1.04
n-pentadecane	0.357	0.403	0.462	0.535	2.54	2.7	751	178	2323	2.69	1.05
n-hexadecane	*	0.341	0.387	0.446	3.03	2.5	669	201	2173	3.26	1.05
ethanol	0.85	0.969	1.09	1.218	1.07	2.4	2141	20	2061	-0.91	0.93
n-propanol	0.455	0.537	0.626	0.72	1.95	3.1	1405	31	2692	-1.19	0.97
n-butanol	0.336	0.393	0.461	0.542	2.54	3.2	1149	68	2742	1.13	0.99

V: viscocity, at 25 °C, 1 centipose (cp) =1 millipascal second. PD: proton density relative to water. * Solid at 15 °C.. At 30, only 2 measurements were taken; these agreed to within 0.1%. TC: Temperature coefficient (fractional increase in the diffusion coefficient per degree).

Using the fitted B and C parameters and Equation 5.4, it is possible to plot D as a function of temperature as shown in Figure 5.1 for all the materials in Table 5-1.

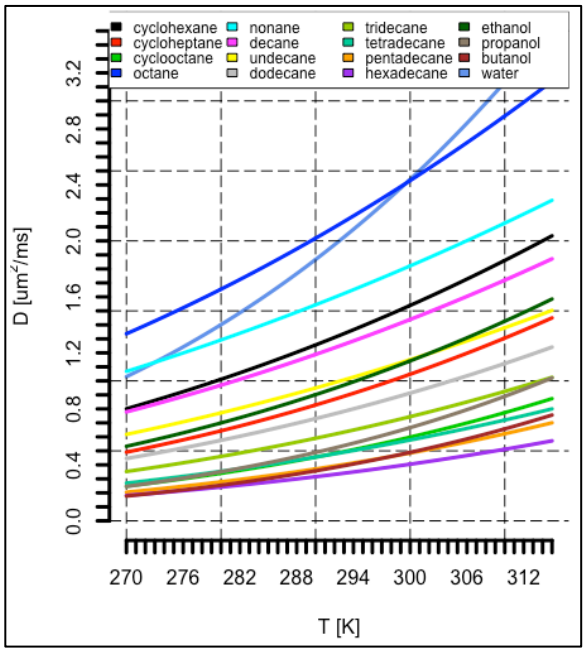

Figure 5.1 Plots of relationship between diffusion coefficient and temperature for the various liquids in Tofts et al 2000.

Arguably at this point, one could simply estimate the diffusion coefficient of a given material from diffusion weighted images, and from this known relationship calculate the temperature of the material. However, a problematic scenario could arise when scanning the phantom in two different scanners and errors in the prescribed *b-value* occur.

Recall that diffusion is a function of the *b-value*. Consider two scans of the same phantom in two scanners with the same imaging protocol. Assume that, due to systematic or user error, the prescribed *b-value* from scanner 1 differs from the actual *b-value*. In estimating the diffusion coefficient from the images, it is the prescribed *b-value* that is used. Therefore, the estimated diffusion coefficient from scanner 1 would be erroneous. Using this diffusion coefficient value to estimate the temperature of the material from the known model, would also result in the incorrect temperature estimate.

This means that when comparing the diffusion coefficients between the two sites, one must first consider the estimated temperature and then asses from the model whether the estimated coefficients are in accordance with that temperature.

It is, therefore, necessary to estimate the temperature of the material with a method that is immune to errors in *b-value*. Of course, one could use a temperature probing device, but this adds a level of complication, cost, and one is not always available.

It can be demonstrated that the ratio between the diffusion weighted images of two different materials, contained within the same housing, and at thermal equilibrium could be used to

estimate the temperature of the phantom, independent of the diffusion weighting (i.e. *b-value*).

Let the materials be labeled material 1 and material 2. The difference between the natural logarithm of the diffusion coefficients of the two materials using Equation 5.4 leads to

$$(C_2 - C_1)\left(\frac{1}{T} - \frac{1}{T_0}\right)^2 + (B_1 - B_2)\left(\frac{1}{T} - \frac{1}{T_0}\right) + \ln\left(\frac{D_{02}}{D_{01}}\frac{D_1}{D_2}\right) = 0$$

which is a quadratic equation with solution

$$\left(\frac{1}{T} - \frac{1}{T_0}\right) = \frac{(B_2 - B_1) \pm \sqrt{(B_1 - B_2)^2 - 4(C_2 - C_1)\ln\left(\frac{D_{02}}{D_{01}}\frac{D_1}{D_2}\right)}}{2(C_2 - C_1)}$$

Solving for T gives

$$T = \left(\frac{(B_2 - B_1) \pm \sqrt{(B_1 - B_2)^2 - 4(C_2 - C_1)\ln\left(\frac{D_{02}}{D_{01}}\frac{D_1}{D_2}\right)}}{2(C_2 - C_1)} + \frac{1}{T_0}\right)^{-1} \qquad \text{Equation 5.5}$$

where the quantity $\frac{D_1}{D_2}$ can be expressed in terms of Equation 5.3 as

$$\frac{D_1}{D_2} = \frac{-\frac{1}{b}\ln\left(\frac{S_{b,1}}{S_{b=0,1}}\right)}{-\frac{1}{b}\ln\left(\frac{S_{b,2}}{S_{b=0,2}}\right)}$$

Assuming uniform *b-value* in the region occupied by the two materials, the quantity $\left(-\frac{1}{b}\right)$ cancels out. This allows for estimating the temperature simply from the non-diffusion and diffusion weighted images (i.e. $S_{b=0}, S_b$) of the two materials independent of *b-value*.

5.3.2 Materials

We selected 4 of the liquids investigated in Tofts, et al. (2000): n-tridecane, n-undecane, n-decane, n-octane. These cover a range of diffusivities at room temperature that are typically observed in brain tissue. The liquids were purchased from Sigma Aldrich (MilliPore Sigma, St. Louis, MO, USA). All were high purity and required no further preparation other than transfer to individual clear glass 30 mL vials for imaging. The vials with the materials were placed in a container with openings at various locations for water to flow through the container and between/around the vials Figure 5.3(B), which itself would be placed inside a backwater PVC valve as is described next.

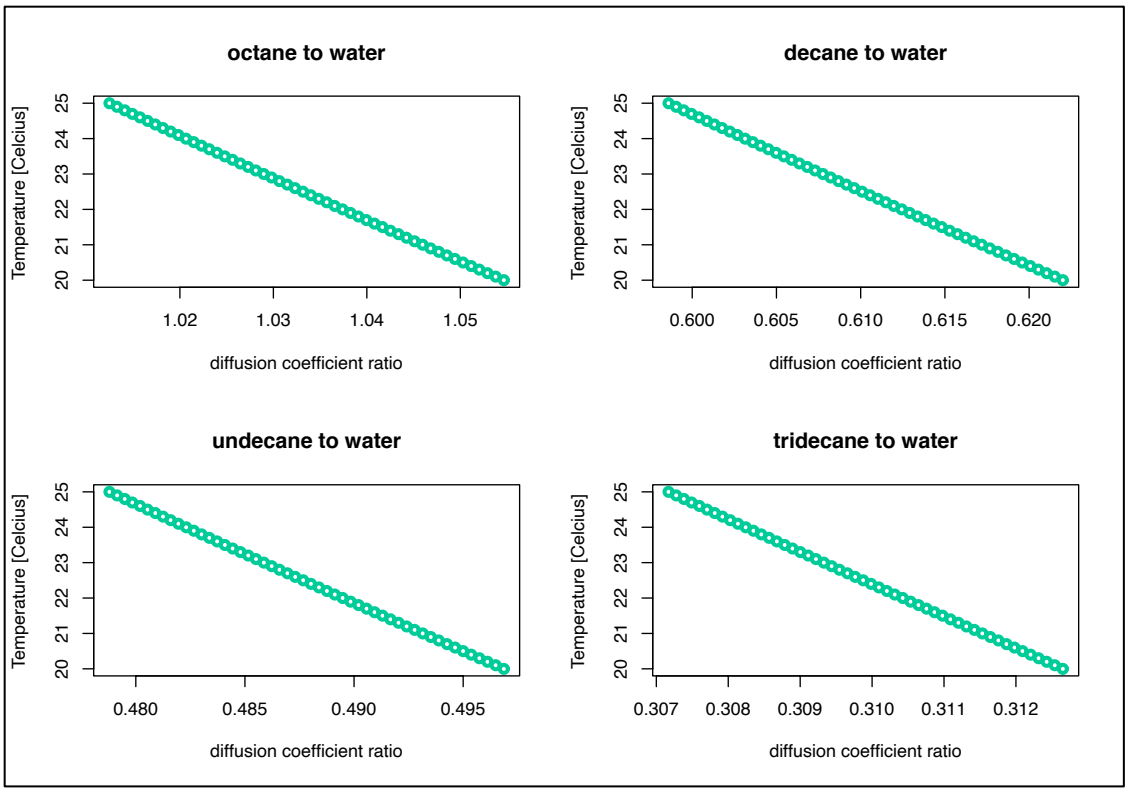

Figure 5.2 Sensitivity of Temperature to ratio of diffusion coefficients between water and each of the chosen liquids for the analysis.

5.3.3 Temperature control and monitoring set-up

A temperature control system was constructed with the purpose of scanning the materials under controlled temperature settings (Figure 5.3). This included circulating water through a closed circuit constructed from high temperature hose and a PVC back-water valve. The back-water valve was chosen as the housing where the perforated container with the vials would be placed for scanning. Water was circulated at high speed through the circuit using a 0.5 hp submersible pump submerged in a reservoir of water. The reservoir and the pump would be placed in the scanner control room. The temperature of the water in the reservoir was controlled by a submersible temperature controlled cooking device. The temperature of the water in the reservoir and in the back-water valve was monitored with an MR-safe fiberoptic temperature probe (Figure 5.3(B)(D)(E)).

Figure 5.3 Temperature control system and monitoring. A) Backwater PVC valve used for housing the vials in the head coil for scanning, connected at two ends to high temperature hose for circulating water from and back to a reservoir in the control room. B) Vials with liquids in perforated plastic container placed inside the backwater valve; yellow fibers are the MR safe temperature probe leads for monitoring the temperature inside the housing. C) Sum pump used to circulate water through the backwater valve housing. D) and E) Digital reading system for temperature probe.

5.3.4 Imaging protocol

The imaging protocol was set equal to the one used in collecting human scans for the TBI study outlined in the previous chapter. Diffusion tensor imaging was performed with a single-shot spin-echo echo-planar imaging pulse sequence. The protocol prescription was 2D sagittal images, a 96x96 matrix, 240 mm FOV, 64 slices, 2.5 mm isotropic resolution, phase encoding in Anterior/Posterior direction, parallel acquisition with a geometric reduction factor of 2. Diffusion settings included diffusion encoding along 64 non-collinear directions with b-value of 1300 s/mm^2, 8 volumes with no diffusion weighting (b=0). TR/TE was 8500/minimum ms.

5.4 Results

Before scanning the vials in the back-water valve with the temperature control system, a pilot scan of 4 vials with the selected liquids placed in a water bath was conducted in order to assess the amount of signal detected by the scanner. This was done with the liquids in the water bath at room temperature.

During this scan, it was discovered that the resonant frequency band was wide and instead of a single center frequency peak there appeared to exist multiple peaks. Thus, the scanner was having trouble tuning to the frequency of water protons in the water bath and other prominent frequency peaks from the protons in the liquids, which were discovered to be closer to that of fat protons. This phenomenon was attributed to the hydrocarbons present in the materials, which are categorized as n-alkanes. As a result, scanning the liquid vials in the water bath produced no usable images. This issue was resolved by placing the vials in a jar of coconut oil (Figure 5.4).

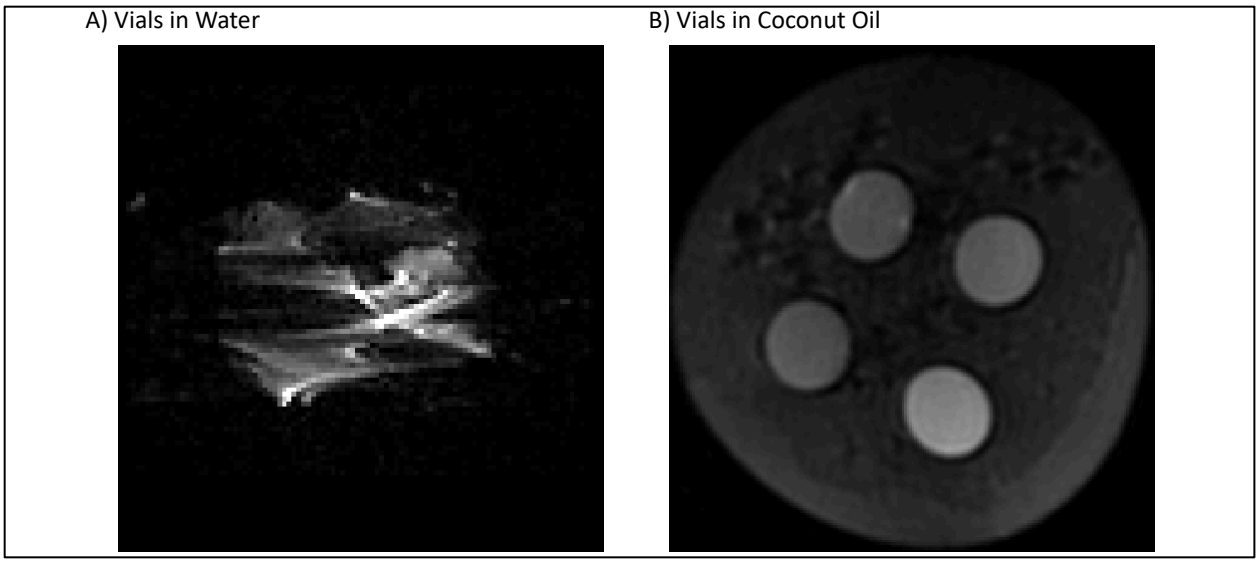

Figure 5.4 Example b0 images from scanning the vials in water A) and in coconut oil B).

Once usable images were produced with the vials in the coconut oil, another pilot scan was run. Analysis of this scan revealed a more serious problem, which proved difficult to resolve. Figure 5.5(A) shows the diffusion coefficients estimated for each the 64 diffusion weighted volumes, averaged over a region placed close to the center of each vial. The observed variability of the diffusion coefficients is likely due to convection currents generated from the very strong diffusion gradients that result in table vibrations.

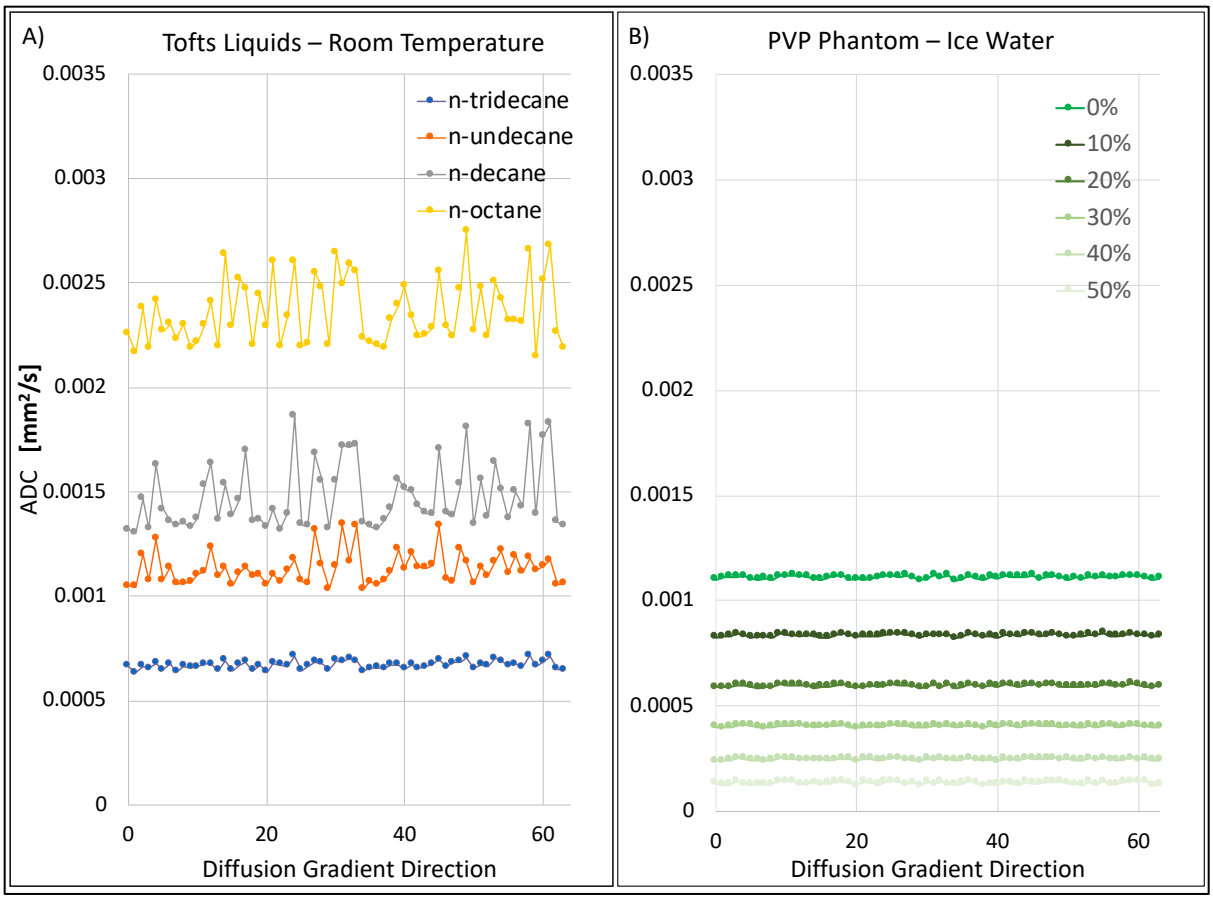

Figure 5.5 Diffusion coefficients from the scanned liquids (A) and the PVP phantom (B) as a function of diffusion gradient direction.

The visually discernable correspondence in the shape of the variability profiles with respect to diffusion encoding gradient direction is consistent with the hypothesis that the variability is related to vibrations linked to the diffusion gradients. This suspicion is also conveyed by the dark and bright regions observed within a single vial diffusion weighted images at different diffusion encoding directions observed in Figure 5.6.

It would be expected that vibration-related convection currents would find it more difficult to take form in more viscous materials. This is supported by the evident decrease in variability for the more viscous material n-tridecane compared to the less viscous liquid n-octane in Figure 5.5(A). For comparison, the vials in the PVP phantom are gelled solutions and it would be

expected that convection currents due to gradient induced vibrations could not form in these vials. This is confirmed by a striking consistency of ADC as a function of diffusion encoding direction for vials in the PVP phantom (Figure 5.5(B)).

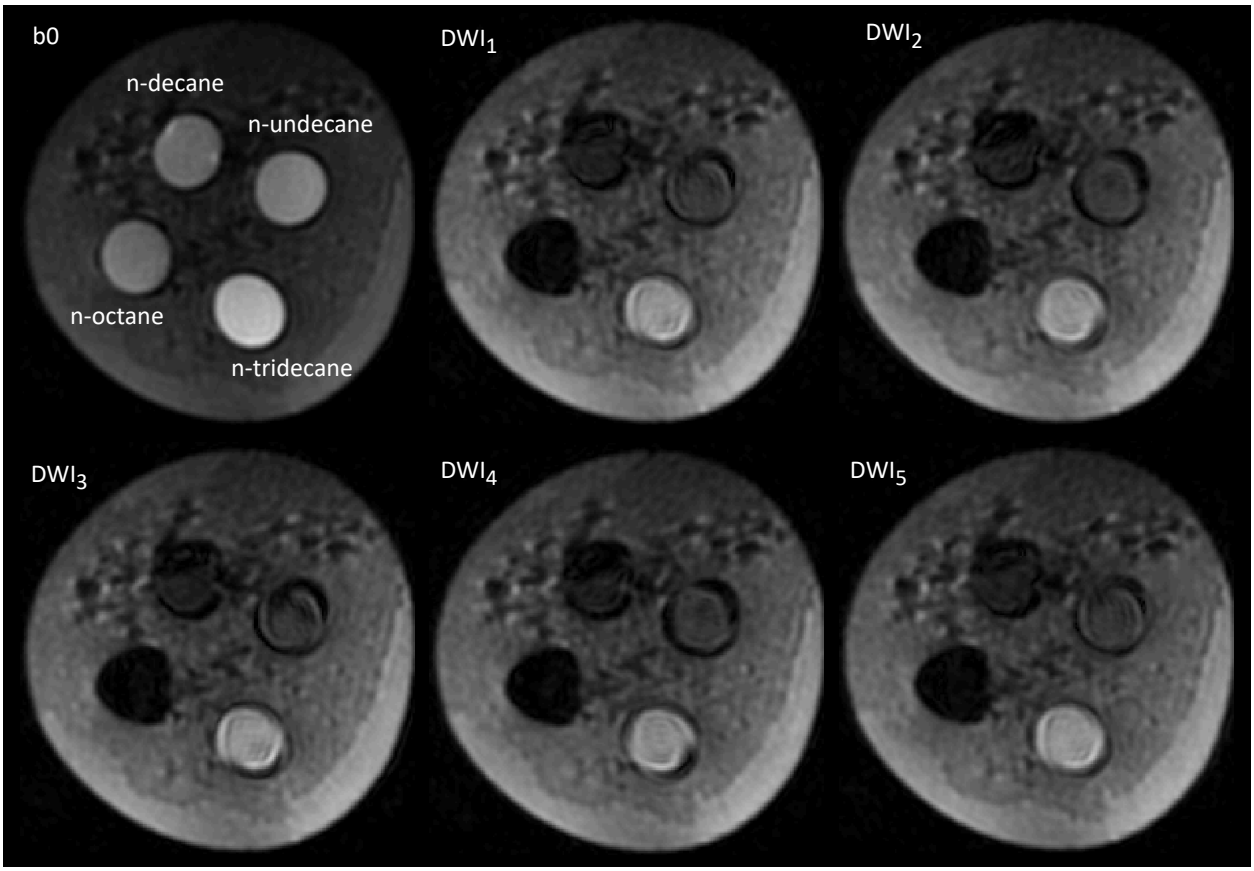

Figure 5.6 Example b0 and diffusion-weighted images for 5 directions of the diffusion gradients. Note the shading in the vials for the diffusion-weighted images due convection currents generated by vibrations in the table from the strong diffusion gradients. Ideally the brightness in the images would be homogeneous throughout each vial and consistent between diffusion directions since these are isotropic media.

Another scan with the phantom placed in an ice-water bath overnight shows the variability in ADC surprisingly increases compared to the scan conducted at room temperature (Figure 5.7). A signal-to-noise ratio (SNR) analysis using the non-diffusion data shows no drop in SNR for the

ice-water-bath run. On the contrary, the variance for the ice-water scan appears to decrease, which is consistent with a reduction in thermal noise due to a temperature drop.

A change in consistency could help explain the increase in variability observed when cooling the oil-phantom. At room temperature, the coconut oil surrounding the vials has a gel-like consistency. After several ours in an ice-water bath, the oil hardens and feels more like the solid wax in a candle. The gel-like state of the coconut oil at room temperature may help in dissipating, to some degree, the vibrations before they arrive to the vials suspended within it. On the other hand, because waves travel faster in solids, the solidified cold coconut oil is more efficient at transferring the vibrational energy to the liquids within the vials.

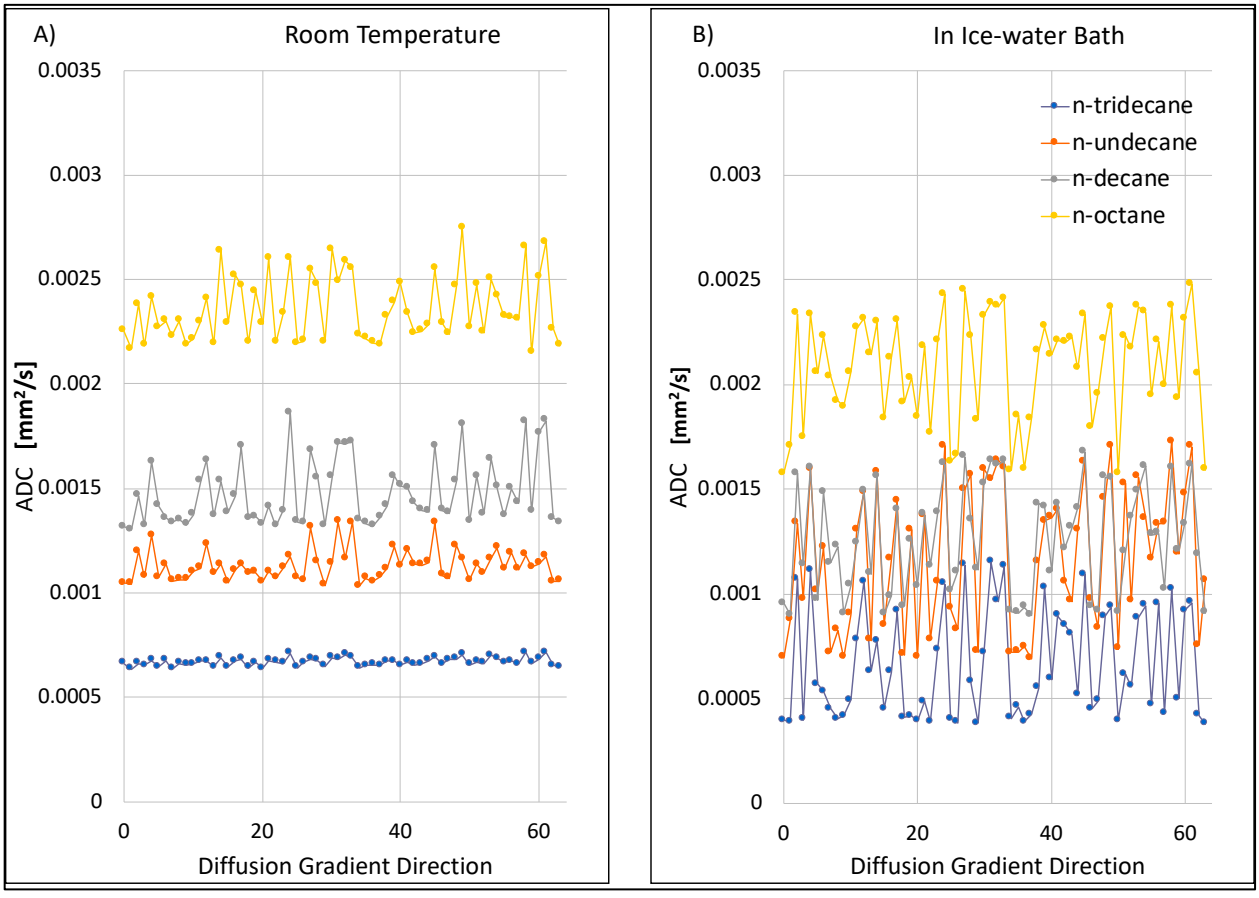

Figure 5.7 Diffusion coefficients from the scanned liquids at room temperature (A) and after being placed in an ice-water bath overnight (B) as a function of diffusion gradient direction.

Despite the presence of vibrational artifacts, it was possible to use the minimum ADC from each scan to test the proposed method, albeit with limited confidence. This yielded mixed results. In some cases, the estimated temperature came close to that measured with the MR-safe temperature probe. In most cases, however, the temperature estimates fluctuate considerably consistent with variability of the ADC estimates.

5.5 Discussion

This work proposes a method for using *known* diffusion-temperature relationships between a pair of materials at thermal equilibrium in estimating their temperature from diffusion weighted images independent of *b-value*. The expectation being that by knowing their temperature at the time of the scan, the diffusion-temperature models for the materials could be used in checking for consistency of diffusion estimates across different scans.

While significant progress was made in the theory behind the proposed method and in manufacturing of the phantom as well as in the temperature control system, difficulties related to artifacts in the diffusion weighted images caused by vibrational motion from the strong diffusion gradients prevented a successful development of the framework.

In order to help gain more insight into the problem, two experiments were implemented in attempts to reduce vibration in the liquids. One of the experiments involved placing a 70-pound sand box on the scanner table in order to dampen bulk table vibrations. The other experiment consisted of placing cotton balls in water vials in order to introduce some structure that could help disrupt vibration-related convection currents.

Three scans were acquired: one without the sand box, one with the sand box in the scanner-bore proximal to the head coil, and one with the sand box outside the scanner bore placed at the most distal end of the table.

These were done using DI water only vials, since the liquids tested earlier are corrosive to plastics and would likely dissolve cotton. Two vials were filled with water, one vial contained water plus lightly packed cotton balls, and a fourth vial contained water plus tightly packed cotton balls. The vials were prepared the night before scanning in order for the cotton to absorb as much water as possible.

The results from these scans are shown in Figure 5.8. Surprisingly, the variability D with respect to diffusion gradients appears to increase for the scans with the sandbox. The variability also appears to be higher for the scan with the box placed inside. One plausible explanation for this may be that the weight is only changing the mode of vibration of the table but not its amplitude. Thus, a more uniform distribution of weight on the table may be necessary.

On the other hand, the lightly packed cotton does seem to have positive impact in reducing variability of the ADC with respect to the diffusion encoding direction. However, a reduction in the ADC magnitude of water in this vial is also evident. Thus, this type of solution would not be ideal for use with the proposed liquids.

The variability in the vial with the tightly packed cotton is higher. This is likely linked to the presence of air pockets within the vial as a result of the compression of the cotton pushing water out, which creates signal voids. Additionally, the tightly packed cotton fibers introduce a

more anisotropic environment for the diffusing water molecules. Thus, diffusion would be higher along certain directions compared to others.

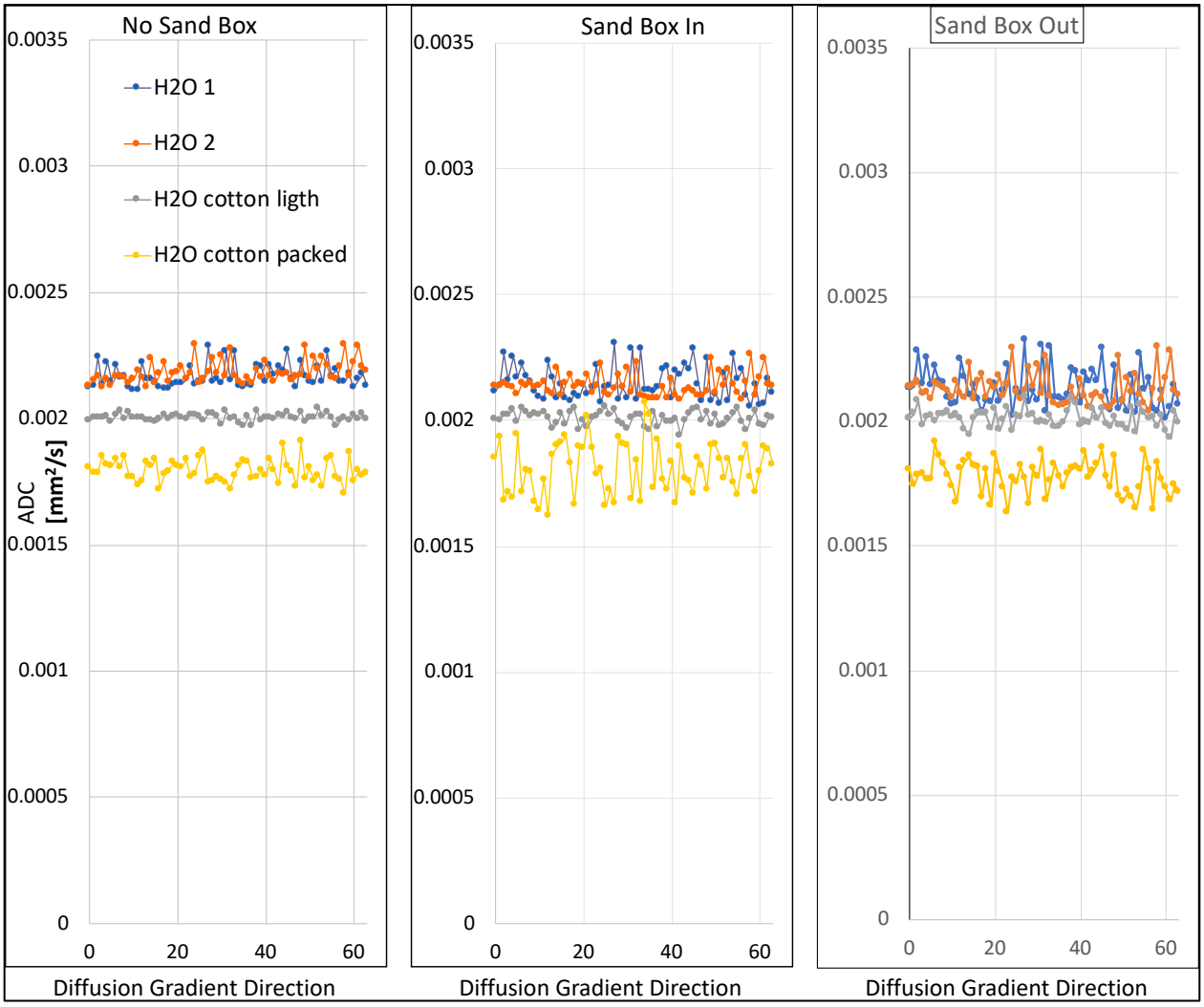

Figure 5.8 Diffusion coefficients of water as a function of direction of the diffusion gradients. Two vials were simply filled with DI water, one vial was filled with water and lightly packed cotton balls, and one vial filled with water and tightly packed cotton balls. Left plot shows results from scan with no additional weight on the scanner table. Middle plot shows results from scan with sand box on table next to head coil. Right plot shows results from scan with sand box place at feet of scanner table.

Although the hurdles were considerable, the analyses and the lessons learned up to this point provide insightful rationale for future work in this project. For example, in getting to the root cause of the problem it would be worth de-rating the diffusion gradients to generate smoother

switching of currents in the coils for creating less vibration of the table. Additionally, other materials (e.g. high viscosity, gels) can be explored. For example, Wagner et al. (2017) [174] have published a similar analysis as that in Tofts et al. (2000) but for varying concentrations of PVP. This could potentially be used with the HPD PVP phantom in hand. Though, it is unclear how well matched the PVP powder that used in the manufacturing of the HPD PVP phantom is to that used in Wagner et al. (2017), in terms of characteristics such as molecular weight. It is worth noting that using high purity liquids like the ones discussed in Tofts et. al (2000) is very appealing due to ease of use in not having to do any additional processing to them after purchase.

Chapter 6 - Concluding Remarks

6.1 Contributions, future work, and lessons learned

This work has outlined specific projects that augment to the field of diffusion MRI regarding topics of biophysical modeling, single-subject tissue microstructure analyses, and diffusion coefficient validation.

At this stage in the field, and really for much of its existence, there is no question that the diffusion-weighted MRI signal conveys information about a material's microstructure. In complex media such as brain tissue, many physiological factors intermingle in the process of molecular water self-diffusion. The question of what the signal means in this case is a difficult one to answer, to say the least. In answering the question, biophysical models remain a powerful tool in the arsenal that the researcher has. But extracting useful information from biophysical models is contingent on the strength of the assumptions made, which are often a fundamental necessity for creating a working framework that is able to converge to a set of biologically sound parameter estimates.

The rapid uptake of NODDI by researchers can be related to its ability in providing parameters that made biological sense and addressed some of the well-known shortcomings of DTI. All this with a model that is simple enough to require an imaging protocol that can be performed in minutes on a clinical scanner. Yet, questions about weaknesses in the model assumptions began to surface in the years that followed. However, no formal inquiries were conducted regarding the assumption of fixed parallel diffusivity. The work presented in Chapter 3 represents to my knowledge the most extensive and formal investigation of this assumption.

The key findings provide a sound reference for trusting the model performance in adult white matter with the original intrinsic diffusivity setting, while providing evidence that in gray matter and in the infant brain this value should be adjusted for optimal performance. Potential future work will consider a similar analysis that includes data with known pathology, ex-vivo samples, small animal, and non-human primates.

The group-level approach for analysis of diffusion-based neuroimaging measures is most effective when considering microstructure changes expected to be spatially consistent across subjects. In conditions such as traumatic brain injury, a single-subject approach is better suited to identify changes whose location in the brain varies from subject to subject. The individual-level analyses framework presented in Chapter 4 offers the ability to focus on a specific region (a streamlines bundle) when it is expected *a priori* that changes are located in that region. Yet, it goes one step further by allowing to locate the spatial distribution of changes within (along) the tract. Conversely, if no specific bundle needs to be inspected, the analysis can be performed on any number of white matter regions simultaneously. All this, while still allowing to conduct a number of tests that is orders of magnitude less than that in a voxel-wise comparison.

While using profiles of metrics along a tract is a technique developed an used by others in comparing groups to one another, the work presented here explicitly set out to use the existing tractometry scaffold and develop a multivariate technique for single-subject analysis complete with a statistical definition of abnormality and image co-registration. These, I believe, are the key contributions of this work.

Finally, the development of a diffusion-based phantom fell short of fruition, unfortunately. Nonetheless, substantial progress was made, and I am confident that the method will work if mechanical vibration associated with the diffusion gradients can be reduced. Two possible solutions will be pursued. One that deals with the root cause of vibration, which are the strong diffusion gradients, and one which deals with preventing vibration-related motion in the materials even when vibration in the table is present.

Artifacts related to diffusion gradient-induced vibrations have been explored elsewhere [175]. Recommendations for helping to reduce vibrations include adjusting imaging parameters such as the magnitude of the *b-value* and modifying the gradient wave forms. Eddy current compensation gradients alongside the use high b-values (>1000 s/mm^2) were observed to worsen mechanical vibrations in the scanner table. Dependence on specific directions (e.g. z-direction along the magnet's bore) were also seen. Therefore, a careful imaging protocol design that takes these three factors into account will be explored. For example, one acquisition scheme could include lower b-value (500 to 800 s/mm^2) without eddy current compensation gradients and correct for eddy current related artifacts in the postprocessing of the data. Strategies that specifically target shapes of the diffusion gradient currents such as those used in vibration-related acoustic noise reduction EPI sequences [176], [177] will also be explored.

The n-alkanes are non-soluble in water. From previous discussions with other researchers in our program, water trapped in an agar-based gel exhibits diffusion coefficients measured with dMRI that are similar as those of free water. Therefore, an emulsion of the n-alkanes with water, which has been achieved elsewhere [178], [179], but suspended in an agar-based gel

could be made in order to prevent the vibration related convection currents that lead to the observed artifacts.

Another solution would be to mechanically de-couple the phantoms from the scanner. This could be achieved by designing an MR-safe frame (e.g. made of wood or PVC pipe) attached to the floor and that can support the phantom in the head-coil inside the scanner board.

Finally, I believe the method still represents a potentially novel approach to estimate the phantom temperature from the diffusion weighted images that is also independent of *b-value*.

While much of the work presented here is in-line with what was contained in the original proposal, some departures did occur and unexpected roadblocks were found. One of the most valuable lessons from this process, was learning to recognize when to pivot from one idea that initially seemed promising into a related but better suited one. A good example is the multi-variate analysis method. This method was inspired by previous work in our lab [140] that conducted a multivariate analysis using the Mahalanobis distance, which was computed using DTI scalar metrics averaged over several white matter regions. In an attempt to get better spatial specificity, the original proposal for the work described in Chapter 4 consisted of a voxel-wise multivariate comparison. Work done over several months exposed two important limitations well-chronicled of the voxel-wise approach: stringent requirements for inter-subject image alignment and an exceedingly large number of multiple comparisons. Extensive work was done for improving co-registration of the data, evaluating the performance of a number of algorithms. However, I was not satisfied with the alignment results.

Then I came across a publication in 2018 [180] that made use of tractometry and carried out a principal component analysis to identify the minimum number of variables that would suffice to explain variability in multidimensional data. I recognized that the basic tractometry framework in that publication could be used to carry out the multivariate analysis that we had originally proposed. Of course, we later improved it by adding an inter-subject data alignment step, but the method is still more forgiving to small alignment errors than the originally proposed voxel-wise approach. And as mentioned earlier, the number of statistical tests is also dramatically reduced.

References

[1] R. Brown, “A brief account of microscopical observations on the particles contained in the pollen of plants: And of the general existence of active molecules in organic and inorganic bodies.,” *Edinb. New Philos. J.*, vol. 4(July-Septmber), pp. 358–71, 1828.

[2] T. A. Gallagher, A. L. Alexander, and A. S. Field, “Diffusion Tensor Magnetic Resonance Imaging: Physical Principles,” in *Functional Neuroradiology*, S. H. Faro, F. B. Mohamed, M. Law, and J. T. Ulmer, Eds. Boston, MA: Springer US, 2011, pp. 709–729.

[3] A. Einstein, *Investigations on the Theory of the Brownian Movement.* New York: Courier Corporation.

[4] F. Bloch, “Nuclear Induction,” *Phys. Rev.*, vol. 70, no. 7–8, pp. 460–474, Oct. 1946, doi: 10.1103/PhysRev.70.460.

[5] F. Bloch, W. W. Hansen, and M. Packard, “Nuclear Induction,” *Phys. Rev.*, vol. 69, no. 3–4, pp. 127–127, Feb. 1946, doi: 10.1103/PhysRev.69.127.

[6] E. M. Purcell, H. C. Torrey, and R. V. Pound, “Resonance Absorption by Nuclear Magnetic Moments in a Solid,” *Phys. Rev.*, vol. 69, no. 1–2, pp. 37–38, Jan. 1946, doi: 10.1103/PhysRev.69.37.

[7] E. L. Hahn, “Spin Echoes,” *Phys. Rev.*, vol. 80, no. 4, pp. 580–594, Nov. 1950, doi: 10.1103/PhysRev.80.580.

[8] H. Y. Carr and E. M. Purcell, “Effects of Diffusion on Free Precession in Nuclear Magnetic Resonance Experiments,” *Phys. Rev.*, vol. 94, no. 3, pp. 630–638, May 1954, doi: 10.1103/PhysRev.94.630.

[9] H. C. Torrey, “Bloch Equations with Diffusion Terms,” *Phys. Rev.*, vol. 104, no. 3, pp. 563–565, Nov. 1956, doi: 10.1103/PhysRev.104.563.

[10] E. O. Stejskal and J. E. Tanner, “Spin Diffusion Measurements: Spin Echoes in the Presence of a Time-Dependent Field Gradient,” *J. Chem. Phys.*, vol. 42, no. 1, pp. 288–292, Jan. 1965, doi: 10.1063/1.1695690.

[11] P. C. Lauterbur, “Image Formation by Induced Local Interactions: Examples Employing Nuclear Magnetic Resonance,” *Nature*, vol. 242, no. 5394, pp. 190–191, Mar. 1973, doi: 10.1038/242190a0.

[12] P. Mansfield and P. K. Grannell, “NMR ‘diffraction’ in solids?,” *J. Phys. C Solid State Phys.*, vol. 6, no. 22, pp. L422–L426, Nov. 1973, doi: 10.1088/0022-3719/6/22/007.

[13] A. Kumar, D. Welti, and R. R. Ernst, “NMR Fourier zeugmatography,” *J. Magn. Reson. 1969*, vol. 18, no. 1, pp. 69–83, Apr. 1975, doi: 10.1016/0022-2364(75)90224-3.

[14] W. A. Edelstein, J. M. S. Hutchison, G. Johnson, and T. Redpath, “Spin warp NMR imaging and applications to human whole-body imaging,” *Phys. Med. Biol.*, vol. 25, no. 4, pp. 751–756, Jul. 1980, doi: 10.1088/0031-9155/25/4/017.

[15] P. Mansfield, “Multi-planar image formation using NMR spin echoes,” *J. Phys. C Solid State Phys.*, vol. 10, no. 3, pp. L55–L58, Feb. 1977, doi: 10.1088/0022-3719/10/3/004.

[16] P. Mansfield, “REAL-TIME ECHO-PLANAR IMAGING BY NMR,” *Br. Med. Bull.*, vol. 40, no. 2, pp. 187–190, 1984, doi: 10.1093/oxfordjournals.bmb.a071970.

[17] R. Rzedzian and I. Pykett, “Instant images of the human heart using a new, whole-body MR imaging system,” *Am. J. Roentgenol.*, vol. 149, no. 2, pp. 245–250, Aug. 1987, doi: 10.2214/ajr.149.2.245.

[18] D. G. Taylor and M. C. Bushell, “The spatial mapping of translational diffusion coefficients by the NMR imaging technique,” *Phys. Med. Biol.*, vol. 30, no. 4, pp. 345–349, Apr. 1985, doi: 10.1088/0031-9155/30/4/009.

[19] D. Le Bihan, E. Breton, D. Lallemand, P. Grenier, E. Cabanis, and M. Laval-Jeantet, “MR imaging of intravoxel incoherent motions: application to diffusion and perfusion in neurologic disorders.,” *Radiology*, vol. 161, no. 2, pp. 401–407, Nov. 1986, doi: 10.1148/radiology.161.2.3763909.

[20] A. L. Alexander, J. E. Lee, M. Lazar, and A. S. Field, “Diffusion tensor imaging of the brain,” *Neurother. J. Am. Soc. Exp. Neurother.*, vol. 4, no. 3, pp. 316–329, Jul. 2007, doi: 10.1016/j.nurt.2007.05.011.

[21] M. E. Moseley, Y. Cohen, and J. Kucharczyk, *Diffusion-weighted MR imaging of anisotropic water diffusion in cat central nervous system*, vol. 176. Radiology, 1990.

[22] M. E. Moseley, J. Kucharczyk, H. S. Asgari, and D. Norman, “Anisotropy in diffusion weighted MRI,” *Magn Reson Med*, 1991.

[23] C. Beaulieu and P. S. Allen, “Water diffusion in the giant axon of the squid: implications for diffusion-weighted MRI of the nervous system,” *Magn Reson Med*, vol. 1994, no. 32, pp. 579–583.

[24] C. Beaulieu and P. S. Allen, “Determinants of anisotropic water diffusion in nerves,” *Magn Reson Med*, vol. 31, pp. 394–400, 1994.

[25] C. Beaulieu, “The basis of anisotropic water diffusion in the nervous system– a technical review,” in *NMR in Biomedicine 2002*, vol. 15, pp. 435–455.

[26] D. K. Jones, “Studying connections in the living human brain with diffusion MRI,” *Cortex*, vol. 2008, no. 44, pp. 936–952.

[27] P. J. Basser, J. Mattiello, and D. LeBihan, “Estimation of the effective self-diffusion tensor from the NMR spin echo,” *J. Magn. Reson. Imaging*, pp. 103–247, 1994.

[28] B. J. Jellison, A. S. Field, J. Medow, M. M. Lazar, S. Salamat, and A. L. Alexander, “Diffusion Tensor Imaging of Cerebral WhiteMatter: A Pictorial Review of Physics, Fiber Tract Anatomy, and Tumor Imaging Patterns,” *AJNR Am J Neuroradiol*, vol. 25, pp. 356–369.

[29] A. L. Alexander, J. E. Lee, M. Lazar, and A. S. Field, “Diffusion Tensor Imaging of the Brain,” *Neurotherapeutics*, vol. 2007, no. 4, pp. 316–329.

[30] P. Mukherjee, S. W. Chung, J. I. Berman, C. P. Hess, and R. G. Henry, “Diffusion Tensor MR Imaging and Fiber Tractography: Theoretic Underpinnings,” *AJNR Am J Neuroradiol*, vol. 29, pp. 632–41.

[31] L. B. D, M. JF, and P. C, “Diffusion Tensor Imaging: Concepts and Applications,” *J. Magn. Reson. Imaging*, vol. 13, pp. 534–546, 2001.

[32] P. Mukherjee, S. W. Chung, J. I. Berman, C. P. Hess, and R. G. Henry, “Diffusion Tensor MR Imaging and Fiber Tractography: Technical Considerations,” *AJNR Am J Neuroradiol*, vol. 29, pp. 842–52.

[33] A. L. Alexander and J. S. Tsuruda, *Parker DL. Elimination of eddy current artifacts in diffusion-weighted echo-planar images: the use of bipolar gradients*. Magn.

[34] K. Setsompop *et al.*, “Improving diffusion MRI using simultaneous multi-slice echo planar imaging,” *NeuroImage*, vol. 63, no. 1, pp. 569–580, Oct. 2012, doi: 10.1016/j.neuroimage.2012.06.033.

[35] P. J. Basser and S. Pajevic, “Statistical artifacts in Diffusion Tensor MRI (DT-MRI) Caused by Background Noise,” in *Magnetic Resonance in Medicine*, vol. 44, 2000, pp. 41–50.

[36] K. M. Hasan and D. L. Parker, “Alexander AL. Comparison of gradient encoding schemes for diffusion-tensor MRI,” *J Magn Reson Imaging*, vol. 13, pp. 769–80.

[37] D. K. Jones, “The effect of gradient sampling schemes on measures derived from the diffusion tensor MRI: a Monte Carlo study,” *Magn Reson Med*, vol. 51, pp. 807–15.

[38] C. F. Westin, S. Peled, H. Gudbjartsson, R. Kikinis, and F. A. Jolesz, “Geometrical diffusion measures for MRI from tensor basis analysis,” in *ISMRM ’97. Vancouver*, Canada, 1997.

[39] S. Pajevic and C. Pierpaoli, *Color schemes to represent the orientation of anisotropic tissues from diffusion tensor data: application to white matter fiber tract mappingin the human brain. Magn Reson Med*, vol. 42. 1999.

[40] P. J. Basser and C. Pierpaoli, “Microstructural and physiological features of tissue elucidated by quantitative-diffusion-tensor MRI,” *J. Magn. Reson.*, pp. 111–209, 1996.

[41] S. Mori and B. J. Crain, *Chacko VP, van Zijl PCM.Three-dimensional tracking of axonal projections in the brain by magnetic resonance imaging*, vol. 45. Ann Neurol, 1999.

[42] T. E. Conturo, N. F. Lori, and T. S. Cull, “Tracking neuronal fiber pathways,” in *the living human brain. Proc Natl Acad Sci USA*, 1999.

[43] A. S. Field, “Diffusion tensor imaging at the crossroads: Fiber Tracking Meets Tissue Characterization in Brain Tumors,” *AJNR AM J Neuroradiol*, vol. 2005, no. 26, pp. 2168–2169.

[44] J. H. Jensen, J. A. Helpern, A. Ramani, H. Lu, and K. Kaczynski, “Diffusional kurtosis imaging: The quantification of non-gaussian water diffusion by means of magnetic resonance imaging,” *Magn. Reson. Med.*, vol. 53, no. 6, pp. 1432–1440, Jun. 2005, doi: 10.1002/mrm.20508.

[45] E. Fieremans, J. H. Jensen, and J. A. Helpern, “White matter characterization with diffusional kurtosis imaging,” *NeuroImage*, vol. 58, no. 1, pp. 177–188, Sep. 2011, doi: 10.1016/j.neuroimage.2011.06.006.

[46] S. Van Cauter *et al.*, “Gliomas: Diffusion Kurtosis MR Imaging in Grading,” *Radiology*, vol. 263, no. 2, pp. 492–501, May 2012, doi: 10.1148/radiol.12110927.

[47] Y. Bai *et al.*, “Grading of Gliomas by Using Monoexponential, Biexponential, and Stretched Exponential Diffusion-weighted MR Imaging and Diffusion Kurtosis MR Imaging,” *Radiology*, vol. 278, no. 2, pp. 496–504, Feb. 2016, doi: 10.1148/radiol.2015142173.

[48] P. Raab, E. Hattingen, K. Franz, F. E. Zanella, and H. Lanfermann, “Cerebral Gliomas: Diffusional Kurtosis Imaging Analysis of Microstructural Differences,” *Radiology*, vol. 254, no. 3, pp. 876–881, Mar. 2010, doi: 10.1148/radiol.09090819.

[49] E. S. Hui *et al.*, “Stroke Assessment With Diffusional Kurtosis Imaging,” *Stroke*, vol. 43, no. 11, pp. 2968–2973, Nov. 2012, doi: 10.1161/STROKEAHA.112.657742.

[50] R. A. Weber *et al.*, “Diffusional Kurtosis and Diffusion Tensor Imaging Reveal Different Time-Sensitive Stroke-Induced Microstructural Changes,” *Stroke*, vol. 46, no. 2, pp. 545–550, Feb. 2015, doi: 10.1161/STROKEAHA.114.006782.

[51] J. S. Cheung, E. Wang, E. H. Lo, and P. Z. Sun, “Stratification of Heterogeneous Diffusion MRI Ischemic Lesion With Kurtosis Imaging: Evaluation of Mean Diffusion and Kurtosis MRI Mismatch in an Animal Model of Transient Focal Ischemia,” *Stroke*, vol. 43, no. 8, pp. 2252–2254, Aug. 2012, doi: 10.1161/STROKEAHA.112.661926.

[52] M. F. Falangola *et al.*, “Non-Gaussian diffusion MRI assessment of brain microstructure in mild cognitive impairment and Alzheimer’s disease,” *Magn. Reson. Imaging*, vol. 31, no. 6, pp. 840–846, Jul. 2013, doi: 10.1016/j.mri.2013.02.008.

[53] N.-J. Gong, C.-S. Wong, C.-C. Chan, L.-M. Leung, and Y.-C. Chu, “Correlations between microstructural alterations and severity of cognitive deficiency in Alzheimer’s disease and mild cognitive impairment: a diffusional kurtosis imaging study,” *Magn. Reson. Imaging*, vol. 31, no. 5, pp. 688–694, Jun. 2013, doi: 10.1016/j.mri.2012.10.027.

[54] M. Yoshida *et al.*, “Diffusional kurtosis imaging of normal-appearing white matter in multiple sclerosis: preliminary clinical experience,” *Jpn. J. Radiol.*, vol. 31, no. 1, pp. 50–55, Jan. 2013, doi: 10.1007/s11604-012-0147-7.

[55] C. Guglielmetti *et al.*, “Diffusion kurtosis imaging probes cortical alterations and white matter pathology following cuprizone induced demyelination and spontaneous remyelination,” *NeuroImage*, vol. 125, pp. 363–377, Jan. 2016, doi: 10.1016/j.neuroimage.2015.10.052.

[56] J. Zhuo *et al.*, “Diffusion kurtosis as an in vivo imaging marker for reactive astrogliosis in traumatic brain injury,” *NeuroImage*, vol. 59, no. 1, pp. 467–477, Jan. 2012, doi: 10.1016/j.neuroimage.2011.07.050.

[57] E. J. Grossman *et al.*, “Thalamus and Cognitive Impairment in Mild Traumatic Brain Injury: A Diffusional Kurtosis Imaging Study,” *J. Neurotrauma*, vol. 29, no. 13, pp. 2318–2327, Sep. 2012, doi: 10.1089/neu.2011.1763.

[58] E. J. Grossman *et al.*, “Cognitive Impairment in Mild Traumatic Brain Injury: A Longitudinal Diffusional Kurtosis and Perfusion Imaging Study,” *Am. J. Neuroradiol.*, vol. 34, no. 5, pp. 951–957, May 2013, doi: 10.3174/ajnr.A3358.

[59] E. T. Næss-Schmidt *et al.*, “Microstructural changes in the thalamus after mild traumatic brain injury: A longitudinal diffusion and mean kurtosis tensor MRI study,” *Brain Inj.*, vol. 31, no. 2, pp. 230–236, Jan. 2017, doi: 10.1080/02699052.2016.1229034.

[60] M. Schachter, M. D. Does, A. W. Anderson, and J. C. Gore, “Measurements of Restricted Diffusion Using an Oscillating Gradient Spin-Echo Sequence,” *J. Magn. Reson.*, vol. 147, no. 2, pp. 232–237, Dec. 2000, doi: 10.1006/jmre.2000.2203.

[61] E. C. Parsons, M. D. Does, and J. C. Gore, “Temporal diffusion spectroscopy: Theory and implementation in restricted systems using oscillating gradients,” *Magn. Reson. Med.*, vol. 55, no. 1, pp. 75–84, Jan. 2006, doi: 10.1002/mrm.20732.

[62] J. Xu *et al.*, “Influence of cell cycle phase on apparent diffusion coefficient in synchronized cells detected using temporal diffusion spectroscopy,” *Magn. Reson. Med.*, vol. 65, no. 4, pp. 920–926, Apr. 2011, doi: 10.1002/mrm.22704.

[63] O. Reynaud, K. V. Winters, D. M. Hoang, Y. Z. Wadghiri, D. S. Novikov, and S. G. Kim, "Pulsed and oscillating gradient MRI for assessment of cell size and extracellular space (POMACE) in mouse gliomas: Probing Tumor Microstructure with POMACE," *NMR Biomed.*, vol. 29, no. 10, pp. 1350–1363, Oct. 2016, doi: 10.1002/nbm.3577.

[64] H. Li, J. C. Gore, and J. Xu, "Fast and robust measurement of microstructural dimensions using temporal diffusion spectroscopy," *J. Magn. Reson.*, vol. 242, pp. 4–9, May 2014, doi: 10.1016/j.jmr.2014.02.007.

[65] M. Aggarwal, M. V. Jones, P. A. Calabresi, S. Mori, and J. Zhang, "Probing mouse brain microstructure using oscillating gradient diffusion MRI," *Magn. Reson. Med.*, vol. 67, no. 1, pp. 98–109, Jan. 2012, doi: 10.1002/mrm.22981.

[66] C. A. Baron and C. Beaulieu, "Oscillating gradient spin-echo (OGSE) diffusion tensor imaging of the human brain: OGSE DTI of the Human Brain," *Magn. Reson. Med.*, vol. 72, no. 3, pp. 726–736, Sep. 2014, doi: 10.1002/mrm.24987.

[67] C. Andica *et al.*, "Spatial Restriction within Intracranial Epidermoid Cysts Observed Using Short Diffusion-time Diffusion-weighted Imaging," *Magn. Reson. Med. Sci.*, vol. 17, no. 3, pp. 269–272, 2018, doi: 10.2463/mrms.cr.2017-0111.

[68] Y. Assaf and P. J. Basser, "Composite hindered and restricted model of diffusion (CHARMED) MR imaging of the human brain," *Neuroimage*, vol. 2005, no. 27, p. 58.

[69] H. Zhang, T. Schneider, C. A. Wheeler-Kingshott, and D. C. Alexander, "NODDI: practical in vivo neurite orientation dispersion and density imaging of the human brain," *NeuroImage*, vol. 61, no. 4, pp. 1000–1016, Jul. 2012, doi: 10.1016/j.neuroimage.2012.03.072.

[70] F. Grussu, T. Schneider, H. Zhang, D. C. Alexander, and C. A. M. Wheeler–Kingshott, "Neurite orientation dispersion and density imaging of the healthy cervical spinal cord in vivo," *NeuroImage*, vol. 111, pp. 590–601, May 2015, doi: 10.1016/j.neuroimage.2015.01.045.

[71] S. R. Cox *et al.*, "Ageing and brain white matter structure in 3,513 UK Biobank participants," *Nat. Commun.*, vol. 7, p. 13629, Dec. 2016, doi: 10.1038/ncomms13629.

[72] S. By, J. Xu, B. A. Box, F. R. Bagnato, and S. A. Smith, "Application and evaluation of NODDI in the cervical spinal cord of multiple sclerosis patients," *NeuroImage Clin.*, vol. 15, pp. 333–342, 2017, doi: 10.1016/j.nicl.2017.05.010.

[73] Q. Wen *et al.*, "Clinically feasible NODDI characterization of glioma using multiband EPI at 7 T," *NeuroImage Clin.*, vol. 9, pp. 291–299, 2015, doi: 10.1016/j.nicl.2015.08.017.

[74] T. Billiet *et al.*, "Characterizing the microstructural basis of 'unidentified bright objects' in neurofibromatosis type 1: A combined in vivo multicomponent T2 relaxation and multi-

shell diffusion MRI analysis," *NeuroImage Clin.*, vol. 4, pp. 649–658, 2014, doi: 10.1016/j.nicl.2014.04.005.

[75] T. Billiet *et al.*, "Age-related microstructural differences quantified using myelin water imaging and advanced diffusion MRI," *Neurobiol. Aging*, vol. 36, no. 6, pp. 2107–2121, Jun. 2015, doi: 10.1016/j.neurobiolaging.2015.02.029.

[76] E. Caverzasi *et al.*, "Neurite Orientation Dispersion and Density Imaging Color Maps to Characterize Brain Diffusion in Neurologic Disorders: NODDI Color Map," *J. Neuroimaging*, vol. 26, no. 5, pp. 494–498, Sep. 2016, doi: 10.1111/jon.12359.

[77] N. Colgan *et al.*, "Application of neurite orientation dispersion and density imaging (NODDI) to a tau pathology model of Alzheimer's disease," *NeuroImage*, vol. 125, pp. 739–744, Jan. 2016, doi: 10.1016/j.neuroimage.2015.10.043.

[78] K. Kamagata *et al.*, "Neurite orientation dispersion and density imaging in the substantia nigra in idiopathic Parkinson disease," *Eur. Radiol.*, vol. 26, no. 8, pp. 2567–2577, Aug. 2016, doi: 10.1007/s00330-015-4066-8.

[79] J. P. Owen *et al.*, "Aberrant White Matter Microstructure in Children with 16p11.2 Deletions," *J. Neurosci.*, vol. 34, no. 18, pp. 6214–6223, Apr. 2014, doi: 10.1523/JNEUROSCI.4495-13.2014.

[80] L. R. Frank, *Characterization of anisotropy in high angular resolution diffusion-weighted MRI. Magn Reson Med 2002:47;1083-1099*. .

[81] J.-D. Tournier, F. Calamante, and A. Connelly, "Robust determination of the fibre orientation distribution in diffusion MRI: non-negativity constrained super-resolved spherical deconvolution," *NeuroImage*, vol. 35, no. 4, pp. 1459–1472, May 2007, doi: 10.1016/j.neuroimage.2007.02.016.

[82] J.-D. Tournier, F. Calamante, D. G. Gadian, and A. Connelly, "Direct estimation of the fiber orientation density function from diffusion-weighted MRI data using spherical deconvolution," *NeuroImage*, vol. 23, no. 3, pp. 1176–1185, Nov. 2004, doi: 10.1016/j.neuroimage.2004.07.037.

[83] P. Hagmann, L. Jonasson, and P. Maeder, *Thiran JP, Wedeen VJ, Meuli R. Understanding Diffusion MR Imaging Techniques: From Scalar Diffusion-weighted Imaging to Diffusion Tensor Imaging and Beyond. RadioGraphics*, vol. 26. 2006.

[84] D. S. Tuch, *Reese TG, Wiegell MR, Wedeen VJ. Diffusion MRI of Complex Neural Architecture. Neuron 2003*, vol. 40. .

[85] V. J. Wedeen and P. Hagmann, "Tseng WY, Reese TG, Weisskoff RM. Mapping complex tissue architecture with diffusion spectrum magnetic resonance imaging," *Magn Reson Med*, vol. 54, pp. 1377–1386.

[86] V. J. Wedeen *et al.*, “Arceuil HD, de Crespigny AJ. Diffusion Spectrum Magnetic Resonance Imaging (DSI) tractography of crossing fibers,” *NeuroImage2008*, vol. 41, pp. 1267–1277.

[87] D. S. Tuch, *qBall imaging. Magnetic Resonance in Medicine 2004*, vol. 52. .

[88] M. A. Griswold *et al.*, “Generalized autocalibrating partially parallel acquisitions (GRAPPA),” *Magn. Reson. Med.*, vol. 47, no. 6, pp. 1202–1210, Jun. 2002, doi: 10.1002/mrm.10171.

[89] K. P. Pruessmann, M. Weiger, M. B. Scheidegger, and P. Boesiger, “SENSE: Sensitivity encoding for fast MRI,” *Magn. Reson. Med.*, vol. 42, no. 5, pp. 952–962, Nov. 1999, doi: 10.1002/(SICI)1522-2594(199911)42:5<952::AID-MRM16>3.0.CO;2-S.

[90] K. Setsompop *et al.*, “Pushing the limits of in vivo diffusion MRI for the Human Connectome Project,” *NeuroImage*, vol. 80, pp. 220–233, Oct. 2013, doi: 10.1016/j.neuroimage.2013.05.078.

[91] T. Zhao *et al.*, “Test-retest reliability of white matter structural brain networks: a multiband diffusion MRI study,” *Front. Hum. Neurosci.*, vol. 9, Feb. 2015, doi: 10.3389/fnhum.2015.00059.

[92] F. Callaghan, J. J. Maller, T. Welton, M. J. Middione, A. Shankaranarayanan, and S. M. Grieve, “Toward personalised diffusion MRI in psychiatry: improved delineation of fibre bundles with the highest-ever angular resolution in vivo tractography,” *Transl. Psychiatry*, vol. 8, no. 1, Dec. 2018, doi: 10.1038/s41398-018-0140-8.

[93] J. M. Guerrero *et al.*, “Optimizing the intrinsic parallel diffusivity in NODDI: An extensive empirical evaluation,” *PLOS ONE*, vol. 14, no. 9, p. e0217118, Sep. 2019, doi: 10.1371/journal.pone.0217118.

[94] S. Eriksson, S. Lasic, and D. Topgaard, “Isotropic diffusion weighting in PGSE NMR by magic-angle spinning of the q-vector,” *J. Magn. Reson.*, vol. 226, pp. 13–18, Jan. 2013, doi: 10.1016/j.jmr.2012.10.015.

[95] S. Lasič, F. Szczepankiewicz, S. Eriksson, M. Nilsson, and D. Topgaard, “Microanisotropy imaging: quantification of microscopic diffusion anisotropy and orientational order parameter by diffusion MRI with magic-angle spinning of the q-vector,” *Front. Phys.*, vol. 2, 2014, doi: 10.3389/fphy.2014.00011.

[96] F. Szczepankiewicz *et al.*, “Quantification of microscopic diffusion anisotropy disentangles effects of orientation dispersion from microstructure: Applications in healthy volunteers and in brain tumors,” *NeuroImage*, vol. 104, pp. 241–252, Jan. 2015, doi: 10.1016/j.neuroimage.2014.09.057.

[97] C.-F. Westin *et al.*, “Q-space trajectory imaging for multidimensional diffusion MRI of the human brain,” *NeuroImage*, vol. 135, pp. 345–362, Jul. 2016, doi: 10.1016/j.neuroimage.2016.02.039.

[98] D. Topgaard, “Chapter 7. NMR Methods for Studying Microscopic Diffusion Anisotropy,” in *New Developments in NMR*, R. Valiullin, Ed. Cambridge: Royal Society of Chemistry, 2016, pp. 226–259.

[99] D. G. Cory, “Measurement of translational displacement probabilities by NMR: An indicator of compartmentation,” *Magn. Reson. Med.*, vol. 14, no. 3, pp. 435–444, Jun. 1990, doi: 10.1002/mrm.1910140303.

[100] F. Szczepankiewicz, J. Sjölund, F. Ståhlberg, J. Lätt, and M. Nilsson, “Tensor-valued diffusion encoding for diffusional variance decomposition (DIVIDE): Technical feasibility in clinical MRI systems,” *PLOS ONE*, vol. 14, no. 3, p. e0214238, Mar. 2019, doi: 10.1371/journal.pone.0214238.

[101] M. Nilsson *et al.*, “Tensor-valued diffusion MRI in under 3 minutes: an initial survey of microscopic anisotropy and tissue heterogeneity in intracranial tumors,” *Magn. Reson. Med.*, vol. 83, no. 2, pp. 608–620, Feb. 2020, doi: 10.1002/mrm.27959.

[102] S. N. Jespersen, H. Lundell, C. K. Sønderby, and T. B. Dyrby, “Orientationally invariant metrics of apparent compartment eccentricity from double pulsed field gradient diffusion experiments: ORIENTATIONALLY INVARIANT DOUBLE PFG DIFFUSION,” *NMR Biomed.*, vol. 26, no. 12, pp. 1647–1662, Dec. 2013, doi: 10.1002/nbm.2999.

[103] J. H. Jensen, E. S. Hui, and J. A. Helpern, “Double-pulsed diffusional kurtosis imaging,” *NMR Biomed.*, vol. 27, no. 4, pp. 363–370, Apr. 2014, doi: 10.1002/nbm.3030.

[104] M. Edén, “Computer simulations in solid-state NMR. III. Powder averaging: Computer Simulations in Solid-State NMR. III,” *Concepts Magn. Reson. Part A*, vol. 18A, no. 1, pp. 24–55, 2003, doi: 10.1002/cmr.a.10065.

[105] M. Röding *et al.*, “The gamma distribution model for pulsed-field gradient NMR studies of molecular-weight distributions of polymers,” *J. Magn. Reson.*, vol. 222, pp. 105–111, Sep. 2012, doi: 10.1016/j.jmr.2012.07.005.

[106] F. Szczepankiewicz, C.-F. Westin, F. Ståhlberg, and M. Nilsson, “Minimum number of diffusion encoding directions required to yield a rotationally invariant powder average signal in single and double diffusion encoding,” in *Proc. Int. Soc. Magn. Reson. Med.*, Singapore, 2016, vol. 24, p. 2065.

[107] D. C. Alexander *et al.*, “Orientationally invariant indices of axon diameter and density from diffusion MRI,” *NeuroImage*, vol. 52, no. 4, pp. 1374–1389, Oct. 2010, doi: 10.1016/j.neuroimage.2010.05.043.

[108] Y. Assaf, T. Blumenfeld-Katzir, Y. Yovel, and P. J. Basser, “AxCaliber: a method for measuring axon diameter distribution from diffusion MRI,” *Magn. Reson. Med.*, vol. 59, no. 6, pp. 1347–1354, Jun. 2008, doi: 10.1002/mrm.21577.

[109] S. N. Jespersen, C. D. Kroenke, L. Østergaard, J. J. H. Ackerman, and D. A. Yablonskiy, “Modeling dendrite density from magnetic resonance diffusion measurements,” *NeuroImage*, vol. 34, no. 4, pp. 1473–1486, Feb. 2007, doi: 10.1016/j.neuroimage.2006.10.037.

[110] G. J. Stanisz, A. Szafer, G. A. Wright, and R. M. Henkelman, “An analytical model of restricted diffusion in bovine optic nerve,” *Magn. Reson. Med.*, vol. 37, no. 1, pp. 103–111, Jan. 1997.

[111] K. V. Mardia and P. E. Jupp, Eds., *Directional Statistics*. Hoboken, NJ, USA: John Wiley & Sons, Inc., 1999.

[112] A. Szafer, J. Zhong, and J. C. Gore, “Theoretical model for water diffusion in tissues,” *Magn. Reson. Med.*, vol. 33, no. 5, pp. 697–712, May 1995.

[113] I. O. Jelescu and M. D. Budde, “Design and Validation of Diffusion MRI Models of White Matter,” *Front. Phys.*, vol. 5, p. 61, Nov. 2017, doi: 10.3389/fphy.2017.00061.

[114] N. P. Skinner, S. N. Kurpad, B. D. Schmit, L. Tugan Muftuler, and M. D. Budde, “Rapid in vivo detection of rat spinal cord injury with double-diffusion-encoded magnetic resonance spectroscopy,” *Magn. Reson. Med.*, vol. 77, no. 4, pp. 1639–1649, 2017, doi: 10.1002/mrm.26243.

[115] S. N. Jespersen, J. L. Olesen, B. Hansen, and N. Shemesh, “Diffusion time dependence of microstructural parameters in fixed spinal cord,” *NeuroImage*, vol. 182, pp. 329–342, 15 2018, doi: 10.1016/j.neuroimage.2017.08.039.

[116] J. Veraart, D. S. Novikov, and E. Fieremans, “TE dependent Diffusion Imaging (TEdDI) distinguishes between compartmental T2 relaxation times,” *NeuroImage*, vol. 182, pp. 360–369, 15 2018, doi: 10.1016/j.neuroimage.2017.09.030.

[117] D. S. Novikov, J. Veraart, I. O. Jelescu, and E. Fieremans, “Rotationally-invariant mapping of scalar and orientational metrics of neuronal microstructure with diffusion MRI,” *NeuroImage*, vol. 174, pp. 518–538, Jul. 2018, doi: 10.1016/j.neuroimage.2018.03.006.

[118] E. Kaden, N. D. Kelm, R. P. Carson, M. D. Does, and D. C. Alexander, “Multi-compartment microscopic diffusion imaging,” *NeuroImage*, vol. 139, pp. 346–359, Oct. 2016, doi: 10.1016/j.neuroimage.2016.06.002.

[119] I. O. Jelescu, J. Veraart, E. Fieremans, and D. S. Novikov, “Degeneracy in model parameter estimation for multi-compartmental diffusion in neuronal tissue: Degeneracy in

Model Parameter Estimation of Diffusion in Neural Tissue," *NMR Biomed.*, vol. 29, no. 1, pp. 33–47, Jan. 2016, doi: 10.1002/nbm.3450.

[120] I. O. Jelescu, J. Veraart, V. Adisetiyo, S. S. Milla, D. S. Novikov, and E. Fieremans, "One diffusion acquisition and different white matter models: how does microstructure change in human early development based on WMTI and NODDI?," *NeuroImage*, vol. 107, pp. 242–256, Feb. 2015, doi: 10.1016/j.neuroimage.2014.12.009.

[121] J. M. Guerrero, N. Adluru, S. R. Kecskemeti, R. J. Davidson, and A. L. Alexander, "Investigating the effects of intrinsic diffu- sivity on neurite orientation dispersion and density imaging (NODDI).," presented at the International Society for Magnetic Resonance in Medicine (ISMRM), Singapore, 2016.

[122] E. Genç *et al.*, "Diffusion markers of dendritic density and arborization in gray matter predict differences in intelligence," *Nat. Commun.*, vol. 9, no. 1, p. 1905, 15 2018, doi: 10.1038/s41467-018-04268-8.

[123] H. Fukutomi *et al.*, "Neurite imaging reveals microstructural variations in human cerebral cortical gray matter," *NeuroImage*, vol. 182, pp. 488–499, 15 2018, doi: 10.1016/j.neuroimage.2018.02.017.

[124] M. Tariq, T. Schneider, D. C. Alexander, C. A. Gandini Wheeler-Kingshott, and H. Zhang, "Bingham-NODDI: Mapping anisotropic orientation dispersion of neurites using diffusion MRI," *NeuroImage*, vol. 133, pp. 207–223, 2016, doi: 10.1016/j.neuroimage.2016.01.046.

[125] H. Farooq *et al.*, "Microstructure Imaging of Crossing (MIX) White Matter Fibers from diffusion MRI," *Sci. Rep.*, vol. 6, p. 38927, 16 2016, doi: 10.1038/srep38927.

[126] E. Panagiotaki *et al.*, "Noninvasive Quantification of Solid Tumor Microstructure Using VERDICT MRI," *Cancer Res.*, vol. 74, no. 7, pp. 1902–1912, Apr. 2014, doi: 10.1158/0008-5472.CAN-13-2511.

[127] M. Jenkinson, C. F. Beckmann, T. E. J. Behrens, M. W. Woolrich, and S. M. Smith, "FSL," *NeuroImage*, vol. 62, no. 2, pp. 782–790, Aug. 2012, doi: 10.1016/j.neuroimage.2011.09.015.

[128] Y. Zhang, M. Brady, and S. Smith, "Segmentation of brain MR images through a hidden Markov random field model and the expectation-maximization algorithm," *IEEE Trans. Med. Imaging*, vol. 20, no. 1, pp. 45–57, Jan. 2001, doi: 10.1109/42.906424.

[129] J. Veraart, E. Fieremans, and D. S. Novikov, "Universal power-law scaling of water diffusion in human brain defines what we see with MRI," *ArXiv160909145 Phys. Q-Bio*, Sep. 2016, Accessed: Jun. 27, 2020. [Online]. Available: http://arxiv.org/abs/1609.09145.

[130] N. Kunz *et al.*, “Assessing white matter microstructure of the newborn with multi-shell diffusion MRI and biophysical compartment models,” *NeuroImage*, vol. 96, pp. 288–299, Aug. 2014, doi: 10.1016/j.neuroimage.2014.03.057.

[131] J. Veraart, E. Fieremans, U. rudrapatna, D. Jones, and D. S. Novikov, “Biophysical modeling of the gray matter: does the ‘stick’ model hold?,” Paris, France, 2018.

[132] P. Mukherjee *et al.*, “Diffusion-tensor MR imaging of gray and white matter development during normal human brain maturation,” *AJNR Am. J. Neuroradiol.*, vol. 23, no. 9, pp. 1445–1456, Oct. 2002.

[133] A. V. Faria *et al.*, “Atlas-based analysis of neurodevelopment from infancy to adulthood using diffusion tensor imaging and applications for automated abnormality detection,” *NeuroImage*, vol. 52, no. 2, pp. 415–428, Aug. 2010, doi: 10.1016/j.neuroimage.2010.04.238.

[134] S. Yoshida, K. Oishi, A. V. Faria, and S. Mori, “Diffusion tensor imaging of normal brain development,” *Pediatr. Radiol.*, vol. 43, no. 1, pp. 15–27, Jan. 2013, doi: 10.1007/s00247-012-2496-x.

[135] D. C. Dean *et al.*, “Mapping White Matter Microstructure in the One Month Human Brain,” *Sci. Rep.*, vol. 7, no. 1, p. 9759, 29 2017, doi: 10.1038/s41598-017-09915-6.

[136] A. Daducci, E. J. Canales-Rodríguez, H. Zhang, T. B. Dyrby, D. C. Alexander, and J.-P. Thiran, “Accelerated Microstructure Imaging via Convex Optimization (AMICO) from diffusion MRI data,” *NeuroImage*, vol. 105, pp. 32–44, Jan. 2015, doi: 10.1016/j.neuroimage.2014.10.026.

[137] F. Grussu *et al.*, “Neurite dispersion: a new marker of multiple sclerosis spinal cord pathology?,” *Ann. Clin. Transl. Neurol.*, vol. 4, no. 9, pp. 663–679, 2017, doi: 10.1002/acn3.445.

[138] B. G. Travers *et al.*, “Diffusion tensor imaging in autism spectrum disorder: a review,” *Autism Res. Off. J. Int. Soc. Autism Res.*, vol. 5, no. 5, pp. 289–313, Oct. 2012, doi: 10.1002/aur.1243.

[139] P. A. Narayana, “White matter changes in patients with mild traumatic brain injury: MRI perspective,” *Concussion*, vol. 2, no. 2, p. CNC35, Jun. 2017, doi: 10.2217/cnc-2016-0028.

[140] D. C. Dean *et al.*, “Multivariate characterization of white matter heterogeneity in autism spectrum disorder,” *NeuroImage Clin.*, vol. 14, pp. 54–66, 2017, doi: 10.1016/j.nicl.2017.01.002.

[141] M. L. Lipton *et al.*, “Robust detection of traumatic axonal injury in individual mild traumatic brain injury patients: Intersubject variation, change over time and bidirectional

changes in anisotropy," *Brain Imaging Behav.*, vol. 6, no. 2, pp. 329–342, Jun. 2012, doi: 10.1007/s11682-012-9175-2.

[142] P. C. Mahalanobis, "On the generalized distance in statistics.," *Natl. Inst. Sci. India*, vol. II, no. 1, 1936.

[143] M. Shaker, D. Erdogmus, J. Dy, and S. Bouix, "Subject-specific abnormal region detection in traumatic brain injury using sparse model selection on high dimensional diffusion data," *Med. Image Anal.*, vol. 37, pp. 56–65, Apr. 2017, doi: 10.1016/j.media.2017.01.005.

[144] W. Van Hecke, A. Leemans, and L. Emsell, "DTI Analysis Methods: Voxel-Based Analysis," in *Diffusion Tensor Imaging: A Practical Handbook*, W. Van Hecke, L. Emsell, and S. Sunaert, Eds. New York, NY: Springer New York, 2016, pp. 183–203.

[145] N. Kim, C. A. Branch, M. Kim, and M. L. Lipton, "Whole brain approaches for identification of microstructural abnormalities in individual patients: comparison of techniques applied to mild traumatic brain injury," *PloS One*, vol. 8, no. 3, p. e59382, 2013, doi: 10.1371/journal.pone.0059382.

[146] G. Gyebnár *et al.*, "Personalized microstructural evaluation using a Mahalanobis-distance based outlier detection strategy on epilepsy patients' DTI data – Theory, simulations and example cases," *PLOS ONE*, vol. 14, no. 9, p. e0222720, Sep. 2019, doi: 10.1371/journal.pone.0222720.

[147] J. D. Yeatman, R. F. Dougherty, N. J. Myall, B. A. Wandell, and H. M. Feldman, "Tract Profiles of White Matter Properties: Automating Fiber-Tract Quantification," *PLoS ONE*, vol. 7, no. 11, p. e49790, Nov. 2012, doi: 10.1371/journal.pone.0049790.

[148] J. Wasserthal, P. Neher, and K. H. Maier-Hein, "TractSeg - Fast and accurate white matter tract segmentation," *NeuroImage*, vol. 183, pp. 239–253, Dec. 2018, doi: 10.1016/j.neuroimage.2018.07.070.

[149] B. Jeurissen, J.-D. Tournier, T. Dhollander, A. Connelly, and J. Sijbers, "Multi-tissue constrained spherical deconvolution for improved analysis of multi-shell diffusion MRI data," *NeuroImage*, vol. 103, pp. 411–426, Dec. 2014, doi: 10.1016/j.neuroimage.2014.07.061.

[150] E. Garyfallidis, M. Brett, M. M. Correia, G. B. Williams, and I. Nimmo-Smith, "QuickBundles, a Method for Tractography Simplification," *Front. Neurosci.*, vol. 6, 2012, doi: 10.3389/fnins.2012.00175.

[151] E. Garyfallidis *et al.*, "Dipy, a library for the analysis of diffusion MRI data," *Front. Neuroinformatics*, vol. 8, Feb. 2014, doi: 10.3389/fninf.2014.00008.

[152] I. Benou, R. Veksler, A. Friedman, and T. R. Raviv, “Combining white matter diffusion and geometry for tract-specific alignment and variability analysis,” *NeuroImage*, vol. 200, pp. 674–689, Oct. 2019, doi: 10.1016/j.neuroimage.2019.05.003.

[153] S. St-Jean, M. Chamberland, M. A. Viergever, and A. Leemans, “Reducing variability in along-tract analysis with diffusion profile realignment,” *NeuroImage*, vol. 199, pp. 663–679, Oct. 2019, doi: 10.1016/j.neuroimage.2019.06.016.

[154] M. Frenkel and R. Basri, “Curve Matching Using the Fast Marching Method,” in *Energy Minimization Methods in Computer Vision and Pattern Recognition*, vol. 2683, A. Rangarajan, M. Figueiredo, and J. Zerubia, Eds. Berlin, Heidelberg: Springer Berlin Heidelberg, 2003, pp. 35–51.

[155] K. I. Penny, “Appropriate Critical Values When Testing for a Single Multivariate Outlier by Using the Mahalanobis Distance,” *Appl. Stat.*, vol. 45, no. 1, p. 73, 1996, doi: 10.2307/2986224.

[156] S. S. Wilks, “Multivariate Statistical Outliers,” *Sankhyā Indian J. Stat.*, vol. 25, no. 4, pp. 407–26, 1963.

[157] F. G. Hillary *et al.*, “Changes in resting connectivity during recovery from severe traumatic brain injury,” *Int. J. Psychophysiol.*, vol. 82, no. 1, pp. 115–123, Oct. 2011, doi: 10.1016/j.ijpsycho.2011.03.011.

[158] V. Anderson and C. Catroppa, “Memory outcome at 5 years post-childhood traumatic brain injury,” *Brain Inj.*, vol. 21, no. 13–14, pp. 1399–1409, Jan. 2007, doi: 10.1080/02699050701785070.

[159] D. P. M. Tromp *et al.*, “Reduced Structural Connectivity of a Major Frontolimbic Pathway in Generalized Anxiety Disorder,” *Arch. Gen. Psychiatry*, vol. 69, no. 9, p. 925, Sep. 2012, doi: 10.1001/archgenpsychiatry.2011.2178.

[160] C. P. Johnson, J. Juranek, L. A. Kramer, M. R. Prasad, P. R. Swank, and L. Ewing-Cobbs, “Predicting Behavioral Deficits in Pediatric Traumatic Brain Injury Through Uncinate Fasciculus Integrity,” *J. Int. Neuropsychol. Soc.*, vol. 17, no. 4, pp. 663–673, Apr. 2011, doi: 10.1017/S1355617711000464.

[161] J. Juranek *et al.*, “Mean diffusivity in the amygdala correlates with anxiety in pediatric TBI,” *Brain Imaging Behav.*, vol. 6, no. 1, pp. 36–48, Mar. 2012, doi: 10.1007/s11682-011-9140-5.

[162] T. B. Fay, K. O. Yeates, S. L. Wade, D. Drotar, T. Stancin, and H. G. Taylor, “Predicting longitudinal patterns of functional deficits in children with traumatic brain injury.,” *Neuropsychology*, vol. 23, no. 3, pp. 271–282, 2009, doi: 10.1037/a0014936.

[163] L. Ewing-Cobbs *et al.*, "Arrested development and disrupted callosal microstructure following pediatric traumatic brain injury: relation to neurobehavioral outcomes," *NeuroImage*, vol. 42, no. 4, pp. 1305–1315, Oct. 2008, doi: 10.1016/j.neuroimage.2008.06.031.

[164] E. D. Bigler *et al.*, "Heterogeneity of brain lesions in pediatric traumatic brain injury.," *Neuropsychology*, vol. 27, no. 4, pp. 438–451, 2013, doi: 10.1037/a0032837.

[165] M. A. Boss, T. Chevenert, and E. Jackson, "Multicenter study of reproducibility of wide range of ADC at 0 C.," presented at the RSNA Annual Meeting, 2015.

[166] A. M. Dale, B. Fischl, and M. I. Sereno, "Cortical Surface-Based Analysis," *NeuroImage*, vol. 9, no. 2, pp. 179–194, Feb. 1999, doi: 10.1006/nimg.1998.0395.

[167] M. Jenkinson, P. Bannister, M. Brady, and S. Smith, "Improved Optimization for the Robust and Accurate Linear Registration and Motion Correction of Brain Images," *NeuroImage*, vol. 17, no. 2, pp. 825–841, Oct. 2002, doi: 10.1006/nimg.2002.1132.

[168] A. Leemans and D. K. Jones, "The *B* -matrix must be rotated when correcting for subject motion in DTI data," *Magn. Reson. Med.*, vol. 61, no. 6, pp. 1336–1349, Jun. 2009, doi: 10.1002/mrm.21890.

[169] B. B. Avants, C. L. Epstein, M. Grossman, and J. C. Gee, "Symmetric diffeomorphic image registration with cross-correlation: evaluating automated labeling of elderly and neurodegenerative brain," *Med. Image Anal.*, vol. 12, no. 1, pp. 26–41, Feb. 2008, doi: 10.1016/j.media.2007.06.004.

[170] J.-D. Tournier *et al.*, "MRtrix3: A fast, flexible and open software framework for medical image processing and visualisation," *NeuroImage*, vol. 202, p. 116137, Nov. 2019, doi: 10.1016/j.neuroimage.2019.116137.

[171] J. M. Guerrero, N. Adluru, D. C. Dean, and A. L. Alexander, "Voxel-wise Mahalanobis Distance (MaD-Vox): a multivariate approach to single subject analysis," Paris, France, 2018.

[172] R. Mills, "Self-diffusion in normal and heavy water in the range 1-45.deg.," *J. Phys. Chem.*, vol. 77, no. 5, pp. 685–688, Mar. 1973, doi: 10.1021/j100624a025.

[173] P. S. Tofts *et al.*, "Test liquids for quantitative MRI measurements of self-diffusion coefficient in vivo," *Magn. Reson. Med.*, vol. 43, no. 3, pp. 368–374, Mar. 2000.

[174] F. Wagner *et al.*, "Temperature and concentration calibration of aqueous polyvinylpyrrolidone (PVP) solutions for isotropic diffusion MRI phantoms," *PLOS ONE*, vol. 12, no. 6, p. e0179276, Jun. 2017, doi: 10.1371/journal.pone.0179276.

[175] J. Hiltunen, R. Hari, V. Jousmäki, K. Müller, R. Sepponen, and R. Joensuu, "Quantification of mechanical vibration during diffusion tensor imaging at 3 T," *NeuroImage*, vol. 32, no. 1, pp. 93–103, Aug. 2006, doi: 10.1016/j.neuroimage.2006.03.004.

[176] D. G. Tomasi and T. Ernst, "Echo planar imaging at 4 tesla with minimum acoustic noise," *J. Magn. Reson. Imaging*, vol. 18, no. 1, pp. 128–130, Jul. 2003, doi: 10.1002/jmri.10326.

[177] C. M. Ireland *et al.*, "A novel acoustically quiet coil for neonatal MRI system: Acoustically Quiet Coil for Neonatal MRI System," *Concepts Magn. Reson. Part B Magn. Reson. Eng.*, vol. 45, no. 3, pp. 107–114, Aug. 2015, doi: 10.1002/cmr.b.21287.

[178] M. Inoue, K. Hashizaki, H. Taguchi, and Y. Saito, "Preparation and Characterization of n-Alkane/Water Emulsion Stabilized by Cyclodextrin," *J. Oleo Sci.*, vol. 58, no. 2, pp. 85–90, 2009, doi: 10.5650/jos.58.85.

[179] M. Inoue, K. Hashizaki, H. Taguchi, and Y. Saito, "Formation and Characterization of Emulsions Using β-Cyclodextrin as an Emulsifier," *Chem. Pharm. Bull. (Tokyo)*, vol. 56, no. 5, pp. 668–671, 2008, doi: 10.1248/cpb.56.668.

[180] M. Chamberland *et al.*, "Dimensionality reduction of diffusion MRI measures for improved tractometry of the human brain," *NeuroImage*, vol. 200, pp. 89–100, Oct. 2019, doi: 10.1016/j.neuroimage.2019.06.020.